GEOLOGICA ULTRAIECTINA

Mededelingen van de
Faculteit Aardwetenschappen der
Rijksuniversiteit te Utrecht

Nr. 311

Geological storage of CO_2:
Mechanical and chemical effects on host and seal formations

Suzanne Hangx

cover: tulip field in May at the Keukenhof, Lisse, the Netherlands

The research described in this thesis was carried out under the program *Earth Materials: properties and processes* of the Vening Meinesz Research School of Geodynamics (VMSG). The project was funded by Shell International Exploration and Production, contract number 4600002284, and also supported by WorkPackage 4 on Mineralisation of the Dutch national research program CATO on CO_2 capture, transport and storage.

The research was carried out at:
Experimental Rock Deformation Laboratory
Faculty of Geosciences
Utrecht University
Budapestlaan 4
3584 CD Utrecht
The Netherlands

www.geo.uu.nl

ISBN/EAN: 978-90-5744-172-1

Geological storage of CO_2:
Mechanical and chemical effects on host and seal formations

Geologische opslag van CO_2:
Mechanische en chemische effecten op
reservoirgesteenten en deklagen

(met een korte samenvatting in het Nederlands)

Proefschrift

ter verkrijging van de graad van doctor aan de Universiteit Utrecht op gezag van de rector magnificus, prof. dr. J.C. Stoof, ingevolge het besluit van het college voor promoties in het openbaar te verdedigen op maandag 14 september 2009 des ochtends te 10.30 uur

door

Suzanne Johanna Theodora Hangx

geboren op 12 juli 1981, te Weert

Promotor: Prof. dr. C.J. Spiers

“

Endurance is one of the most difficult disciplines, but it is to the one who endures that the final victory comes.

- Buddha

Members of the dissertation committee:

Prof. A. Hajash
Texas A&M University, United States of America

Dr. J.P. Kaszuba
University of Wyoming, United States of America

Prof. P.G. Meredith
University College, London, United Kingdom

Prof. W.C. Turkenburg
Utrecht University, the Netherlands

Prof. T.-f. Wong
State University of New York at Stony Brook, United States of America

Contents

Summary **XIII**

Chapter 1. General introduction **1**
1.1 Background and scope of the study 3
1.2 Main mechanisms and processes occurring during subsurface storage of CO_2 4
1.2.1 Hydrodynamic trapping modes and the properties of CO_2 4
1.2.2 Mineral trapping of CO_2 - geochemical effects 7
1.2.3 Structural trapping of CO_2 - geomechanical and hydromechanical effects 9
1.3 The road so far: outstanding research questions 11
1.4 Aims of this study 12
1.5 Structure 12

Chapter 2. Reaction of plagioclase feldspars with CO_2 under hydrothermal conditions **15**
Abstract 16
2.1 Introduction 17
2.2 Methodology 18
2.2.1 Preparation of samples and solutions 18
2.2.2 Experimental design and procedure 20
2.3 Results 22
2.3.1 Anorthite-CO_2-water/brine experiments 23
2.3.1.1 SEM observations on anorthite grain surfaces 23
2.3.1.2 XRD data 24
2.3.1.3 Infrared spectra 24
2.3.1.4 Thermogravimetric analyses 26
2.3.1.5 FEG EPMA results 27
2.3.2 Albite-CO_2-water/brine experiments 27
2.3.3 Magnesite precipitation experiments 28
2.4 Discussion 29
2.4.1 Feldspar experiments - identity and formation of

secondary phases 30
2.4.2 Comparison with previous work on plagioclase 31
2.4.3 Significance of the carbonate control experiments 33
2.4.4 Implications 33
2.5 Conclusions 35
Acknowledgements 36

Chapter 3. Creep of simulated reservoir sands and coupled chemical-mechanical effects of CO_2 injection 37
Abstract 38
3.1 Introduction 39
3.2 Experimental method 40
3.2.1 Materials and pore fluid preparation 40
3.2.2 Experimental set-up 41
3.2.3 Testing procedure 43
3.2.4 Data acquisition and processing 46
3.2.5 Microstructural and analytical methods 47
3.3 Mechanical data 47
3.3.1 Quartz data 47
3.3.1.1 Instantaneous vs. time-dependent strain 47
3.3.1.2 Effect of pH and chemical environment on creep 48
3.3.2 Feldspar data 49
3.3.2.1 Instantaneous vs. time-dependent strain 49
3.3.2.2 Compaction creep in the presence of water only (no CO_2 injection) 50
3.3.2.3 Influence of added CO_2 on creep – effects on grain size dependence and AE 53
3.3.2.4 Effect of fluid composition on creep rate 55
3.4 Microstructural observations 56
3.4.1 Quartz microstructures 57
3.4.2 Feldspar microstructures 58
3.4.2.1 Effect of grain size without added CO_2 58
3.4.2.2 CO_2, pH and salinity effects 60
3.5 Discussion 61
3.5.1 Time-independent compaction of quartz 61
3.5.2 Mechanisms of compaction creep in the wet quartz experiments 63
3.5.3 Time-independent compaction of feldspar 65
3.5.4 Mechanisms of compaction creep in wet feldspar

experiments without additives 66
3.5.5 Effects of CO_2 on compaction creep of wet feldspar 68
3.5.6 Effect of acid/alkaline additives, salinity and dry CO_2 on compaction creep 69
3.5.7 Implications 70
3.6 Conclusions 71
Appendix A 73
Acknowledgements 75

Chapter 4. Mechanical behaviour of anhydrite caprock and implications for CO_2 sealing integrity 77
Abstract 78
4.1 Introduction 79
4.2 Experimental methods 80
4.2.1 Sample material and pore fluid preparation 82
4.2.2 Experimental set-up 83
4.2.3 Sample assembly 84
4.2.4 Testing procedure 85
4.2.5 Data acquisition and processing 86
4.3 Results 86
4.3.1 Mechanical data and failure modes 86
4.3.2 Dry experiments at room temperature 86
4.3.3 Dry experiments at 80°C 90
4.3.4 Wet experiments (saturated $CaSO_4$ solution) 92
4.3.5 Wet/CO_2 experiments (CO_2-saturated $CaSO_4$ solution) 94
4.4 Microstructural observations 95
4.4.1 Brittle regime: dry anhydrite 97
4.4.2 Semi-brittle regime: dry anhydrite 99
4.4.3 Semi-brittle regime: wet and wet/CO_2 experiments 99
4.5 Discussion 99
4.5.1 Failure and dilatancy criteria for dry anhydrite at 20 and 80°C 101
4.5.2 Effect of temperature on strength and dilatation 103
4.5.3 Comparison with previous strength data 104
4.5.4 Effects and mechanisms of fluid penetration: water vs. CO_2 105
4.5.5 Implications of mechanical data for seal integrity – a simple generic study of caprock flexure during depletion/injection 107
4.5.6 Possible long-term effects of reaction with supercritical CO_2 and water 112

4.6 Conclusions 113
Acknowledgements 115

Chapter 5. The effect of deformation on permeability development in anhydrite and implications for caprock integrity during geological storage of CO_2 117
Abstract 118
5.1 Introduction 119
5.2 Experimental methods 120
5.2.1 Samples 121
5.2.2 Experimental apparatus 121
5.2.3 Sample assembly 123
5.2.4 Experimental procedure 123
5.2.5 Data acquisition and processing 125
5.3 Results 127
5.3.1 Mechanical data and sample failure modes 127
5.3.2 Permeability data 129
5.3.2.1 Dynamic experiments 129
5.3.2.2 Static experiments 132
5.3.3 Microstructural observations 133
5.4 Discussion 135
5.4.1 Failure behaviour and permeability evolution 136
5.4.2 Permeability development with strain - comparison with other studies of low porosity rocks 139
5.4.3 Effect of mean stress on post-failure permeability 140
5.4.4 Implications for caprock integrity 142
5.5 Conclusions 144
Acknowledgements 146

Chapter 6. Coastal spreading of olivine to control atmospheric CO_2 concentrations: a critical analysis of viability 147
Abstract 148
6.1 Introduction 149
6.2 Reaction of CO_2 with olivine and associated sequestration capacity 150
6.3 Dissolution of olivine under Earth surface conditions 152
6.3.1 Dissolution rate of olivine: Effect of pH and temperature 152
6.3.2 Effect of fluid composition on dissolution rate 153

6.3.3 Effects at the dissolving olivine surface 155
6.3.4 Practical estimates of R_{diss} 155
6.4 Reaction progress with time and effect of grain size: a simple model 156
6.5 CO_2 production due to mining and grinding 160
6.6 Feasibility of CO_2 sequestration via coastal spreading of olivine 164
6.6.1 Global scenario 164
6.6.2 The Dutch scenario 166
6.6.3 Synthesis 167
6.7 Coastal vs. land spreading 168
6.8 Conclusions 168
Acknowledgements 170

Chapter 7. General conclusions and suggestions for future research 171
7.1 Conclusions 173
7.1.1 CO_2 mineralisation reactions in feldspathic sandstones 173
7.1.2 Creep phenomena in sandstones and chemical-mechanical effects of CO_2 injection 174
7.1.3 Mechanical behaviour of anhydrite caprock and the effect of CO_2 175
7.1.4 Permeability development in deforming anhydrite 175
7.1.5 A critical analysis of coastal weathering of olivine 176
7.2 Suggestions for future research 177

Bibliography 181

Samenvatting 203

Acknowledgements 207

Curriculum Vitae 213

Summary

The socio-economic impact of global warming resulting from anthropogenic CO_2 emissions has lead to much attention for carbon mitigation strategies in recent years. One of the most promising ways of disposing of CO_2 is through Carbon Capture and Storage (CCS), entailing CO_2 capture at source, followed by long-term geological storage. Possible storage sites include depleted oil and gas reservoirs, saline aquifers and unminable coal seams. The former is relevant for countries with an extensive hydrocarbon production and transport infrastructure, such as the Netherlands. However, long-term subsurface storage of CO_2 in depleted reservoirs may induce a range of chemical and mechanical processes in response to disturbances in existing chemical equilibria and in the state of stress within the reservoir-caprock system. Such processes include, but are not limited to, mineralisation reactions, reservoir creep induced by CO_2-water-rock interactions, and mechanical failure of and permeability development in the seal formation. While some of these processes, such as mineralisation, may enhance the CO_2 storage capacity of a reservoir, others may potentially reduce reservoir and caprock integrity, causing leakage of CO_2 to the geological environment and ultimately to the atmosphere. To date, many of these processes are still poorly constrained.

The work presented in this thesis focuses on obtaining a fundamental understanding of the effect of CO_2 on mineralisation reactions and on time-dependent (i.e. long-term) reservoir compaction or creep phenomena, as well as on caprock stability and permeability development. As the project formed part of the Dutch National Research Program CATO, on CO_2 capture, transport and storage, it has been directed at reaction and deformation effects in sandstone and anhydrite, which are the main rock types representing potential host and seal formations for subsurface CO_2 storage in the Netherlands. In response to much media attention for the concept of CO_2 removal from the atmosphere by (coastal) weathering of imported, sand-grade olivine, the feasibility of this concept has also been assessed.

The following lines of attack were adopted to achieve the goals of the project:

- Batch reaction experiments under hydrothermal conditions to investigate the

nature of mineralisation reactions occurring in plagioclase-CO_2-water/brine systems,
- Compaction creep experiments on wet quartz and feldspar aggregates to understand the effect of CO_2 on creep phenomena under reservoir conditions,
- Conventional triaxial compression experiments on anhydrite caprock samples, with special attention for material strength, damage development and the effects of (CO_2-saturated) fluids under reservoir conditions,
- Permeability experiments on anhydrite caprock samples at room temperature aimed at addressing the effect of deformation, mechanical damage and failure on permeability development,
- An analysis of literature data and the development of a kinetics-based model to calculate the rate and evaluate the feasibility of CO_2 removal from the atmosphere by coastal weathering of olivine.

The scope and scientific context of this thesis are introduced in **Chapter 1** and the aims of the present research are defined. The first part of this thesis (Chapters 2 and 3) focuses on the chemical and mechanical effects of CO_2 injection on sandstone host formations. **Chapter 2** addresses the nature of mineralisation reactions occurring in feldspar-bearing sandstones. To gain insight into these reactions, batch reaction experiments were performed on plagioclase feldspars (anorthite and albite) in the presence of CO_2, under hydrothermal conditions (T = 200-300°C, P_T = 6-18 MPa). Geochemical codes predict precipitation of CO_2-bearing phases (calcite and dawsonite) under conditions ranging from in-situ pressures and temperatures to those used in these experiments. However, we observed precipitation of secondary clays (kaolinite and illite and/or smectite), boehmite and hydrotalcite. Additional experiments showed that carbonates would have been preserved if formed, though precipitation was dependent on the presence of carbonate substrate, indicating a nucleation barrier for precipitation. The results imply that reaction strongly depends on conditions and fluid-rock composition, and that in plagioclase-bearing systems, clay precipitation will tend to occur in advance of or preferentially to carbonate precipitation, unless a suitable carbonate-seeding material or substrate is present.

In addition to chemical reactions with the reservoir rock, chemical-mechanical effects related to CO_2 injection may also be expected, such as creep due to dissolution reactions, CO_2-enhanced microcracking, or diffusive mass transfer processes like pressure solution. Such creep effects can potentially lead to reservoir compaction and associated damage to well-bore, caprock and fault-seal systems, particularly in the long term. **Chapter 3** describes a series of uniaxial experiments on wet granular quartz and feldspar aggregates, aimed at investigating the effect of CO_2 on compaction creep at pressures and temperatures up to reservoir conditions. Grain size, temperature, CO_2

partial pressure and applied effective stress were varied through relevant ranges to determine their individual effects. Solution pH was varied by the injection of CO_2 and the addition of acids and alkalis. Mechanical, microstructural and acoustic emission data suggested that the main mechanism of deformation was microcracking and associated grain rearrangement, with stress corrosion cracking (subcritical crack growth) controlling creep rate. Creep rates decreased with increasing solution pH for both wet quartz and feldspar samples. In the wet feldspar samples without added CO_2, creep rate depended positively on grain size and showed an apparent power law dependence upon applied effective stress, with a stress sensitivity of 1-2.5. Feldspar creep rate also depended weakly on temperature, with an apparent activation energy of ~10 kJ/mol. Injection of CO_2 at high pressure (10 MPa) and the concomitant acidification of the pore fluid significantly reduced creep rates in both quartz and feldspar aggregates, which is in line with known pH effects on stress corrosion cracking. The results thus show that the injection of CO_2 into quartz and feldspar-bearing sands and sandstones inhibits grain-scale microcracking processes. On this basis, it is inferred that geomechanical effects associated with CO_2 injection into depleted reservoirs, such as compaction creep and associated surface subsidence, will be negligible compared with the expected poro-elastic expansion or heave of the reservoir.

The second part of this thesis (Chapters 4 and 5) is concerned with seal integrity, which is the key factor controlling successful long-term geological CO_2 storage in depleted gas reservoirs. Changes in stress state induced by CO_2 injection, and associated mechanical deformation and damage effects, can potentially influence caprock and fault integrity. In the longer term, the mechanical strength and transport properties of both caprocks and sealed faults can be affected by chemical interactions. In **Chapter 4**, we address the mechanical strength and damage behaviour of anhydrite caprock taken from the base of the Dutch Zechstein formation (Permian). Conventional triaxial compression experiments were performed at 20-80°C, 1.5-50 MPa confining pressure and relatively rapid strain rates of ~10^{-5} s^{-1}. In addition, we investigated the effect of high-pressure pore fluids (P_f = 15 MPa), namely $CaSO_4$ solution and CO_2-saturated $CaSO_4$ solution, on strength and dilatation. Fluid penetration prior to failure resulted in a reduction in failure strength of our wet ± CO_2 samples according to the effective stress principle, while the volumetric behaviour remained unchanged compared with dry samples. Fluid penetration during failure was too slow to influence mechanical and volumetric behaviour. No significant short-term chemical weakening effects, such as enhanced stress corrosion cracking, were observed. Penetration by CO_2-saturated fluid was easier than by $CaSO_4$ solution due to the lower interfacial tension of the former. The results for dry anhydrite allowed derivation of failure and

dilatancy envelopes in (Mogi) stress space. We combined simple analytical flexure calculations with these envelopes to assess if anhydrite will fracture or exhibit dilatant damage during reservoir depletion or CO_2 injection. The results showed that caprock flexure, under such conditions, will not compromise caprock integrity. For simple CO_2 penetration of the seal formation by reaction with pore fluid (no advective transport), penetration depths of ~30 cm in 1000 years and ~3 m in 10000 years may be reached, which is insignificant for typical anhydrite caprock thicknesses (e.g. 30-50 m in the Netherlands).

The effects of deformation and state of stress on permeability development in anhydrite are quantified and discussed in **Chapter 5**. A further series of triaxial compression experiments, now combined with argon gas permeametry, were performed at room temperature, confining pressures of 3.5-25 MPa, pore pressures of 1-1.2 MPa and strain rates of $\sim 10^{-6}$-10^{-7} s^{-1}. For Zechstein anhydrite, argon gas permeametry performed during deformation showed a change from "impermeable" to permeable as a result of deformation and dilatation. The onset of measurable permeability ($\kappa > 10^{-21}$ m^2) was associated with an increase in rate of dilatation with axial strain at low confining pressure, and, at higher confining pressures, by the turning point from compaction to dilatation in the volumetric vs. axial stress-strain curve. The observed permeability development was related to the establishment of a connected crack/void network, which could be explained in terms of percolation theory for low permeability rocks undergoing microcrack damage and failure. Sample permeability in our tests was largely controlled by the permeability of the shear faults developed. Static, post-failure permeability measurements showed an inverse dependence of fault permeability on effective mean stress. The results predicted that, taking into account the localised nature of caprock failure expected under in-situ conditions, the bulk permeability of failed caprock above a hypothetical reservoir at ~3 km depth would be of the order of 10^{-19}-10^{-25} m^2. This means that in practice, caprock integrity will not be compromised by mechanical damage and permeability development.

Chapter 6 consists of a critical analysis of the concept of reducing atmospheric CO_2 concentrations by coastal weathering of olivine. This method has been presented in the media as a cheap, safe and green alternative for current CCS technologies but has not been quantitatively evaluated. It consists of coastal spreading of sand-grade olivine along beaches worldwide, with natural weathering reactions promoting increased atmospheric CO_2 uptake by seawater. In order for the method to compete with current CCS technology, it has to be able to reduce atmospheric CO_2 concentrations significantly within the next 15-20 years, i.e. a steady state uptake rate of ~6.25 Gt/yr by approximately 2025. The analysis presented here investigates the dissolution rate of olivine under Earth surface conditions, the CO_2 uptake capacity of the dominant

reaction and the CO_2 footprint of the method. The main conclusions reached are that dissolution rates of sand-grade olivine are orders of magnitude too slow to be significant within the next few decades. In order to speed up these rates, much finer grained, dust-grade material (< 10 μm) is required. However, this fine particulate matter poses possible public health risks, especially as fine-grained olivine-rich material may contain asbestos minerals. In addition, though the CO_2 uptake capacity of the (suggested) reaction is significant (i.e. 1.25 ton CO_2 per ton of olivine) and the direct CO_2 footprint acceptable (< 20%); vast quantities of material (> 5.0 Gt of olivine/yr) are required to achieve useful CO_2 uptake targets. Since olivine rocks are highly localised in their occurrence, this poses major infrastructural and worldwide transport challenges, on the scale of present oil and gas transport. On this basis, we infer that coastal spreading of olivine is not viable on the scale needed and cannot replace current CCS technology.

Finally, **Chapter 7** summarises the main conclusions of this thesis, and presents suggestions for future research.

1

General introduction

1.1 Background and scope of the study

It has been widely recognised that significant reduction of current CO_2 emissions is necessary to maintain atmospheric greenhouse gas concentrations at around 450 ppm CO_2 equivalent, thus limiting climate change [*Bernstein et al.*, 2007]. Reduction targets of the European Union suggest a 30% reduction of 1990-levels by 2020 and even up to 80% by 2050 [*Commission of the European Union*, 2007]. One way of achieving these targets is through Carbon Capture and Storage (CCS) technologies, which entail CO_2 capture at source, followed by long-term storage. A range of carbon dioxide storage or equivalent mitigation strategies have been suggested, including oceanic storage, industrial mineralisation, natural rock-weathering processes and, most importantly, geological CO_2 storage. Geological storage concepts involve the injection of liquid or supercritical carbon dioxide into unminable coal seams, saline aquifers, or depleted oil and gas reservoirs. The latter are particularly interesting and recognised as an important CCS route for countries with a major oil or natural gas production and transport infrastructure, such as the United States, Norway and the Netherlands [*Bachu*, 2000; *Voormeij and Simandl*, 2002]. More recently, natural rock-weathering processes have also attracted much media attention, especially in the Netherlands [*Biersma*, 2007; *Eshuis*, 2007; *Tangerman*, 2009].

To assess the efficiency, safety, useable CO_2 sequestration capacity and cost of any of these geological storage or mitigation options, the controlling chemical and physical processes must be understood at a quantitative level. In the case of storage in depleted oil and gas reservoirs, for example, both the mechanical and chemical response of the reservoir and top-sealing caprock must be understood. However, the necessary data is often lacking, particularly regarding mechanical and coupled chemical-mechanical interaction and long-term effects.

In this thesis, I report and discuss the results of a series of experiments and calculations, set up to explore on chemical and mechanical processes and the effects of fluid-rock interaction occurring in reservoirs and caprocks, at simulated, in-situ conditions. State-of-the-art experimental techniques employed include chemical batch experiments to investigate relevant mineral reactions (feldspar-CO_2-water system), compaction experiments on simulated reservoir sandstones to investigate the importance of time-dependent deformation or creep phenomena, and triaxial compression experiments on a typical, Dutch caprock material (anhydrite). These mechanical tests were coupled with permeametry, to study caprock fracture, damage and permeability development during deformation, and hence to assess caprock integrity evolution during CO_2 injection and storage. As an additional extra, a critical assessment is made of olivine rock weathering processes seen by some as offering an alternative CO_2 mitigation strategy to CCS involving subsurface storage.

The work was carried out in the context of the Dutch National Research Program

CATO on CO_2 capture, transport and storage, in close collaboration with Shell International Exploration and Production. The relevant phase of CATO (CATO-1, 2004-2008) has aimed to build a knowledge network on all aspects of CO_2 mitigation strategies of relevance to the Netherlands. The research reported in this thesis was incorporated in the CATO program under WorkPackage 4 on Mineralisation, since it aimed, in the first instance, to develop a fundamental understanding of the coupled chemical (mineral reactions) and mechanical processes operating during CO_2 sequestration. As the CATO program progressed, emphasis became increasingly steered towards caprock integrity and the olivine weathering issue.

1.2 Main mechanisms and processes occurring during subsurface storage of CO_2

Geological storage of CO_2 in depleted oil and gas reservoirs and, in aquifers, entails a wide range of hydrological, chemical and mechanical processes, which influence trapping of the injected CO_2 (see Figure 1.1). In such formations, CO_2 can be stored in two main ways: (1) in the pore space, as a supercritical phase (structural trapping) and/or dissolved in the pore fluid (hydrodynamic trapping), and (2) through mineral trapping, i.e. formation of stable carbonate minerals (mineral trapping) [*Gunter et al.*, 1993; *Bachu et al.*, 1994; *Hitchon*, 1996]. However, mineralisation reactions are very slow [*Baines and Worden*, 2000; *Xu et al.*, 2004; *Zerai et al.*, 2006] and most depleted reservoirs have low mineralisation potential [*Baines and Worden*, 2000; *Gilfillan et al.*, 2009]. Therefore, CO_2 injected into a depleted reservoir, or aquifer, will mainly be present in the supercritical phase and/or dissolved in any residual formation fluid [*Baines and Worden*, 2004; *Gilfillan et al.*, 2009], and will be kept in place by a top seal formation (caprock) and/or by sealed faults bounding the reservoir (large-scale structural trapping).

Currently, several test sites for CO_2 injection and storage are in operation worldwide, making use of both aquifers and reservoirs. These include aquifers, such as Sleipner and Snøhvit, Norway; Frio, United States; and hydrocarbon reservoirs, such as In Salah, Algeria; Ketzin, Germany; Teapot Dome and Rangely, Unites States; Weyburn and Zama Field, Canada; Nagaoka, Japan; Otway Basin, Australia; and Le Lacq, France. More test sites are planned in the Barendrecht gas field, the Netherlands, and the Michigan Basin, United States, and Gorgon, Australia, aquifers amongst others.

1.2.1 Hydrodynamic trapping modes and the properties of CO_2

Hydrodynamic trapping involves the storage of CO_2 as a dissolved phase in the reservoir pore fluid (solubility trapping – see Figure 1.1, box 1) and/or as a liquid

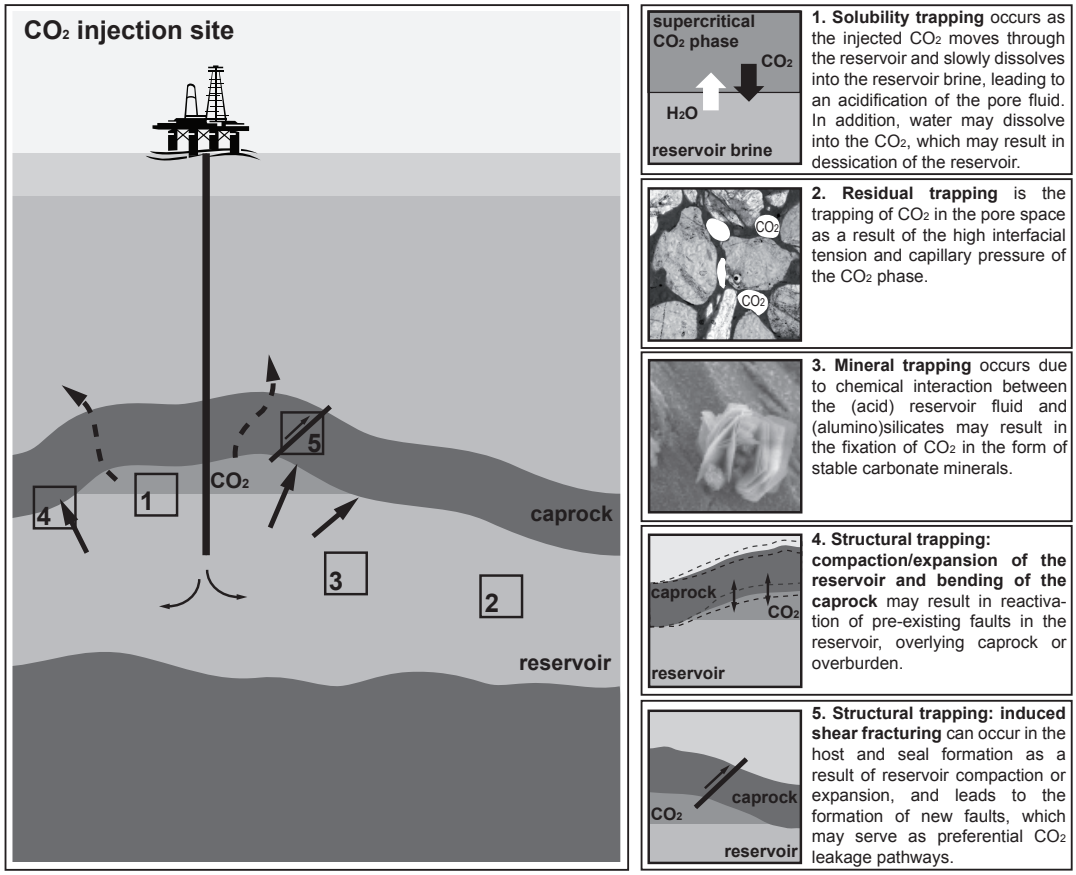

Fig. 1.1 Schematic diagram illustrating a CO_2 injection site consisting of a depleted oil or gas reservoir. After injection CO_2 spreads through the reservoir, displacing reservoir fluid and exerting forces on the overlying caprock. We have highlighted five of the key storage (box 1-3) and leakage (4-5) mechanisms that may occure after CO_2 injection. Mechanisms 3 to 5 will be discussed in more detail in this thesis.

or supercritical phase in bubbles in the formation-fluid-filled pore space (capillary trapping – see Figure 1.1, box 2) [*Suekane et al.*, 2008].

Immobility of the CO_2 is achieved by the local hydrological regime, i.e. the very low flow velocity of the formation fluid [*Hitchon*, 1996]. CO_2 will generally be injected into a given reservoir or aquifer at depths of > 800 m (P_{CO2} > 8 MPa) and stored as either a dense liquid or supercritical phase [*Hitchon*, 1996]. The critical temperature and pressure for CO_2 are 31°C and 7.4 MPa, respectively [*Span and Wagner*, 1996]. The amount of CO_2 that can be stored by either solubility or capillary trapping, its chemical activity, and its interaction with pre-fluid and rock, are controlled by its P-V-T and thermodynamic properties. The physical properties of CO_2 under varying temperature and pressure conditions can be predicted using the Equation of State (EOS), as given by *Span and Wagner* [1996]. The phase diagram is shown in Figure 1.2.

To date the most complete CO_2 solubility model available is that of *Duan and Sun*

[2003; 2006], which models the solubility of CO_2 in pure water and aqueous solutions from 0 to 260°C and from 0 to 200 MPa total pressure, up to ionic strengths of 4.5 mol/kg solution. This model has been extended to predict not only the solubility of CO_2 in pure water and NaCl solution but also in more complex systems, which may include Ca^{2+}, K^+, Mg^{2+}, and SO_4^{2-} ions. The following general effects of temperature, CO_2 pressure and salinity on CO_2 solubility are observed [see *Duan and Sun*, 2003; *Duan et al.*, 2006, and other references therein]

- At temperatures below ~100°C, CO_2 solubility decreases with increasing temperature, at constant pressure and salinity. At higher temperatures solubility increases with temperature.
- With increasing CO_2 pressure, at constant temperature and salinity, the solubility of CO_2 increases.
- Increasing salinity reduces CO_2 solubility, though brine composition is also of importance, as monovalent salt solutions, e.g. NaCl or KCl, inhibit CO_2 solubility more than divalent salt solutions, e.g. $CaCl_2$ or $MgCl_2$.

At the reservoir scale, dissolution of CO_2 into the reservoir brine is slow, as it depends on the diffusion of the CO_2 through the pore water [*Ennis-King and Paterson*, 2002], and will initially contribute only a few percent to the total CO_2 trapping capacity of a reservoir or aquifer. While CO_2 will dissolve in the pore fluid, water will also dissolve in the CO_2 phase [*Tödheide and Franck*, 1963]. Under reservoir conditions (T = 50-100°C, P_{CO2} > 8 MPa), this is typically < 5 mol-% but can lead to local (partial) desiccation (i.e. drying out) of the reservoir [*Müller et al.*, 2009] and to reaction between rock and the CO_2-rich phase [*Bachu et al.*, 1994].

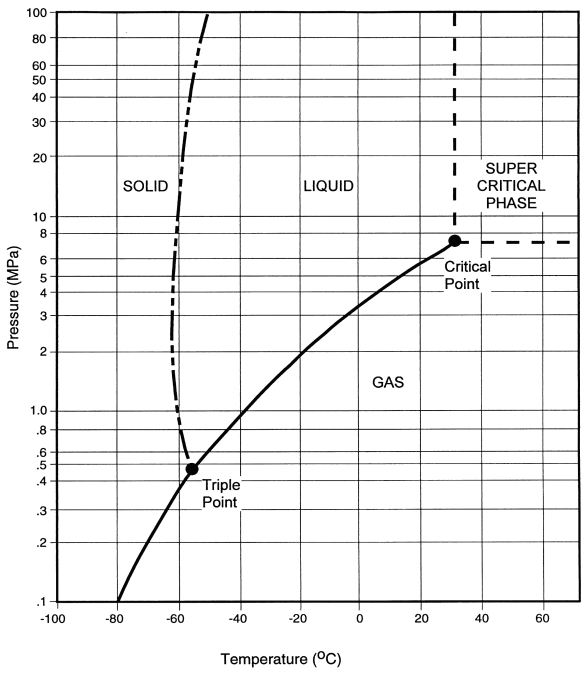

Fig. 1.2 Phase diagram for CO_2 showing the critical point (T = 31°C, P = 7.4 MPa) and the various phases of CO_2 as a function pressure and temperature [after *Bachu,* 2000].

In addition, as CO_2 moves through a given reservoir, away from the injection point, pore fluid brine present will be displaced by the CO_2 phase. As liquid or supercritical CO_2 passes through pores and pore throats, and if the pore fluid content is high enough, part of the CO_2 phase may become disconnected

and trapped in the pores. The strong non-wetting behaviour of CO_2 (high contact angle) [*Wesch et al.*, 1997; *Dickson et al.*, 2006] results in high capillary pressures, especially in the far field, where P_{CO2} is lower and the interfacial tension (IFT) of the CO_2/brine system is high [*Chalbaud et al.*, 2006; *Chiquet et al.*, 2007b; *Bachu and Bennion*, 2009]. This is called capillary trapping. It should be noted that at higher CO_2 partial pressure (P_{CO2} > 10 MPa) IFT for the CO_2/ brine system is lowered significantly (~50%), reducing the residual trapping capacity of a reservoir.

1.2.2 Mineral trapping of CO_2 - geochemical effects

In contrast to hydrodynamic trapping, which results in CO_2 *storage* sensu-stricto, mineralisation leads to *fixation* of the injected CO_2 through the precipitation of carbonate minerals (see Figure 1.1, box 3). The principle behind CO_2 sequestration by mineral trapping is based on a number of sequential chemical reactions: (1) CO_2 dissolves in the reservoir water to form carbonic acid, and subsequently bicarbonate; (2) H^+ attacks minerals in the rock and, depending on composition, releases relevant cations (e.g. Ca^{2+}, Mg^{2+}, Fe^{2+}); (3) the bicarbonate reacts with cations present in the reservoir water in order to form stable carbonates. This whole process can be represented schematically as

$$CO_{2\,(g)} + H_2O_{(l)} \leftrightarrow H_2CO_{3\,(aq)} \leftrightarrow H^+_{(aq)} + HCO^-_{3\,(aq)} \quad (1.1)$$

$$\text{silicate mineral} + 2H^+ \leftrightarrow M^{2+} + \text{silica} \quad (1.2)$$

$$Mg^{2+}_{(aq)} + HCO^-_{3\,(aq)} \leftrightarrow H^+_{(aq)} + MgCO_{3\,(s)}\ \text{(magnesite)} \quad (1.3a)$$

$$Ca^{2+}_{(aq)} + HCO^-_{3\,(aq)} \leftrightarrow H^+_{(aq)} + CaCO_{3\,(s)}\ \text{(calcite)} \quad (1.3b)$$

$$Fe^{2+}_{(aq)} + HCO^-_{3\,(aq)} \leftrightarrow H^+_{(aq)} + FeCO_{3\,(s)}\ \text{(siderite)} \quad (1.3c)$$

where M^{2+} represents a generic cation. When CO_2 is injected into an impure sandstone reservoir, feldspars, micas and clays present in the rock will act as the cation sources, and protons present in the reservoir water (see reaction (1.1)) will leach out the necessary cations from the silicate structure, precipitating carbonates, secondary clays and silica, according to the following, more general overall reaction [*Gunter et al.*, 1993].

$$\text{feldspar} + \text{clays} + CO_2 \rightarrow \text{calcite} + \text{dolomite} + \text{kaolinite} + \text{quartz} \quad (1.4)$$

However, mineral trapping is a slow, long-term process [*Baines and Worden*, 2000] that strongly depends on the availability of reactive minerals, such as feldspars, Mg/Fe-rich clays and micas, and Fe-oxides or olivine [*Gunter et al.*, 2000; *Johnson et al.*, 2001; *Wawersik et al.*, 2001; *Sass et al.*, 2002; *Aagaard et al.*, 2004; *Carroll and Knauss*, 2005; *Fernandez-Bastero et al.*, 2005; *Giammar et al.*, 2005; *Palandri and*

Kharaka, 2005; *Xu et al.*, 2005; *Zerai et al.*, 2006].

It is believed that the rate of mineralisation depends mainly on the dissolution rate of these aluminosilicates [*Baines and Worden*, 2000; *Zerai et al.*, 2006] and not on the dissolution of CO_2 or the precipitation of secondary phases. Dissolution rates for aluminosilicates are of the order of ~10^{-14}-10^{-12} mol/m^2 s under reservoir conditions (T = 50-100°C, pH = 5-6) [for example see - *Carroll and Walther*, 1990; *Hellmann*, 1995; *Oelkers and Schott*, 1995; *Köhler et al.*, 2003; *Carroll and Knauss*, 2005].

To date, experiments on sands and sandstones of various composition, at pressures and temperatures in the range 10-30 MPa P_{CO2} and 70-350°C, have demonstrated dissolution of carbonate and anhydrite cements [*Shiraki and Dunn*, 2000; *Bateman et al.*, 2005; *Bertier et al.*, 2006;], etching of feldspars [*Shiraki and Dunn*, 2000; *Kaszuba et al.*, 2003] and quartz [*Kaszuba et al.*, 2003; *Liu et al.*, 2003], and precipitation of carbonates [*Kaszuba et al.*, 2003; *Bateman et al.*, 2005; *Kaszuba et al.*, 2005], clays [*Shiraki and Dunn*, 2000; *Kaszuba et al.*, 2003; 2005], zeolites [*Kaszuba et al.*, 2003, 2005], and Ca-aluminosilicates [*Kaszuba et al.*, 2003; *Liu et al.*, 2003].

In addition to these experiments, numerous geochemical modelling efforts are in progress to predict the secondary phases formed when CO_2 is stored in upper crustal reservoir rocks. Numerically simulated CO_2 storage in sandstones, consisting mainly of quartz, alkali feldspar and minor quantities of clay minerals, predicts precipitation of phases such as dawsonite, siderite [*Xu et al.*, 2004; *Lagneau et al.*, 2005; *Xu et al.*, 2005; *Zerai et al.*, 2006], ankerite, illite, calcite [*Xu et al.*, 2004; 2005] and quartz [*Lagneau et al.*, 2005]. Storage in glauconite sandstone is predicted to precipitate similar phases, notably illite, K-feldspar, dolomite, dawsonite, ankerite, and siderite [*Xu et al.*, 2004]. Such predictions, made using geochemical models, such as TOUGHREACT [*Xu et al.*, 2006], Geochemist's Workbench [*Bethke*, 1996] and Hytec [*van der Lee et al.*, 2002; *van der Lee et al.*, 2003], are to some extent supported by experimental observations, but are often difficult to compare due to the complexity of the reactive systems. In addition, most geochemical models are based on kinetic data obtained for reactions occurring at Earth surface conditions, i.e. surface temperatures and atmospheric pressure. It is important to investigate if these reactions also occur under subsurface conditions in CO_2-rich environments, and at what rates.

Aside from geochemical aspects of mineral trapping, dissolution of the minerals in a given host rock, and precipitation of secondary phases may lead to changes in the transport properties (i.e. porosity and permeability) of the reservoir [*Gunter et al.*, 1993], and to changes in mechanical properties (creep, strength, dilatation, porosity and permeability). However, very few studies attempt to couple geochemical, hydrological and especially mechanical processes occurring within the reservoir rock as a result of CO_2 injection [*Xu et al.*, 2004, 2005; *Le Guen et al.*, 2007; *Van Bergen et al.*, 2008]. Numerical modelling efforts for sandstone reservoirs predict only a few

percent decrease in solid volume (i.e. porosity) as a result of aluminosilicate reacting with CO_2 over a time span of > 1000 years [*Xu et al.*, 2004, 2005]. In contrast, reaction rates of silicate minerals such as olivine and pyroxene are up to 4-6 orders of magnitude faster under reservoir conditions [*Oelkers and Schott*, 2001; *Hänchen et al.*, 2006] and give rise to a solid volume increase of up to 80%, which may be undesirable. However, reaction of these minerals with CO_2 and water are only of interest for CO_2 injection into peridotites and fractured basalts [*Matter et al.*, 2007], as these minerals are rarely found in large quantities in sedimentary formations. In addition to fluid-rock interactions, salt precipitation from brine as a result of desiccation may also affect permeability and CO_2 injectivity [*Giorgis et al.*, 2007; *Müller et al.*, 2009] and should be taken into account, as it may strongly affect reservoir permeability.

1.2.3 Structural trapping of CO_2 - geomechanical and hydromechanical effects

The main factor affecting (large-scale) structural trapping, and the key to successful long-term geological CO_2 storage as a whole, is maintaining seal integrity. As pointed out by *Hawkes et al.* [2005] the key aspects influencing seal integrity are: (1) reactivation of faults within or bounding the reservoir, (2) reactivation of faults within the caprock or overburden, (3) mechanical damage and induced shear failure of unfaulted caprock, (4) hydraulic fracturing near the point of injection and (5) well bore leakage. To date, most efforts have focused on predicting (numerically) the geomechanical response of reservoir and overlying caprock to CO_2 injection.

It is possible that CO_2 will reactivate existing faults, either in the reservoir or in the overlying caprock [*Rutqvist et al.*, 2007; *Soltanzadeh and Hawkes*, 2008]. According to *Hawkes et al.* [2005], there are several important mechanisms that can cause fault reactivation during fluid depletion or injection. These include pore pressure changes in fault planes and connected porosity throughout the reservoir rock, which may reactivate faults in the reservoir [*Streit and Hillis*, 2004; *Chiaramonte et al.*, 2007; *Soltanzadeh and Hawkes*, 2008]. In addition, CO_2-enhanced creep processes may cause compaction, while the poro-eleastic response of the reservoir to CO_2 injection may result in reservoir heave, as seen in Figure 1.1, box 4 and 5. Such processes can potentially cause flexure of the top-seal, which may result in the reactivation of faults in the caprock or overburden [*Rutqvist and Tsang*, 2002; *Rutqvist et al.*, 2008] and/or induce shear failure, leading to the formation of new faults [*Rutqvist et al.*, 2008]. As these mechanisms are dependent on the magnitude of the changes in the state of stress, this puts constraints on the maximum CO_2 pressure that can be injected. Furthermore, hydraulic fracturing near the injection point, as a result of high injection rates and cold injection fluids [*Hawkes et al.*, 2005], as well as bore-hole instability, such as casing impairment [*Dusseault et al.*, 1998] and well bore cement degradation [*Kutchko et al.*, 2007], may pose additional problems for maintaining seal integrity.

As shown in Figure 1.3, changes in stress state not only affect the geomechanical response of the reservoir-caprock system to CO_2 injection, but indirectly also the transport properties. Numerical modelling efforts by *Rutqvist and Tsang* [2002] on hydromechanical changes during CO_2 injection into a hypothetical aquifer-caprock system, resembling a sandstone aquifer and shale caprock, have shown that at an injection pressure of ~40 MPa a factor of ~2 increase in caprock permeability may be expected at the caprock-reservoir interface. In addition, after around 10 years the CO_2 is predicted to penetrate some 10 m into the caprock, while the overlying caprock and overburden will have remained intact. Combining experimental (strength and permeability) data with finite element modelling is a way to predict the permeability response of a seal formation to changes in stress state. However, very little experimental data exists for permeability development in response to deformation of a typical caprock, e.g. shale, limestone, dolomite, halite or anhydrite [for example see *Peach*, 1991; *Zhang et al.*, 1994; *Peach and Spiers*, 1996; *De Paola et al.*, 2009], to verify

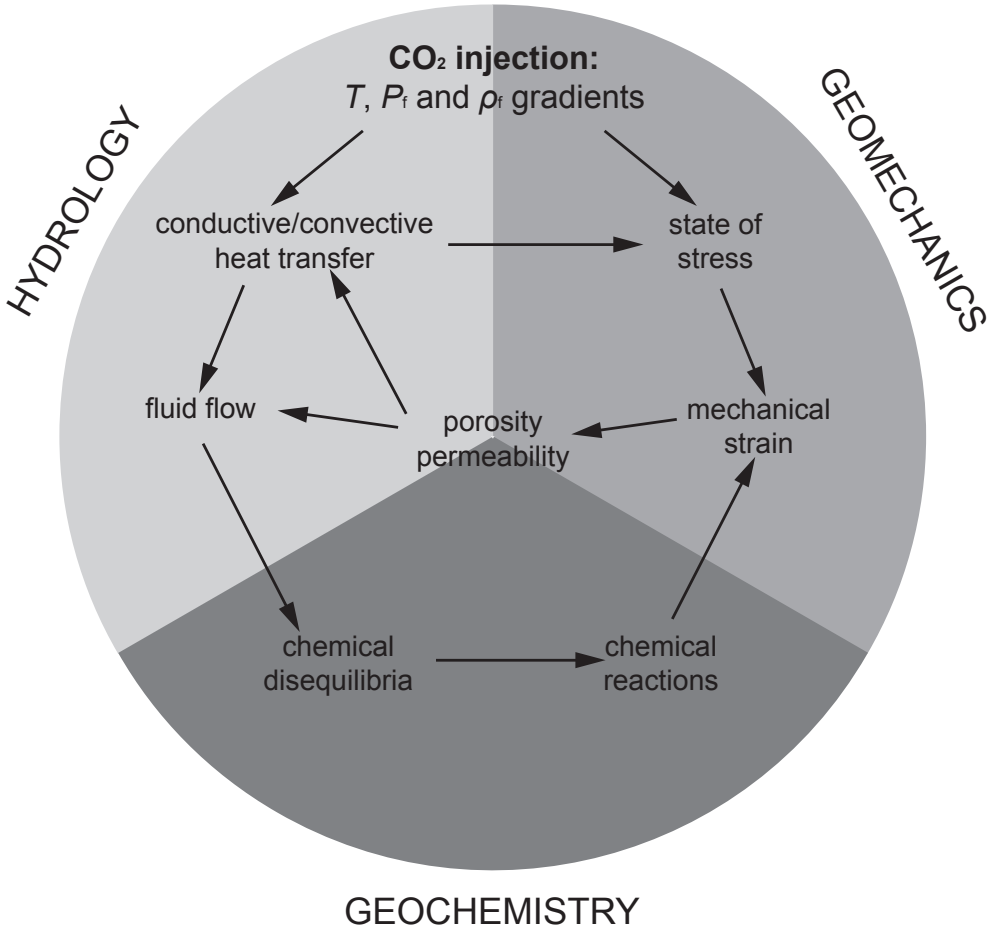

Fig. 1.3 Schematic diagram showing the subsurface processes that are perturbed by CO_2 injection, and the concomitant changes in temperature, pressure and pore fluid density. As can be seen, porosity and permeability are the key variables linking the hydrological, geochemical and geomechanical regimes [after *Johnson et al.*, 2004].

such calculations.

Intimately coupled with geomechanical and permeability changes are geochemical fluid-rock interactions, which in the long-term may affect porosity and permeability development further (see Figure 1.3). Geochemical transport modelling efforts on the shaly caprock of the Sleipner field (Norwegian North Sea) predict that fluid-rock interactions result in a slight decrease in porosity in the lower few meters of the seal formation [*Gaus et al.*, 2005]. Coupling of geomechanical and geochemical processes has shown that it is likely that an increase in permeability due to hydromechanical response may be counterbalanced by these chemical reactions [*Johnson et al.*, 2004], as the increase in permeability is offset by the solid volume increase of the fluid-rock interactions. However, counterbalancing of geomechanical and geochemical changes may not hold for all caprock types as it strongly depends on mineralogical composition.

1.3 The road so far: outstanding research questions

It will be clear from the above that geological storage of CO_2 in depleted oil and gas reservoirs and aquifers is a complex matter, influenced by many, in their own rights complex, interlinked processes and mechanisms [see Figure 1.3 - after *Johnson et al.*, 2004]. This has lead to many questions regarding in-situ rates of mineralisation reactions, fluid flow, effects of CO_2-water interaction on mechanical processes operating, such as compaction creep, and the influence these phenomena may have on transport properties (i.e. permeability). Over the past two decades, much research has focussed on elucidating some of these key questions, through geochemical [*Johnson et al.*, 2004; *Xu et al.*, 2004; 2005; *Zerai et al.*, 2006] as well as geomechanical modelling [*Rutqvist and Tsang*, 2002; *Johnson et al.*, 2004; *Hawkes et al.*, 2005; *Rutqvist et al.*, 2007; *Rutqvist et al.*, 2008; *Soltanzadeh and Hawkes*, 2008], and through experimental efforts [*Kaszuba et al.*, 2003, 2005; *Rosenbauer et al.*, 2005; *Bertier et al.*, 2006; *Le Guen et al.*, 2007; *Matter et al.*, 2007; *Liteanu and Spiers*, 2009]. One of the main foci of experimental studies has been to determine the nature and rates of mineralisation reactions [for example see - *Kaszuba et al.*, 2003; *Carroll and Knauss*, 2005; *Golubev et al.*, 2005; *Kaszuba et al.*, 2005; *Hänchen et al.*, 2006], to assess mineral trapping potential. In addition, experimental studies have been performed to determine capillary entry pressures [*Hildenbrand et al.*, 2004], CO_2 wettability [*Chiquet et al.*, 2007a; *Yang et al.*, 2008] and relative permeabilities [*Bachu and Bennion*, 2008; *Bennion and Bachu*, 2008] of host and seal rocks. However, to date, very little experimental data exists on the effect of CO_2 on coupled chemical-mechanical processes occurring in reservoir and seal formations, and indeed on purely mechanical damage, for real rocks under in-situ conditions. Results from appropriate

geomechanical experiments, together with fluid-rock interaction rate data, are essential to provide a basis for the (finite element) modelling efforts required to predict long-term behaviour and performance of geological CO_2 storage systems, such as depleted reservoirs and aquifers.

1.4 Aims of this study

It has been shown above that a range of new experimental data are needed to assess the effect of CO_2 on mechanical and chemical-mechanical processes occurring in host and seal formations constituting realistic geological storage systems, such as depleted oil and gas reservoirs. In the Netherlands, particularly important are sandstone reservoirs and anhydrite caprock. Olivine weathering under Earth surface conditions will also be discussed as it has gained quite some media attention, especially in the Netherlands. The following aims are accordingly defined for this thesis:

1. Characterization of the nature and rate of chemical reactions occurring in impure (feldspar-bearing) sandstone reservoirs, to establish whether or not the same reactions occur at elevated pressures, temperatures, and CO_2 partial pressures, as under Earth surface conditions.
2. Investigation of the coupled chemical-mechanical effects of fluid-rock interaction, as well as the effects of grain size, applied stress, temperature and pore fluid composition, on creep phenomena in impure sandstones.
3. Experimental determination of the mechanical behaviour and damage characteristics of anhydrite caprock and of any short-term effect of CO_2-water-rock interactions.
4. Determination of permeability development in deforming anhydrite caprock, as well as the effect of the state of stress on fault permeability.
5. A critical analysis of the concept of beach weathering of crushed olivine, with the aim of demonstrating quantitatively whether or not it can contribute significantly to CO_2 sequestration targets.

1.5 Structure

The first part of this thesis is concerned with the effect of CO_2 on host or reservoir rocks, with aims 1 and 2 being addressed in Chapters 2 and 3, which tackle the effect of CO_2 on fluid-rock interaction and chemical-mechanical behaviour in simulated feldspar-bearing sandstones. The second part of this thesis (Chapters 4 and 5) focuses on anhydrite caprock or seal behaviour and discusses the effect of CO_2 injection, and the resulting change in stress state, on the damage behaviour and transport properties

of anhydrite (aims 3 and 4). Finally, Chapter 6 consists of a critical analysis of the beach-weathering concept put forward in the Netherlands as an alternative CO_2 mitigation strategy, i.e. as an alternative to CCS. General conclusions and suggestions for future research are summarized in Chapter 7.

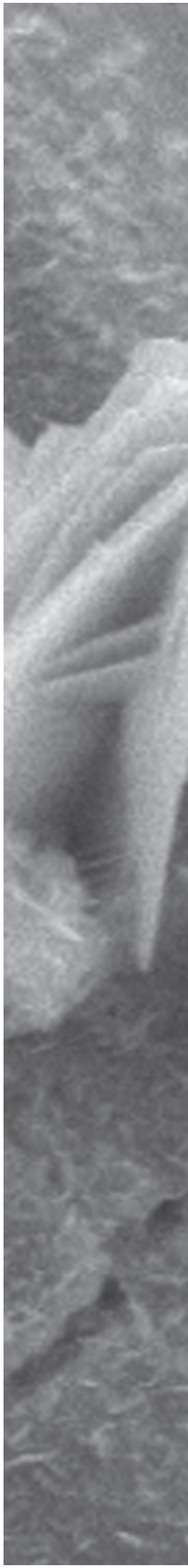

2

Reaction of plagioclase feldspars with CO_2 under hydrothermal conditions

S.J.T. Hangx and C.J. Spiers

Chemical Geology (2009), 265(1-2), 88-98.

Abstract

Geological storage of CO_2 in plagioclase-bearing sediments, granitic rocks and fractured basalts is expected to have a variety of geochemical and geomechanical effects, including mineral trapping and porosity-permeability changes. The amount of CO_2 trapped by mineralisation and the extent of any changes in host rock transport or mechanical properties depend on rock composition. To date, studies of mineralisation have mainly been based on dissolution and precipitation experiments performed at ambient surface conditions, or at slightly elevated temperature and pressure. However, the reactions that occur under in-situ conditions are poorly constrained. In an attempt to determine the secondary phases formed in the plagioclase-CO_2-water system under such conditions, we performed a set of batch experiments, at temperatures in the range 200-300°C, using carbon dioxide pressures from 0.4 to 15 MPa. We investigated reaction of anorthite and albite, which are expected to precipitate calcite and kaolinite, and dawsonite and quartz, respectively. However, in most of our experiments, reactions precipitating clays (kaolinite and smectite or illite), boehmite, and a Mg,Ni,Fe-hydrotalcite-like phase dominated, the nickel being derived from the reaction vessel. Little or no carbonate and no dawsonite were detected. Additional feldspar-free control experiments employing Mg-rich brine showed that carbonates would be preserved in our feldspar experiments if formed, but that a carbonate substrate is needed to promote precipitation. Since the secondary phases formed in our plagioclase experiments are stable under a wide range of conditions we expect that they will also form under CO_2 storage systems with suitable fluid-rock composition. From our results we conclude that clay precipitation can proceed or accompany carbonate precipitation, depending on the availability of carbonate substrate. Though an artefact in our experiments, in the context of subsurface alkaline waste injection, hydrotalcite may play a positive role here by immobilising heavy metals, while carbonates will mineralise the CO_2.

2.1 Introduction

In order to maintain atmospheric CO_2 concentrations below 450 ppm, thus limiting climate change, global CO_2 emissions reduction of the order of at least 30% of 1990 levels is needed by 2020, and up to 80% by 2050 [*Commission of the European Communities*, 2007]. Injection and storage of CO_2 in geological formations is widely considered to be a promising option for helping to achieve these targets [*Bachu et al.*, 1994; *Holloway*, 1996; *Gunter et al.*, 2000; *Wawersik et al.*, 2001]. Possible formations include depleted oil and gas reservoirs and deep saline aquifers. In such formations, CO_2 can be stored in two main ways: (1) in the pore space, as a supercritical phase and/or dissolved in the pore fluid, and (2) through mineral trapping, i.e. formation of stable carbonated minerals [*Bachu et al.*, 1994; *Hitchon*, 1996]. However, mineral trapping is a slow, long-term process [*Baines and Worden*, 2000] that strongly depends on the availability of reactive minerals, such as feldspars, Mg/Fe-rich clays and micas, and Fe-oxides or olivine [*Gunter et al.*, 2000; *Johnson et al.*, 2001; *Sass et al.*, 2002; *Aagaard et al.*, 2004; *Carroll and Knauss*, 2005; *Fernandez-Bastero et al.*, 2005; *Giammar et al.*, 2005; *Palandri and Kharaka*, 2005; *Wawersik et al.*, 2001; *Xu et al.*, 2005; *Zerai et al.*, 2006].

Most studies of feldspar reaction with CO_2 performed to date focused on sodium and potassium feldspars (albite and microcline) [*Xu et al.*, 2004; 2005; *Zerai et al.*, 2006; *Pauwels et al.*, 2007]. Though Ca-bearing feldspars are generally not abundant in sandstones, their fast reaction kinetics and reactivity with CO_2 may significantly affect the transport properties of reservoir rocks by increasing porosity, as pointed out by *Sorai et al.* [2007]. Moreover, significant amounts of Ca-rich plagioclase feldspars are often present in plutonic rocks [e.g. granite - see *Suto et al.*, 2007], geothermal fields [e.g. granodiorites - see *Ueda et al.*, 2005], fractured basalt [*Matter et al.*, 2007], and even ophiolite sequences [*Okamoto et al.*, 2006], making them also serious candidates for mineral trapping. For the plagioclase-CO_2-H_2O system, the following reaction is assumed, when the Ca-rich end-member anorthite is the reactive mineral [*Wawersik et al.*, 2001]:

$$\underset{\text{anorthite}}{CaAl_2Si_2O_{8\,(s)}} + CO_{2\,(g)} + 2\,H_2O_{(l)} \leftrightarrow \underset{\text{calcite}}{CaCO_{3\,(s)}} + \underset{\text{kaolinite}}{Al_2Si_2O_5(OH)_{4\,(s)}} \qquad (2.1)$$

This implies that calcite will precipitate as the CO_2 trapping phase. In the case of Na-rich plagioclases (albite), on the other hand, modelling efforts predict that dawsonite will precipitate as the CO_2-bearing phase [J*ohnson et al.*, 2001; *Xu et al.*, 2004; *Bateman et al.*, 2005; *Lagneau et al.*, 2005; *Xu et al.*, 2005; *Zerai et al.*, 2006] according to the reaction:

$$\underset{\text{albite}}{NaAlSi_3O_{8\,(s)}} + CO_{2\,(g)} + H_2O_{(l)} \leftrightarrow \underset{\text{dawsonite}}{NaAl(CO_3)(OH)_{2\,(s)}} + 3\ \underset{\text{silica}}{SiO_{2\,(s)}} \qquad (2.2)$$

These reactions are observed during natural weathering and diagenetic processes occurring at the Earth's surface [*Brady and Carroll*, 1994; *Baker et al.*, 1995; *Dyni*, 1996]. However, little data is available for reaction under subsurface conditions and it is important to establish whether or not the same reactions indeed occur at elevated pressures, temperatures, and CO_2 partial pressures.

To this end, we performed batch experiments on anorthite and albite plagioclases under hydrothermal conditions in the presence of water or brine and supercritical CO_2. Experiments were performed at temperatures of 200-300°C, CO_2 partial pressures (P_{CO2}) of 0.4-15 MPa, and total pressures of 6-18 MPa. Various salt solutions (0.1-0.2 M $MgCl_2$ and 0.1 M NaCl) were chosen to represent reservoir brines. Following the approach adopted in previous work on K-feldspar-bearing sandstones [*Kaszuba et al.*, 2003, 2005], we chose relatively high temperatures to accelerate reaction rates [*Hellmann*, 1994; *Oelkers and Schott*, 1995]. It was assumed that reactions (2.1) and (2.2) will occur at high temperature (200-300°C) and could be extrapolated to reservoir conditions (T = 50-100°C, P_{CO2} > 8 MPa). Besides our feldspar experiments, a set of control experiments was performed to investigate the precipitation of magnesite ($MgCO_3$), from $MgCl_2$ solution, on various substrates, under hydrothermal conditions. Magnesite does not precipitate commonly in nature. However, we performed these experiments to confirm the feasibility of carbonate precipitation and preservation under the conditions of our feldspar experiments. Note that our experimental design gave us semi-quantitative and qualitative results on the extent and nature of reactions occurring in the feldspar-CO_2-water/brine system under hydrothermal conditions. No kinetic data or solution chemistry could be deduced. Nonetheless, our results can provide useful information for validating modelling predictions regarding secondary phases and for assessing the effect of reaction on transport properties.

2.2 Methodology

2.2.1 Preparation of samples and solutions

Anorthite was obtained from anorthite-olivine rock samples (cm-sized aggregates), originating from Miyake Island, Tokyo Bay, Japan (Mineralogical Research Co.). Miyake Island is known for its unusual olivine-anorthite rocks (allivalites), which consist of Ca-rich plagioclase feldspar (>An90) and olivine (>Fo80) [*Amma-Miyasaka and Nakagawa*, 2002; *Plechov et al.*, 2008]. The anorthite was separated from the olivine by crushing the material to mm-scale particles, using a pestle and mortar, and

Table 2.1
Chemical composition of the feldspars used in this study (wt%).

mineral	SiO_2	Al_2O_3	Fe_2O_3	CaO	Na_2O	K_2O	total
anorthite	44.15	34.79	0.44	19.44	0.45	-	99.26
albite	68.84	20.17	0.01	0.15	11.12	0.19	100.47

Mean composition: anorthite $Ca_{0.92}Na_{0.08}(Al_{1.92}Fe^{3+}_{0.01}Si_{2.07})O_8$, albite $Na_{0.99}K_{0.01}AlSi_3O_8$
Anorthite and albite analysis was performed by electron microprobe analysis of thin sections of crushed, unsieved material. Analysis was taken as an average of 10 grains.

selecting suitably pure feldspar particles under an optical microscope. The resulting feldspar was further crushed and separated into two grain size fractions (<15 μm and 25 ± 10 μm), by sieving and gravitational settling from an aqueous suspension. Chemical analysis (Table 2.1) of a thin section of unsieved crushed material, performed using an electron microprobe, yielded an average feldspar composition of $Ca_{0.92}Na_{0.08}(Al_{1.92}Fe^{3+}_{0.01}Si_{2.07})O_8$. Additional thermogravimetric analysis (TGA) revealed that trace amounts of gibbsite (0.50 wt%), boehmite (0.33 wt%), and calcite (0.08 wt%) were present in the sieved material.

Albite was obtained from Ward's Natural Science and was supplied as mm- to cm-sized crystals with few visible impurities. After crushing, using a pestle and mortar, the material was sieved to produce a grain size fraction of 40 ± 10 μm. Electron microprobe analysis of a thin section of the unsieved albite yielded an average chemical composition of $Na_{0.99}K_{0.01}AlSi_3O_8$ (Table 2.1).

The above feldspar fractions were reacted with CO_2 plus water or brine, prepared using analytical grade NaCl (Merck no. 106495) or $MgCl_2$ (Merck no. 105833) and

Table 2.2
Summary of the batch experiments performed on the feldspar-CO_2-water/brine system

sample/ expt	sample material	grain size	aqueous solution	T	P_T	P_{CO2}	reaction time	Teflon liner
		[μm]		[°C]	[MPa]	[MPa]	[days]	Yes/No
An301	anorthite	25±10	H_2O	300	6	0.4	7	N
An302	anorthite	25±10	H_2O	300	6	0.4	21	N
An303	anorthite	< 15	H_2O	300	18	12	11	N
An201	anorthite	25±10	H_2O	200	18	12	14	Y
An210	anorthite	25±10	H_2O + 0.1 M NaCl	200	15	12	20	Y
An211	anorthite	25±10	H_2O + 0.2 M $MgCl_2$	200	15	12	21	Y
Ab201	albite	40±10	H_2O + 0.2 M $MgCl_2$	200	18	15	20	Y
Ab202	albite	40±10	H_2O + 0.2 M $MgCl_2$	200	18	15	21	Y

demineralised water. The salt concentrations used were 0.1 and 0.2 M, thus being of the same order as concentrations observed in reservoir brines [*Kaszuba et al.*, 2003; 2005]. A summary of the batch experiments performed on feldspars, showing the corresponding sample and aqueous solution compositional details, is shown in Table 2.2.

To check the feasibility of carbonate precipitation under our experimental conditions, and to verify carbonate preservation during apparatus cooling and depressurisation, we also performed a set of feldspar-free control experiments, designed to precipitate magnesite from Mg-rich brine (Table 2.3). Various types of substrate were used to investigate their effect on magnesite precipitation. These included finely ground quartz (grain size 300 ± 100 μm), granular calcite ($CaCO_3$) substrate prepared from ground Carrara marble (grain size 140 ± 20 μm, 99% purity) and analytical grade hydromagnesite ($4\ MgCO_3 \cdot Mg(OH)_2 \cdot 5\ H_2O$, Merck no. 105827, grain size < 10 μm) (see Table 2.3).

2.2.2 Experimental design and procedure

Batch method was used to study the reactions occurring in the feldspar-CO_2-water/brine system (Table 2.2), and in the substrate-CO_2-brine system (Table 2.3), at elevated P_{CO2} (≤ 15 MPa) and temperature (200-300°). The experiments were performed using a cold-seal pressure vessel and internal K-Monel 500 reaction vessel as shown in Figure 2.1. The vessel was heated externally and sample temperature was measured using a type K (chromel/alumel) thermocouple embedded in the vessel wall and pre-calibrated against reaction vessel temperature. In early experiments performed at 300°C, Ni-contamination from the K-Monel reaction vessel significantly influenced the reactions (chemical composition of K-Monel 500: 57-63.0 % Ni and Co, 27.0-33.0 % Cu, 3.20-3.15 % Al, 0.35-0.85 % Ti, < 2.0 % Fe, < 1.5 % Mn, < 0.5 % Si, < 0.25 %

Table 2.3
Summary of the feldspar-free control experiments performed on Mg-rich brine using various types of substrate.

sample/ expt	substrate material[†]	substrate mass [g]	brine	substrate grain size [μm]	T [°C]	P_T [MPa]	reaction time [days]
P01	Q	0.09806	0.1 M $MgCl_2$	300±100	200	18	3
P02	HM	0.01171	0.1 M $MgCl_2$	< 15	200	18	7
P03	C	0.10290	0.1 M $MgCl_2$	140±20	200	18	5
P04	Q + HM	Q: 0.11054 HM: 0.00568	0.1 M $MgCl_2$	300±100	200	18	5

Note: In all experiments the internal reaction vessel was lined with Teflon
[†] Q is quartz, HM is hydromagnesite and C is calcite
[*] CO_2 partial pressure was 15 MPa in all experiments

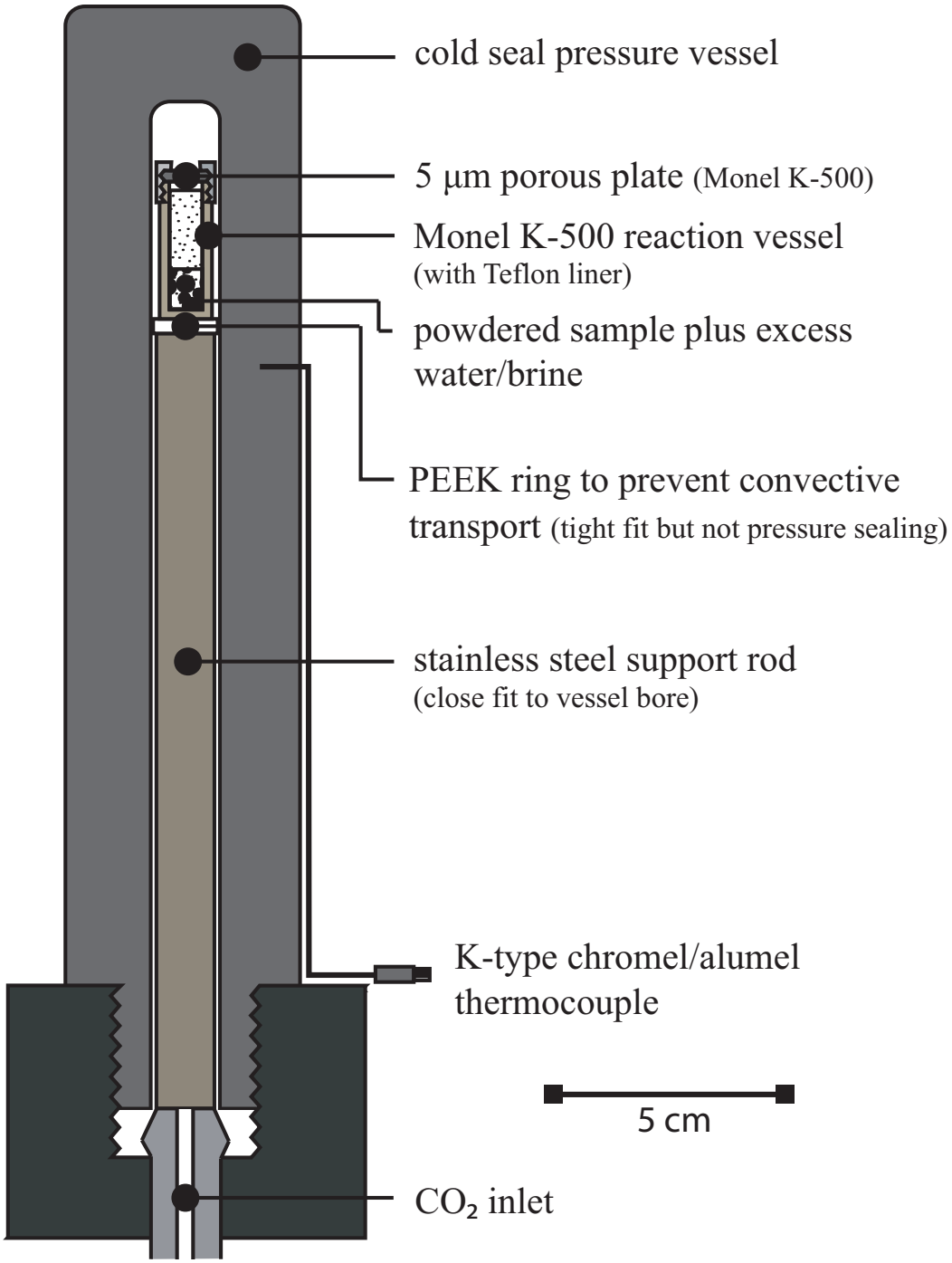

Fig. 2.1. Schematic diagram showing the cold seal pressure vessel and internal set-up used in the present batch experiments.

C, and < 0.01 % S). The reaction vessel was subsequently lined with Teflon restricting the temperature of further experiments to 200°C (An200-, Ab200- and P-series).

For each experiment, the reaction vessel was typically filled with ~ 0.1 g of crushed sample (or substrate) material, adding 0.5 to 1 ml of water or brine to completely submerge the sample or substrate. Water/brine to rock mass ratios thus started out between 5:1 and 10:1. The reaction vessel and sample were then placed in the pressure vessel and the system was pressurised using a nitrogen buffered CO_2 supply, at a fixed initial pressure of 9 MPa (6 MPa for experiments An301 and An302), and heated to the desired temperature. After final adjustment, applied total pressures ranged from 6 to 18 MPa, while CO_2 partial pressures, calculated for the reaction vessel following *Tödheide and Franck* [1963], varied from 0.4 to 15 MPa. Under the chosen experimental conditions, supercritical CO_2 can contain up to 90 mol% of water (i.e. 90 moles of water per 100 moles of CO_2 + water) [*Tödheide and Franck*, 1963]. In order to prevent desiccation of the sample, due to evaporation of water into the supercritical CO_2 phase, and possible transport of water to cooler parts of the pressure vessel, excess water or brine was added. The amount of added solution (0.5-1 ml in total) was sufficient to saturate the supercritical CO_2 with water and still leave the solid sample submerged. The mutual solubilities of CO_2 and H_2O resulted in changing solution composition at the start of the experiments. However, it was not possible to accurately predict these changes.

Experiments were run for 3 to 21 days. They were terminated by rapidly removing pressure from the system, prior to cooling causing water or brine to be expelled from the sample and preventing re-dissolution of any precipitated secondary phases. Though dissolution of part of the water/brine phase into the supercritical CO_2 phase would have lead to supersaturation with respect to salts and possible secondary phases, it is unlikely that any of these phases would have precipitated, within the short time of depressurisation (< 1 min). After extraction, the samples were analysed by means of Scanning Electron Microscopy (SEM - Philips XL30FEG), X-Ray Diffraction (XRD), Fourier Transform Infrared spectroscopy (FTIR - JASCO FTIR-470 Plus, with infrared microscope Irtron IRT-30), Thermogravimetric Analysis (TGA) and Microprobe (FEG EPMA – JEOL JXA8500F) in order to obtain an indication of the composition and amounts of products formed.

2.3 Results

Upon removal from the reaction vessel, samples were moist but most of the added water/brine had been lost. Neither the crushed feldspar nor substrate materials showed any significant “cementation” or aggregation. Optical microscopy did not reveal any visible secondary precipitates. However, some samples (Ab201, Ab202, and P03)

did show a pale greenish to yellowish discoloration upon removal from the reaction vessel.

2.3.1 Anorthite-CO_2-water/brine experiments

2.3.1.1 SEM observations on anorthite grain surfaces

Feldspar grain surfaces, investigated by SEM prior to reaction, appear to be devoid of any mineral coatings. However, all anorthite grain surfaces analysed after reaction with CO_2 at 200 and 300°C, show precipitation of secondary phases, as well as occasional dissolution features such as etch pits.

The anorthite samples reacted with CO_2 and (initially) pure water at 300°C (An301-303; no Teflon-liner) show widespread surface precipitates of the types illustrated in Figure 2.2. These surface precipitates consist mainly of fine, platy crystals, generally less than 1 μm in size (Figures 2.2a, b, e, f, g), forming a thin and discontinuous porous layer or "frosting" covering approximately 10% (An302) to 40% (An301, 303) of the anorthite grain surfaces. The crystal morphology of the "frosting" resembles that of hydrotalcite, formed under hydrothermal conditions, as reported by *Kovanda et al.* [2005], and boehmite [see Figure 9 in *Bénézeth et al.*, 2007]. Sample An301 shows rare, lath-like crystals, up to 5 μm in size, which morphologically resemble aragonite (Figure 2.2b). Sample An302 (6 MPa, 21 days) shows coarser honeycomb-like clusters of platy crystals (see centre of Figure 2.2c and higher magnification in Figure 2.2d). Run An303 (18 MPa, 11 days) shows additional larger rosettes and "booklets" (10 μm) of hexagonally shaped plates (< 5% coverage - Figures 2.2f, g), as well as clusters of irregularly shaped crystals (1-10 μm in size - see Figures 2.2f and h). Experiment An303 also displays prismatic etch pits developed in the anorthite surface (Figure 2.2h), giving it a roughened appearance. From their morphology, the coarser platy crystals observed in samples An301-303 presumably represent clays or other phyllosilicate phases, such as illite, smectite, or kaolinite. No morphological evidence was found for the precipitation of calcite.

Compositional characterisation of the secondary phases was attempted using SEM-EDX (electron dispersive X-ray analysis). However, due to the small size of the crystals and the limited thickness of the precipitated layers these analyses only permitted to show that the frosting of fine platy crystals contained high concentrations of nickel.

Sample An201 (200°C, 18 MPa, 14 days, Teflon-liner) shows up to ~ 80% surface coverage by a "frosting" of fine platy secondary phases. These phases are closely similar to the ones obtained at 300°C but are morphologically less developed and finer in grain size (below 1 μm). The similarity suggests that the same Ni-rich phase is formed as in samples An301-303. Samples An210 and An211 were not studied by SEM.

2.3.1.2 XRD data

The relatively large grain surface coverage (80 %) by the precipitates secondary phase in experiment An201 made XRD analysis possible (detection limit: ~ 1 wt%). Some of the peaks obtained can be correlated with anorthite, while other peaks represent newly precipitated phases (see Figure 2.3). These peaks suggest a talc- or smectite-like phase, as shown by comparison with standard talc and a smectite-type phyllosilicate XRD patterns (Figure 2.3). A number of the observed peaks (e.g. at $2\theta = 13.56°$, 26.10° and 44.98°), not belonging to anorthite, quartz, talc or smectite, might reflect the presence of a hydrotalcite-like (HTL) phase, as they coincide with powder XRD patterns for a synthetic Mg-Al hydrotalcite formed at 200°C, reported by Kovanda et al. [2005]. Note that the broadness of the peaks at 5.98 and 19.92° indicates that the mineral grains related to those peaks are small in size.

2.3.1.3 Infrared spectra

Fourier Transform Infrared (FTIR) transmittance spectra obtained from anorthite samples reacted with CO_2 and water at 300°C (e.g. An302) show a clear anorthite spectrum at wavelengths in the range 900-1200 cm^{-1} (Figure 2.4a). Additional peaks, not present in unreacted anorthite reference spectra (Figure 2.4b), are observed in reacted samples at 1360 cm^{-1}, 1615 cm^{-1}, and in the region 2820 to 3600 cm^{-1}, as seen in Figure 2.4a. The peaks at 1360 cm^{-1} are related to the presence of HCO_3^- [*Gadsen*, 1975], while those at 1615 and 2820-3600 cm^{-1} correspond respectively to the interlayer OH bending and stretching vibrations [*Gadsen*, 1975]. Comparison of the IR spectra of sample An302 with reference spectra measured for fine grained kaolinite (Figure 2.4c) and calcite (Figure 2.4d) shows that none of the characteristic peak combinations of these minerals are present in the spectrum of the reacted anorthite. The non-anorthite peaks in the reacted anorthite spectrum do show some similarity with a reference spectrum measured for hydrotalcite, $Mg_{2x}Al_2(OH)_{4x+4}CO_3 \cdot nH_2O$, obtained from Sasol Germany GmbH (Figure 2.4e). The disproportionally large peak at 1600 cm^{-1} together with the peak at 2950 cm^{-1} in the reacted sample may indicate the presence of boehmite [Figure 2.4f; *Kloprogge et al.*, 2002]. It is possible that the large peak observed at 980-1070 cm^{-1} indicates the presence of a Si-rich, gel-like leached layer on the anorthite surface, as characteristic bands of Si and Si-O are

→ Fig. 2.2. SEM (secondary electron) images of samples An301-An303 (see Table 2.1). a) Low magnification image of sample. b) Higher magnification image of a portion of sample An301. Note the precipitation of very fine platy crystals and, locally, larger lath-shaped crystals. c) Low magnification image of sample An302. d) Higher magnification image of the coarser honeycomb-like, platy crystals (An302). e) Higher magnification of the "frosting" of the anorthite surface (An302) by very fine platy crystals. f) Low magnification image of sample An303. g) Higher magnification image of one of the rosettes (An303). h) Dissolution features on the surface of an anorthite grain in sample An303. Arrows indicate clusters of irregularly shaped crystals.

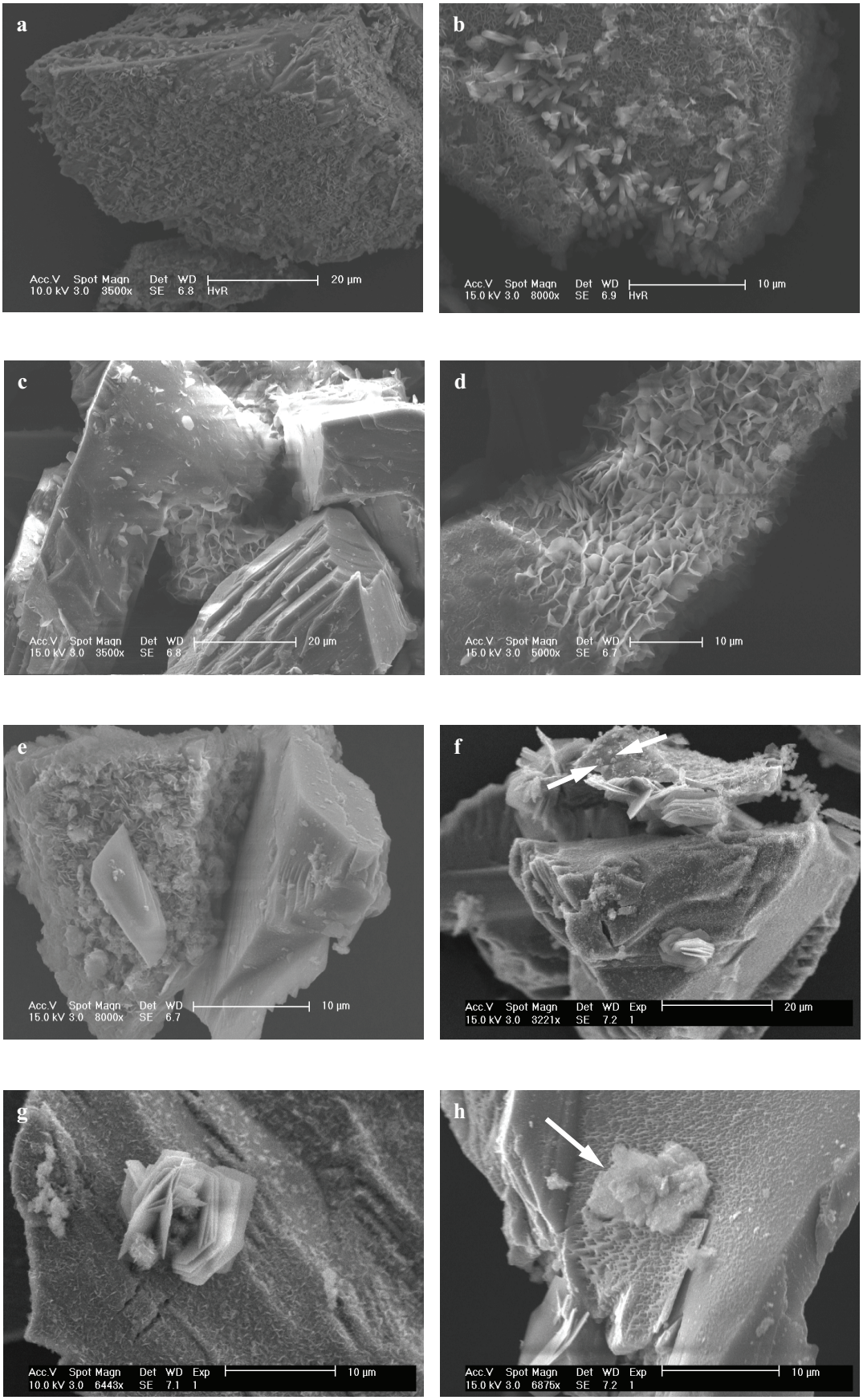
a
Acc.V Spot Magn Det WD 20 µm
10.0 kV 3.0 3500x SE 6.8 HvR
b
Acc.V Spot Magn Det WD 10 µm
15.0 kV 3.0 8000x SE 6.9 HvR
c
Acc.V Spot Magn Det WD 20 µm
15.0 kV 3.0 3500x SE 6.8
d
Acc.V Spot Magn Det WD 10 µm
15.0 kV 3.0 5000x SE 6.7
e
Acc.V Spot Magn Det WD 10 µm
15.0 kV 3.0 8000x SE 6.7
f
Acc.V Spot Magn Det WD Exp 20 µm
15.0 kV 3.0 3221x SE 7.2 1
g
Acc.V Spot Magn Det WD Exp 10 µm
10.0 kV 3.0 6443x SE 7.1 1
h
Acc.V Spot Magn Det WD Exp 10 µm
15.0 kV 3.0 6875x SE 7.2 1

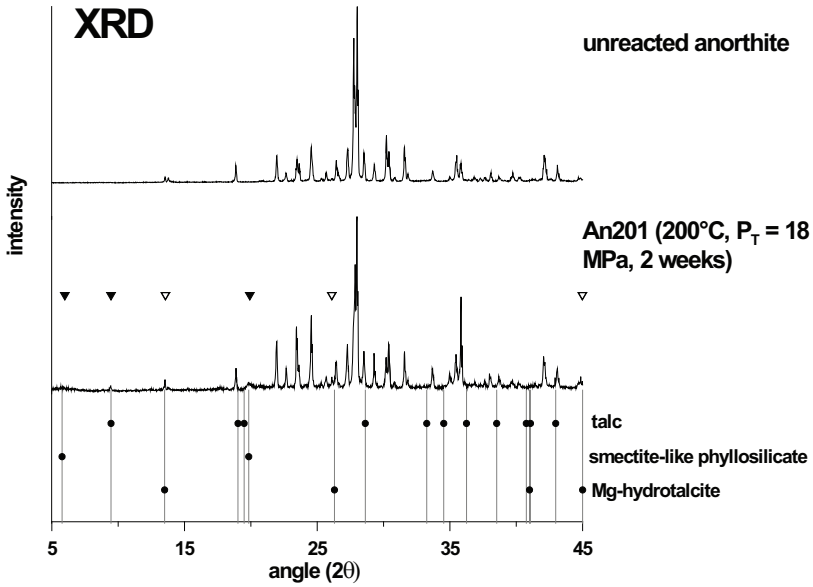

Fig. 2.3. X-ray diffraction pattern for sample An201 (T = 200°C, P_T = 18 MPa) showing peaks that coincide with unreacted anorthite, and one or more other phases. The peaks that are not related to the anorthite substrate (e.g. peaks at 2θ = 5.98°, 9.46°, 13.56°, 19.92°, 26.34° and 44.98°) appear to coincide with those of talc-like and smectite-type phyllosilicate minerals (▼) and hydrotalcite (▽ - see also *Kovanda et al.* [2005]).

generally observed in the range 1200-400 cm^{-1}. Peaks observed at 2818, 2792 and 2721 cm^{-1} remain unidentified.

In contrast to anorthite samples reacted with water at 300°C, samples An210 and An211 reacted with NaCl and $MgCl_2$ solution and CO_2 at 200°C show anorthite peaks only and no signs of any secondary precipitate, such as calcite, magnesite, hydrotalcite or hydrocalumite (a hydrotalcite-like mineral with Ca^{2+} and Al^{3+} as the main cations and Cl^- as the interlayer anion).

2.3.1.4 Thermogravimetric analyses

A 50 mg portion of sample An303 was analysed using TGA (detection limit TGA: < 1 μg; ~ 0.002 wt%). The results reveal three episodes of mass loss, as seen in Figure 2.5. The temperature range of the first episode (350-400°C) coincides with that of combined dehydroxylation and decarboxylation of hydrotalcite [*Kanezaki*, 1998; *Ogawa and Kaiho*, 2002; *Roelofs et al.*, 2002], supporting the above evidence for the presence of a (Ni-bearing) hydrotalcite-like phase in our experiment. If a hydrotalcite composition of $Ni_2Al(OH)_6(CO_3)_{0.5} \cdot H_2O$ is assumed, then taking into account the fact that the interlayer water ($\cdot H_2O$) is removed from hydrotalcite at 100 to 190°C [*Roelofs et al.*, 2002], the observed extent of dehydroxylation and decarboxylation would correspond to the presence of 0.14 wt% Ni-hydrotalcite. The two remaining peaks (500-580°C and 580-670°C) correspond well with those expected for 0.49 wt% boehmite [*Kloprogge et al.*, 2002] and 0.64 wt% kaolinite [*Huertas et al.*, 1999],

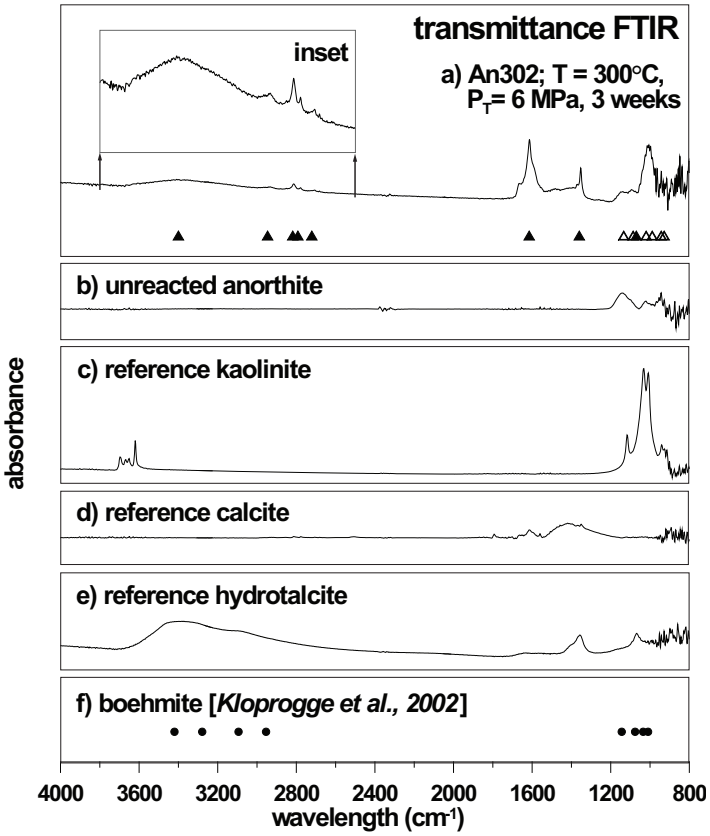

Fig. 2.4. Fourier Transform Infrared transmittance spectra of anorthite reacted for with CO_2 at 300°C and a total pressure of 6 MPa (An302) (a) and unreacted anorthite (b). For clarity, part of the spectrum of the reacted sample (in the wavelength range 2500-3800 cm^{-1}) has been enlarged and the vertical scale has been exaggerated – see inset. The spectrum measured for anorthite is visible in the wavelength range 900 to 1200 cm^{-1} (peaks marked △). Clearly visible in the spectrum for reacted material are the non-anorthite peaks (marked ▲) in the region 2820 to 3600 cm^{-1}, 1615 cm^{-1} and 1360 cm^{-1}, all indicative for OH bending and stretching bonds. Reference spectra for kaolinite (c), calcite (d), hydrotalcite (e) and boehmite (f) have been added for comparison.

respectively. This indicates a roughly 50% increase in boehmite content, and complete dissolution of gibbsite and calcite from the anorthite surface, compared to the starting material.

2.3.1.5 FEG EPMA results

We also performed an elemental analysis on sample An301 using a JEOL Microprobe FEG EPMA at JEOL Ltd. Tokyo. At acceleration voltages of 12 kV, the results show that the precipitate is rich in Al, O, Mg and Ni, with trace amounts of Fe (Figure 2.6). Some of the Al can be correlated to the occurrence of Mg, Ni, and Fe, though not all. The frosting is therefore interpreted as containing a Al-rich, Si-free phase (e.g. boehmite) and a Mg,Ni,Fe-bearing hydrotalcite of type $(Mg,Ni,Fe)_{1-x}Al_x(OH)_2(CO_3)_{x/2} \cdot m\,H_2O$ [following *Cavani et al.*, 1991]. The Mg:Ni:Fe ratio for the hydrotalcite-like phase is approximately 1.25:1:1.

2.3.2 Albite-CO_2-water/brine experiments

Reflectance IR spectroscopy of sample Ab201 displays a clear albite spectrum in the wavelength range 800-1300 cm^{-1} (Figures 2.7a,b). A secondary phase is also revealed, with a spectrum in the range 2400-3800 cm^{-1} very similar to that measured

for our Sasol reference Mg-hydrotalcite (see Figure 2.7c). No evidence for dawsonite (e.g. peaks at 3285, 1570 and 1403 cm^{-1} – see Figure 2.7d [*Gadsen*, 1975]) or magnesite (e.g. 1446 and 886 cm^{-1} – see Figure 2.7e [*Dubrawski et al.*, 1989]) is observed. Possible peaks for quartz are located at the lower frequency end of the wavelength spectrum (< 1200 cm^{-1}) but are not observed in the reacted material. The infrared spectrum measured for sample Ab202 shows no evidence of secondary phases, though experimental conditions were identical to Ab201. Presumably, either no precipitate is formed or it is too minor to be detected by FTIR.

2.3.3 Magnesite precipitation experiments

The dry substrate or seeding material in samples P01-04 (Table 2.3) was weighed before and after the experiments in order to analyse for any mass increase as a result of precipitation. Because of the absence of Al in all cases, any mass increase after the experiments must be due to the precipitation of magnesite ($MgCO_3$) on the surface of the seeding material. No change in mass was observed after experiments P01 (quartz substrate) and P03 (calcite substrate). XRD analysis of sample P01 shows that no other phase but the quartz substrate was detectable. A mass increase of approximately 100% and 10% is observed in samples P02 (hydromagnesite substrate) and P04 (quartz and hydromagnesite substrate), respectively. This is equivalent to that expected from precipitation of all Mg^{2+} from the added solution phase, in the form of magnesite, together with the conversion of $Mg(OH)_2$, present in the hydromagnesite substrate, to $MgCO_3$. No additional analysis was performed on these samples.

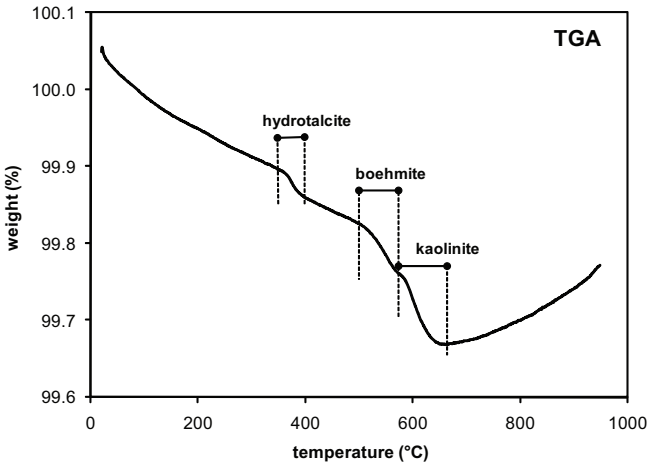

Fig. 2.5. Thermogravimetric analysis data for sample An303 (T = 300°C, P_T = 18 MPa) showing three regions of mass loss, interpreted as Ni-hydrotalcite ($Ni_2Al(OH)_6(CO_3)_{0.5}•H_2O$), boehmite (AlOOH) and kaolinite ($Al_2Si_2O_5(OH)_4$), respectively.

2.4 Discussion

In our experiments, initial water/brine to rock mass ratios varied between 5:1 and 10:1. However, supercritical CO_2 can contain 17 to 90 mol% of water, at 200 to 300°C and 6 to 18 MPa total pressure [*Tödheide and Franck*, 1963]. Part of the added water dissolved in the supercritical CO_2 phase during our experiments and may have been transported to cooler parts of the pressure vessel. For these reasons, it is not possible to calculate the exact amount of solution remaining in the reaction vessel during the experiment. This, coupled with a lack of quantitative data on solution chemistry, prevented us making chemical calculations on the feldspar-CO_2-water/brine and substrate-CO_2-brine systems. As the analyses on both anorthite and albite feldspar samples yielded broadly similar results they will be discussed together in the following sections, focussing on the identity of the reaction products and implications for understanding subsurface CO_2 injection.

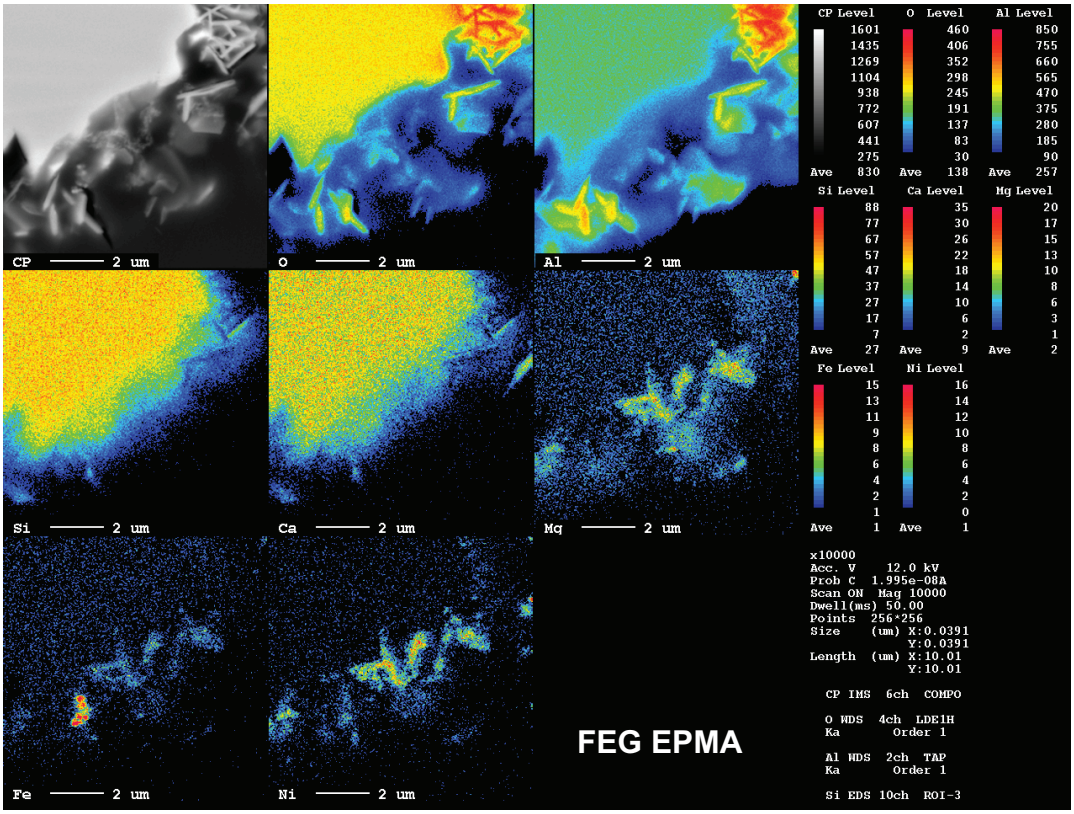

Fig. 2.6. FEG EPMA maps of the fine platy frosting of secondary phase observed to have grown on the anorthite grain surfaces in samples treated with CO_2 and water at 200-300°C (here sample An301, T = 300°C, P_T = 6 MPa). (Performed using the JXA 8500F FEG EPMA instrument at the SA Group, Electron Optics Division, JEOL Ltd., Tokyo – see acknowledgements).

2.4.1 Feldspar experiments - identity and formation of secondary phases

Most experiments on the feldspar-CO_2-water/brine system (6-18 MPa, 200-300°C) showed precipitation of secondary phases (An301-303, An201, and Ab201) within 1-3 weeks. Precipitation was mainly limited to a very thin, discontinuous layer or "frosting" of micron-sized platy crystals on the feldspar surface, which made analysis very difficult. Our morphological observations and FTIR, TGA and FEG EPMA results indicate that the "frosting" contained a Mg,Ni,Fe-bearing hydrotalcite-like phase. Following the general composition for HTL phases, suggested by *Cavani et al.* [1991], the composition of this HTL phase would be $(Mg,Ni,Fe)_{1-x}Al_x(OH)_2(CO_3)_{x/2} \cdot m\ H_2O$ (Mg:Ni:Fe ≈ 1.25:1:1). Nickel present in this phase was an artefact derived from the reaction vessel. Booklets and rosettes observed on the anorthite surface (An303), together with TGA data, indicate the presence of kaolinite. Honeycomb-like clusters observed in sample An302 show a morphological resemblance to phyllosilicate phases like smectite and illite. Precipitation of boehmite is suggested by TGA and FEG EPMA data. Additionally, a Si-enriched leached layer had probably

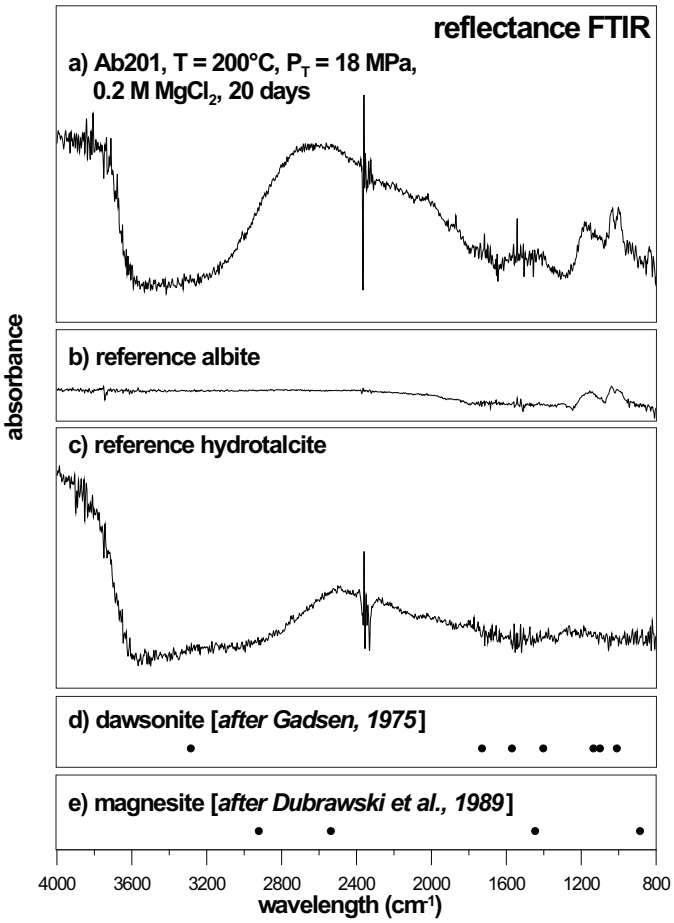

Fig. 2.7. Fourier Transform Infrared reflectance spectra of albite reacted at 200°C and 18 MPa total pressure in the presence of 0.2 M $MgCl_2$ solution (Ab201) (a), unreacted albite (b), hydrotalcite (c), dawsonite (d), and magnesite (e).

formed on the anorthite grain surfaces, as suggested by FTIR. Minor other phases were also detected, including lath-like crystals, which may correspond to aragonite, based on the morphological resemblance, and irregularly shaped crystal aggregates. No calcite or dawsonite was observed. Either these phases had not precipitated or in quantities too minor to be detected (< 1 wt%). The presence of both kaolinite and, possibly, aragonite in sample An301 indicates that reaction (2.1) may have taken place. However this reaction occurred to a much lesser extent than the other reactions observed, such as precipitation of boehmite and a Mg,Ni,Fe-bearing hydrotalcite-like phase. No observations to support reaction (2.2) were made. Moreover, precipitation of secondary phases was not observed in experiments An201-211 and Ab202 in presence of salt solutions.

The well-developed morphology of most of the observed secondary minerals, in particular the assumed HTL phase, kaolinite, boehmite and possibly smectite or illite, is an indication that these phases had sufficient time to grow from supersaturated solution during the progress of the experiments. The depressurisation procedure may have lead to supersaturation of the aqueous solution, and the concomitant precipitation of secondary phases. However, the depressurisation procedure was performed very rapidly (in less than 1 min) and likely expelled most of the solution from the reaction vessel. This probably did not leave enough time for any crystalline phases to precipitate from solution. The absence of any salt precipitates on the grain surfaces also suggests that most of the solution was expelled during depressurisation, preventing salt precipitation.

2.4.2 Comparison with previous work on plagioclase

Naturally weathered detrital (plagioclase) feldspars from diagenetic arkosic sandstone systems generally show extensive corrosion [*Walderhaug and Bjørkum*, 1992; *Pearce et al.*, 2000; *Baines and Worden*, 2004; *Gaus et al.*, 2004]. From previous studies, dissolution of Ca-rich plagioclase feldspar appears to be more extensive than of the Na-rich and K-rich feldspars. Secondary porosity generated by the dissolution of feldspar is filled by carbonate cement (calcite and dolomite), as well as clays (kaolinite). We have some indication that a similar reaction, that is precipitating kaolinite and possibly a small amount of aragonite, occurred in our experiment An301. Occurrences of dawsonite in nature are generally limited to alkaline or highly-alkaline environments [*Baker et al.*, 1995; *Dyni*, 1996]. Experimental studies on the solubility and stability of dawsonite [*Bénézeth et al.*, 2007] have shown that at temperatures below 150°C, dawsonite is in equilibrium with bayerite, while at higher temperatures, equilibrium with boehmite dominates. In addition, *Bénézeth et al.* [2007] predicted that the presence of a pH buffering assemblages, such as albite, will impose tight constraints on dawsonite precipitation.

Precipitation of kaolinite and boehmite is in agreement with previous results [*Murakami et al.*, 1998; *Carroll and Knauss*, 2005] of Ca-rich feldspar batch experiments (30-210°C, pH 3.2-5.4), both in the absence and presence of CO_2. In addition, Si-enriched leached layers, similar to the ones implied from our observations, are generally observed on the surfaces of acid treated feldspars [*Casey et al.*, 1989; *Hellmann et al.*, 1990]. Our data also agree favourably with the study of *Suto et al.* [2007] on crushed granite treated with CO_2 at 100-350°C, 0-25 MPa P_{CO2} and in the presence of pure water. In their experiments, precipitation of μm-sized platy minerals, with a very similar morphology to our "frosting", on the plagioclase surfaces was observed. Identification of the constituent phases proved to be difficult, but on the basis of geochemical computations it was concluded that the precipitated secondary phases were kaolinite, smectite, muscovite and calcite – similar to the kaolinite and smectite/illite observed in our runs. In view of the remarkable similarity between the "frosting" reported by *Suto et al.* [2007] and by ourselves, and as their reaction vessel consisted of a Ni-Cr alloy (Hastelloy), it might be possible that the *Suto et al.* [2007] experiments were also contaminated with Ni and that a HTL phase was formed.

Hydrotalcite and hydrotalcite-like (HTL) phases with a wide range of compositions are known to precipitate naturally in industrial alkaline waste (e.g. fly ash) deposits at temperatures in the range 20-70°C [*Schweizer*, 1999; *Piantone et al.*, 2004]. They are also synthesised in the laboratory under conditions ranging from room temperature to hydrothermal conditions (up to 300°C), P_{CO2} up to 130 MPa, and a wide range of pH [*Cavani et al.*, 1991]. Moreover, the other phases produced in our experiments are known to be stable under conditions ranging from weathering to elevated pressures and temperatures. Hydrotalcite and HTL phases and other minerals, observed in our experiments, can form under a wide range of conditions. This suggests that our results, obtained under hydrothermal conditions, can be applied to lower temperature (CO_2 sequestration) conditions provided suitable ions available, notably Al, Mg, Fe and heavy metals for HTL phases. In other words, if appropriate ions are present, reacting plagioclase with CO_2 and water under temperatures of 50-100°C and P_{CO2} of > 8 MPa may lead to precipitation of HTL phases, boehmite, kaolinite and other phyllosilicate phases like smectite or illite. However, since hydrotalcite and HTL phases and reactions are not included in most geochemical codes, they will generally not be anticipated by reactive transport simulations.

In our feldspar experiments, no dawsonite or magnesite and possibly very little aragonite were observed. Precipitation of these minerals may have been inhibited if the solution did not attain the critical saturation state required for nucleation. However, it is not unlikely that carbonates would ultimately precipitate, given enough time for sufficient suitable ions, such as Ca^{2+} or Al^{3+}, to be liberated by anorthite or albite dissolution, respectively. Longer term (~2.5 months) batch experiments performed

by *Kaszuba et al.* [2003, 2005] have shown that carbonate (magnesite and siderite) precipitation occurs in sandstone-shale systems, at 200°C and 20 MPa total pressure, alongside a range of secondary phases (e.g. smectite clays, carbonates and zeolites).

2.4.3 Significance of the carbonate control experiments

Our Mg-solution experiments with substrates (Table 2.3) showed that carbonate (magnesite) could precipitate under the conditions used in the present study, provided that the substrate had a chemical composition similar to that of the precipitate. The experiments also showed that the precipitation survived depressurisation of the apparatus, and did not dissolve as a result of contact with an acidic solution. Hence, we can conclude that if, in addition to the minor amount of aragonite, more carbonates (magnesite, calcite or dawsonite) were formed in our feldspar experiments they would have been preserved. The lack of carbonate precipitation may be due to the absence of appropriate substrate material to promote carbonate precipitation. This conclusion is fully supported by previous studies on magnesite [*Giammar et al.*, 2005], aragonite [*de Boer*, 1977] and calcite [*de Boer*, 1977; *Lin and Singer*, 2005] precipitation. These studies show that, even if a solution is saturated with the respective carbonate, the nucleation process will inhibit precipitation in the absence of the appropriate seed material. Diagenetic studies also show that calcite cementation within sandstones is typically concentrated in horizons rich in carbonate fossils. However, it remains unclear if this reflects enhanced nucleation on the fossil substrate [*Wilkinson and Dampier*, 1990] or higher concentrations of dissolved calcite within these carbonate-rich layers [*Bjørkum and Walderhaug*, 1990].

2.4.4 Implications

Our anorthite experiments confirmed reaction (2.1) to some extent, by the precipitation of kaolinite and possibly minor amounts of aragonite. The albite experiments showed no precipitation of dawsonite, following reaction (2.2). Precipitation was dominated by the formation of boehmite, a Mg,Ni,Fe-bearing hydrotalcite-like phase, kaolinite and possibly smectite or illite. Our experiments were done at relatively high temperatures. However, on the basis of the arguments given above (section 2.4.1), we believe that our results are relevant in a general sense to understanding CO_2 injection, and associated changes in porosity and permeability, into arkosic sands and sandstones [Frio Formation, Texas, USA; *Kharaka et al.*, 2006; Nagaoke, Japan; *Mito et al.*, 2008; e.g. Sleipner Field, Norway; *Pearce et al.*, 2000], as well as CO_2 injection into geothermal fields [e.g. Ogachi Hot Dry Rock site, Japan; *Ueda et al.*, 2005] or even injection into plagioclase-rich basalts [e.g. Palisades Sill, New York/New Jersey, USA; *Matter et al.*, 2007].

For example, we noted that in our experiments plagioclase feldspars show features of dissolution within a few days. Taking into account pH and the activation energy for dissolution of Ca-rich feldspar [e.g. 18.4 kJ/mol for anorthite; *Oelkers and Schott*, 1995], such effects will likely be slowed down by a factor of 3-30 at reservoir conditions (assuming dissolution reaction control). This may improve the transport properties, i.e. porosity and permeability, of plagioclase-bearing arkosic reservoirs, plutonic rocks, geothermal fields and fractured basalts shortly after CO_2 injection, notably in the region around the injection well. However, any improvements of transport properties, as a result of the formation of secondary porosity, may be offset by the precipitation of clays (kaolinite, smectites or illites) and carbonates. On the other hand, in the absence of appropriate substrates, precipitation of carbonate minerals may be delayed as a result of nucleation inhibition making the sites of carbonate precipitation difficult to predict. In this context, we noted that geochemical models [*Xu et al.*, 2004; *Lagneau et al.*, 2005; *Xu et al.*, 2005; *Zerai et al.*, 2006] generally do not incorporate the effects of substrate on precipitating phases. These effects might be of particular importance when attempting to model coupled reaction and transport. Much is known about nucleation and growth [*Bjørkum and Walderhaug*, 1990; *Dove and Hochella Jr.*, 1993; *Gratz et al.*, 1993; *Lebrón and Suarez*, 1996], however, little is applied to the field of CO_2 sequestration. Carbonate-rich horizons (cf. diagenesis) may lead to local precipitation of carbonate minerals. Injection of carbonate suspensions may offer ways to steer precipitation, especially in reservoirs containing little or no carbonate.

Precipitation of heavy metal hydrotalcites, similar to the Mg,Ni,Fe-bearing hydrotalcite-like phase formed in our experiments, might occur around CO_2 injection and abandoned wells due to release of Fe from the well bore system, as long as excess water and dissolved Al^{3+} is present to continue reaction. More importantly, HTL phases may have important significance in relation to combined CO_2 storage and heavy metals immobilisation through injection of fluidised industrial waste (e.g. fly ash) into reservoirs or saline aquifers [*Canty and Everett*, 2006]. Fly ash is an alkaline waste product, mainly consisting of silicate glass (SiO_2), mullite ($Al_2Si_2O_8$) and carbonates, hydroxides and sulphates containing elements like iron, calcium and heavy metals. The high alkalinity of ash make it highly suitable for CO_2 mineralization [*Back et al.*, 2007] either in a reservoir, saline aquifer or salt cavern environment. *Back et al.* [2007] predict that more than 0.1 kg CO_2 can be sequestered per kg of brown coal ash. Sequestration of CO_2 by reaction with fly ash and water will mainly occur through precipitation of carbonates (calcite) [*Piantone et al.*, 2004]. Trapping of CO_2 by hydrotalcite precipitation, i.e. by absorption of bicarbonate anions into the interlayer space of hydrotalcite-like phases, will be much less extensive. However, precipitation of HTL phases and hydrotalcite may play a substantial role in preventing heavy metal

contamination of ground water. Injection of fluidised fly ash may also prove highly suitable for sealing leaky wells or faults at CO_2 storage sites, or for channelling CO_2 migration in a given reservoir or saline aquifer, while immobilising the heavy metals via hydrotalcite precipitation [*Waring and Taylor*, 2001].

2.5 Conclusions

We have investigated the reactions occurring in the plagioclase-CO_2-water/brine system under hydrothermal conditions (200-300°C, P_{CO2} = 0.4-15 MPa) as well as precipitation of carbonates from Mg-rich brines in the absence of plagioclase (200°C, P_{CO2} = 15 MPa). Our main findings can be summarised as follows:

1. In the experiments on plagioclase, precipitation of boehmite, kaolinite, a Mg,Ni,Fe-bearing hydrotalcite-like phase, and a phyllosilicate phase, possibly smectite or illite, occurred within 1 to 3 weeks, depending on conditions and solution composition. Silicon enriched leached layers probably formed on the feldspar grain surfaces. In addition, a minor quantity of a mineral resembling aragonite was observed. This suggests that reaction (2.1) (Ca-plagioclase + CO_2 + water → kaolinite and $CaCO_3$) may have occurred to a limited extent. However, reactions precipitating boehmite, clays and the hydrotalcite-like phase dominated, the nickel in the hydrotalcite-like phase being derived from the reaction vessel. No calcite, dawsonite, magnesite or other CO_2-bearing phases were detected, with the exception of a small amount of aragonite.
2. The secondary phases observed in our plagioclase experiments are known to be stable over a wide range of conditions. We therefore believe that the phases formed in our high temperature experiments will also form under lower temperature CO_2 sequestration conditions in systems with suitable fluid-rock composition.
3. Carbonate (magnesite) precipitates from Mg-rich solution under hydrothermal conditions in the presence of CO_2 and was preserved during termination of our experiments. This confirms that carbonates would have been observed in our feldspar experiments if they had formed. However, a chemically similar substrate is required to promote carbonate nucleation and precipitation. Without a suitable substrate, precipitation did not occur in our experiments but may in longer term experiments or in nature.
4. Under CO_2 storage conditions in systems containing Ca-rich plagioclase, early clay precipitation could occur in advance of or alongside carbonate precipitation, depending on the availability of suitable carbonate-substrate. The effect of the nucleation barrier on carbonate precipitation should be taken into account when modelling coupled reaction and transport, as it may strongly

influence the location of carbonate precipitation.

5. Though hydrotalcite precipitation occurred in our plagioclase experiments due to Ni contamination from the reaction vessel, it may be important in certain situations relevant to geological CO_2 sequestration. In particular, hydrotalcite may form as a result of subsurface injection and CO_2 mineralization of fluidised alkaline wastes, such as fly ash. Injection and mineralization of alkaline waste can also be used to seal leaky well bores and faults or for channelling CO_2 migration. Though carbonates will be the main mineral trapping phases in such operations, precipitation of hydrotalcites would have the beneficial effect of immobilising heavy metals.

Acknowledgements

This research was financed by Shell International Exploration and Production (contract number 4600002284) and performed within WorkPackage 4.1 (Subsurface mineralisation) of the Dutch national BSIK research project CATO on CO_2 capture, transport and storage. We thank Peter van Krieken, Saskia ten Grotenhuis, Tilly Bouten and Pieter Kleingeld for their assistance during the experiments and analyses. We also thank Mrs. Ayako Sato (from SA Group, Electron Optics Division, JEOL Ltd.) for providing us with preliminary test results of the JXA 8500F FEG EPMA. Dr. P. Bénézeth, Dr. C. Noiriel, Dr. J. Kaszuba, and an anonymous reviewer are thanked for extensive feedback on the draft manuscript, which much improved the final version.

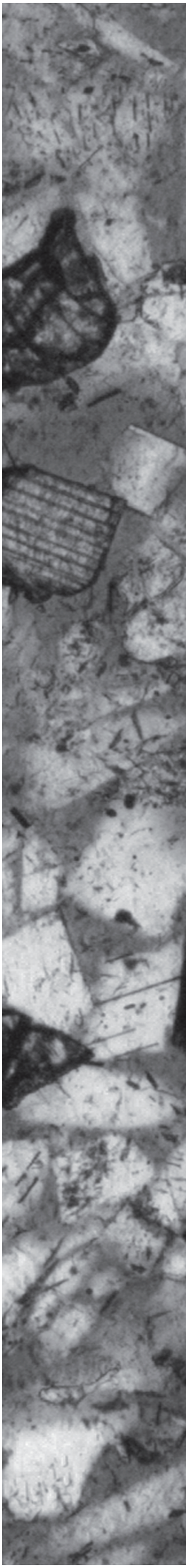

3

Creep of simulated reservoir sands and coupled chemical-mechanical effects of CO_2 injection

S.J.T. Hangx, C.J. Spiers and C.J. Peach

Submitted to the Journal of Geophysical Research

Abstract

Geological storage of CO_2 in clastic reservoirs and aquifers is expected to have a variety of coupled chemical-mechanical effects. To investigate the effects of CO_2 injection on creep phenomena, we performed uniaxial compaction experiments on granular aggregates of quartz and feldspar under both wet and dry control conditions. The experiments were performed in constant stress mode. Grain size, temperature, CO_2 partial pressure, and effective stress were varied in order to determine their individual effect. Pore fluid pH was varied by the injection of CO_2 and by addition of acidic and alkaline additives. Pore fluid salinity was increased by the addition of NaCl. Wet samples showed instantaneous compaction upon load application, followed by time-dependent creep. From the mechanical data and microstructures, the main compaction mechanism was inferred to be chemically enhanced microcracking in both quartz and feldspar, with subcritical crack growth, i.e. stress corrosion cracking, controlling deformation in the creep stage. The injection of CO_2 and the concomitant acidification of the pore fluid inhibited microcracking in both the quartz and feldspar samples in line with known effects of pH on stress corrosion cracking. We infer that the injection of CO_2 into quartz- and plagioclase-bearing sandstones will inhibit grain-scale microcracking process, and that related geomechanical effects, such as reservoir compaction and surface subsidence, will be negligible compared with the poro-elastic response.

3.1 Introduction

It is now widely accepted that, in order to maintain atmospheric CO_2 concentrations below 450 ppm and thus limit climate change, anthropogenic CO_2 emissions need to be reduced by 30% of 1990 levels by 2020 and up to 80% by 2050 [*Commission of the European Union,* 2007]. One of the most promising ways of contributing to this is through CO_2 capture at source, coupled with geological storage in depleted oil and gas reservoirs, saline aquifers, or coal seams. These storage options are now being widely considered across the world [*Bachu*, 2000; *Orr Jr.*, 2004].

Geological storage of carbon dioxide in clastic hydrocarbons reservoirs, or in aquifers, will result in several effects on the host rock. Aside from the direct poro-elastic response to changing pore pressure as CO_2 is injected [*Wang*, 2000], possible effects include CO_2 mineralisation reactions and associated porosity-permeability changes. In addition, chemically coupled mechanical effects, such as creep due to dissolution reactions, CO_2-enhanced microcracking, or diffusive mass transfer processes like pressure solution, may lead to time-dependent reservoir compaction. The ultimate extent of any CO_2 mineralisation reactions depends on the availability of reactive cations present in phases such as Ca-rich feldspars, Fe/Mg-rich phyllosilicates (clays and micas), and Fe-oxides [*Gunter et al.*, 2000; *Johnson et al.*, 2001; *Wawersik et al.*, 2001; *Sass et al.*, 2002; *Aagaard et al.*, 2004; *Carroll and Knauss*, 2005; *Fernandez-Bastero et al.*, 2005; *Palandri et al.*, 2005; *Xu et al.*, 2005; *Zerai et al.*, 2006]. By contrast, rates of reaction and of coupled chemical-mechanical creep effects are expected to depend on factors such as pore fluid pH, grain size, temperature and effective stress [*Atkinson*, 1979; *Schutjens*, 1991; *Dewers and Hajash*, 1995; *Hajash et al.*, 1998; *Niemeijer et al.*, 2002; *Karner et al.*, 2003; *Chester et al.*, 2004; *Chester et al.*, 2007].

The importance of CO_2-related creep effects lies in their potential to cause reservoir rock compaction and hence deformation-induced damage to well-bore, caprock and fault-seal systems, particularly in the long term. However, very few data exist on the rates of the relevant reservoir compaction processes [*Le Guen et al.*, 2007; *Liteanu and Spiers*, 2009], so that the magnitude of such effects remains hard to evaluate. In this paper, we report uniaxial (i.e. 1-D) compaction creep experiments performed on dry and wet granular aggregates of quartz and of Ca-bearing feldspar, the latter being chosen to simulate reactive feldspar-rich sandstones. Our aim was to assess the mechanical effects of fluid-rock interaction due to CO_2 injection under reservoir conditions, as well as the effect of grain size, applied stress, temperature and pore fluid composition on creep phenomena.

3.2 Experimental method

We performed our quartz experiments on dry and wet granular samples with a fixed initial grain size ($d = 425 \pm 25$ μm) at room temperature, using an effective axial stress (σ_{eff}) of 35 MPa and a CO_2 partial pressure (P_{CO2}) of ~$4 \cdot 10^{-5}$ MPa (atmospheric CO_2 pressure) to 15 MPa. Pore fluid pH was varied not only by varying the CO_2 pressure, but also by the addition of NaOH and $Ca(OH)_2$ to solution. As quartz is unreactive with CO_2, no chemical reactions were expected to occur in the quartz experiments, besides possible dissolution-precipitation effects. In this sense, our quartz experiments can be regarded as "control experiments" compared with our tests on feldspars, which can react with CO_2, potentially precipitating calcite, secondary clays or even hydrotalcite, depending on conditions and fluid-rock compositions [*Hangx and Spiers*, 2009].

In our experiments on feldspar aggregates, we aimed to maximise any contribution of mineralisation reactions to creep and/or porosity reduction by using Ca-rich feldspar, i.e. labradorite. Several factors were systematically varied in order to determine their individual effect on compaction behaviour, namely water content (dry vs. wet), initial grain size ($25 \leq d \leq 275$ μm), temperature ($20 \leq T \leq 100$°C), CO_2 partial pressure (~$4 \cdot 10^{-5} \leq P_{CO2} \leq 10$ MPa), and effective axial stress ($20 \leq \sigma_{eff} \leq 100$ MPa). We specifically investigated the dependence of volumetric strain and strain rate on grain size, with and without carbon dioxide at a pressure of 10 MPa, at 80°C and at an effective stress of 36 MPa. We chose these particular pressure-temperature-stress conditions, as they represent realistic in-situ conditions for a reservoir at approximately 1.5 km depth. To investigate the effect of pore fluid composition, we varied the solution pH by the addition of CO_2, organic acids and NaOH. Pore fluid salinity was varied by the addition of NaCl. We also assessed the effect of dry supercritical carbon dioxide on the compaction creep behaviour of feldspar. Besides the mechanical data obtained, acoustic emission (AE) data were recorded, in some tests, to determine the role of cataclasis.

Note that since the maximum temperature investigated in our experiments was only 100°C, CO_2 partial pressures in our experiments were approximately equal to the total pressure applied to the pore fluid by injecting CO_2. We therefore treat the CO_2 partial pressure (P_{CO2}) and pore fluid pressure (P_f) as identical in experiments at elevated CO_2 pressure. In experiments performed wet (i.e. with an aqueous pore fluid phase) but in the absence of high pressure CO_2, the pore fluid was maintained at atmospheric pressure ($P_{CO2} = 4 \cdot 10^{-5}$ MPa).

3.2.1 Materials and pore fluid preparation

The quartz sand used in our experiments was obtained from the Heksenberg Formation exposed in the Beaujean Quarry near Heerlen, The Netherlands. The material was sieved to prepare a grain size fraction of 425 ± 25 μm, cleaned with 10%

HCl to remove any organic material present, washed with distilled water and dried at 50°C. The resulting material was almost pure quartz with less than 1 wt% feldspar present as a trace mineral.

Our feldspar starting material was obtained from a private collection in the form of cm-sized polycrystalline aggregates consisting of mm-sized crystals. The material was crushed, sieved and/or gravimetrically settled to produce grain size fractions of 25 ± 10 μm, 76.5 ± 13.5 μm, 120 ± 30 μm, and 275 ± 25 μm. After separation, each fraction was ultrasonically cleaned in distilled water to remove fines adhering to the grain surfaces. The mean grain sizes of the final fractions were confirmed by microstructural analysis. Particle size analysis (Malvern sizer) was also performed but systematically overestimated the mean grain size by 1.5 times, probably due to agglomeration effects. X-ray fluorescence analysis showed that the chemical composition of the granular feldspar product was $Ca_{0.5}Na_{0.4}K_{0.1}(Si_{2.5}Al_{1.25}Fe_{0.25})O_8$ or, in terms of the albite (Ab) content, Ab40. Optical analysis revealed the presence of trace amounts of biotite (< 1%), as well as a small fraction (< 5%) of corroded feldspar grains, coated by kaolinite or similar clay minerals.

Saline pore fluid solutions with molar salt concentrations of 0.001 M and 0.5 M were prepared using analytical grade NaCl. In addition, for compaction experiments in alkaline environments, two solutions of different pH and chemical composition were prepared. A solution of pH 11 was made using analytical grade NaOH, while a saturated $Ca(OH)_2$ solution of pH 12.4 was made by adding excess analytical grade $Ca(OH)_2$ to a fixed volume of distilled water (DW). An acidic solution of pH 4.4 was prepared by mixing solutions of 0.07 M ammonium acetate with 0.005 M citric acid monohydrate, resulting in a mixture of acetic (HAc) and citric (H_3Cit) acid. This particular fluid composition was chosen to allow direct comparison with the feldspar (albite) compaction creep experiments performed by *Hajash et al.* [1998]. In experiments performed using pure (distilled) water and NaCl solution as pore fluid, pH was determined by the imposed CO_2 (partial) pressure and temperature, and was calculated using Henry's constant (K_H), the dissociation constants for carbonic acid (K_1 and K_2) given by *Plummer and Busenberg* [1982] and the dissociation constant of water (K_W) given by *Bandura and Lvov* [2006]. None of the solutions used in the experiments were pre-saturated with silica or feldspar.

3.2.2 Experimental set-up

Our compaction experiments were performed using an Instron 1362 servo-controlled testing machine equipped with a 1-D (uniaxial) compaction vessel (Figure 3.1). The vessel used is a modified version of the high temperature oedometer described by *Schutjens* [1991].

The main features of the compaction vessel are as follows. The vessel and loading

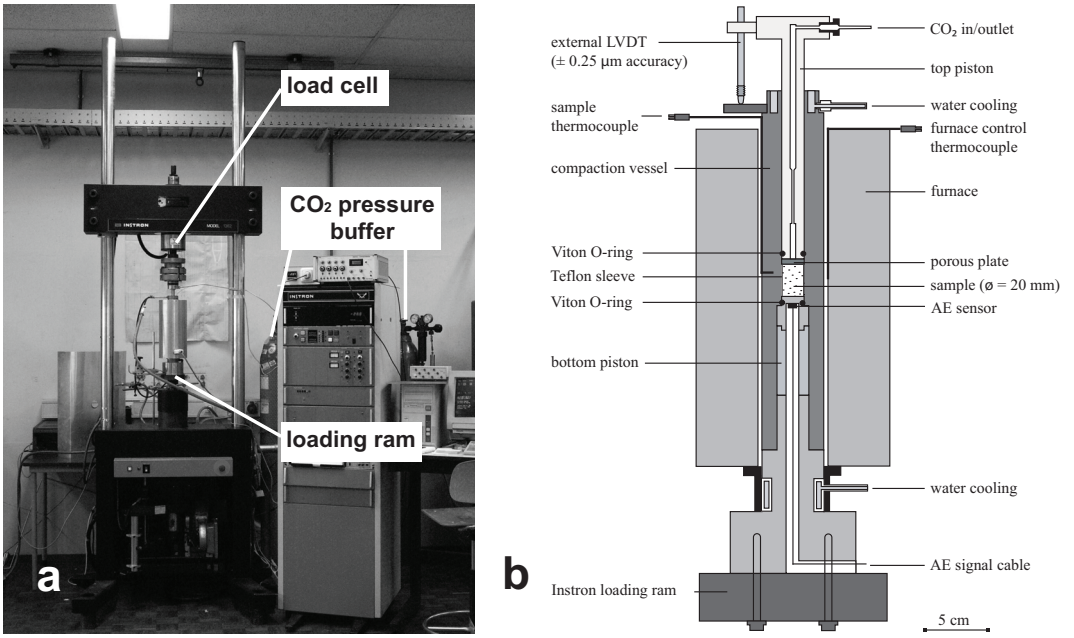

Fig. 3.1 a) Overview of the experimental set-up showing the location of the Monel compaction vessel in the Instron loading frame, and the carbon dioxide pressure buffer system. b) Schematic diagram showing the details of the compaction vessel used.

pistons are constructed from Monel K-500, a corrosion resistant copper-nickel-molybdenum alloy, employed to minimise sample contamination by corrosion. The bottom piston is fixed within the vessel. The moveable top piston contains a pore fluid bore and is tipped with a porous plate. This enables CO_2 to enter the sample from a nitrogen-buffered separator connected to the fluid in/outlet in the top piston. Sealing of the top and bottom piston is achieved using Viton O-rings. In order to reduce the sample size for experiments on small quantities of sample material (feldspar), a Monel liner and reduced-section pistons can be inserted into the main vessel. Sample temperatures up to 300°C can be achieved using an external furnace enclosing the compaction vessel, though the maximum temperature used in the present experiments was 100°C.

Force applied to the top piston is measured externally using the Instron load cell (100 kN range, resolution ± 0.025 kN). Piston position and displacement are measured using both the internal LVDT (linear variable differential transformer, range ± 50 mm, resolution ± 2.5 µm) located in the Instron drive unit and an external LVDT (range ± 2 mm, resolution ± 0.25 µm) located between the upper piston and the vessel. Temperature is controlled to within 0.1°C using a type-K (chromel/alumel) thermocouple positioned in the furnace windings and a proportional-integral-derivative (PID) controller. Sample temperature is measured using a second type-K thermocouple embedded in the vessel wall (Figure 3.1). Carbon dioxide pressure is monitored using a high-resolution pressure transducer (range 0 - 35 MPa, resolution ± 0.0175 MPa) located in the CO_2 supply line.

Table 3.1
Compaction experiments on granular quartz

	d	T	P_{CO2}	σ_{eff}	pore fluid	φ_0	e_v^0	φ_i	e_v
	[μm]	[°C]	[MPa]	[MPa]	[pH]	[%]	[%]	[%]	[%]
Q-C1	425 ± 25	20 ± 2	~4·10^{-5}	35.3	lab dry air [-]	44.2	10.8	37.4	2.4
Q-C2	425 ± 25	20 ± 2	~4·10^{-5}	35.5	DW [5.5]	44.0	10.6	37.3	2.5
Q-C11	425 ± 25	20 ± 2	15.02	35.3	DW [2.8]	43.1	8.2	38.0	2.2
Q-C12	425 ± 25	20 ± 2	~4·10^{-5}	35.3	NaOH solution [11.0]	45.0	11.3	38.0	2.9
Q-C13	425 ± 25	20 ± 2	~4·10^{-5}	35.5	saturated $Ca(OH)_2$ solution [12.4]	42.4	10.2	35.8	3.1

Symbols: d, initial grain size [μm]; T, temperature [°C]; P_{CO2}, carbon dioxide partial pressure [MPa]; σ_{eff}, applied effective stress [MPa]; φ_0: starting porosity, prior to the time-independent compaction stage [%]; e_v^0: volumetric strain at the end of the time-independent compaction stage [%]; φ_i: porosity at the start of the creep stage [%], e_v: volumetric strain after 17h of time-dependent compaction creep [%]. Note that for the temperature range in our experiments (20-100°C), the applied CO_2 partial pressure ($P_{CO2} > 4 \cdot 10^{-5}$ MPa) was approximately equal to the total pore fluid pressure. In experiments performed dry or wet without added CO_2, the pore fluid pressure was maintained at atmospheric pressure. In wet experiments, DW denotes distilled water.

In order to detect grain scale brittle failure events, acoustic emissions can be counted using an acoustic emission (AE) monitoring system [*Brzesowsky*, 1995]. This enables sensing, amplification, frequency filtering, discrimination and counting of wave packets emanating from microseismic events within the sample. The AE sensor (PZT, ceramic piezoelectric resonator), located in the upper section of the bottom piston, is connected to a precision pre-amplifier (36 dB gain) and multistage signal conditioning system, the latter providing 24 dB gain and incorporating a 100 kHz to 1 MHz band pass filter to eliminate low frequency interference and sensor resonance effects. Events are counted using two counter channels, for which a constant discrimination trigger-threshold of 100 mV was set for the present experiments (just above noise level). Pulse stretching times (PST) for the two channels were set at 500 and 250 μs respectively, which served as a check for wave packet arrival-bunching effects and counter saturation [*Brzesowsky*, 1995]. For well-spaced (i.e. discrete) events, the count rates obtained by the two channels should be identical.

3.2.3 Testing procedure

The experiments were performed under the conditions summarised in Tables 3.1 and 3.2. Those on quartz (Table 3.1) were performed using 5.5 g of sample material, while those on feldspar (Table 3.2) were performed using approximately 0.65 g. After funneling the sample into the compaction vessel and adding the appropriate amount of

Table 3.2
Compaction experiments on granular feldspar

	d	T	P_{CO2}	σ_{eff}	pore fluid	φ_0	e_v^0	φ_i	e_v
	[µm]	[°C]	[MPa]	[MPa]	[pH]	[%]	[%]	[%]	[%]
Grain size dependence									
L-G1	25 ± 10	81.6	~4·10^{-5}	36.0	DW [5.7]	38.2	6.8	34.1	2.2
L-G1a(*AE*)	25 ± 10	79.6	~4·10^{-5}	36.3	DW [5.7]	38.5	8.6	33.0	2.1
L-G1b(*AE*)	25 ± 10	80.7	~4·10^{-5}	36.1	DW [5.7]	38.1	8.0	33.3	2.2
L-G1c(*AE*)	25 ± 10	80.5	~4·10^{-5}	36.5	DW [5.7]	38.1	10.9	28.9	2.1
L-G1d(*AE*)	25 ± 10	80.7	~4·10^{-5}	36.7	DW [5.7]	37.5	10.2	28.8	2.0
L-G2	76.5 ± 13.5	81.4	~4·10^{-5}	36.7	DW [5.7]	38.5	7.3	31.4	2.5
L-G3a	120 ± 30	81.6	~4·10^{-5}	36.4	DW [5.7]	38.4	10.2	31.9	3.1
L-G3b	120 ± 30	81.8	~4·10^{-5}	35.9	DW [5.7]	38.1	8.9	29.5	2.1
L-G3c	120 ± 30	80.8	~4·10^{-5}	36.0	DW [5.7]	38.3	10.5	28.4	2.4
L-G4	275 ± 25	79.9	~4·10^{-5}	36.4	DW [5.7]	38.2	13.2	29.1	2.8
L-G5(*AE*)	275 ± 25	79.7	~4·10^{-5}	36.1	DW [5.7]	37.8	13.0	28.5	2.3
L-G11(*AE*)	25 ± 10	79.4	10.12	35.2	DW [3.1]	38.7	13.9	28.9	1.0[†]
L-G12a	76.5 ± 13.5	79.7	10.49	33.3	DW [3.1]	39.0	11.2	31.6	0.7
L-G12b	76.5 ± 13.5	80.8	9.99	36.1	DW [3.1]	39.1	11.7	30.3	1.4
L-G13	120 ± 30	79.3	10.21	35.3	DW [3.1]	40.1	14.6	29.4	2.3
L-G14a	275 ± 25	79.9	9.83	36.1	DW [3.1]	38.9	13.3	29.7	3.0
L-G14b	275 ± 25	81.0	10.53	34.0	DW [3.1]	40.5	17.4	27.5	2.9
L-G14c	275 ± 25	79.8	10.10	36.3	DW [3.1]	39.2	17.4	26.0	2.6
Temperature dependence									
L-T40	120 ± 30	41.8	~4·10^{-5}	36.1	DW [5.6]	37.6	8.1	29.0	3.1
L-T50	120 ± 30	56.1	~4·10^{-5}	36.2	DW [5.7]	38.2	10.4	28.5	2.6
L-T60	120 ± 30	61.8	~4·10^{-5}	35.7	DW [5.7]	38.4	11.0	28.0	2.7
L-T100	120 ± 30	98.3	~4·10^{-5}	36.3	DW [5.8]	38.4	11.2	27.9	2.7
Stress dependence									
L-S20	120 ± 30	80.5	~4·10^{-5}	20.9	DW [5.7]	38.5	4.8	33.8	2.6
L-S60	120 ± 30	81.3	~4·10^{-5}	60.5	DW [5.7]	38.2	19.1	22.9	2.1
L-S100	120 ± 30	80.0	~4·10^{-5}	101.3	DW [5.7]	38.3	22.2	15.7	2.2
pH and salinity effect									
L-P1	120 ± 30	24.2	~4·10^{-5}	36.2	lab dry air	38.8	8.0	33.8	1.9
L-P2	120 ± 30	23.9	~4·10^{-5}	36.5	DW [5.5]	38.5	9.3	32.5	2.3
L-P11	120 ± 30	19.3	10.02	35.5	DW [2.8]	37.7	10.9	29.4	1.1

Table 3.2 (continued)
Compaction experiments on granular feldspar

	d	T	P_{CO2}	σ_{eff}	pore fluid	φ_0	e_v^0	φ_i	e_v
	[µm]	[°C]	[MPa]	[MPa]	[pH]	[%]	[%]	[%]	[%]
L-P11	120 ± 30	19.3	10.02	35.5	DW [2.8]	37.7	10.9	29.4	1.1
L-P12a	120 ± 30	19.1	~4·10^{-5}	36.3	NaOH solution [11.0]	38.8	8.1	33.3	2.5
L-P12b	120 ± 30	19.1	~4·10^{-5}	36.5	NaOH solution [11.0]	38.6	8.9	32.8	2.5
L-P12c	120 ± 30	25.8	~4·10^{-5}	35.9	NaOH solution [11.0]	38.6	9.5	32.7	2.4
L-P13	120 ± 30	80.7	~4·10^{-5}	37.2	0.07 M HAc + 0.005 M H_3Cit [4.4]	38.1	11.5	29.9	2.1
L-P14	120 ± 30	80.8	10.53	33.5	dry SC CO_2	40.0	14.7	30.7	1.3
L-P21	120 ± 30	24.8	~4·10^{-5}	37.5	1 mM NaCl solution [5.5]	38.6	9.2	32.4	2.4
L-P22	120 ± 30	25.2	~4·10^{-5}	36.0	0.5 M NaCl solution [5.5]	38.7	8.8	30.8	2.4

Symbols: d, initial grain size [µm]; T, temperature [°C]; P_{CO2}, carbon dioxide partial pressure [MPa]; σ_{eff}, applied effective stress [MPa]; φ_0: starting porosity, prior to the time-independent compaction stage [%]; e_v^0: volumetric strain at the end of the time-independent compaction stage [%]; φ_i: porosity at the start of the creep stage [%], e_v: volumetric strain after 17h of time-dependent compaction creep [%]. Note that for the temperature range in our experiments (20-100°C), the applied CO_2 partial pressure ($P_{CO2} > 4{\cdot}10^{-5}$ MPa) was approximately equal to the total pore fluid pressure. In experiments performed dry or wet without added CO_2 the pore fluid pressure was maintained at atmospheric pressure. In wet experiments, DW denotes distilled water.
† time-dependent volumetric strain e_v is recorded after 12h for this sample.

solution to fill the pore space completely (in the case of wet experiments), the upper piston was inserted and the vessel was located into the Instron loading frame. The sample was then brought to the required temperature and a small load was applied to obtain a fixed starting porosity (φ_0) of 43.7 ± 1.3% and 39.4 ± 1.9%, for the quartz and feldspar aggregates respectively. Where used, CO_2 was subsequently injected into the system at high pressure, holding the Instron in position control mode. The system was left to equilibrate for 3 hours after CO_2 injection. The initial small load was re-established and the required axial stress was then applied to the sample by increasing the applied load in a linear ramp, over a period of approximately 25-50 seconds. Subsequent deformation of the sample was measured for periods of up to 6 days at constant effective axial stress, maintained using load control. In both wet and dry experiments without CO_2, the pore fluid (aqueous solution or lab air) was maintained at atmospheric pressure throughout.

The experiments were terminated by retracting the loading ram to remove the load

applied during the load ramp and switching the system into position control, followed by removal of the CO_2 pressure where used. The sample was then fully unloaded, by retracting the loading ram, and carefully pressed out of the compaction vessel using a closely fitting glass rod. All samples were retrieved intact. The wet samples were subsequently dried at 50°C for 2 days before preparation for microstructural study.

3.2.4 Data acquisition and processing

Throughout the experiments, axial load, Instron position, sample temperature, external LVDT position, and CO_2 pressure signals were logged at time intervals of 5, 10, 50 and 100 s, increasing the logging interval as the experiment progressed. The cumulative number of acoustic emission events was logged by a separate system using the same time base. The raw data were processed, correcting for distortion of the apparatus, to yield effective axial stress, volumetric strain, porosity, volumetric strain rate and AE rate as functions of time. In most experiments, seal friction was less than 1 MPa and therefore we made no attempts to correct for this.

Analysis of the compaction curves and strain rate data obtained showed that compaction occurring during the initial loading stage (i.e. the first 75-100 s, consisting of the load ramp plus the following 50 s) of all experiments was so rapid as to be essentially time-independent (near-instantaneous). This part of our data was therefore treated separately from the subsequent (slow) creep stage. Finite volumetric strain accumulated in each stage was defined as the change in length of the sample (ΔL) with respect to its initial length (L_0). For the instantaneous compaction stage, L_0 was thus

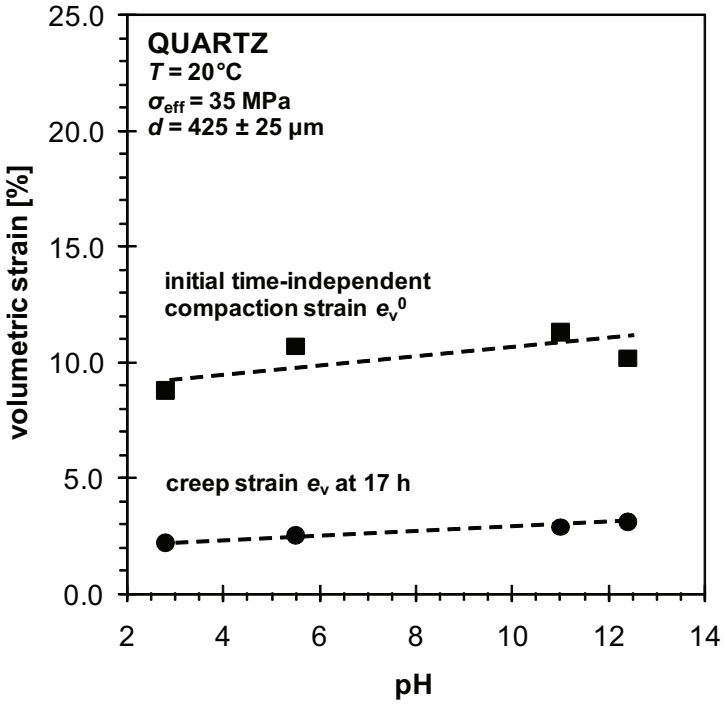

Fig. 3.2 Dependence of instantaneous and time-dependent volumetric strains e_v^0 and e_v (after 17 h) on pore fluid pH seen in the quartz compaction experiments. T denotes temperature, σ_{eff} the effective axial stress and d the initial grain size.

taken to be the length of the sample prior to loading, yielding the instantaneous strain e_v^0. For the time-dependent stage, L_0 was taken to represent the length of the sample at the end of the initial loading stage, yielding creep strains e_v. Instantaneous volumetric strain rates, defined as $\dot{\varepsilon} = -\frac{1}{L}\frac{dL}{dt}$, were calculated by performing linear regression fits to the corrected displacement vs. time data, using a moving displacement interval chosen such that the maximum error in compaction rate was always less than ± 5%. Note that in our series of uniaxial experiments, volumetric strain is equal to the axial strain, due to the lateral confinement of the samples. For the experiments that included acoustic emission event counting, we calculated the instantaneous AE event rate from the change in cumulative events occurring in the same time window as used for the strain rate calculations.

3.2.5 Microstructural and analytical methods

After drying, representative samples were impregnated with a low-viscosity epoxy resin containing a blue dye. Thin sections, cut parallel to the loading axis, were then prepared and optical microscopy was used to analyse the microstructure. Crack density (defined here as the mean number of cracks per grain) was calculated for all selected samples by determining the crack to grain frequency ratio along a linear trajectory across a thin section. Per thin section, 5-15 trajectories amounting to a total of ~50-100 grains were analysed, in order to obtain the fraction of failed grains and an average crack density, representative for the sample. In addition, for a selected series of feldspar samples (grain size fractions 76.5 ± 13.5 μm, 120 ± 30 μm and 275 ± 25 μm, T = 80°C, σ_{eff} = 36 MPa, no CO_2 pressure), a 50 mg portion of material was taken from the centre of the sample after drying. This was analysed using the Malvern particle sizer to determine changes in the average grain size and grain size distribution of each sample due to deformation.

3.3 Mechanical data

3.3.1 Quartz data

3.3.1.1 Instantaneous vs. time-dependent strain

In all our quartz experiments (Table 3.1), we observed an essentially instantaneous, or time-independent, compaction stage during the first ~100 s of the experiment (i.e. during the load ramp plus subsequent 50 s), followed by a distinct, time-dependent phase of continuously decelerating creep. In the wet experiments (i.e. containing aqueous pore fluid), the instantaneous strain (e_v^0) increased slightly with pH, as did the time-dependent strain (e_v) measured at fixed time (17 h – see Figure 3.2). Our single

lab dry sample (Q-C1) showed similar instantaneous strain compared to material with distilled water only (Q-C2), but slightly less creep strain (Table 3.1).

3.3.1.2 Effect of pH and chemical environment on creep

Volumetric strain (e_v) versus time plots for the creep stages of all quartz experiments are shown in Figure 3.3a. From this data, log-log plots showing the dependence of volumetric strain rate ($\dot{\varepsilon}$) on volumetric creep strain (e_v) have been constructed (Figure 3.3b) to show the effect of chemical environment (pH 2.8 to 12.4) on compaction creep rate. These data confirm that the addition of distilled water as a pore fluid (sample Q-C2) enhances creep, compared to lab dry material (sample Q-C1). It is also clear from Figure 3.3 that the pH of the pore fluid has a significant effect on the amount of creep of the samples, as well as on the creep rate at constant strain. In general, it is seen that alkaline pore fluids enhance compaction and compaction rates, compared to near-neutral fluids (Q-C2: pore water in equilibrium with atmospheric CO_2). In contrast, the injection of CO_2 into wet samples at 15 MPa, and the subsequent

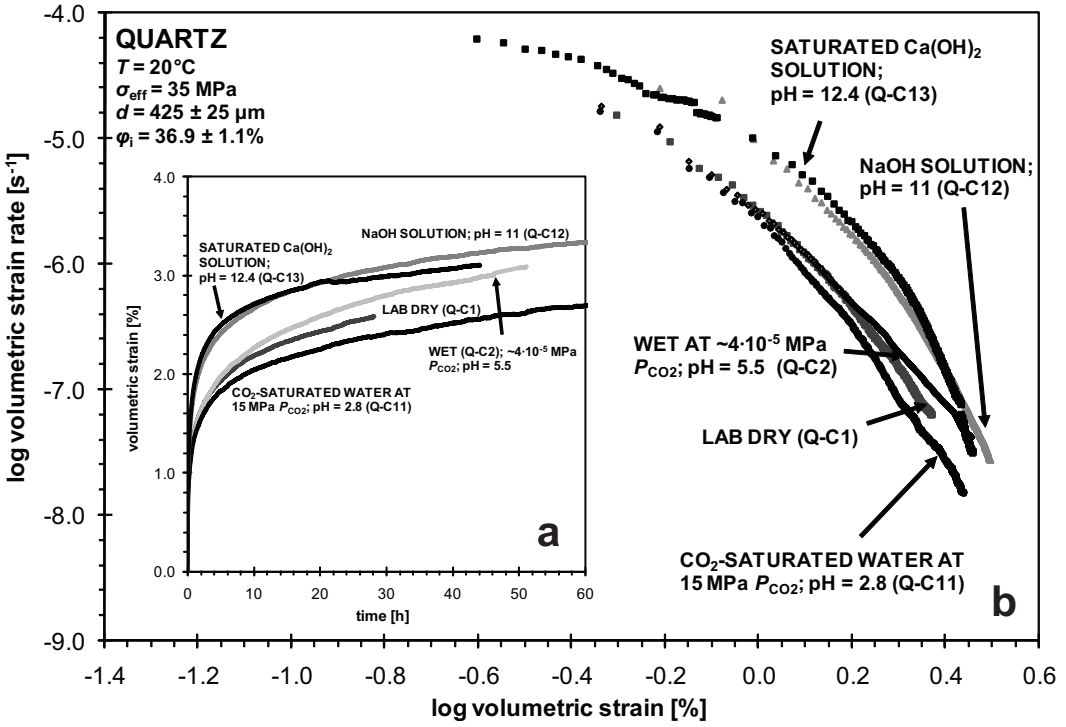

Fig. 3.3 Creep stage data for the quartz experiments performed at room temperature and an effective stress of 35 MPa (φ_i = 36.9 ± 1.1%). a) Volumetric strain e_v vs. time plot. Note that the addition of distilled water (Q-C2) enhanced compaction creep compared with lab dry material (Q-C1), whereas injection of CO_2 into wet material reduced creep response (Q-C11). Overall, volumetric strain and strain rates increase with increasing solution pH. b) Log volumetric strain rate vs. log volumetric strain plot showing that the compaction rate at fixed creep strain (e_v) increases with increasing pH. Errors in volumetric strain rate (± 5%) are smaller than the symbol size. *T* denotes temperature, σ_{eff} is effective axial stress, *d* is initial grain size, P_{CO2} is CO_2 partial pressure and φ_i is porosity at the start of the time-dependent creep stage.

lowering of fluid pH (experiment Q-C11), results in less compaction and lower creep rates, compared to near-neutral pH environments.

3.3.2 Feldspar data

3.3.2.1 Instantaneous vs. time-dependent strain

As for quartz, all feldspar experiments showed instantaneous compaction during initial loading (~25 s load ramp plus subsequent 50 s), followed by a distinct, time-dependent compaction or creep stage (Figure 3.4). In wet experiments with varying

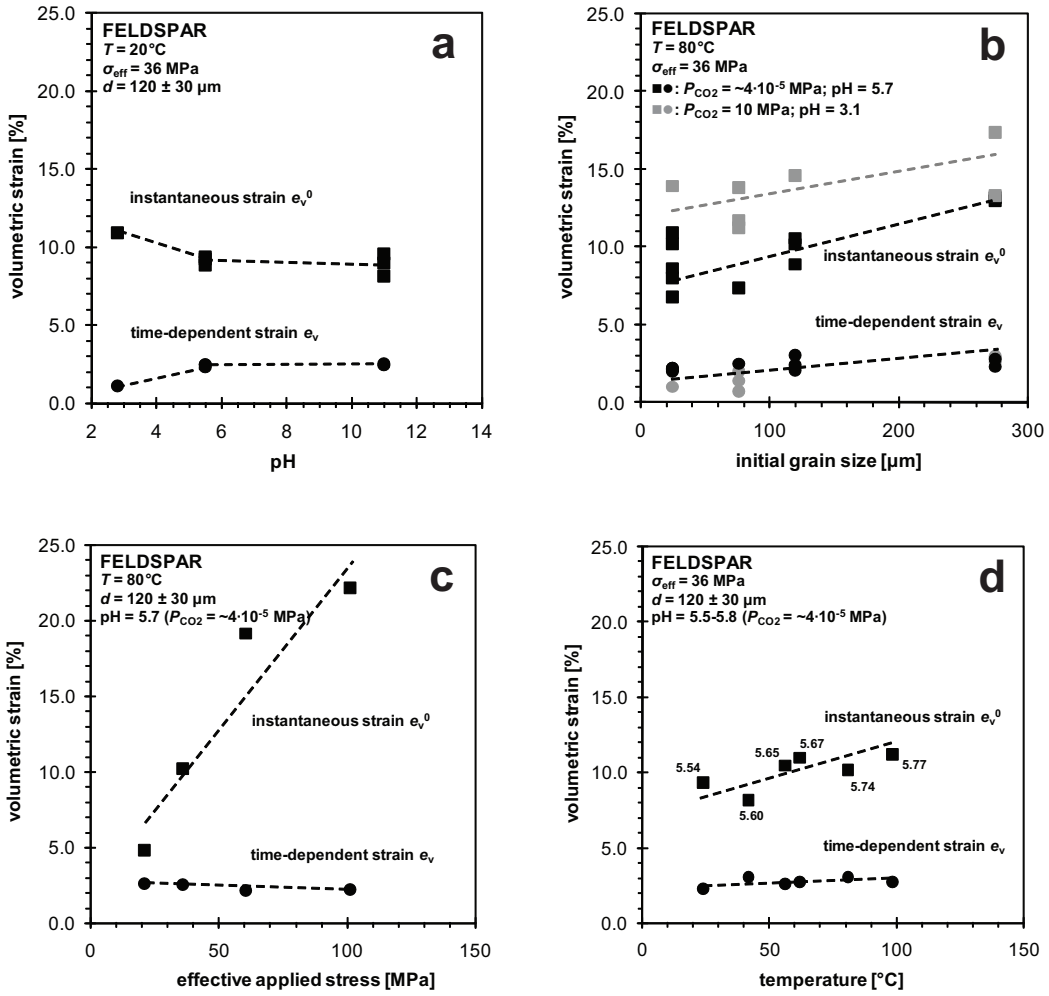

Fig. 3.4 Dependence of volumetric strains e_v^0 and e_v, achieved during the instantaneous and time-dependent stages of wet feldspar experiments, on a) pH, b) initial grain size (samples containing distilled water with and without CO_2 added at high pressure), c) effective stress (distilled water in equilibrium with atmospheric CO_2; pH = 5.7), and d) temperature (distilled water in equilibrium with atmospheric CO_2; pH = 5.5-5.8, as indicated for each temperature). Time-dependent (creep) strain e_v is plotted after 17 hours. Note the different dependencies of strain on pH in the two stages of the experiments, and the low-sensitivity of time-dependent strain to effective stress and temperature. *T* denotes temperature, σ_{eff} is effective axial stress, *d* is initial grain size and P_{CO2} the CO_2 partial pressure.

pore fluid pH at room temperature, time-independent strain (e_v^0) decreased with increasing pH in the pH range 2.8 to 5.5, and remained more or less constant between pH 5.5 and 11 (Figure 3.4a). Time-dependent strain (e_v) measured after 17h increased slightly with pH between pH 2.8 to 5.5 and remained constant over the pH range 5.5 to 11. Lab dry material (L-P1) generally compacted less than wet samples in both stages of our experiments (Table 3.2).

In our experiments at in-situ conditions (80°C, 36 MPa effective stress), we observed a clear, positive dependence of instantaneous and time-dependent strain on grain size (Figure 3.4b) both in wet samples (distilled water in equilibrium with atmospheric CO_2) and in wet/CO_2 samples (CO_2 present at 10 MPa pressure). The sensitivity of strain to grain size was similar in all cases. However, more instantaneous strain was observed in the wet/CO_2 tests than in the wet tests without added CO_2 (Figure 3.4b).

In wet samples without added CO_2 at 80°C (pH 5.7), increasing the effective axial stress led to an increase in instantaneous strain, though there appeared to be little or no dependence of creep strain, accumulated at fixed time, on effective stress (Figure 3.4c). A similar observation was made for the temperature dependence of strain: there was a clear positive dependence of instantaneous strain on temperature, while time-dependent strain, accumulated at fixed time, was only weakly depended on temperature (Figure 3.4d).

3.3.2.2 Compaction creep in the presence of water only (no CO_2 injection)

As already indicated, the addition of distilled water to our feldspar samples (e.g. L-P2) enhanced compaction creep compared to lab dry material (L-P1 – see e_v in Table 3.2). In wet samples containing distilled water in equilibrium with atmospheric CO_2 (pH = 5.7), compaction creep rates showed a weak positive dependence on grain size under the experimental conditions investigated, i.e. 25 to 275 μm, 80°C and 36 MPa (Figure 3.5). This is best seen in Figure 3.6, which suggests a rough power law relation of the form $\dot{\varepsilon} \propto d^{0.25}$. Note that we plotted Figures 3.5 and 3.6 for samples within a specific pre-creep porosity range (φ_i = 29.9 ± 0.7%), chosen to reduce noise related to sample-to-sample variability in this quantity.

→ Fig. 3.5 Effect of grain size on the compaction creep behaviour of wet feldspar samples at 80°C and 36 MPa effective stress (φ_o = 29.6 ± 0.7%). a) Volumetric strain (e_v) vs. time plot for compaction creep with added water and no CO_2 injection (pH = 5.7). b) Log volumetric strain rate ($\dot{\varepsilon}$) vs. log volumetric strain (e_v) plot for the feldspar creep experiments shown in (a). c) Volumetric strain vs. time plot for compaction creep in wet feldspar samples with CO_2 added at 10 MPa pressure. d) Log volumetric strain rate vs. log volumetric strain plot for the feldspar creep experiments shown in (c). All plotted samples have an initial porosity φ_o in the range 29.6 ± 0.7%, chosen to reduce noise related to sample-to-sample variability in this quantity. Errors in volumetric strain rate (± 5%) are smaller than the symbol size. *T* denotes temperature, σ_{eff} the effective axial stress, P_{CO2} CO_2 partial pressure, and φ_i porosity at the start of the time-dependent creep stage.

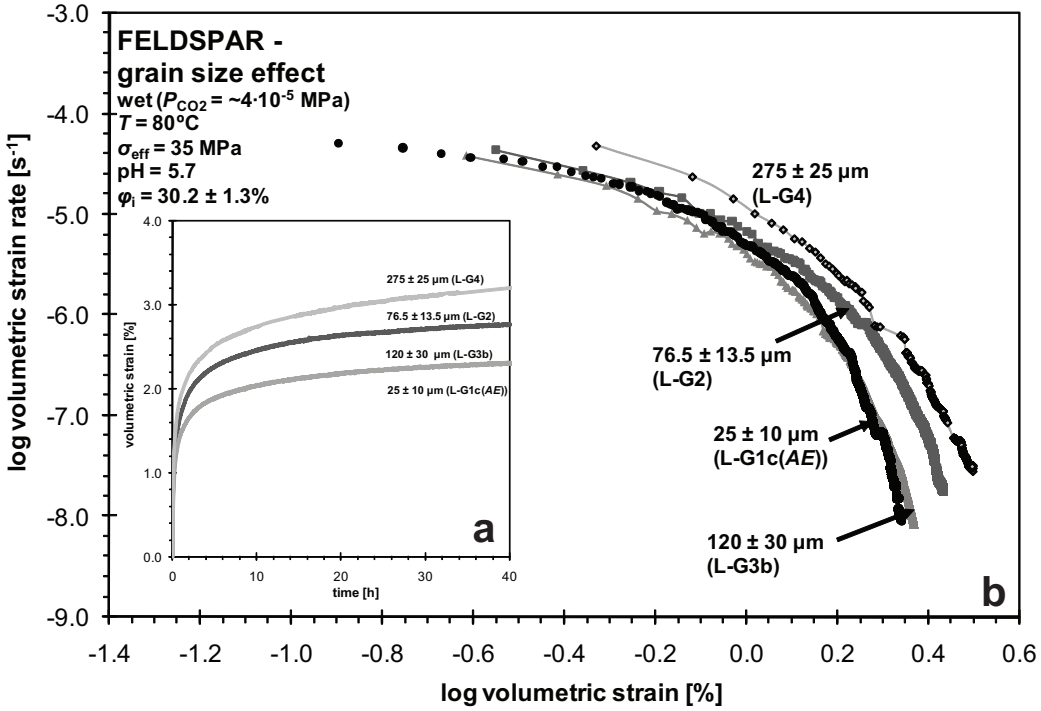
FELDSPAR -
grain size effect
wet (P_{CO2} = ~4·10^{-5} MPa)
T = 80°C
σ_{eff} = 35 MPa
pH = 5.7
φ_i = 30.2 ± 1.3%
log volumetric strain rate [s^{-1}]
log volumetric strain [%]
275 ± 25 µm (L-G4)
76.5 ± 13.5 µm (L-G2)
25 ± 10 µm (L-G1c(AE))
120 ± 30 µm (L-G3b)
volumetric strain [%]
time [h]
a
b

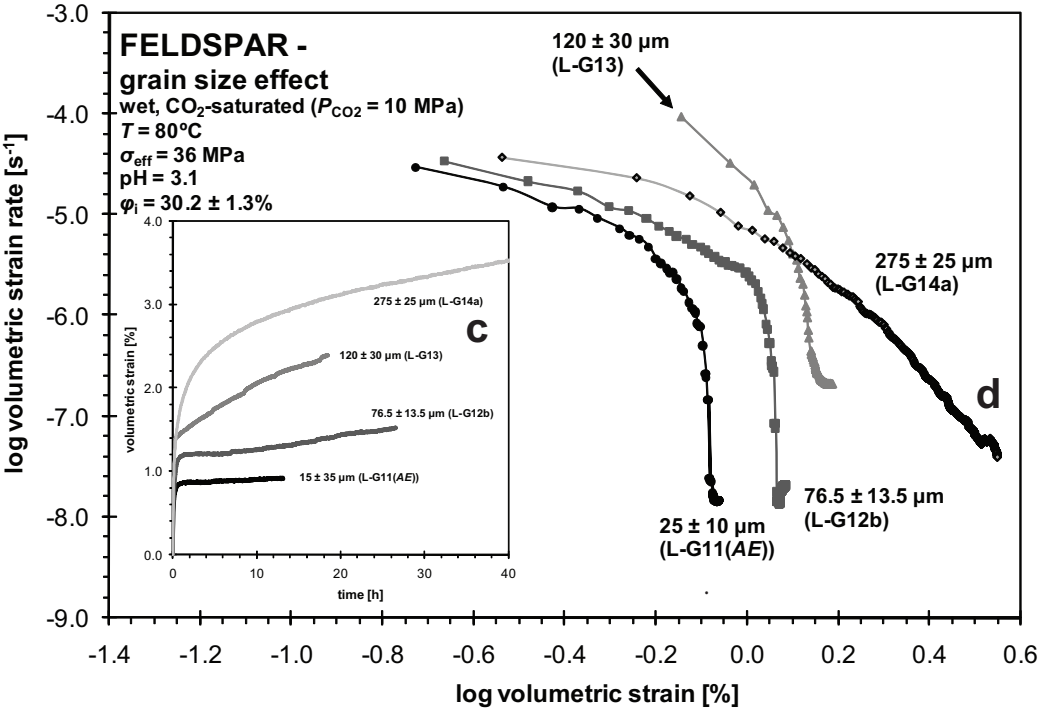
FELDSPAR -
grain size effect
wet, CO_2-saturated (P_{CO2} = 10 MPa)
T = 80°C
σ_{eff} = 36 MPa
pH = 3.1
φ_i = 30.2 ± 1.3%
log volumetric strain rate [s^{-1}]
log volumetric strain [%]
120 ± 30 µm (L-G13)
275 ± 25 µm (L-G14a)
76.5 ± 13.5 µm (L-G12b)
25 ± 10 µm (L-G11(AE))
15 ± 35 µm (L-G11(AE))
volumetric strain [%]
time [h]
c
d

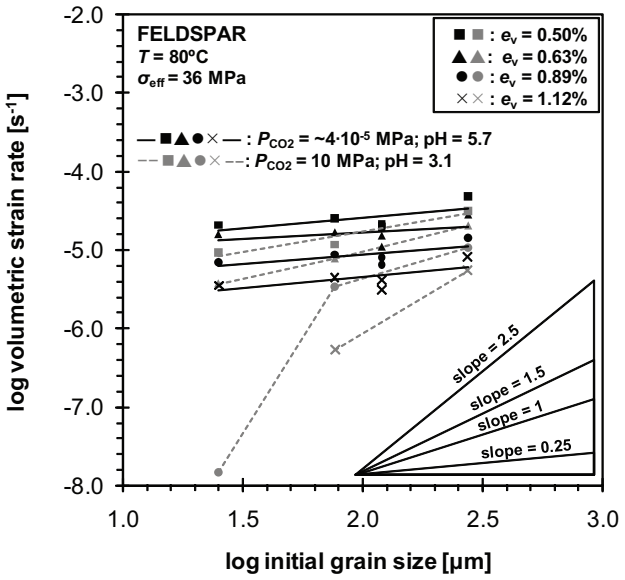

Fig. 3.6 Log-log plot showing the grain size dependence of feldspar compaction creep rates at constant volumetric strains (e_v) under wet conditions (i.e. with distilled water as pore fluid), with and without CO_2 added at high pressure (10 MPa). Dark symbols and solid lines = wet experiments, light symbols and dashed lines = wet/CO_2 experiments. The grain size sensitivity of creep rate is significantly enhanced in the presence of carbon dioxide at high pressure, especially at low strains. Errors in volumetric strain rate (± 5%) are smaller than the symbol size. To eliminate sample variability effects, data are plotted only for samples with pre-creep porosity φ_i in the range 29.6 ± 0.7%. T denotes temperature, σ_{eff} the effective axial stress and P_{CO2} the CO_2 partial pressure.

Varying the applied axial stress (σ_{eff}) had a major effect on the instantaneous compaction of our wet feldspar samples (see Figure 3.4c), producing very different porosities (φ_i = 15.7-33.8%) - and presumably microstructures - at the start of the creep stage. Apparently as a result of this, creep strain rates measured at fixed time (cf. Figure 3.4c) or fixed creep strain showed little (systematic) effect of applied stress. In an attempt to compare experiments at different stresses more usefully, we constructed log strain rate vs. normalised porosity (φ/φ_i) plots (Figure 3.7a). This approach showed that at a fixed normalised porosity, the creep rate data can be roughly described by a power law dependence of compaction rate on stress, with a stress sensitivity (n-value) of 1.0-2.5, as seen in Figure 3.7b.

Over the temperature range studied (T = 20-100°C), wet samples tested at constant stress and grain size, without added CO_2, showed a weak positive dependence of strain rate on temperature, as shown in Figure 3.8a. Plotting the natural logarithm of strain rate against the inverse of temperature, at constant strain (Figure 3.8b), suggested an apparent activation energy of around 10 kJ/mol.

To discriminate between the possible processes that control compaction creep in our experiments (e.g. dissolution, reaction or fluid enhanced microcracking), we monitored the acoustic emissions produced during creep of selected feldspar samples (two grain sizes). In wet samples with no added CO_2 or other additives, cumulative AE hits increased with increasing creep strain, initially quite linearly, and showed a positive dependence on grain size (Figure 3.9a). The two grain size fractions investigated (d = 25 ± 10 µm and d = 275 ± 25 µm) showed saturation in cumulative AE hits at strains above about 2%, demonstrating that fewer AE events occurred

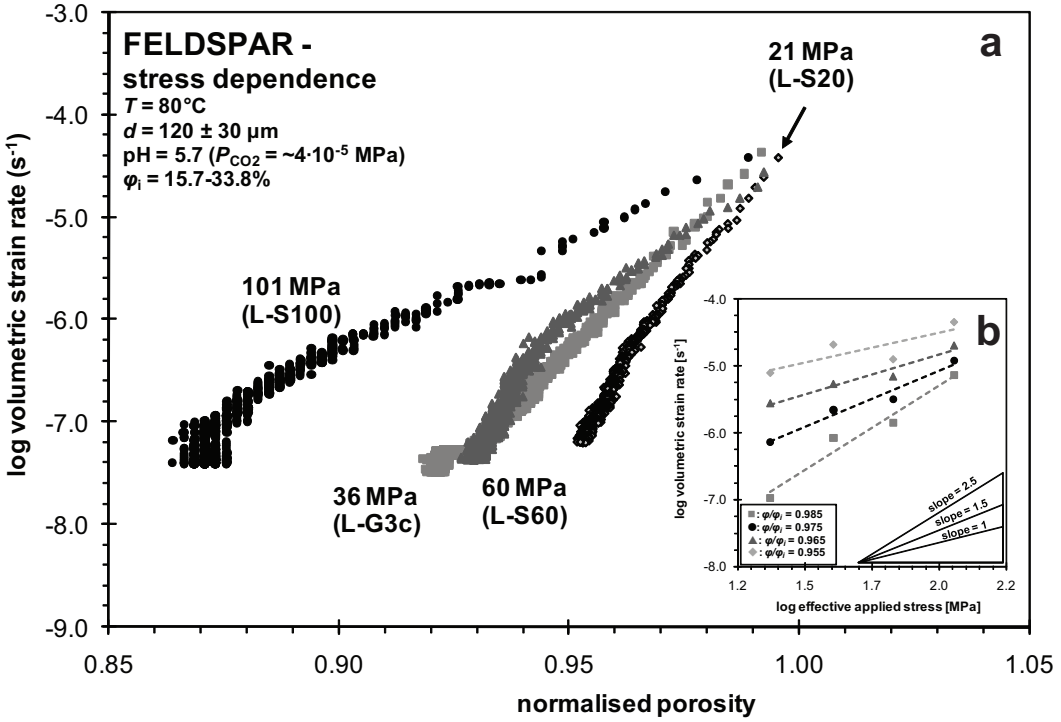

Fig. 3.7 Stress dependence of the feldspar compaction creep behaviour at 80°C and a grain size of 120 ± 30 µm under wet conditions without added CO_2. a) Log volumetric strain rate vs. normalised porosity. b) Log volumetric strain rate vs. log effective stress at constant normalised porosity (φ/φ_i). Errors in volumetric strain rate (± 5%) are smaller than the symbol size. *T* denotes temperature, *d* the grain size, P_{CO2} the CO_2 partial pressure, and φ_i the porosity at the start of the time-dependent creep stage.

towards higher strains though compaction continued. Figure 3.9b (log AE rate vs. e_v) shows that AE rates were about one order of magnitude higher in the coarser grained wet sample (L-G5(*AE*)) than in the fine grained wet sample (L-G1d(*AE*)).

3.3.2.3 Influence of added CO_2 on creep – effects on grain size dependence and AE

The most striking result of the experiments on wet feldspar samples (i.e. with distilled water as pore fluid - Table 3.2) was that, under otherwise similar conditions, the addition of high-pressure carbon dioxide generally decreased compaction creep rates within the grain size range investigated (*d* = 25-275 µm), as seen in Figure 3.6. As in wet systems without added CO_2, compaction creep rates obtained with added carbon dioxide were positively correlated with initial grain size (Figure 3.6). However, this dependence was stronger (P_{CO2} = 10 MPa) than in wet samples without added CO_2, with the data being roughly described by a power law relation of the form $\dot{\varepsilon} \propto d^{0.5-2.5}$ (Figure 3.6).

An additional effect of adding high-pressure CO_2 to wet samples was a sharper deceleration of creep in many cases (compare Figures 3.5c and d with 3.5a and b). Moreover, the variability in experimental data obtained in tests performed with high-

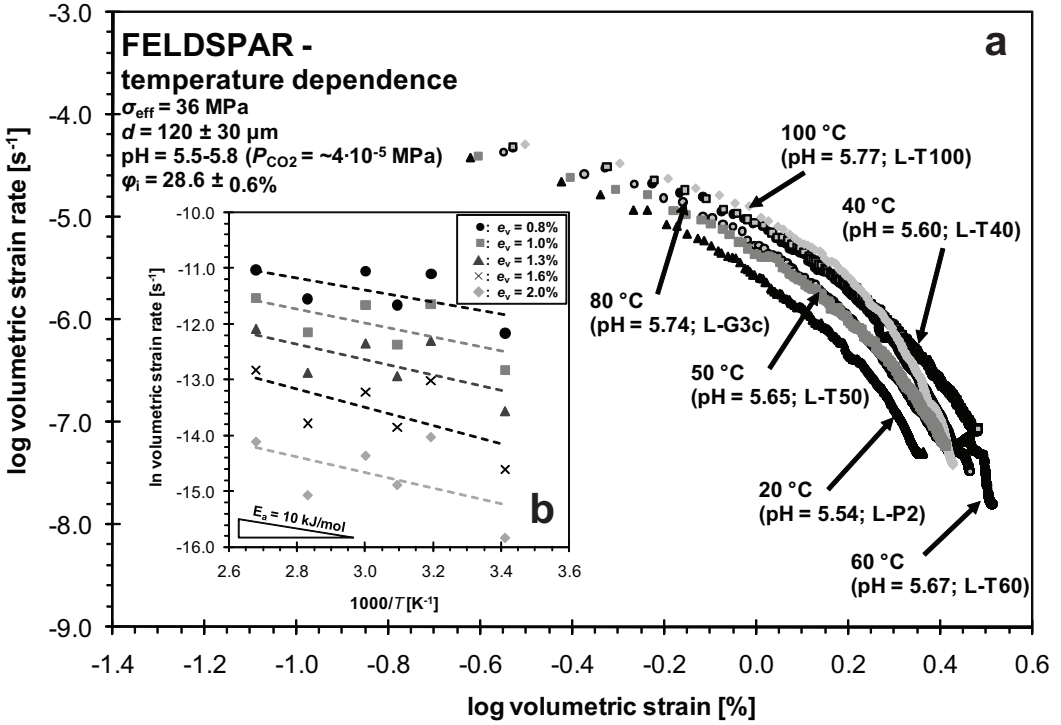

Fig. 3.8 Effect of temperature on the compaction creep behaviour of feldspar samples at a grain size of 120 ± 30 µm and 36 MPa effective stress, under wet conditions with no CO_2 added at high pressure (pH = 5.5-5.8). a) Log volumetric strain rate vs. creep strain (e_v) at different temperatures. b) Log volumetric strain rate vs. 1000/T at constant volumetric strain e_v. Best fits to the data at constant volumetric strain yield an apparent activation energy of ~10 kJ/mol. Errors in volumetric strain rate (± 5%) are smaller than the symbol size. Note that σ_{eff} denotes effective axial stress, d the initial grain size, P_{CO2} the CO_2 partial pressure and φ_i the porosity at the start of the time-dependent creep stage.

pressure CO_2 appeared to be greater than for the other experiments. Key variations between the different experiments (L-G11 series) include variations in porosity φ_i at the start of the creep phase (leading to volumetric strain variations), unexpectedly high initial strain rates, and variable rates of reduction in compaction rate with strain (Table 3.2). As already described, such "noise" effects were reduced in the construction of Figures 3.5 and 3.6 by plotting data only for samples with similar pre-creep porosities (φ_i = 29.6 ± 0.7%). In addition, in constructing Figure 3.6 we removed experiment L-G13, as it showed anomalously high initial strain rates (high φ_0).

Injection of carbon dioxide into wet samples (e.g. L-G11(*AE*), d = 25 ± 10 µm, P_{CO2} = 10 MPa) also resulted in a reduction of typically 90% in the cumulative number of AE events recorded at fixed strain, compared with similar wet samples tested without added CO_2 (see Figure 3.9a). As seen in Figure 3.9b, at volumetric strains in the range 0.1 to 1%, AE rates decreased 1-2 orders of magnitude due to CO_2 injection at 10 MPa.

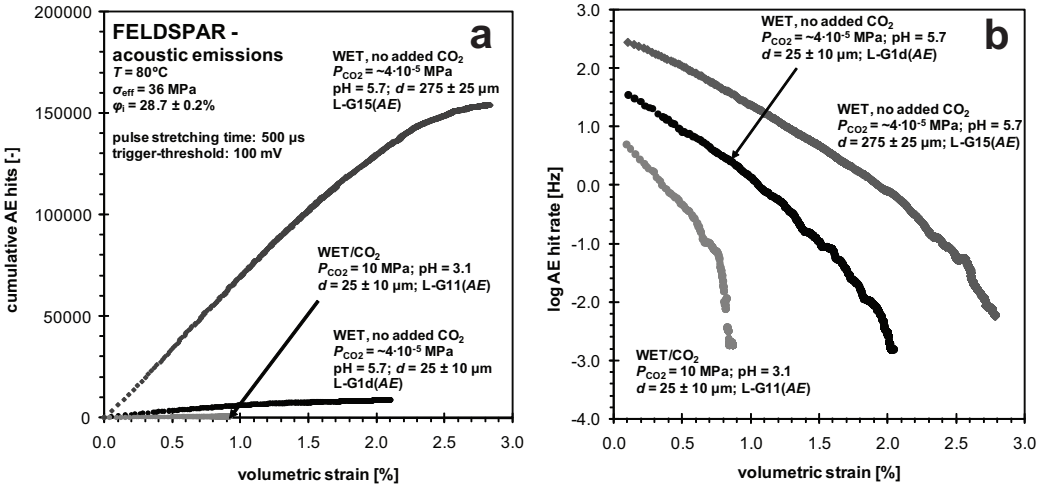

Fig. 3.9 a) Volumetric strain vs. cumulative acoustic emission hits for the creep stages of feldspar experiments L-G1d(AE), L-G11(AE), and L-G5(AE). b) Log acoustic emission rate vs. log volumetric strain (e_v) for the same samples. AE hits and rates decrease strongly with decreasing grain size in the two samples tested with water but without added CO_2 at high pressure. The presence of CO_2 at a pressure of 10 MPa significantly decreases AE activity in fine grained material (25 ± 10 µm). T denotes temperature, σ_{eff} effective axial stress, d the initial grain size, P_{CO2} the CO_2 partial pressure and φ_i the porosity at the start of the time-dependent creep stage.

3.3.2.4 Effect of fluid composition on creep rate

The enhancement of creep caused by addition of aqueous pore fluid to our feldspar samples is explicitly illustrated in Figure 3.10a. We also investigated the effect of fluid pH on compaction creep behaviour over the pH range 2.8 to 11 at room temperature (σ_{eff} = 36 MPa, d = 120 ± 30 µm), through the addition of a variety of acids and alkalis. As seen in Figure 3.10b, compaction creep rates were unaffected by pH at low strains but increased with increasing solution pH at strains greater than 0.6-1.0% (log e_v > -0.2). Clearly, addition of CO_2 at 10 MPa decelerated creep strongly at these strains (pH ≈ 2.8) compared with samples tested with pore fluid pH's in the range 5.7 to 11. This behaviour differs from that of quartz, which showed a more steady increase in creep rate with pH (Figure 3.3).

Since natural reservoir pore fluids are generally saline and since the formation fluid will typically be displaced by injected carbon dioxide near injection wells, we investigated the effect of salt content, as well as of dry supercritical (SC) CO_2 on the compaction creep behaviour of our feldspar samples, as seen in Figures 3.11 and 3.10, respectively. Our results suggest minor enhancement of creep with increasing salinity (no added high pressure CO_2), for salt concentrations in the range 0-0.5 M, though the effect is very small. As seen in Figure 3.10, experiment L-P14 showed that the injection of SC carbon dioxide into lab dry feldspar (T = 80°C, P_{CO2} = 10 MPa) dramatically reduced creep rates, compared with lab dry samples tested under room temperature conditions.

3.4 Microstructural observations

Representative micrographs of the microstructures observed in the deformed quartz and feldspar samples are shown in Figures 3.12 and 3.13, along with the results of our grain failure (fraction of failed grains) and crack density (average number of cracks per grain) measurements. Description of the microstructures will focus mainly on the effects of pore fluid composition at otherwise similar, room temperature

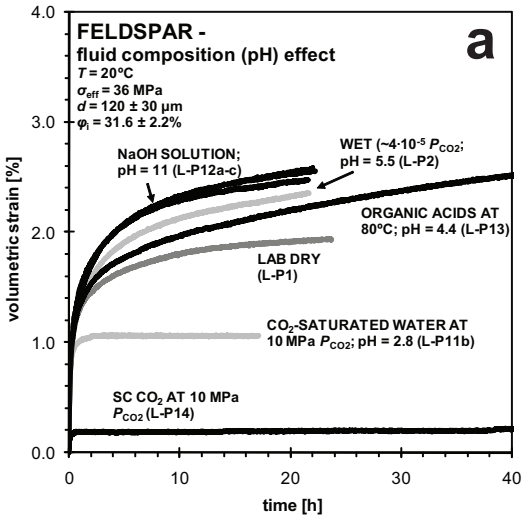

Fig. 3.10 Effect of fluid composition (pH) on the compaction creep behaviour of feldspar samples at room temperature and at 36 MPa effective stress ($\varphi_i = 31.6 \pm 2.2\%$). a) Volumetric strain (e_v) vs. time plot. b) Corresponding log volumetric strain rate vs. log volumetric strain plot. Note the enhanced compaction and increased creep rates caused by the introduction of fluid into the system, and by increasing fluid pH. The introduction of CO_2 at 10 MPa, and the associated decrease in pH to ~2.8, leads to a major reduction in creep rate at $e_v > 0.6\%$ (log $e_v > 0.2$). The injection of supercritical CO_2 into lab dry granular feldspar strongly reduces compaction rates. Errors in volumetric strain rates (± 5%) are smaller than the symbol size. T denotes temperature, σ_{eff} effective axial stress, d is initial grain size, P_{CO2} is CO_2 partial pressure and φ_i is porosity at the start of the time-dependent creep stage.

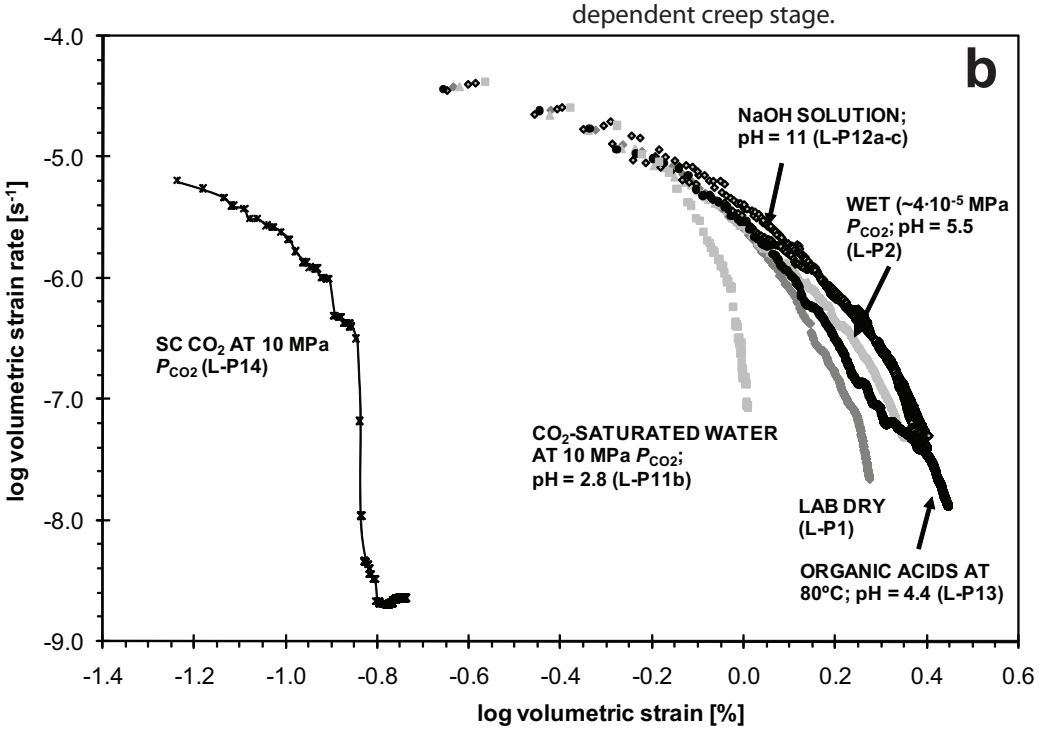

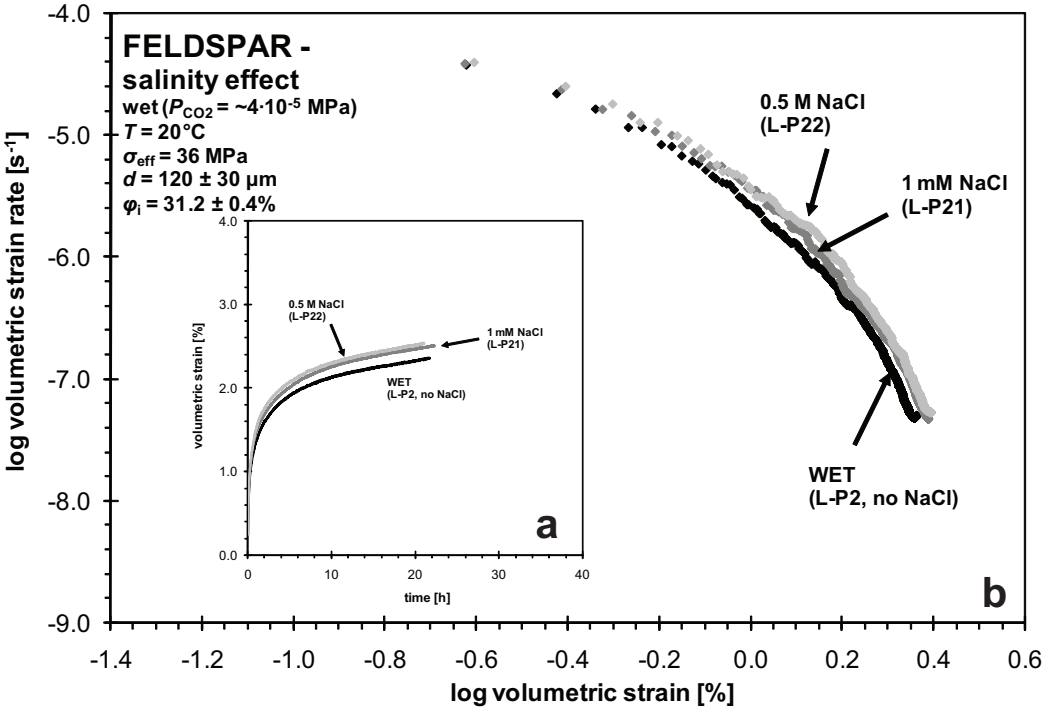

Fig. 3.11 Effect of pore fluid salinity on the compaction creep behaviour of feldspar samples at room temperature and at 36 MPa effective stress (φ_i = 31.2 ± 0.4%, no added CO_2). a) Volumetric strain (e_v) vs. time plot. b) Corresponding log volumetric strain rate vs. log volumetric strain plot. Creep rates appear to increase slightly with increasing salinity especially at strains > 1%. Errors in volumetric strain rates (± 5%) are smaller than the symbol size. T denotes temperature, σ_{eff} the effective axial stress, d the initial grain size, P_{CO2} the CO_2 partial pressure (atmospheric) and φ_i the porosity at the start of the time-dependent creep stage.

conditions (quartz: σ_{eff} = 35 MPa, d = 425 ± 25 µm; feldspar: σ_{eff} = 36 MPa, d = 120 ± 30 µm). We use the terminology of *Wu et al.* [2004] to describe the grain-scale crack microstructures observed.

Our starting quartz sand showed well-rounded grains and a narrow grain size distribution, while the undeformed feldspar fractions were much more angular. Nonetheless, the deformation-induced microstructures observed in both the quartz and feldspar samples were very similar. All compacted samples show evidence of intra- and transgranular cracking of individual grains by cone cracks, as well as divergent ("spalling") and convergent ("onion peel") cracks, fanning out from grain-to-grain contacts. In both materials, the observed cracks are more or less homogeneously distributed throughout the samples and show no obvious preferred orientation.

3.4.1 Quartz microstructures

For material deformed under lab dry conditions (Q-C1 – see Figures 3.12a and e) an average crack density of 0.81 cracks per grain was measured, along with ~35%

grain failure. The addition of water in equilibrium with atmospheric CO_2 (e.g. Q-C2) significantly increased the amount of grain-scale microcracking and visibly reduced the grain size (Figures 3.12b and e). An average crack density of 1.84 cracks/grain was observed in wet sample Q-C2, and approximately 50% of the grains had failed by microcracking.

The injection of high pressure CO_2 into wet granular quartz (sample Q-C11) led to significantly lower amounts of microcracking, similar to the densities seen in lab dry material (cf. Figures 3.12a and c). Fewer cracks per grain were observed than under water-wet conditions, and the crack density was reduced to ~0.77 cracks per grain (Figure 3.12e). Overall, roughly 30% of the grains in the sample had failed by microcracking, with the majority of *failed* grains showing multiple fractures, i.e. up to 5 cracks per grain.

In the presence of alkaline pore fluid (Q-C12), roughly 65% of the grains in the sample failed with an average crack density of ~2.1 cracks/grain (Figures 3.12d and e), i.e. more than seen in water-wet samples. Also interesting to notice was corrosion of the quartz grains by the alkaline fluid resulting in more rounded grains.

In summary, the main deformation mechanism evidenced in the wet quartz samples was grain-scale microcracking, this being enhanced with increasing pore fluid pH, and inhibited by CO_2 injection (Figure 3.12e). We did not observe any pressure solution features, precipitation of secondary phases or fine-scale contact crushing.

3.4.2 Feldspar microstructures

As in the case of quartz, our feldspar samples showed an increase in microcracking with the addition of pore fluid with a pH ≥ 5.5 and with increasing pH (Figure 3.13d). Sample L-P1, compacted under lab dry conditions at room temperature displayed a crack density of ~0.56 cracks/grain, with microcracking resulting in failure of roughly 55% of the grains in the aggregate. The addition of water (L-P2; pH ≈ 5.5) as a pore fluid led to an increase in the density of microcracking such that on average 0.98 cracks were present per grain and ~80% of the feldspar grains in the sample had failed by microcracking (Figure 3.13d). Though the differences between the microstructures of different samples are not immediately visible in optical micrographs (compare Figure 3.13a and b – wet samples without and with added CO_2, respectively), our grain failure and crack density measurements (on samples L-G3, -4, L-P1, -2, -11, -12a, -13 and -22) demonstrated marked differences between the various experimental conditions.

3.4.2.1 Effect of grain size without added CO_2

We studied the microstructures of wet feldspar samples of two different grain sizes, tested at 80°C and 36 MPa effective stress, without added CO_2. The finer

grained sample, L-G3 (120 ± 30 μm), showed approximately 50% grain failure by microcracking and a crack density of ~1.04 cracks/grain. The coarser-grained sample, L-G4 (275 ± 25 μm), showed an increase in the fraction of microcracking and in crack density to ~70% and ~1.23 cracks/grain, respectively. In addition, particle size analysis was performed on three different grain size fractions before and after testing at 80°C and 36 MPa effective stress (samples L-G2, L-G3c and L-G5(*AE*), Table 3.2). Though particle size analysis systematically overestimates sieved grain size by a factor of 1.5 (see Section 3.2.1), the data do show a monotonic reduction in average grain size after compaction (Figure 3.13c). In addition, all three fractions showed an

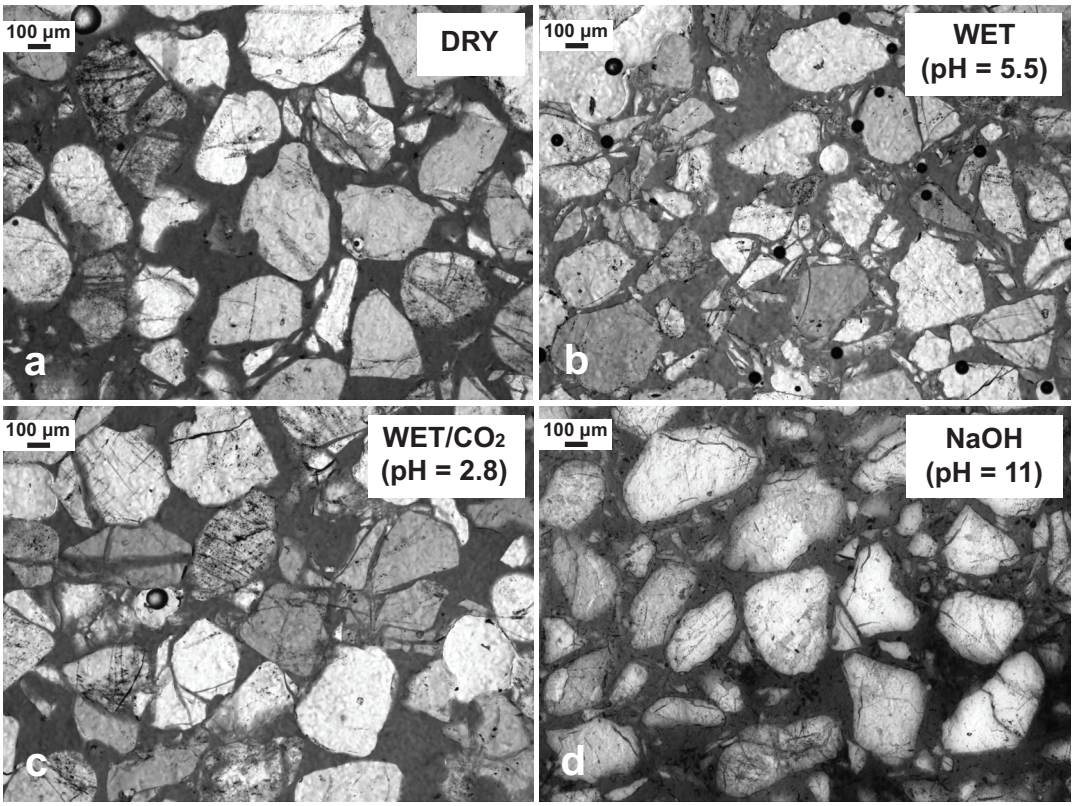

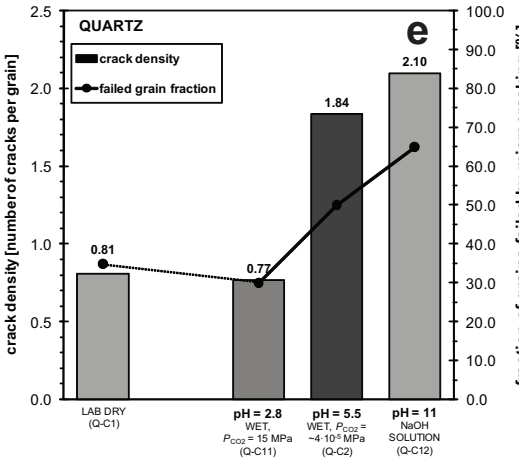

Fig. 3.12 Quartz microstructures observed in samples compacted at room temperature, σ_{eff} = 35 MPa, d = 425 ± 25 μm, using different pore fluids. a) Lab dry (sample Q-C1). b) Distilled water, pH = 5.5 (sample Q-C2). c) Distilled water with CO_2 added at high pressure (P_{CO2} = 10 MPa) and pH = 2.8 (sample Q-C11). d) NaOH solution with pH = 11.0 (sample Q-C12). e) Crack density (columns) and grain failure data (line) vs. pH. Note the increase in crack density and grain failure frequency with the addition of fluids with a pH ≥ 5.5, as well as with increasing pore fluid pH. Crack density is the average number of cracks per grain, and grain failure frequency is the fraction of failed grains.

increase in the proportion of finer material, which was absent in the starting material.

3.4.2.2 CO_2, pH and salinity effects

As in quartz, the injection of carbon dioxide into wet feldspar material at a pressure of 10 MPa at room temperature (sample L-P11; pH ≈ 2.8) resulted in a decrease in grain cracking relative to both water-wet and lab dry samples (L-P2 and L-P1), yielding a crack density of 0.43 cracks/grain and ~50% grain failure (see Figure 3.13d). In material compacted at 80°C with a pore fluid containing organic acids (L-P13; pH ≈ 4.4), we observed a closely similar microstructure, again with an average crack density of ~0.43 cracks/grain and a grain failure frequency by microcracking of roughly 45% (Figure 3.13d).

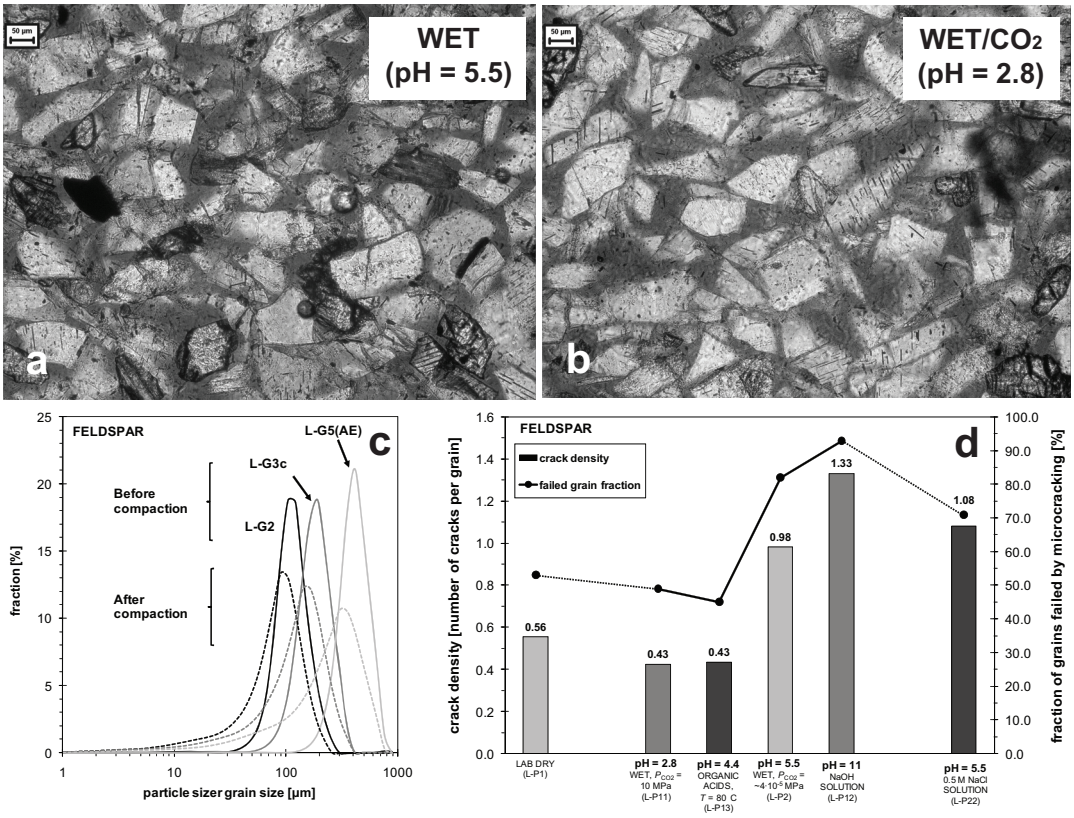

Fig. 3.13 Feldspar microstructures observed in samples compacted at room temperature with σ_{eff} = 36 MPa, d = 120 ± 30 µm, and with varying pore fluid compositions. a) Distilled water with no added CO_2 (P_{CO2} = 4·10^{-5} MPa), pH = 5.5 (sample L-P2). b) Water with added CO_2 at high pressure (P_{CO2} = 10 MPa), pH = 2.8 (sample L-P11). c) Particle size analysis of three different grain size fractions L-G2 (mesh size: 76.5 ± 13.5 µm), L-G3c (mesh size: 120 ± 30 µm), and L-G5(AE) (mesh size: 275 ± 25 µm) before and after compaction; solid lines = starting material, dashed lines = compacted material. Particle size analysis yields mean grain sizes that are systematically 1.5 times larger than sieved mesh grain sizes. Nonetheless, all samples show a finer mean grain size and a wider grain size distribution with more fine particles after deformation, pointing to microcracking as the main deformation mechanism. d) Crack density (columns) and failed grain fraction (line) vs. pH diagram. Note the increase in crack density and grain failure frequency with the introduction of fluids with a pH > 5, as well as with increasing pore fluid pH.

The addition of an alkaline solution of NaOH (L-P12a; pH ≈ 11) increased the crack density, compared to water-wet conditions (L-P2), to ~1.33 cracks per grain. Approximately 90% of the grains in the sample had failed by microcracking (Figure 3.13d). In contrast to the quartz sample deformed at the same conditions (Q-C12), the feldspar did not display obvious signs of corrosion by the alkaline pore fluid. Wet sample L-P22 with added NaCl (0.5 M NaCl; pH ≈ 5.5), showed a similar microstructure to L-P2 (wet, no additives, pH ≈ 5.5) with on average 1.08 cracks per grain, and approximately 70% grain failure (Figure 3.13d).

In summary, both microstructural evidence and particle size analysis indicate that the main deformation mechanism in the wet feldspar samples was grain-scale failure by microcracking, this being enhanced by increasing pH and grain size, and inhibited by injecting CO_2. In none of the samples did we observe any pressure solution features, precipitation of secondary phases or microgranulation/crushing at grain contacts.

3.5 Discussion

The mechanical data obtained in our experiments on quartz and feldspar have been separated into two parts: (1) an essentially time-independent or instantaneous compaction stage, which consisted of the initial 75 to 100 s of each experiment, and (2) a strongly time-dependent compaction creep stage. The behaviour observed during these stages clearly depends on pH and/or CO_2 pressure, and, in the case of feldspar, also on grain size, effective stress, and temperature. In the following, we discuss the effects of CO_2 injection, grain size, stress, temperature and fluid composition on the compaction behaviour of quartz and feldspar, and attempt to explain these effects in terms of operative microscale processes.

3.5.1 Time-independent compaction of quartz

At the low temperatures of our experiments, compaction of wet quartz in the time-independent stage could involve: (1) grain rearrangement through intergranular sliding and rolling, (2) elastic distortion of the grains, and/or (3) failure of grains and grain contacts due to the propagation of pre-existing cracks or flaws.

Pure grain rearrangement, through sliding and rolling of particles until a "locked" aggregate is created, generally produces small strains (a few %) which depend on the starting porosity of the aggregate [*Brzesowsky*, 1995; *Chuhan et al.*, 2003; *Chester et al.*, 2007]. However, our quartz experiments showed instantaneous strains (e_v^0) of ~10% with no systematic dependence on starting porosity φ_0 – see Table 3.2. This implies that other processes were important in determining the amount of time-independent strain achieved.

After "locking" of an aggregate by grain rearrangement, further compaction can only be achieved through deformation of the grains and grain contacts, allowing more rearrangement. Even at high stresses, elastic deformation of grains and grain contacts can result in only very small volumetric strains (< 1%). On the other hand, grain or grain contact failure can produce large volumetric strains. In our wet quartz experiments (d = 425 ± 25 μm, T = 20°C, σ_{eff} = 35 MPa, pH = 2.8-12.4), time-independent compaction is characterised not only by quite large volumetric strains (~10%), but also by a weak positive dependence of strain on solution pH (Figure 3.2), indicating some effect of chemical environment. Moreover, the final microstructures seen in the quartz samples show widespread grain cracking (Figure 3.12). We therefore propose that the main mechanism operating during time-independent compaction was a chemically enhanced, yet time-independent or near time-independent (i.e. very rapid), grain-scale microcracking process.

Fracture mechanics studies employing Hertzian contact theory [*Hertz*, 1881] have shown that grain-scale brittle failure in sands and sandstones occurs when surface flaws at the margin of grain contacts become critically stressed, i.e. when the Griffith criterion for crack extension is locally satisfied [*Zhang et al.*, 1990]. For spherical grains of diameter d (i.e. for grain contacts with a radius of curvature d/2), this leads to the grain failure criterion

$$F = \frac{Ad^2}{c^{3/2}} K_{IC}^3 \tag{3.1}$$

where F is the contact force required to break individual grains, A is a constant reflecting the elastic properties of the grains, c is the mean flaw half length and K_{IC} is the fracture toughness or critical stress intensity factor [*Zhang et al.*, 1990; *Brzesowsky*, 1995]. For a mode I opening crack in an ideal elastic/brittle material, K_{IC} can in turn be written as

$$K_{IC} = \sqrt{\frac{2E\gamma}{1-\nu^2}} \tag{3.2}$$

where E is the Young's Modulus of the solid, γ is its surface energy and v is Poisson's Ratio [*Shah and Wong*, 1997].

Using equations (3.1) and (3.2), the observed pH dependence of compaction by the inferred grain-scale microcracking mechanism can now be explained by two possible processes: (1) a reduction in surface energy and hence quartz fracture toughness (K_{IC}) and grain failure strength with increasing solution pH [*Atkinson and Meredith*, 1981], or (2) an acceleration of subcritical crack growth with pH such that an increasingly large population of subcritical flaws reaches the critical half length (c) for Griffith-type failure during the loading phase [cf. *Zhang et al.*, 1990]. In quartz, surface energy and

subcritical crack growth are respectively controlled by H^+, H_2O and OH^- adsorption onto quartz surface groups (≡Si-OH), and by hydrolysis of siloxane (≡Si-O-Si≡) bonds by these species [*Charles*, 1958; *Xiao and Lasaga*, 1994; *Dove*, 1995]. In solutions at the pH point of zero charge (pH_{PZC}), which is 2.4 for quartz and independent of temperature in our experimental range [*Sverjensky and Sahai*, 1998], the solid surface contains an equal number of positively (≡Si-OH_2^+) and negatively charged (≡Si-O^-) surface groups [*Parks*, 1967]. At higher pH values, reaction with OH^- dominates so that the surface contains more ≡Si-O^- surface groups and is negatively charged [*Dove*, 1995]. Measurements have shown that the surface energy of quartz decreases with increasing pH above the pH_{PZC} [*Li and De Bruyn*, 1966], in association with this increasing negative surface charge. Numerous experiments [*Atkinson and Meredith*, 1981; *Michalske and Bunker*, 1987; *Dunning et al.*, 1994] have confirmed that an increase in solution pH above the pH_{PZC} results in an increase in subcritical crack growth velocity in quartz. In this case, however, the rate of crack growth is thought to be controlled by the breaking of siloxane bonds (≡Si-O-Si≡) by OH^- attack, and by H_2O interactions aided by the negative charge on the quartz surface which attracts the protons in H_2O [*Dove*, 1995]. Taking all of these effects of pH into account, and since the transition from time-independent to slower time-dependent deformation in our quartz experiments is distinct but not sharp, we suggest that the effect of pH in the time-independent stage probably involves both surface energy reduction and enhanced subcritical crack growth.

3.5.2 Mechanisms of compaction creep in the wet quartz experiments

Discounting high-temperature creep processes, possible mechanisms for compaction creep in our wet quartz tests, with and without CO_2 or other additives, include: (1) dissolution at grain contacts due to undersaturation of the pore fluid with respect to the solid, (2) pressure solution at grain contacts, (3) subcritical crushing at grain contacts, and (4) subcritical, grain-scale microfracturing [cf. *Niemeijer et al.*, 2002; *van Noort et al.*, 2008]. Strain rates resulting from dissolution or pressure solution processes alone can easily be estimated for the experimental conditions employed (room temperature, pH 3 to 11), using the dissolution rate data for quartz given by *Brady and Walther* [1990] and the pressure solution model of *Spiers et al.* [2004], assuming a simple cubic pack of spherical grains (see Appendix A). This yields strain rates of the order of 10^{-12} s^{-1} or less, which is more than 4-8 orders of magnitude slower than the creep rates measured in our experiments. Taking into account the lack of any dissolution or precipitation microstructures except at pH 12.3, we infer that neither dissolution nor pressure solution were the main processes causing creep in our quartz experiments. Instead, since compaction creep was clearly promoted by increasing pH (see Figures 3.2 and 3.3), and since microstructural evidence for grain-

scale cracking is ubiquitous (Figure 3.13), we infer that the main process during the creep stage was probably grain-scale failure involving subcritical crack growth, plus serial grain rearrangement.

Subcritical crack growth in quartz in the presence of aqueous fluids is classically explained in terms of "stress corrosion cracking" [*Atkinson and Meredith*, 1981; *Atkinson*, 1984; *Fisk and Michalske*, 1985; *Michalske and Bunker*, 1987; *Dunning et al.*, 1994]. As mentioned above, this is thought to involve the weakening of strained Si-O bonds at the crack tip through the chemical interactions with water mentioned above (Section 3.5.1). For quartz and silica glasses it is believed that at low pH (pH $\approx$ pH_{PZC}) this interaction produces weaker, hydrogen-bonded, silanol groups, via the following hydrolysis reaction

$$\equiv Si\text{-}O\text{-}Si\equiv + H_2O \leftrightarrow \equiv Si\text{-}OH \bullet HO\text{-}Si\equiv \qquad (3.3)$$

Since the resulting ≡Si-OH (silanol) surface groups are only weakly joined by hydrogen bonds (•) they are more prone to rupture than the stronger ≡Si-O-Si≡ (siloxane) groups, so that subcritical crack growth rates become enhanced. With increasing solution pH at pH > pH_{PZC}, the quartz surface becomes more negatively charged, due to the formation of $\equiv Si\text{-}O^-$ surface groups [*Charles*, 1958] via the reaction

$$\equiv Si\text{-}O\text{-}Si\equiv + OH^- \leftrightarrow \equiv Si\text{-}O^- + \equiv Si\text{-}OH \qquad (3.4)$$

The sum of the rates of the solvent-surface interactions described by reactions (3.3) and (3.4) determines the net fracture rate ($R_{Si\text{-}O}$) of stressed Si-O bonds at a crack tip [*Dove*, 1995] according to

$$R_{Si\text{-}O} = k_{H2O}\,(\theta_{H2O}) + k_{OH\text{-}}\,(\theta_{OH\text{-}}) \qquad (3.5)$$

where k_i are the rate constants for bond rupture by H_2O or OH^-, and θ_i is the surface site fraction of Si-O bonds reacting with (i.e. occupied by) with either molecular water or hydroxyl ions. The concentration $\theta_{OH\text{-}}$ is directly dependent on pH (i.e. increase in OH^- concentration), while θ_{H2O} also increases with increases pH, but as a result of electrostatic reorientation of the water in response to the increasing negative surface charge (i.e. increased interaction of protons with the quartz surface). The relative contributions of water- and OH^--dominated mechanisms to the net fracture rate are thus affected by increasing solution pH. Since the relatively weak nucleophilic nature of H_2O results in less aggressive attack (i.e. corrosion) of the bridging oxygen bond compared to OH^- interactions [*Casey et al.*, 1990; *Dove*, 1995], the $k_{OH\text{-}}$ ($\theta_{OH\text{-}}$)-term

in reaction (3.4) increases faster with increasing pH than the k_{H2O} (θ_{H2O})-term, leading to an increase in crack growth rate which becomes progressively dominated by OH^- attack.

On this basis, we conclude that the creep stage of our wet quartz experiments can be explained in terms of grain failure due to subcritical crack growth, probably by stress corrosion cracking. Similar creep behaviour of granular quartz in the presence of chemically active fluids has also been reported by *Brzesowsky* [1995], *Chester et al.* [2004] and *Chester et al.* [2007], for example. Clearly, closely related processes are also active during the time-independent stages of our experiments on quartz, though on a much shorter time-scale, presumably reflecting the near-instantaneous growth of the largest flaws present to a length causing Griffith failure (see Section 3.5.1).

3.5.3 Time-independent compaction of feldspar

Our final feldspar microstructures (Figure 3.13d – effect of pH) show that more grain-scale cracks developed in the presence of fluids (pH > 5) than in dry samples, suggesting that chemically assisted grain failure was again the main deformation mechanism during the time-independent and/or time-dependent stages of compaction. This is supported by the observed pH dependence of instantaneous and time-dependent strain (Figure 3.4a), though the effects are small. However, the pH dependence of instantaneous volumetric strain (e_v^0) seen in our feldspar experiments (d = 120 ± 30 μm, T = 20°C, σ_{eff} = 36 MPa, pH = 2.8-11.0) is slightly different than observed for quartz: the feldspar data show a slight decrease of time-independent strain with pH up to pH 5.5, after which strain seems to be roughly independent of pH (see Figure 3.4a, cf. Figure 3.2). Unfortunately, not much is known about feldspars in relation to surface energy and surface charge, especially as a function of pH, so it is difficult to interpret this data further.

In addition to the effect of solution pH, we also investigated the dependence of instantaneous strain on grain size (d = 25-275 μm), effective stress (σ_{eff} = 20-100 MPa) and temperature (T = 20-100°C), as shown in Figures 3.4b-d. We found that time-independent strain increases with increasing grain size in wet samples with and without CO_2 injected at high pressure. This observation is in accordance with results obtained by *Brzesowsky* [1995] on quartz sand under "dry vacuum" conditions. Rewriting the grain failure criterion given in equation (3.1) in terms of the applied stress F/d^2 required for grain failure, it is easily seen that aggregate strength σ_c is independent of grain size as $\sigma_c = AK_{IC}^3/c^{3/2}$ [see also *Zhang et al.*, 1990; *Brzesowsky*, 1995]. However, when it is assumed that flaw size c scales with grain size d [*Zhang et al.*, 1990], or that the mean radius of curvature at grain contacts increases non-linearly with d due to irregularities in grain size [*Brzesowsky*, 1995], it becomes evident that increasing grain size can reduce failure strength. Assuming a distributed

grain size, this means that for a constant applied effective stress, more instantaneous strain will be achieved in aggregates with a coarser mean grain size. We observed a positive effect of grain size on instantaneous strain in both wet and wet/CO_2 tests, with the magnitude of instantaneous strain in CO_2-rich environments (pH 3.1) being significantly greater than in wet experiments without added CO_2 (pH 5.7) – see Figure 3.4b. Our conclusion is that the effects of grain size and pH or CO_2 on the time-independent or instantaneous strain seen in feldspars can be viably explained by a microcracking mechanism, provided that flaw size or grain surface curvature are grain size dependent.

Over the stress range investigated, instantaneous strain measured in our wet feldspar experiments increased strongly with effective stress (Figure 3.4c), similarly to observations made by *Brzesowsky* [1995] on dry and wet quartz. This is consistent with grain-scale microcracking as the main deformation mechanism but does not exclude other processes of course. Our observation that time-independent strain (e_v^0) increases with increasing temperature (Figure 3.4d) is also consistent with deformation by microcracking. Fracture mechanics experiments on quartz [*Atkinson*, 1979] have shown that increasing temperature in the range 20 to 80°C reduces the critical stress intensity factor, so that a lower applied stress is needed to extend pre-existing cracks. *Atkinson* [1979] did not explain this behaviour. However, it is possible that an increase in temperature increases solution pH through the competing effects of an increase in the dissociation constant of water K_w [*Bandura and Lvov*, 2006] accompanied by a decrease in dissolved atmospheric CO_2. The pH_{PZC} may be lowered as well, due to a reduction in the affinity between H^+ and OH^- ions with the quartz surface with increasing temperature [*Bérubé and de Bruyn*, 1968]. However, quartz and feldspar have relatively low activation enthalpies for H^+ and OH^- protonation, which means that the pH point of zero charge will be relatively temperature insensitive under the experimental conditions [*Sverjensky and Sahai*, 1998]. As a result, the surface energy of the solid may have decreased, or fast crack growth may have been promoted. Similar effects may have occurred in our experiments on wet feldspar, resulting in enhanced grain-scale failure and increasing time-independent strain as temperature is increased.

3.5.4 Mechanisms of compaction creep in wet feldspar experiments without additives

In the creep stages of our experiments on wet feldspar without injected CO_2 or other additives, the same range of possible mechanisms can be expected to operate as in the quartz compaction creep experiments, i.e. dissolution at grain contacts, pressure solution, subcritical crushing at grain contacts, and subcritical grain-scale microfracturing. Under the experimental conditions employed (T = 20-100°C, σ_{eff}

= 36 MPa, d = 25-275 μm), dissolution and pressure solution mechanisms would result in an expected strain rate of < 10^{-9} s^{-1}, according to the dissolution kinetics data of *Oxburgh et al.* [1994] and the pressure solution model of *Spiers et al.* [2004] (see Appendix A). Such rates are more than an order of magnitude slower than the slowest creep strain rates observed in the experiments, so that dissolution and/or pressure solution processes are unlikely to have been significant compaction creep mechanisms. In addition, the mechanical data (i.e. positive grain size dependence), the acoustic emission data for wet samples without added CO_2 (Figure 3.9) and our microstructural evidence rule out pressure solution as a dominant process, and suggest that the main process was microcracking as a result of subcritical crack growth.

In feldspars, subcritical crack growth is more complicated than for quartz due the additional Al-O bonds in the mineral framework, and it is unclear to what extent the proposed model of stress corrosion cracking for quartz (see Section 3.5.2) is applicable to feldspars [*Atkinson*, 1984]. Nonetheless, hydrolysis of Al-O bonds is believed to proceed through similar molecular mechanisms as hydrolysis of Si-O bonds [*Xiao and Lasaga*, 1994]. Calculations performed by *Xiao and Lasaga* [1994] have shown that hydrolysis of ≡Al-O-Si≡ bridging bonds by H_2O requires less energy than hydrolysis of ≡Si-O-Si≡ bridging bonds. We therefore suggest that, in materials containing both Si-O and Al-O bonds, hydrolysis of the Al-O bonds is favoured. This would mean that less energy (lower activation energy) is required to break Al-O bonds, leading to their preferential rupturing. As a result, more compaction is to be expected in feldspar aggregates than in quartz samples, especially at solution pH's > 7, where the feldspar surface contains both negatively charged ≡Al-O^- and ≡Si-O^- surface groups [*Parks*, 1967]. Some evidence for enhanced compaction of feldspar relative to quartz is seen in Figure 3.4b, especially if the creep strain vs. grain size trend is extrapolated to grain sizes comparable to those of the quartz experiments, i.e. to 425 ± 25 μm (cf. Figure 3.2).

In our wet feldspar experiments (T = 80°C, σ_{eff} = 36 MPa, no injected CO_2), we observed a weak power law relationship (exponent n ≈ 0.25) between creep rate and grain size (Figures 3.4b and 3.6). This was less pronounced than the dependence observed by *Brzesowsky* [1995] for compaction creep of wet quartz ($\dot{\varepsilon} \propto d^9$). Moreover, for quartz compacted under atmospheric conditions the strain rate dependence on stress at constant strain, as well as at constant normalised porosity, was suggested to be $\dot{\varepsilon} \propto \sigma^{15}$ by *Brzesowsky* [1995], while a power law exponent of approximately 1.5 was observed in our feldspar experiments at 80°C at constant normalised porosity (see Figure 3.7b). Though different in detail, the fact that *Brzesowsky* [1995] attributed the direct dependence of creep rate on grain size and stress to deformation by subcritical crack growth and progressive grain failure supports our conclusion that these processes dominated our tests on feldspar.

In addition, a weak dependence of creep rate on temperature (T = 20-100°C) was observed in our wet feldspar tests, characterised by an apparent activation energy of 10 kJ/mol. If creep rates are linearly related to subcritical crack growth velocity one would expect an activation energy of < 50 kJ/mol, the value obtained in stress corrosion crack growth experiments on quartz in wet environments [*Atkinson*, 1979]. On the other hand, processes such as the self-diffusion of water or OH^- (10-30 kJ/mol – *Nakashima* [1995]) or even dissolution (18.4 kJ/mol for anorthite – *Oelkers and Schott* [1995]) could equally control creep by microcracking [*Atkinson and Meredith*, 1981]. At present then, while we infer that creep of wet feldspar, without injected CO_2 or other additives, was controlled by some kind of subcritical or stress corrosion crack growth behaviour, the exact rate-controlling mechanism remains unknown.

3.5.5 Effects of CO_2 on compaction creep of wet feldspar

The injection of CO_2, and associated acidification of the pore fluid to pH values of 2.8-3.1, generally resulted in a decrease in the amount of compaction and in creep rate in the feldspar experiments, as seen in Figures 3.4, 3.5 and 3.6. In addition, the AE behaviour and the microstructure of the deformed feldspar samples showed a significant decrease in the amount of grain-scale microcracking in tests whereby CO_2 was introduced at high pressure (Figures 3.9 and 3.13). This suggests that CO_2 injection (partly) inhibited the active stress corrosion or subcritical cracking process inferred to be active in wet samples. This interpretation is supported by the fact that in acidic solutions resulting from CO_2 injection (pH ≈ 3), the feldspar surface will contain positively charged ≡Al-OH^{2+} bonds, while the ≡Si-O-Si≡ bonds will on average be neutrally charged [*Parks*, 1967]. This will mean less interaction between the feldspar and the pore fluid at the solid-fluid interface than at higher pH (i.e. above the pH_{PZC} of 2.4 for Si-O and 5-7 for Al-O [*Parks*, 1967]), where all bonds will be increasingly negatively charged.

Aside from the reduction in wet feldspar creep rates due to CO_2 injection, the sensitivity of creep rates to grain size (d = 25-275 μm) became significantly increased in the presence of CO_2 at 10 MPa pressure. The grain size dependence of creep rate changed from a rough power law dependence with exponent n = 0.25 to one with n = 0.5-2.5 as a result of CO_2 injection (Figure 3.6). At coarse grain sizes (d > 275 μm), compaction creep rates in the presence of CO_2 at high pressure accordingly approach those for samples without added CO_2. We cannot explain this effect of CO_2 on grain size dependence at present. One possibility is that grain contact or asperity curvature, hence contact stress magnitude, may be influenced by pH-dependent surface dissolution effects. However, the effect could also be due to an artefact linked to poor reproducibility of the pre-creep starting porosity (φ_i) in the experiments with pressurised CO_2.

3.5.6 Effect of acid/alkaline additives, salinity and dry CO_2 on compaction creep

In addition to the effects of added CO_2, we investigated the effect of solution pH on the compaction creep behaviour of feldspar (d = 120 ± 30 μm, T = 20-80°C, σ_{eff} = 36 MPa) by the addition of organic acids (H_3Cit plus HAc) and NaOH to the pore fluid. As reported in Figure 3.10, samples compacted at room temperature showed an increase in time-dependent strain and strain rate with increasing solution pH, notably at strains > 0.6% or so. Moreover, experiment L-P13 (organic acids, pH 4.4) performed at 80°C showed a decrease in creep rate, compared to wet experiments at both room temperature and 80°C (cf. Figure 3.8). These mechanical data (i.e. the pH dependence seen in Figure 3.10) together with the microstructures and crack density measurements made on the corresponding samples (Figure 3.13), indicate that microcracking was the main process causing grain failure and strain accumulation. The implication is that the observed compaction creep can again be explained in terms of the stress corrosion creep concept presented above (see Section 3.5.4 and 3.5.5).

Though solution pH was not varied independently of other chemical components or even temperature in the experiments shown in Figure 3.10, results from crack propagation experiments on quartz in oxalic acid have shown that it is the solution pH (i.e. H^+ activity) that controls crack propagation and not other chemical species in solution [*Dunning et al.*, 1994]. Therefore, the pH dependence observed in our quartz and feldspar experiments is most likely not affected by the different anions in solution (i.e. HCO_3^-, CO_3^{2-}, Ac^-, H_2Cit^-, $HCit^{2-}$ and Cit^{3-}).

Returning to sample L-P13 (Figure 3.10, Table 3.2), we found that addition of organic acids to the pore fluid resulted in a decrease in the amount and rate of both time-dependent and instantaneous compaction, compared to distilled water. This is in accordance with the proposed stress corrosion cracking model. However, our results conflict with those obtained by *Hajash et al.* [1998] who performed compaction experiments on granular albite at 100°C. These authors observed a factor of two increase in strain rate after injection of acetate-citrate solution, which they attributed to dissolution at grain contacts and/or stress-corrosion cracking. In their compaction experiments, however, the organic acid solution was passed (0.08 ml/h) through the samples, which may have enhanced dissolution or stress corrosion processes. Alternatively, the discrepancy between our data and those of *Hajash et al.* [1998] could reflect the difference in chemical composition of the feldspar used. Crack growth experiments on glass containing alkali ions [*Wiederhorn and Johnson*, 1973] have shown that H^+-ion exchange with the alkali ions tends to weaken the glass in acidic solutions and strengthen it in basic solutions. Albite, a compositional analogue of alkali aluminosilicate glass, would most likely behave similarly.

We have investigated the mechanical effects of varying CO_2 pressure, temperature, applied effective stress and solution pH on the compaction behaviour of granular quartz

and feldspar. However, when injecting CO_2 into a depleted gas or oil reservoir several additional factors have to be taken into account. Reservoir pore fluids generally consist of brines containing salts that may affect compaction creep behaviour, compared to (pure) water. We observed a slight increase in compaction creep rates using solutions of increasing salinity (0, 0.001 to 0.5 M NaCl – see Figure 3.11). Similar trends have been reported in compaction creep experiments on quartz sand, performed under atmospheric conditions [*Brzesowsky*, 1995], and were attributed to an acceleration of stress corrosion cracking through the formation of surface complexes. Dissolution experiments on quartz have indeed shown that surface complexation of Na^+ with ≡Si-O^- surface groups to form ≡Si-O^-Na^+ results in the opening and stretching of ≡Si-O^- Na^+ bonds, making them more prone to H_2O attack [*Dove and Elston*, 1992]. This effect has also been predicted theoretically by *Hiemstra and Van Riemsdijk* [1990]. By analogy, it may also apply for the Si-O bonds in feldspar, leading to enhanced subcritical crack growth, and hence creep, with increasing salinity.

In addition, when CO_2 is injected into a reservoir rock for sequestration purposes, it will generally be devoid of water near the injection well. This effect is caused by displacement of the pore fluid as a result of injection, as well as desiccation caused by water dissolving in the moving CO_2 [*Giorgis et al.*, 2007; *Müller et al.*, 2009]. The near-well volume of rock will therefore usually be in contact with (relatively) dry, supercritical CO_2. We studied the compaction creep behaviour of feldspar in such a chemical environment (L-P14). Our results (Figure 3.10) showed that the injection of supercritical CO_2 into a lab dry sample significantly reduced the amount and rate of compaction compared to lab dry systems. The most likely explanation is that any water present in the system was taken up by (i.e. dissolved in) the carbon dioxide [*Tödheide and Franck*, 1963], so that even less water was available at crack tips than under lab dry conditions. Near-well creep due to water-enhanced subcritical microcracking of grains is therefore expected to be inhibited when (dry) supercritical CO_2 is injected.

3.5.7 Implications

Our experimental results are directly relevant for evaluating the likely long-term effects of CO_2 injection into quartz and plagioclase-rich sandstone reservoirs and aquifers, both in the context of CO_2 storage and enhanced oil recovery (EOR). Our results imply that CO_2 injection will not enhance grain-scale microcracking processes, i.e. crack growth by stress corrosion cracking, in sand-grade quartz and feldspar rocks with grain sizes up to several hundred micrometers. Rather, microcracking will tend to be inhibited, especially in finer grained sandstones. We infer that CO_2 injection into either quartzitic or plagioclase-bearing arkosic sandstone reservoirs will not lead to any increased reservoir compaction or creep. Indeed, compaction creep will remain negligible since porosities and hence grain contact stresses are much lower in natural

reservoir rocks than in our experiments. Thus, following CO_2 injection, we do not expect any related geomechanical effects, such as caprock flexure and associated fracture, surface subsidence, well bore deformation or fault reactivation, either near injection wells or in the far field. However, more research is required to determine whether creep effects may play a role in very coarse-grained reservoirs.

Mineralisation reactions were not observed in our feldspar experiments but might occur in the long term. For a typical reservoir injected with CO_2 (T = 50-100°C, pH = 3-5), containing ~5% plagioclase feldspar and 15% porosity, literature data [*Oxburgh et al.*, 1994; *Oelkers and Schott*, 1995] imply that dissolution controlled reaction of plagioclase feldspar will take ~100-1000 years. Transformation of plagioclase within sandstone to form calcite and kaolinite will result in a solid volume increase of 35%, relative to the initial plagioclase volume. However, dissolution of the small proportion of feldspar grains followed by precipitation of the product phases in the pores will not lead to permanent compaction, as the load-supporting framework of the reservoir will limit compaction. The only likely effect may be a very minor poroelastic compaction of the reservoir. In the case of feldspar replacement reactions, precipitation of the products phases will occur on the pore walls (unstressed surfaces with fluid access) [*Moore et al.*, 2005] and not in (stressed) grain boundaries, particularly when reaction is controlled by dissolution, as expected [*Baines and Worden*, 2000; *Zerai et al.*, 2006]. Therefore, we infer that mineralisation reactions will not lead to reservoir deformation, though a decrease in porosity as a result of precipitation may be expected. It should be kept in mind, however, that large amounts of carbonate cement or frequent intercalated carbonate beds might change the overall picture. Experiments on calcite indicate significant effects of CO_2-charged fluids [*Pokrovsky et al.*, 2005; *Liteanu and Spiers*, 2009; *Pokrovsky et al.*, 2009] and more work is needed to assess the effects of CO_2 on compaction in such systems.

3.6 Conclusions

This paper has addressed compaction phenomena in simulated reservoir sands consisting of wet granular aggregates of quartz and feldspar (labradorite). We performed constant stress, uniaxial compaction experiments on these materials to investigate the mechanical effect of fluid-rock interaction due to CO_2 injection (P_{CO2} = $4 \cdot 10^{-5}$-15 MPa). We also addressed the effects of grain size (d = 25-425 μm), temperature (T = 20-100°C), effective stress (σ_{eff} = 20-100 MPa) and pore fluid composition (organic acids, NaOH, $Ca(OH)_2$, NaCl, dry supercritical CO_2). Our main findings can be summarised as follows:

1. The compaction behaviour of both quartz and feldspar aggregates was characterised by two different stages: (1) an essentially instantaneous or time-

independent stage (first 75-100 s) and (2) a subsequent time-dependent or creep stage.

2. Quartz compaction experiments performed at room temperature using an aqueous pore fluid showed that both time-independent (instantaneous) strain and time-dependent creep rate increase with increasing solution pH, at least at pH values above ~2.8, which is close to the PZC for quartz (pH 2.4 at 20°C). The injection of high-pressure CO_2 into wet samples accordingly reduced creep rates in quartz compared with creep under near-neutral pH conditions, e.g. under wet conditions in the absence of injected CO_2 (pH ≈ 5.5).
3. In feldspar experiments at room temperature, instantaneous strain decreased with increasing pore fluid pH in the pH range 2.8-5.5, and remained roughly constant at pH 5.5-11. In the absence of added CO_2 (pH = 5.5-5.8) but at reservoir temperature and stresses, time-independent strain increased with increasing grain size, applied stress and temperature. Creep strains and rates generally increased with increasing solution pH (pH 2.8-12.4) and (slightly) with salinity. We also observed a weak, positive dependence of creep rate on grain size. The dependence of creep rate on applied effective stress could be crudely described by a power law with a stress exponent (n-value) of 1-2.5 at constant normalised porosity. We also observed a weak temperature dependence of creep rate characterised by an apparent activation enthalpy of ~10 kJ/mol.
4. The injection of high pressure CO_2 into wet feldspar samples inhibited creep in comparison to near-neutral solutions, at least at fine grain sizes, and increased the grain size sensitivity of creep rate. In addition, injection of supercritical CO_2 into dry granular feldspar significantly reduced creep rates, compared with lab dry conditions.
5. The mechanical, microstructural and acoustic emission data obtained for wet quartz and feldspar samples, with and without added CO_2, indicate that microcracking plus grain rearrangement was the main mechanism of deformation in both the time-independent and time-dependent stages of the experiments. In both materials, time-independent compaction was most likely controlled by progressive grain failure related to extension of Griffith cracks at grain contact margins during and shortly after initial loading. This was enhanced towards higher pH, probably because of decreasing crack surface energy and rapid subcritical growth (at least in quartz).
6. Similarly, the main creep process operating in wet quartz and feldspar samples, with and without CO_2, was chemically enhanced subcritical microcracking, or stress corrosion cracking, leading to time-independent grain failure and rearrangement. No evidence was found for pressure solution or other dissolution processes, and rate estimates showed they were far too slow to be

of importance in our experiments. No mineralisation reactions were observed. The acceleration of creep with increasing pH and salinity can be attributed to enhanced stress corrosion cracking.

7. Injection of CO_2 into quartz- and feldspar-bearing sandstone reservoirs will generally reduce pH and thus inhibit grain-scale microcracking mechanisms. Geomechanical effects, such as reservoir compaction, surface subsidence, caprock flexure and fracture, well bore deformation or fault reactivation, related to these processes will therefore be negligible, both near injection wells and in the far field. Though no especially negative effects are expected, more research is required to clarify the behaviour of coarser grained reservoir rocks, as well as the long-term effect of slow mineralisation reactions on reservoir deformation and transport properties.

Appendix A

Strain rates resulting from simple grain-scale dissolution and from intergranular pressure solution were calculated using the pressure solution model of *Spiers et al.* [2004] adapted to cover the simple dissolution case.

Pressure solution models such as that presented by *Spiers et al.* [2004] state that in a stressed granular aggregate containing fluid in the pores and in the grain boundaries, compaction by intergranular pressure solution is driven by the difference in normal stress, and therefore the normal component of the chemical potential of the solid, between grain contacts and pore walls [*Lehner*, 1995; *Niemeijer et al.*, 2002; *Spiers et al.*, 2004]. The thermodynamic driving force for transport is given by the difference in chemical potential ($\Delta\mu_n$) of the solid between the stressed grain boundary and the unstressed pore wall and can be expressed as

$$\Delta\mu_n = \mu_{gb} - \mu_p = (\sigma_n - P_f)\Omega^s \qquad \text{(A1)}$$

where μ_i is the chemical potential of the grain boundary (gb) or pore wall (p), σ_n is the stress component normal to grain contacts [Pa], P_f is the pore fluid pressure acting on pore walls [Pa] and Ω^s is the chemical potential of the solid [m^3/mol]. This difference in chemical potential between high-stress source (grain contact) and low-stress sink (pore wall) sites corresponds to an enhancement of the solubility of the solid at the source, compared to the sink, given via the relation

$$\Delta\mu_n = RT \ln\left(\frac{C_p + \Delta C}{C_p}\right) \approx RT \frac{\Delta C}{C_0} \qquad \text{(A2)}$$

where ΔC is the solubility enhancement [m^3/m^3] and C_p is the solubility of the solid at

the sink [m^3/m^3], which will generally be almost equal to the solubility C_0 of the solid grains under purely hydrostatic conditions.

Assuming a simple cubic pack of spherical grains and dissolution controlled pressure solution, strain rates as a result of dissolution-controlled pressure solution can be calculated according to the following equation

$$\dot{\varepsilon}_s = A_s \frac{I_s}{d} \frac{\Delta\mu_n}{RT} = A_s \frac{I_s}{d} \frac{\sigma_e \Omega^s}{RT} f_s(\varphi) \qquad \text{(A3)}$$

obtained by inserting the above expressions for driving force (A1 and 2) into a linear kinetic law describing grain boundary dissolution [see *Spiers et al.*, 2004]. Here $\dot{\varepsilon}_s$ is the strain rate for dissolution-controlled pressure solution [s^{-1}], A_s is a geometrical constant, I_s is the reaction rate coefficient for dissolution at the grain boundary [m/s] defined as $I_s = k_s \Omega^s$, where k_s is the standard geochemical dissolution rate coefficient [mol/m^2 s], d is the initial grain size [m], R is the universal gas constant, T is absolute temperature [K], σ_e is the applied effective axial stress [Pa], and $f_s(\varphi)$ is a dimensionless function of porosity φ. For a granular aggregate with a porosity of 5 to 40%, this function can be approximated as $f_s(\varphi) \approx 1/(1\text{-}2\varphi)$ [*Spiers et al.*, 2004].

Now, using equation (A3) together with dissolution rate data (k_s) for quartz and feldspar at pH 3 to 11 and at 20 and 80°C [see Table A1 and *Brady and Walther*, 1990; *Oxburgh et al.*, 1994; *Oelkers and Schott*, 1995], we can calculate strain rates generated by dissolution -controlled pressure solution under our experimental conditions. For quartz (d = 425 μm, σ_e = 37 MPa, φ = 36.9%), strain rates induced by dissolution-controlled pressure solution are predicted to be of the order of 10^{-12}-10^{-14} s^{-1}, while those for feldspar (d = 120 μm, σ_e = 36 MPa, φ = 31.6%) are predicted to be of the order of 10^{-9}-10^{-11} s^{-1}. As discussed by *Spiers et al.* [2004], diffusion-controlled pressure solution is generally likely to be faster than

Table A1
Dissolution rate data for quartz and feldspar.

solution pH	T [°C]	dissolution rate coefficient k_s [mol/m^2 s]
Quartz†		
2.2	25	$8.9 \cdot 10^{-13}$
5.5	25	$3.6 \cdot 10^{-13}$
11.0	25	$8.3 \cdot 10^{-12}$
12.3	25	$5.4 \cdot 10^{-11}$
Feldspar‡		
3.0	22	$2.0 \cdot 10^{-10}$
5.0	22	$1.2 \cdot 10^{-11}$
3.0	80*	$6.0 \cdot 10^{-10}$
5.0	80*	$3.9 \cdot 10^{-11}$

† Quartz dissolution rate data are from *Brady and Walther* [1990] and the molar volume of quartz is taken to be $2.3 \cdot 10^{-5}$ m^3/mol.
‡ Dissolution rate data for bytownite are from *Oxburgh et al.* [1994] and the molar volume of feldspar is taken to be $1.0 \cdot 10^{-4}$ m^3/mol.
* The activation energy for feldspar was taken from *Oelkers and Schott* [1995] and yielded 18.4 kJ/mol.

reaction-controlled mechanisms in silicate minerals, and therefore not rate-controlling. Moreover, at higher porosities such as those characterising our experiments, the area of dissolving grain contacts is much smaller than the pore wall area, so that dissolution will generally control pressure solution rather than precipitation [*Spiers et al.*, 2004]. This justifies our assumption of dissolution control. However, if diffusion or precipitation were to be rate controlling, then the resulting rate of pressure solution would be slower then calculated for dissolution control, implying that the rates calculated here are upper bound values.

We now apply the above model to evaluate strain rates in a granular aggregate due to simple dissolution caused by undersaturation of the pore fluid with the solid phase. When the initial solution is completely undersaturated (solute-free) and no stress σ_{eff} is applied, $\Delta C = C_0$ in equation (A2), so that $\Delta\mu_n = RT$. Putting this into (A3) yields strain rates due to dissolution at the grain contact of 10^{-12}-10^{-14} s^{-1} for quartz and 10^{-10}-10^{-11} s^{-1} for feldspar.

Acknowledgements

This research was funded by Shell International Exploration and Production and performed under contract number 4600002284. It was also supported by and carried out under WorkPackage 4.1 of the Dutch national research project CATO on CO_2 capture, transport and storage. We thank Peter van Krieken, Gert Kastelein, and Eimert de Graaff for their technical assistance. Nadja Muller, Michiel Groeneveld and Claus Otto of Shell are thanked for their support of the research and for permission to publish the manuscript.

4

Mechanical behaviour of anhydrite caprock and implications for CO_2 sealing integrity

S.J.T. Hangx, C.J. Spiers and C.J. Peach

Submitted to Journal of Geophysical Research

Abstract

Maintaining caprock integrity is pre-requisite for geological storage of CO_2. We investigated the mechanical strength and damage behaviour of anhydrite-rich caprock, which seals many potential CO_2 storage sites around the world. Conventional triaxial tests were performed at temperatures of 20-80°C, confining pressures of 1.5-50 MPa and strain rates of ~10^{-5} s^{-1}. We determined the failure and dilatancy envelopes for dry anhydrite and studied the effect upon strength and dilatation of high-pressure pore fluids (P_f = 15 MPa), namely pre-saturated $CaSO_4$ solution and CO_2-saturated $CaSO_4$ solution. For dry samples, we observed an increase in strength with confining pressure and a slight weakening with temperature. Fluid penetration prior to failure resulted in a direct effective pressure effect on strength, but not on volumetric behaviour. Fluid penetration during failure is too slow to influence mechanical and volumetric behaviour. Overall, we found no short-term chemical effects of CO_2 and pore fluid on the strength of anhydrite. Penetration of the samples by CO_2-saturated pore fluid was more effective than by solution alone, most likely as a result of the lower interfacial tension of the CO_2/water system. Simple analytical calculations based on the elastic flexure of a seal formation, combined with our failure and dilatancy envelopes, show that for realistic conditions caprock integrity will not be compromised by mechanical damage. In addition, long-term chemical reactions of anhydrite with CO_2 will most likely not lead to significant CO_2 penetration, though more research is needed.

4.1 Introduction

Carbon dioxide capture at source, coupled with geological storage in depleted oil and gas reservoirs, saline aquifers, or coal seams, is currently seen as one of the most promising ways of mitigating anthropogenic carbon dioxide emissions [*Bachu*, 2000; *Orr Jr.*, 2004]. Depleted oil and gas reservoirs form a particularly attractive option for implementation of CO_2 storage in the short term, especially in industrialised countries with a major hydrocarbons production and transportation infrastructure, such as the United States, Norway or the Netherlands.

Since CO_2 mineralisation reactions are very slow under typical reservoir conditions [*Baines and Worden*, 2004; *Xu et al.*, 2004; *Zerai et al.*, 2006], and since most depleted oil and gas reservoirs have low mineralisation potential [*Baines and Worden*, 2004; *Gilfillan et al.*, 2009], injected CO_2 will mainly be present in the supercritical phase and dissolved in any residual or connate formation fluid [*Baines and Worden*, 2004; *Gilfillan et al.*, 2009]. Long-term storage in depleted reservoirs is therefore dependent upon maintaining trap integrity, i.e. on maintaining caprock and fault integrity [*Hawkes et al.*, 2005]. Caprock and fault integrity can potentially be affected by purely mechanical damage effects linked to stress and strain changes accompanying reservoir depletion and/or CO_2 injection into an associated reservoir [*Hawkes et al.*, 2005]. In addition, chemical attack by CO_2 may modify the mechanical strength and transport properties of the caprock, or may promote reactivation and/or leakage of sealed faults.

One of the most widespread sealing formations topping hydrocarbon reservoirs around the world is anhydrite rock. Anhydrite also forms the caprock at several trial CO_2 injection sites currently under operation (e.g. Teapot Dome, USA [*Chiaramonte et al.*, 2007]; the Weyburn and Zama Fields, Canada [*Li et al.*, 2005; *Bennion and Bachu*, 2008]; the K12-B field, the Netherlands [*Van der Meer et al.*, 2006a]). However, very little data is available on the mechanical and transport properties of anhydrite rock [*Müller and Siemes*, 1974; *Bell*, 1981; *Liang et al.*, 2007; *De Paola et al.*, 2009], especially on its failure strength, on fault reactivation behaviour, and on the chemical effects of water and CO_2 at in-situ conditions. Alongside the direct mechanical (effective pressure) effects of water and CO_2, chemical interactions might well reduce failure strength through crack energy reduction effects or subcritical microcracking processes similar to those seen in silicate and carbonate rocks [*Atkinson and Meredith*, 1981; *Atkinson*, 1984; *Baud et al.*, 2000b; *Hangx et al.*, 2009 (submitted) - see also Chapter 3]. Moreover, at sufficiently high pressures, anhydrite can potentially react with supercritical CO_2 and water to form calcite via the reaction $CaSO_4 + H_2O + CO_2 \leftrightarrow CaCO_3 + H_2SO_4$. The associated 20% reduction in solid volume might also affect mechanical behaviour, damage development and transport properties.

This study reports conventional triaxial deformation experiments performed on

anhydrite rock from the base of the Permian Zechstein sequence [*Van de Sande et al.*, 1996], which caps many depleted gas reservoirs and potential CO_2 storage sites in the Netherlands and the North Sea. Our aim was to determine the mechanical behaviour and damage characteristics of this material and to assess if there are any mechanical or chemically coupled effects of CO_2-charged pore fluid that might threaten integrity as stresses evolve during injection, or might pose a risk in the longer term. A potential risk associated with such anhydrite caprocks is that CO_2 might gain access to interbedded carbonates with sufficient permeability to allow lateral migration. Our experiments were performed at (near) in-situ reservoir conditions, i.e. at temperatures of 20-80°C, confining pressures (P_c) of 1.5-50 MPa and fluid pressures (P_f) up to 15 MPa, using strain rates of ~10^{-5} s^{-1}. We determined both mechanical failure and dilatancy envelopes for dry anhydrite and investigated the effect upon failure and dilatation of high-pressure pore fluids consisting of $CaSO_4$ solution and CO_2-saturated $CaSO_4$ solution. We use our results to assess the effect of reservoir depletion and CO_2 injection on caprock response to changing stress states. Furthermore, we briefly assess the likelihood of reaction and its long-term effects.

4.2 Experimental methods

Three types of conventional triaxial test were carried out:

(1) Dry experiments. These were performed on dry anhydrite and were aimed at establishing the dry failure and dilatancy envelopes at room temperature and 80°C.

(2) Wet experiments. This set of tests was carried out to investigate the effect of aqueous pore fluid, i.e. pre-saturated $CaSO_4$ solution, on the mechanical behaviour of anhydrite.

(3) Wet/CO_2 experiments. The third set was performed to investigate the effect of saturating the above pore fluid with CO_2 at high pressure.

All experiments conducted are listed in Tables 4.1 and 4.2, along with the corresponding test conditions. The dry experiments were carried out at 20 and 80°C, at confining pressures in the range 1.5-50 MPa. The wet and wet/CO_2 experiments were performed at 20°C and 80°C, using a confining pressure of 25 MPa and a pore fluid pressure of 15 MPa. In the wet and wet/CO_2 experiments, we performed runs on both intact samples and on samples that had been pre-deformed dry to ~85-95% of the expected peak strength at 10 MPa confining pressure, i.e. under dilatant conditions. This was done to ensure that the pore fluid phase penetrated at least the pre-deformed samples, so that any short-term, fluid-rock (i.e. chemical) interaction effects would be revealed.

Table 4.1
Conventional triaxial compression experiments performed on intact dry anhydrite samples at 20 and 80°C, plus key parameters obtained in the tests.

sample	P_c [MPa]	$(\sigma_1 - \sigma_3)_{max}$ [MPa]	σ_y [MPa]	E [MPa]
Dry experiments, 20°C				
HBG-7	1.5	97.7	93.4	36.3
HBG-9	3.0	129.2	124.2	31.3
HBG-4	5.0	149.3	145.0	29.0
HBG-6	10.0	173.5	156.4	48.0
HBG-5	15.0	167.4	156.0	33.5
HBG-49	25.0	195.6	172.7	49.7
HBG-48	50.0	232.5	189.8	50.1
HBG-35*	10.0	109.6	-	-
HBG-43†	10.0	139.7	112.2	-
Dry experiments, 80°C				
HBG-18	1.5	121.3	117.0	50.3
HBG-17	3.0	137.6	130.5	50.1
HBG-12	5.0	127.9	121.0	46.1
HBG-8	10.0	140.0	123.8	34.4
HBG-10	15.0	168.5	146.8	55.8
HBG-13	25.0	180.5	159.9	51.4
HBG-14	35.0	197.9	173.4	45.8
HBG-15	50.0	222.2	185.1	61.5
HBG-22‡	10.0	132.7	-	-
	10.0	152.2	148.1	-

Symbols: P_c represents test confining pressure, $(\sigma_1 - \sigma_3)_{max}$ is the peak differential stress measured at failure, σ_y is the yield stress defined as the differential stress at which the differential stress vs. strain curve deviates from linearity, and E is the Young's Modulus obtained from a linear fit to the linear (elastic) part of the stress-strain curve.

* Sample deformed up to 65% of the peak stress expected at the same conditions (cf. sample HBG-6), for assessing pre-failure microstructure.

† Pre-heated sample before deformation at the conditions shown, sample HBG-43 was first heated to 80°C, then pressurised at 10 MPa confining pressure, and subsequently cooled to room temperature while maintaining the confining pressure constant. This was done to assess the possible weakening effect of heating alone, such as dehydration of any gypsum present.

‡ Pre-deformed sample subjected to initial loading to ~95% of the expected compressive strength (i.e. up to 132.7 MPa, cf. sample HBG-8), followed by a second loading cycle to failure at 152.2 MPa.

4.2.1 Sample material and pore fluid preparation

The anhydrite rock used in the present experiments was obtained from a core retrieved from the Hardenberg-5 well, Hardenberg, the Netherlands, courtesy of Shell International Exploration and Production (SIEP) and the Nederlandse Aardolie Maatschappij BV (NAM). The material was taken from the Zechstein 1 Anhydrite Member at the base of the Permian Zechstein formation. Cylindrical samples, meaning 35 mm in diameter by ~80 mm in length, were drilled from the core and the ends ground square and parallel to a final length of 75 mm to ensure uniform load distribution. Prior to use, the samples were allow to dry for one day at room conditions. The retrieval depth of the samples varied from 3195 to 3225 m.

The prepared samples were greyish-white to grey in colour and appeared mostly quite homogeneous at the sample scale. Millimetre-sized, acicular anhydrite rosettes were clearly visible in the hand specimens, embedded in a fine, crystalline matrix. The rosettes made up ~60 vol% of the material. Some samples contained darker grey patches or bands of fine-grained material (bedding) orientated at an angle of up to 60° to the sample axis. Thermogravimetric Analysis (TGA) plus Fourier Transform Infrared (FTIR) spectroscopy showed that besides anhydrite the samples contained between 10 and 33 wt% carbonate, mainly dolomite. Thin section analysis indicated

Table 4.2
Conventional triaxial compression experiments performed on wet anhydrite samples at 20 and 80°C, with and without high-pressure CO_2.

sample	condition	T [°C]	P_c [MPa]	P_f [MPa]	$(\sigma_1 - \sigma_3)_{max}$ [MPa]
Wet experiments ($CaSO_4$ solution)					
HBG-16	intact	20	25.0	15	174.6
HBG-20*	pre-deformed*	80	10.0	0	133.2
			25.0	15	177.1
HBG-21	intact	80	25.0	15	187.8
Wet/CO_2 experiments (CO_2-saturated $CaSO_4$ solution)					
HBG-37*	pre-deformed*	20	10.0	0	129.4
			25.0	15	170.7
HBG-46	intact	20	25.0	15	158.7
HBG-40*	pre-deformed*	80	10.0	0	119.3
			25.0	15	149.9
HBG-42	intact	80	25.0	15	153.8

Symbols: T denotes test temperature, P_c represents test confining pressure, P_f is the pore fluid pressure, and $(\sigma_1 - \sigma_3)_{max}$ is the peak differential stress measured at failure.
* Pre-deformed samples: first deformation cycle up to ~85-95% of the expected compressive strength (no fluid pressure); second cycle (P_f = 15 MPa) up to failure.

that this was present as a fine-grained phase in the bands defining the bedding. The connected porosity of the intact samples varied from 0.1 to 0.3 %, as determined by weighing of the samples dry, as well as saturated with n-heptane (courtesy of Shell IEP and NAM), while the permeability was unmeasurable, i.e. less than 10^{-21} m^2. Sample density varied between 2900 and 2960 kg/m^3.

For all experiments employing a pore fluid phase, saturated anhydrite solution was prepared by adding excess ground sample material (> 2.72 g/l) to distilled water and stirring for at least two days at room temperature. Following the experiments of *Kontrec et al.* [2002], such a solution should reach equilibrium after ~1 day. No gypsum precipitation from solution was expected, as the conversion of anhydrite to gypsum is relatively slow under atmospheric conditions, particularly in the absence of gypsum seeds [*Kontrec et al.*, 2002].

4.2.2 Experimental set-up

Our deformation experiments were performed in axi-symmetric compression, using a modified version of the Heard triaxial machine described by *Peach* [1991] and *Peach and Spiers* [1996]. This consists of an externally heated triaxial testing machine, with silicone oil as the confining medium (see Figure 4.1). It comprises a main pressure vessel containing the sample, a linked auxiliary pressure vessel, and a load transmitting yoke/piston assembly driven by a motor/gearbox/ball-screw system. The yoke/piston assembly is advanced to load the sample, while simultaneously displacing confining fluid from the main vessel to the auxiliary vessel, keeping the

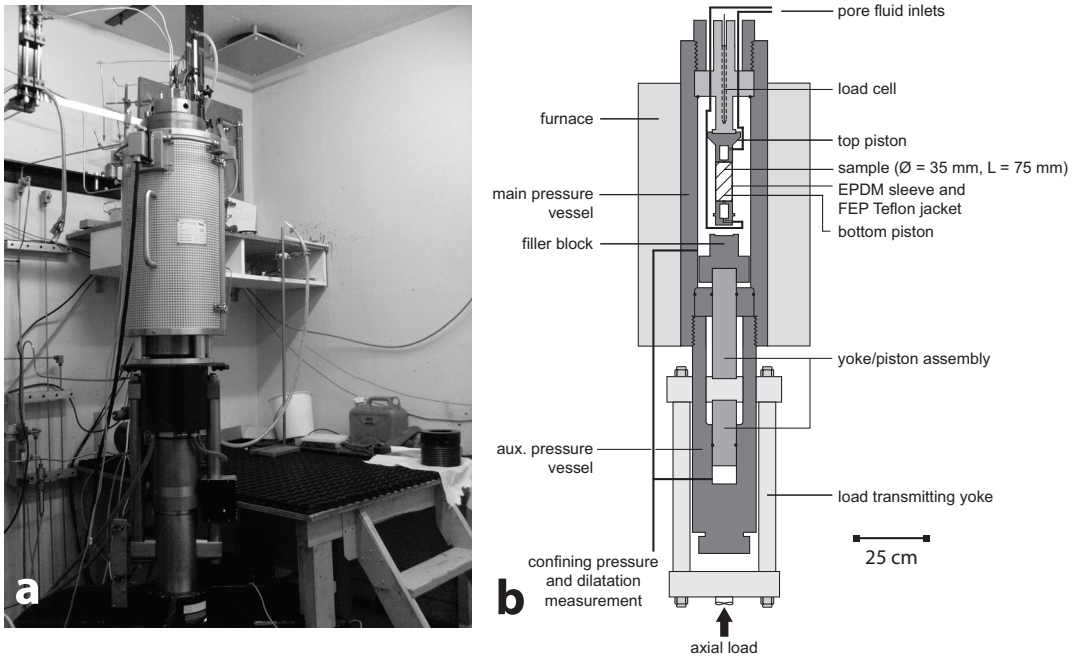

Fig. 4.1 Overview of the triaxial compression apparatus used in our experiments. a) The apparatus in its bunker. b) Semi-schematic diagram showing the internal details of the machine.

system volume nominally constant. Viton O-rings are used to achieve sealing on all dynamic and static seals.

Sample volume changes are measured using a linear potentiometer, which records the piston displacement of a servo-controlled volumometer pump maintaining constant confining pressure in the system during deformation (resolution ± 20 μl). Confining pressure is measured using a Jensen pressure transducer (100 MPa range, resolution ± 0.02 MPa). Axial load on the sample is measured using a DVRT based, semi-internal load cell located at the top of the vessel (400 kN range, resolution ± 0.035 kN, DVRT = differential variable reluctance transformer). Piston displacement is measured at the yoke using a high-precision LVDT (linear variable differential transformer, 100 mm range, resolution ± 0.8 μm). Sample temperature is measured midway along the sample surface using two, inconel-sheathed, K-type (chromel/alumel) thermocouples, brought into the main pressure vessel through a port in the load cell block. Temperature is controlled using a PID (proportional/integral/derivative) process controller (400°C range, resolution ± 0.02 °C) and a K-type thermocouple located in the windings of the external furnace.

Pore fluid pressure is introduced into the sample via ports in the load cell block, using stainless steel tubes connected to inlets at the top and bottom ends of the sample assembly (Figure 4.1). In our wet experiments, saturated $CaSO_4$ solution was injected into both ends of the samples at fixed pressure, using a second servo-controlled volumometer pump plus linear potentiometer to record piston displacement and hence connected pore volume changes. Pore fluid pressure was again measured using a Jensen pressure transducer (50 MPa range, resolution ± 0.02 MPa). In experiments exploring the effects of CO_2 on wet samples, supercritical carbon dioxide was injected into both ends of a pre-wet sample using a third, servo-controlled, volumetric pump (ISCO 65D) equipped with CO_2-proof seals plus Honeywell TJE pressure transducer (150 MPa range, volume resolution ± 10 μl).

4.2.3 Sample assembly

As already indicated, the experiments were performed on cylindrical samples measuring 35 mm in diameter by ~75 mm in length, with square-ground and polished ends (Figure 4.2a). To allow free access of fluid to the ends of the samples, the faces of the top and bottom piston components of the sample assembly (Figure 4.1) were grooved both radially and concentrically. In addition, both pistons contained a small fluid chamber (~1.5 ml). In the wet/CO_2 experiments, this was pre-filled with saturated solution during sample assembly and later pressurised with CO_2. All samples were jacketed using an EPDM (ethylene propylene diene monomer rubber) inner sleeve, of the same length as the sample, covered by a larger FEP (fluorinated ethylene propylene) outer sleeve. This was sealed against the top and bottom pistons using a

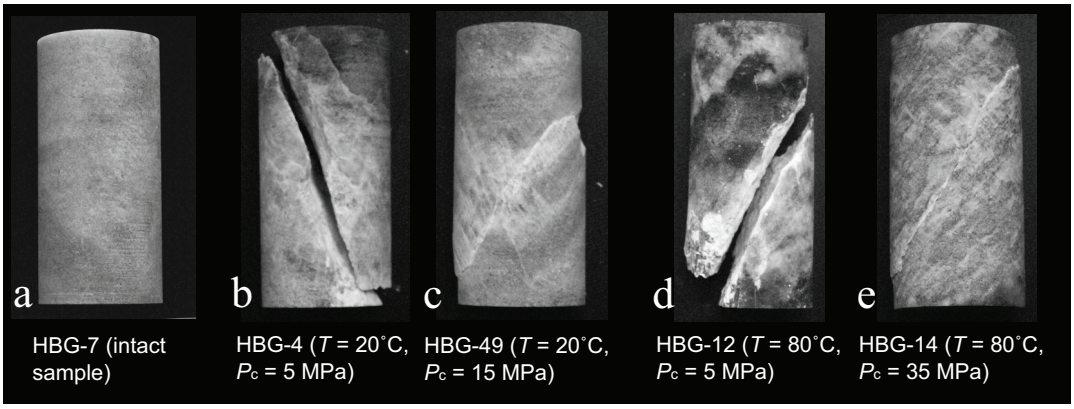

Fig.4.2 Photographs of a) undeformed anhydrite sample HBG-7, and b-e) samples deformed dry at 20 or 80°C and 5-35 MPa. Note that increasing the confining pressure at constant temperature led to more cohesive, distributed deformation. *T* denotes temperature and P_c confining pressure.

wire tournique and underlying EPDM band countersunk in the piston surfaces. The EPDM sleeve was included to reduce the risk of outer jacket rupture during sample failure. To reduce piston/sample friction during the experiments, thin Teflon sheets (50 μm) were placed between each piston and the sample. In all wet and wet/CO_2 experiments, these sheets were perforated to facilitate free access of fluid.

4.2.4 Testing procedure

After sealing, the sample assembly was located into the oil-filled vessel. The sample was then brought to the required temperature (~3 hours to reach ~80°C), maintaining the confining pressure below the target value for the deformation experiment. The required confining pressure was then applied, and the system temperature and volume left to equilibrate for ~12 hours. In the wet experiments, the pore fluid system was subsequently evacuated and pressurised with saturated solution. In case of the wet/CO_2 experiments, the system was directly pressurised with CO_2 without evacuation, to avoid removal of solution from the pre-filled fluid chambers in the top and bottom pistons of the sample assembly. After pressurisation, the pore fluid was left to equilibrate with the sample and, in the case of CO_2, with the solution present in the pistons. We assumed that equilibrium was approached when the system volume and pore fluid volumes reached a constant value, i.e. when no more volume change was registered by the respective volumometers. This generally took up to 5 hours.

The deformation experiment was subsequently started by advancing the yoke/piston assembly at a constant displacement rate corresponding to a near-constant strain rate of $1 \cdot 10^{-5}$ s^{-1}. The experiments were terminated by halting and then reversing the drive motor, removing the applied load to a small residual value determined by dynamic seal friction. This was followed by release of the pore fluid pressure, where used. The sample was then fully unloaded by hydraulically retracting the yoke/piston assembly, followed by removal of the confining pressure and cooling to room

temperature. Samples were finally extracted from the vessel and their outer and inner sleeves carefully cut off, enabling vacuum impregnation with epoxy resin to facilitate sectioning. Wet samples were allowed to dry at room temperature for 1-2 weeks before the impregnation stage.

4.2.5 Data acquisition and processing

Throughout the experiments, the internal axial load, piston displacement, confining pressure, sample temperature, system volume change, pore fluid pressure and pore fluid volume change signals were logged at time intervals of 10 s, using a PC equipped with a 12-bit National Instruments VI Logger system. The raw data were processed to yield differential stress ($\sigma_1 - \sigma_3$), axial strain (e), axial strain rate ($\dot{\varepsilon}$), volumetric strain (e_{vol}), and pore volume change (V_{pore}) data versus time. All displacement and volume change data were accurately corrected for apparatus distortion using pre-determined, polynomial stiffness calibrations. Sample volume and pore fluid volume data were also accurately corrected for the thermal expansion effects associated with fluid transfer between pressure vessels and for drift in room temperature.

4.3 Results

4.3.1 Mechanical data and failure modes

In this paper, we adopt the convention that compressive stresses, compressive axial strains and dilatant volumetric strains (dilatation) are measured positive. The principal compressive stresses recorded in our triaxial tests are accordingly denoted σ_i, with $\sigma_1 > \sigma_2 = \sigma_3 = P_c$, where P_c is the confining pressure. We define peak strength as the maximum differential stress $(\sigma_1 - \sigma_3)_{max}$ supported by a given sample and failure as the loss of strength of the material beyond the peak, either through catastrophic brittle fracturing or more gradual strain softening. We define sample yield strength (σ_y) as the differential stress at which the differential stress vs. axial strain curve deviates from linearity, following *Fredrich et al.* [1989]. The apparent Young's Modulus (E) of individual samples was determined from the linear portion of the stress-strain curves [*Zoback and Byerlee*, 1975a; *Baud et al.*, 2000a]. Key data on these quantities, obtained under dry and wet conditions, are listed in Tables 4.1 and 4.2, respectively.

4.3.2 Dry experiments at room temperature

To illustrate the real-time behaviour typically observed in dry experiments, Figure 4.3 shows differential stress and volumetric strain plotted as a function of time for two room temperature experiments performed at 5 and 25 MPa confining pressure. Note

the closely reproducible stress-time behaviour, plus the steady rate of dilatation up to failure observed at 5 MPa confining pressure compared with the initial compaction and then marked dilatation at failure seen at 25 MPa.

The differential stress and volumetric strain vs. axial strain curves obtained for the dry anhydrite samples deformed at room temperature are shown in Figure 4.4. These samples showed quasi-elastic loading behaviour followed by yielding and then failure at a peak stress, which generally increased with confining pressure. Broadly speaking two regimes of behaviour can be distinguished, based on the mechanical behaviour.

At confining pressures up to 5 MPa, the stress-strain curves show yielding followed by rapid hardening towards a peak differential stress and then abrupt, catastrophic brittle failure (Figure 4.4a). A pressure-dependent residual strength is attained at 1.3-1.5% axial strain. Failure was accompanied by audible acoustic emission. At confining pressures of 1.5 to 3 MPa, the volume change data show net compaction up to ~0.15% axial strain, beyond which dilatation (positive-going volume change) is observed (Figure 4.4b). At 5 MPa confining pressure, dilatant volume change is observed throughout the entire deformation test. Post-test inspection showed that samples deformed in this regime ($P_c \leq 5$ MPa) are characterised by brittle failure along

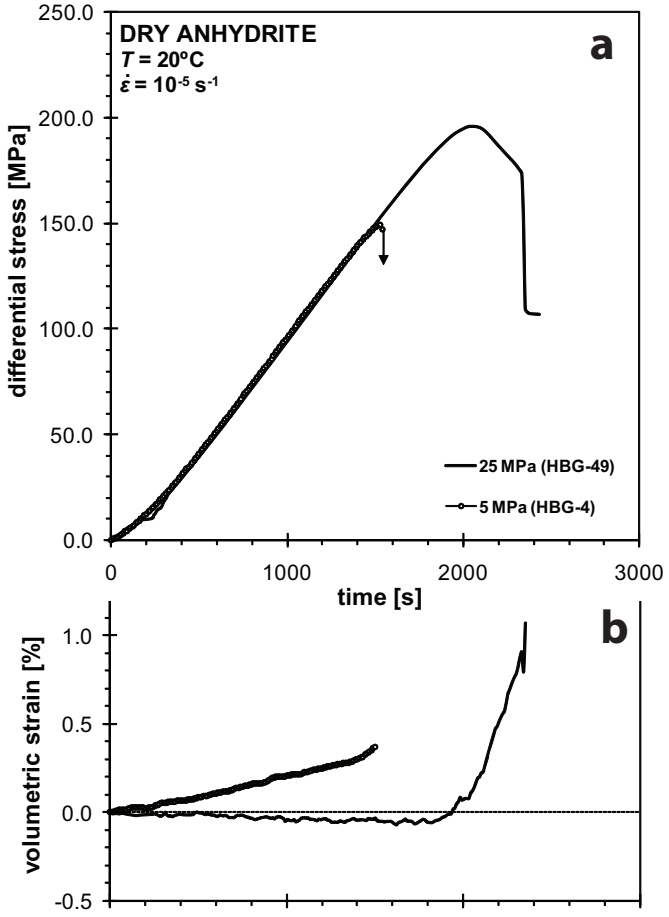

Fig. 4.3 a) Differential stress vs. time and b) volumetric strain vs. time curves for two representative experiments performed on dry samples at room temperature and at 5 and 25 MPa confining pressure. Note the sudden drop in differential stress at failure at 5 MPa versus gradual softening seen at 25 MPa. Note also the rapid increase in volumetric strain seen during the transient strain softening stage at 25 MPa, compared with the gradual dilatation before failure seen at 5 MPa. *T* denotes temperature and $\dot{\varepsilon}$ the initially imposed strain rate.

a single macroscopic shear fracture (Figure 4.2b), with the failure plane orientated at approximately 30° to the σ_1 direction.

In the higher confining pressure regime (> 5 MPa), the stress-strain curves (Figure 4.4a) show gradual strain softening beyond the peak stress, falling rapidly to a more or less steady, pressure-dependent residual strength at 1.5-2.5% axial strain. As seen from Figure 4.4b, positive but decreasing volume changes are observed at confining pressures in the range 5-15 MPa. At the highest confining pressures (25-50 MPa), volumetric behaviour is initially characterised by compaction up to the peak stress. During subsequent strain softening, however, large dilatant volume changes of 1-1.5% occur (Figure 4.4b). Macroscopically, the samples deformed in this regime (P_c > 5 MPa) display semi-brittle behaviour, characterised by a network of distributed, conjugate shear fractures oriented at ~30° to the compression direction, together with minor shear displacement along one macroscopic fracture, without loss of cohesion (Figure 4.2c). Little or no barrelling of the samples was observed under these conditions.

The main trends in the above, room temperature, mechanical data are summarised

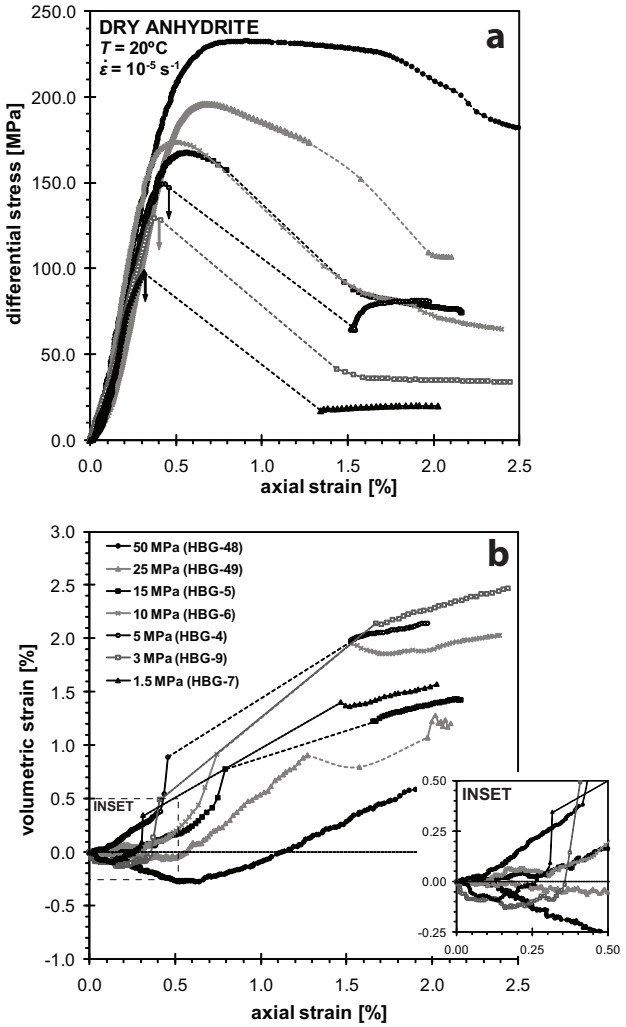

Fig. 4.4 a) Differential stress vs. axial strain and b) volumetric strain vs. axial strain curves for the triaxial experiments performed on dry anhydrite at 20°C. Confining pressures ranged from 1.5 to 50 MPa. At low confining pressures (1.5-5 MPa), failure occurred by abrupt brittle fracturing (indicated by arrows). At higher confining pressure (5-50 MPa), more gradual yielding plus strain softening were observed. Note that failure was often characterised by a rapid decrease in differential stress followed by a rapid increase in axial and volumetric strain, as elastic strain stored in the machine and sample were released. Where changes were too rapid to measure, differential stress and volumetric strain vs. axial strain behaviour are interpolated linearly (dotted lines). *T* denotes temperature and $\dot{\varepsilon}$ is the initially imposed strain rate. Samples HBG-35 and -43 are omitted because of their non-standard treatment (see Table 4.1).

in Figure 4.5. This shows that overall both the peak differential stress $(\sigma_1 - \sigma_3)_{max}$ and yield stress σ_y increase strongly with confining pressure (see Table 4.1 and Figure 4.5a). Prior to yielding, net volumetric strains measured at constant axial strain (e.g. 0.2%), increase with increasing confining pressure from negative values (compaction) at 1.5 MPa to positive values (dilatation) at 5 MPa (Figure 4.5b). At higher pressures (P_c > 5 MPa), however, the trend reverses, showing a clear transition from net dilatation at P_c = 5-15 MPa to net compaction at 25-50 MPa. Volumetric strains measured at yield show a similar trend (Figure 4.5b). At failure, i.e. at the peak stress, the volumetric strain data show a shift of the dilatation-compaction transition to higher confining pressures, with net dilatation occurring at 5-25 MPa and net compaction at 50 MPa (Figure 4.5b).

In addition to the above data, the Young's Modulus values determined from the stress-strain behaviour of our dry anhydrite samples at room temperature were

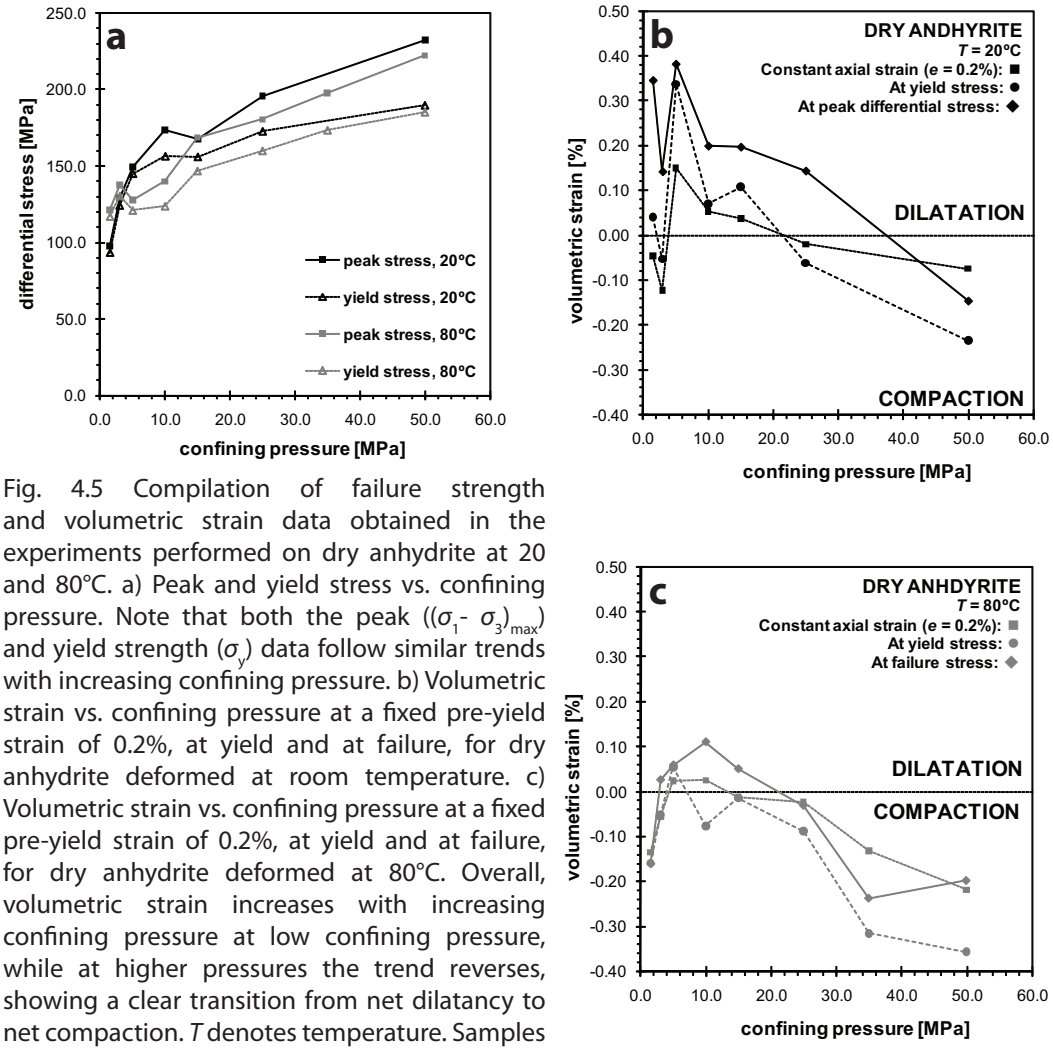

Fig. 4.5 Compilation of failure strength and volumetric strain data obtained in the experiments performed on dry anhydrite at 20 and 80°C. a) Peak and yield stress vs. confining pressure. Note that both the peak ($(\sigma_1 - \sigma_3)_{max}$) and yield strength ($\sigma_y$) data follow similar trends with increasing confining pressure. b) Volumetric strain vs. confining pressure at a fixed pre-yield strain of 0.2%, at yield and at failure, for dry anhydrite deformed at room temperature. c) Volumetric strain vs. confining pressure at a fixed pre-yield strain of 0.2%, at yield and at failure, for dry anhydrite deformed at 80°C. Overall, volumetric strain increases with increasing confining pressure at low confining pressure, while at higher pressures the trend reverses, showing a clear transition from net dilatancy to net compaction. *T* denotes temperature. Samples HBG-35 and -43 are omitted because of their non-standard treatment (see Table 4.1).

found to vary between 29 and 50 GPa (see Table 4.1). No systematic dependence on confining pressure was evident.

4.3.3 Dry experiments at 80°C

The differential stress and volumetric strain vs. axial strain data obtained in the dry experiments performed at 80°C are plotted in Figure 4.6. The stress-strain behaviour is similar to that observed at room temperature. However, at 80°C, the brittle regime extends up to 15 MPa confining pressure rather than 5 MPa. In this regime, catastrophic failure is observed more or less immediately after attaining the peak differential stress (Figure 4.6a). Volumetric strain under these conditions is characterised by compaction during the initial stages of loading, followed by dilatation after yielding and failure (Figure 4.6b). Failure is again accompanied by audible acoustic emissions and occurred on a single macroscopic fracture oriented at ~30° to the σ_1 direction (see

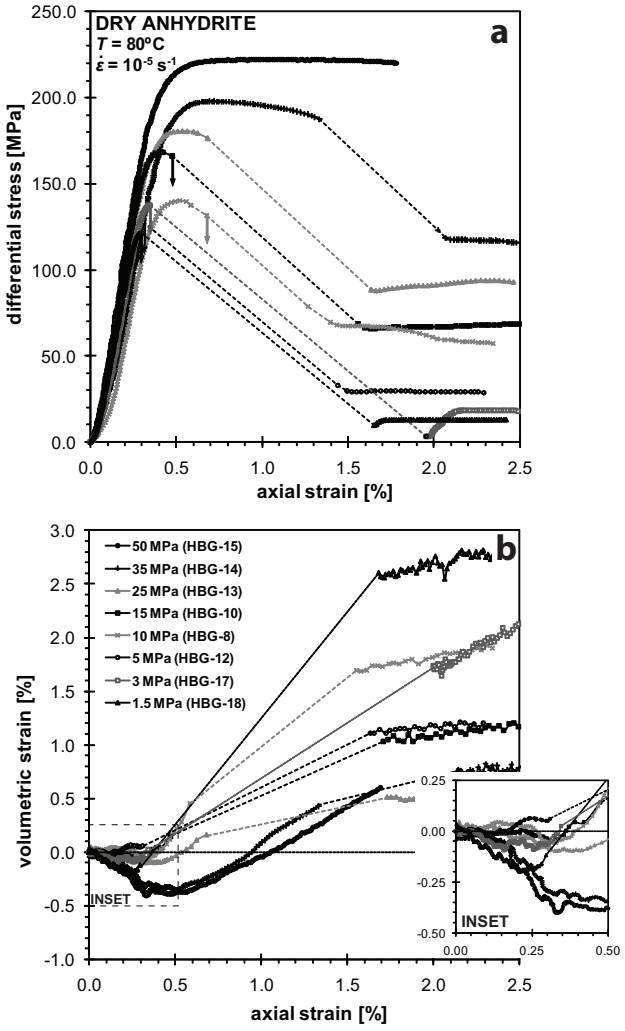

Fig. 4.6 a) Differential stress vs. axial strain and b) volumetric strain vs. axial strain curves for the triaxial experiments performed on dry anhydrite at 80°C. Confining pressure ranged from 1.5 to 50 MPa. At low confining pressures ($P_c \leq 15$ MPa), abrupt brittle failure (indicated by arrows) occurred at low strains, with little preceding yield behaviour. At higher confining pressure ($P_c > 15$ MPa), a progressively broader yield point develops followed by strain softening and finally more abrupt strength loss (except at 50 MPa). In all cases, failure was characterised by a decrease in differential stress and a rapid increase in volumetric strain. Differential stress and volumetric strain vs. axial strain behaviour is interpolated linearly where changes in stress and volume were too rapid to measure (dotted lines). *T* denotes temperature and $\dot{\varepsilon}$ the initially imposed strain rate.

Figure 4.2d).

Semi-brittle behaviour is observed at confining pressures in the range 25 to 50 MPa, the stress-strain curves show a broad yield and peak stress stage followed by strain softening (Figure 4.6a). More abrupt strength loss is finally seen at strains of 0.7 to 1.5% at 25 and 35 MPa respectively, but did not occur at 50 MPa. Negative volume changes (compaction) are observed during initial loading, while the yield and strain softening stages are characterised by a transition to dilatation (Figure 4.6b). Sample HBG-13, deformed at 25 MPa confining pressure, failed across a single macroscopic shear fracture with loss of cohesion, surrounded by a network of similarly oriented cracks. Samples deformed at higher confining pressure showed multiple conjugate shear fractures distributed throughout at ~30° to σ_1, plus minor displacement along a single fracture, without loss of cohesion (see Figure 4.1e). As at room temperature, samples displaying this semi-brittle behaviour showed no barrelling.

Over the entire confining pressure range studied (1.5-50 MPa), the dry samples deformed at 80°C show a positive dependence of both the peak differential stress $(\sigma_1 - \sigma_3)_{max}$ and yield stress σ_y upon P_c – as did the samples tested at room temperature (see Table 4.1 and Figure 4.5a). However, on average the 80°C samples appear around 10% weaker than samples deformed at room temperature, notably at higher confining pressures (> 5 MPa), while their strength is comparable to or slightly higher than the

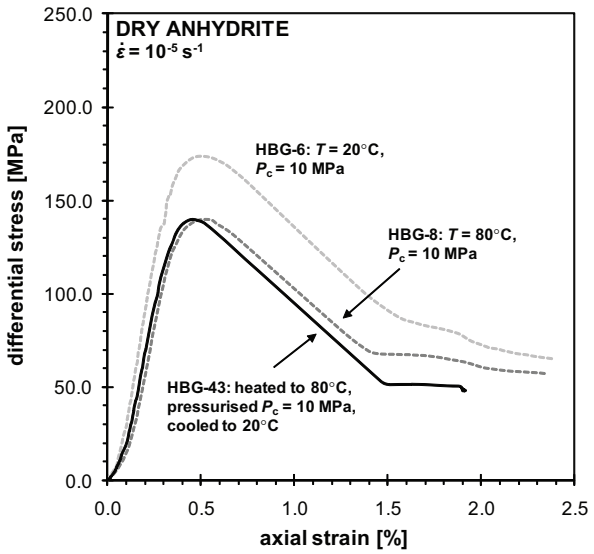

Fig. 4.7 Differential stress vs. axial strain behaviour for sample HBG-43 tested dry at 20°C and 10 MPa confining pressure. Prior to deformation, the sample was pre-heated to 80°C and pressurised at P_c = 10 MPa, following the cycle used in our triaxial tests at 80°C. It was then cooled down to room temperature and deformed. The aim was to determine if pre-heating to 80°C would influence the strength of the sample at 20°C. For comparison, curves are added for dry anhydrite samples deformed in standard tests at 10 MPa, at both room temperature and 80°C. Note that though sample HBG-43 was deformed at room temperature, it displays the same behaviour as sample HBG-8 deformed at 80°C. *T* denotes temperature, $\dot{\varepsilon}$ the initially imposed strain rate and P_c confining pressure.

room temperature values at low confining pressure (Figure 4.5a). Prior to yield, that is at 0.2% axial strain, volumetric strain at 80°C increases with confining pressure up to 5 MPa, from negative to positive values (Figure 4.5c), as observed at room temperature (Figure 4.5b). At higher confining pressures (P_c > 10 MPa), a reversal in trend occurs leading to net compaction at 15 MPa and above (Figure 4.5c). A similar trend is observed for volumetric strains measured at yield and at failure. As observed at room temperature, dilatation at failure is observed up to 15 MPa confining pressure. Overall, however, less dilatation is observed in the experiments at 80°C. Finally, the Young's Modulus values derived from the stress-strain data for dry anhydrite samples deformed at 80°C were found to vary between 34 and 61 GPa. As at room temperature, these values showed no systematic variation with P_c (see Table 4.1).

To assess the possible influence of deformation-independent effects of temperature on strength, we performed a single room temperature test on a sample previously heated to 80°C (HBG-43, P_c = 10 MPa, Table 4.1), following the heating and pressurisation cycle used in the triaxial tests at 80°C. Pre-heating of the sample in this way, irreversibly weakened the sample (Figure 4.7), indeed suggesting some kind of deformation-independent weakening process.

4.3.4 Wet experiments (saturated $CaSO_4$ solution)

As explained in Section 4.2, our wet experiments were performed at 20 and 80°C using a confining pressure of 25 MPa and a pore fluid pressure of 15 MPa. The experiments were performed on both intact samples and on samples that were pre-loaded dry to ~85-95% of their expected peak strength at P_c = 10 MPa. Pre-deformation of dry samples did not reduce the peak and yield strength of dry material, as illustrated by experiment HBG-22 (see Table 4.1).

The differential stress, volumetric strain and internal pore fluid volume vs. axial strain data obtained in our wet experiments are shown in Figure 4.8. Prior to fluid

→ Fig. 4.8 Mechanical behaviour observed during the wet experiments performed on anhydrite using $CaSO_4$ solution at P_c = 25 MPa and P_f = 15 MPa (solid curves). For comparison, the curves obtained for dry anhydrite deformed at 10 and 25 MPa confining pressure are added (dashed curves). a-c) Differential stress, volumetric strain and internal pore fluid volume vs. axial strain data for experiments performed at 20°C. d-f) Differential stress, volumetric strain and internal pore fluid volume vs. axial strain data for experiments performed at 80°C. Fluid penetration occurred at the yield point in material deformed at 20°C (a-c), but not until failure (i.e. the peak strength) in samples deformed at 80°C (d-f). At room temperature, where fluid penetration occurred before failure, i.e. at yield, the post-yield stress-strain behaviour is similar to dry samples deformed at the same effective confining pressure. At 80°C, where fluid penetration occurred at failure (peak strength), the stress-strain behaviour was similar to dry samples deformed at the same absolute confining pressure. In all cases, the volumetric behaviour was comparable to dry samples deformed at the same absolute confining pressure. No evidence was found for any chemical effects of $CaSO_4$ solution on the strength of the anhydrite after penetration. *T* denotes temperature, $\dot{\varepsilon}$ the initially imposed strain rate, P_c confining pressure and P_f fluid pressure.

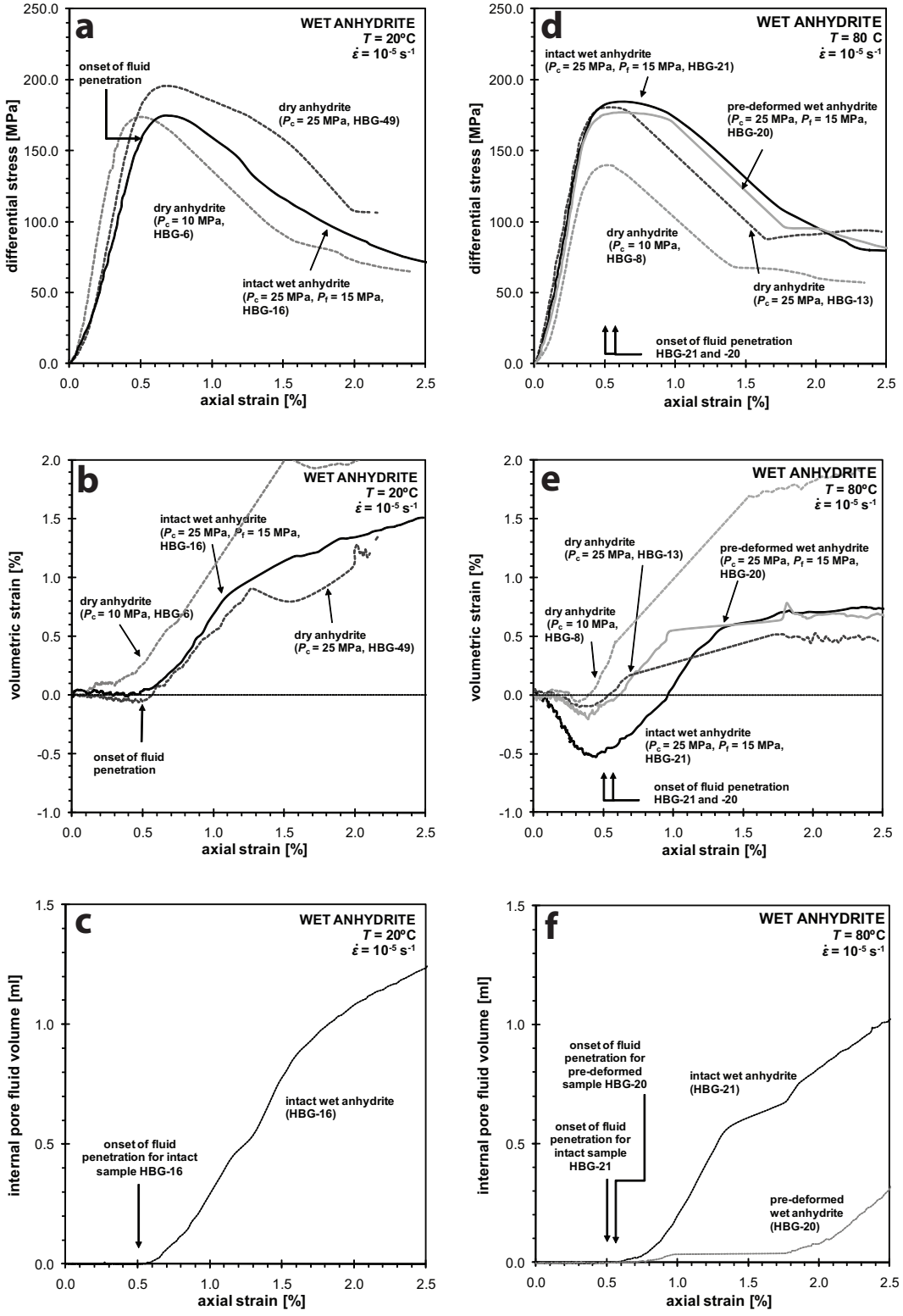
a
WET ANHYDRITE
T = 20ºC
ε̇ = 10-5 s-1
onset of fluid penetration
dry anhydrite (Pc = 25 MPa, HBG-49)
dry anhydrite (Pc = 10 MPa, HBG-6)
intact wet anhydrite (Pc = 25 MPa, Pf = 15 MPa, HBG-16)
differential stress [MPa]
axial strain [%]
d
WET ANHYDRITE
T = 80 C
ε̇ = 10-5 s-1
intact wet anhydrite (Pc = 25 MPa, Pf = 15 MPa, HBG-21)
pre-deformed wet anhydrite (Pc = 25 MPa, Pf = 15 MPa, HBG-20)
dry anhydrite (Pc = 10 MPa, HBG-8)
dry anhydrite (Pc = 25 MPa, HBG-13)
onset of fluid penetration HBG-21 and -20
differential stress [MPa]
axial strain [%]
b
WET ANHYDRITE
T = 20ºC
ε̇ = 10-5 s-1
intact wet anhydrite (Pc = 25 MPa, Pf = 15 MPa, HBG-16)
dry anhydrite (Pc = 10 MPa, HBG-6)
dry anhydrite (Pc = 25 MPa, HBG-49)
onset of fluid penetration
volumetric strain [%]
axial strain [%]
e
WET ANHYDRITE
T = 80ºC
ε̇ = 10-5 s-1
dry anhydrite (Pc = 25 MPa, HBG-13)
pre-deformed wet anhydrite (Pc = 25 MPa, Pf = 15 MPa, HBG-20)
dry anhydrite (Pc = 10 MPa, HBG-8)
intact wet anhydrite (Pc = 25 MPa, Pf = 15 MPa, HBG-21)
onset of fluid penetration HBG-21 and -20
volumetric strain [%]
axial strain [%]
c
WET ANHYDRITE
T = 20ºC
ε̇ = 10-5 s-1
intact wet anhydrite (HBG-16)
onset of fluid penetration for intact sample HBG-16
internal pore fluid volume [ml]
axial strain [%]
f
WET ANHYDRITE
T = 80ºC
ε̇ = 10-5 s-1
onset of fluid penetration for pre-deformed sample HBG-20
intact wet anhydrite (HBG-21)
onset of fluid penetration for intact sample HBG-21
pre-deformed wet anhydrite (HBG-20)
internal pore fluid volume [ml]
axial strain [%]

penetration, the mechanical and volumetric behaviour of both intact and pre-deformed samples is similar to dry samples deformed at the same absolute confining pressure (i.e. 25 MPa) – see Figures 4.8a, b, d and e. Fluid penetration does not occur until close to or at failure and is recognised by an increase in (connected) internal pore fluid volume (Figure 4.8c and f), though volumetric strain remains unaffected at this stage (Figures 4.8b and e). By the end of the experiments, on the other hand, the amount of fluid uptake by the samples is comparable to the externally measured sample volume change.

At room temperature, the intact sample (HBG-16) shows fluid penetration prior to failure, i.e. at the yield point ($e \approx 0.5\%$; $(\sigma_1\text{-}\sigma_3) \approx \sigma_y$). After penetration, the mechanical behaviour (i.e. peak and residual strength) of the sample is similar to dry sample HBG-6 deformed at the same effective pressure (i.e. 10 MPa), while the volumetric behaviour is similar to dry sample HBG-49 deformed at the same absolute pressure (25 MPa). Our pre-deformed, room temperature sample showed premature failure during the unloading stage of the dry, pre-deformation test, so that the effect of adding pre-saturated $CaSO_4$ solution cannot be assessed for this sample. In contrast to the room temperature experiment on intact material, the experiments performed at 80°C show no penetration of the pore fluid into the intact sample (HBG-21) or the pre-deformed sample (HBG-20), until failure occurs (Figures 4.8d and f). After failure, the mechanical and volumetric behaviour remains similar to dry samples deformed at the same absolute confining pressure (25 MPa, semi-brittle regime), despite fluid uptake. Note that, though the intact sample shows much more compaction at low axial strains (< 0.5%) than the pre-deformed, or the dry sample at the same absolute confining pressure, final volumetric strains are comparable for all three samples (Figure 4.8e). Macroscopic inspection of the wet samples after testing at 20 and 80°C revealed a distributed network of conjugate shear fractures, plus non-cohesive brittle failure on a discrete conjugate set of two macroscopic shear fractures at 35-45° to the compression direction.

In summary, the mechanical data indicate that deformation of the wet samples occurred in a manner similar to semi-brittle failure of dry samples. When fluid penetration occurs prior to failure, the mechanical behaviour of the samples obeys the law of effective stress. However, in the case of fluid penetration after failure, no change in mechanical behaviour is observed. Overall, volumetric behaviour is unaffected in all experiments. Besides the above effective pressure effect, no major chemical effect of high-pressure $CaSO_4$ solution is observed.

4.3.5 Wet/CO_2 experiments (CO_2-saturated $CaSO_4$ solution)

Figure 4.9 displays the differential stress, volumetric strain and pore fluid volume vs. axial strain data obtained in our wet/CO_2 experiments on intact and pre-deformed

samples at 20 and 80°C. In contrast to the wet experiments, fluid penetration occurs at or prior to the start of the experiments, except in the case of sample HBG-40 (T = 80°; intact). Again with the exception of HBG-40, all samples show a peak strength comparable to dry samples deformed at the same effective confining pressure and volumetric behaviour similar to dry samples deformed at the same absolute confining pressure (Figures 4.4.9a, b, d, and e).

Sample HBG-40 (T = 80°; intact) shows no measurable fluid uptake until after failure (e ~1.3% - see Figure 4.9f). However, its mechanical behaviour is intermediate between that of dry samples deformed at the same effective and absolute confining pressures (Figure 4.9d), while the volumetric behaviour is most similar to that of a dry sample deformed at the same effective pressure (Figure 4.9e). This suggests that, though no fluid uptake was measured in the early stages of the experiment, the sample must have been penetrated by fluid. Despite this, the final fluid uptake for sample HBG-40 was much less than expected from the observed volumetric strain. The other wet/CO_2 experiments showed uptake volumes comparable to the measured external volume change.

Macroscopically, all wet/CO_2 samples showed a network of distributed, conjugate shear fractures at 30 to 40° to σ_1. In addition, samples HBG-37 and -42 showed minor shear along a single, conjugate set of fractures, without loss of cohesion. Samples HBG-46 and -40 displayed non-cohesive brittle failure along a set of conjugate shear fractures. All samples deformed at 80°C showed a faint yellowish discoloration along the entire sample length.

The above mechanical data, and to some extent the macroscopic observations, indicate that the wet/CO_2 samples showed semi-brittle failure behaviour similar to dry and wet samples deformed under the same conditions. No major chemical interaction or reaction effects were observed. Rather, the observed stress-strain behaviour is consistent with an effective pressure reduction associated with fluid penetration prior to failure, though the volumetric behaviour shows no effect of fluid penetration.

4.4 Microstructural observations

Optical analysis of thin sections of the undeformed starting material shows a clearly bimodal microstructure consisting of coarse (mm-sized) acicular anhydrite rosettes (~60 vol%) embedded in a banded matrix of fine euhedral to subhedral anhydrite and dolomite grains (< 50 μm, ~35 vol%) defining the bedding of the material. Millimeter sized aggregates of subhedral anhydrite crystals (50-200 μm) are scattered throughout, totalling ~5 vol% of the material. The anhydrite needles in the rosettes display undulose extinction, twinning, subgrain development and grain boundary migration. Fluid inclusions (< 10 μm) can be observed in the anhydrite

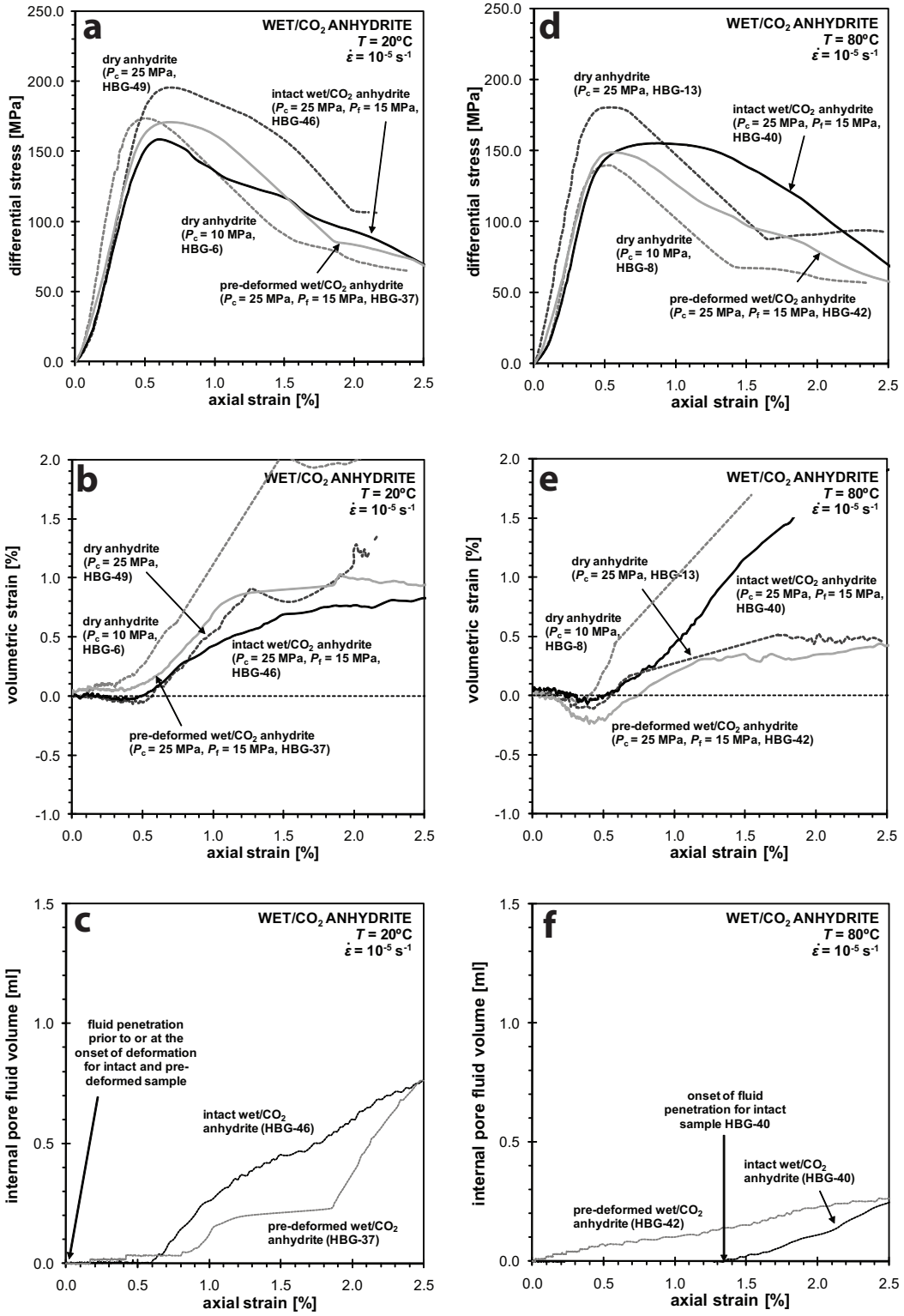
a
WET/CO2 ANHYDRITE
T = 20°C
ε̇ = 10-5 s-1
dry anhydrite (Pc = 25 MPa, HBG-49)
intact wet/CO2 anhydrite (Pc = 25 MPa, Pf = 15 MPa, HBG-46)
dry anhydrite (Pc = 10 MPa, HBG-6)
pre-deformed wet/CO2 anhydrite (Pc = 25 MPa, Pf = 15 MPa, HBG-37)
differential stress [MPa]
axial strain [%]
d
WET/CO2 ANHYDRITE
T = 80°C
ε̇ = 10-5 s-1
dry anhydrite (Pc = 25 MPa, HBG-13)
intact wet/CO2 anhydrite (Pc = 25 MPa, Pf = 15 MPa, HBG-40)
dry anhydrite (Pc = 10 MPa, HBG-8)
pre-deformed wet/CO2 anhydrite (Pc = 25 MPa, Pf = 15 MPa, HBG-42)
differential stress [MPa]
axial strain [%]
b
WET/CO2 ANHYDRITE
T = 20°C
ε̇ = 10-5 s-1
dry anhydrite (Pc = 25 MPa, HBG-49)
dry anhydrite (Pc = 10 MPa, HBG-6)
intact wet/CO2 anhydrite (Pc = 25 MPa, Pf = 15 MPa, HBG-46)
pre-deformed wet/CO2 anhydrite (Pc = 25 MPa, Pf = 15 MPa, HBG-37)
volumetric strain [%]
axial strain [%]
e
WET/CO2 ANHYDRITE
T = 80°C
ε̇ = 10-5 s-1
dry anhydrite (Pc = 25 MPa, HBG-13)
dry anhydrite (Pc = 10 MPa, HBG-8)
intact wet/CO2 anhydrite (Pc = 25 MPa, Pf = 15 MPa, HBG-40)
pre-deformed wet/CO2 anhydrite (Pc = 25 MPa, Pf = 15 MPa, HBG-42)
volumetric strain [%]
axial strain [%]
c
WET/CO2 ANHYDRITE
T = 20°C
ε̇ = 10-5 s-1
fluid penetration prior to or at the onset of deformation for intact and pre-deformed sample
intact wet/CO2 anhydrite (HBG-46)
pre-deformed wet/CO2 anhydrite (HBG-37)
internal pore fluid volume [ml]
axial strain [%]
f
WET/CO2 ANHYDRITE
T = 80°C
ε̇ = 10-5 s-1
onset of fluid penetration for intact sample HBG-40
intact wet/CO2 anhydrite (HBG-40)
pre-deformed wet/CO2 anhydrite (HBG-42)
internal pore fluid volume [ml]
axial strain [%]

needles. Following *Chang et al.* [1996], both the acicular habit of the anhydrite crystals in the rosettes and the fluid inclusions in these needle-shaped grains indicate replacement of gypsum rosettes by anhydrite. Rare, pre-existing transgranular and intergranular cracks are present (2-3 grains in length).

Representative micrographs of the microstructures observed in the deformed anhydrite samples are shown in Figure 4.10. Our mechanical data and sample-scale observations reported above point to two different deformation regimes across the full range of dry and wet ± CO_2 conditions investigated, (1) namely abrupt brittle failure involving cataclastic shear localisation, and (2) more gradual semi-brittle failure with more homogenously distributed microcracking, and cohesive or non-cohesive (conjugate) shear. We described the microstructures of our deformed samples according to these regimes.

4.4.1 Brittle regime: dry anhydrite

Thin sections of representative samples (HBG-4 and -12) deformed dry in the brittle regime at 20 and 80°C show a single main shear fracture at an angle of 26-28° to the compression direction (σ_1), of the type seen in Figure 4.10a. The main shear plane typically cuts the bedding and is irregular in outline. The fracture walls are lined with a thin layer of fine (fault) gouge up to 200 μm thick and are surrounded by a damage zone some 0.5-2 mm in width. Though such fractures may initially have been completely filled with gouge, handling probably led to disruption and dilatation. Some samples show fractures branching from the main shear fracture into the damage zone, with either conjugate orientation or an orientation nearly parallel to the compression direction (Figures 4.10a and b). The damage zones are highly fractured, displaying mainly dilatant transgranular and intergranular cracks, as well as en echelon crack arrays. Most cracks are aligned sub-parallel to the compression axis (Figure 4.10b). Overall, cracks are fewer, shorter and less well connected in the "bulk" material remote from the fracture, with intragranular and/or transgranular cracks becoming progressively more abundant relative to intergranular cracks (Figure 4.10c).

Material deformed in the brittle regime but to only 65% of the expected peak

← Fig. 4.9 Mechanical behaviour observed in the wet/CO_2 experiments performed at P_c = 25 MPa and P_f = 15 MPa (solid curves). For comparison, curves obtained for dry anhydrite, deformed at 10 and 25 MPa confining pressure, are added (dashed curves). a-c) Differential stress, volumetric strain and internal pore fluid volume vs. axial strain data for experiments performed at 20°C. d-f) Differential stress, volumetric strain and internal pore fluid volume vs. axial strain data for experiments performed at 80°C. With the exception of sample HBG-40, all samples showed fluid penetration prior to or at the onset of deformation. All such samples showed mechanical behaviour similar to dry samples deformed at the same effective confining pressure, while the volumetric behaviour was comparable to dry samples deformed at the same absolute confining pressure. No evidence for additional chemical effects was observed, compared with the dry and wet experiments. T denotes temperature, $\dot{\varepsilon}$ the initially imposed strain rate, P_c confining pressure and P_f fluid pressure.

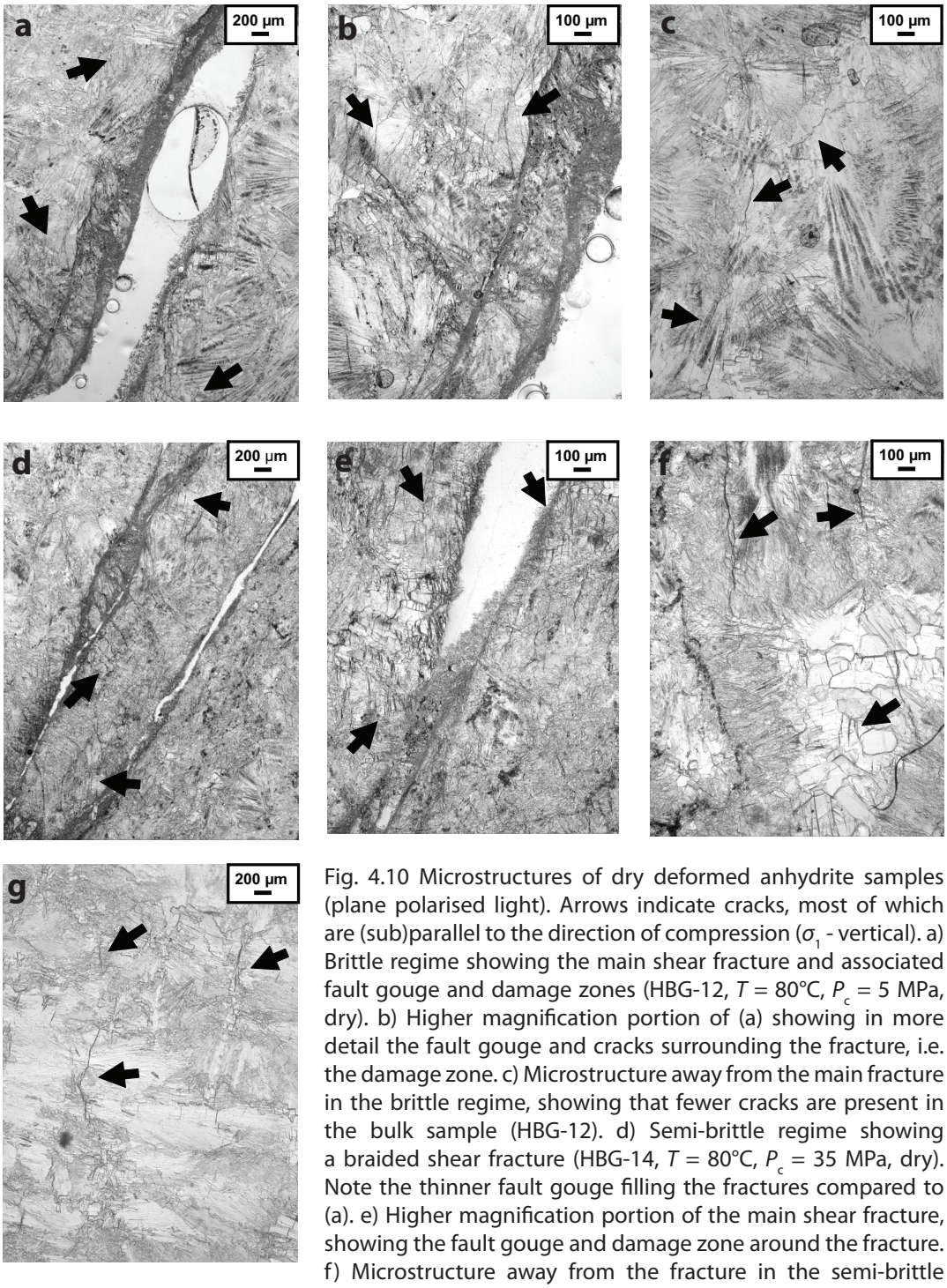

Fig. 4.10 Microstructures of dry deformed anhydrite samples (plane polarised light). Arrows indicate cracks, most of which are (sub)parallel to the direction of compression (σ_1 - vertical). a) Brittle regime showing the main shear fracture and associated fault gouge and damage zones (HBG-12, T = 80°C, P_c = 5 MPa, dry). b) Higher magnification portion of (a) showing in more detail the fault gouge and cracks surrounding the fracture, i.e. the damage zone. c) Microstructure away from the main fracture in the brittle regime, showing that fewer cracks are present in the bulk sample (HBG-12). d) Semi-brittle regime showing a braided shear fracture (HBG-14, T = 80°C, P_c = 35 MPa, dry). Note the thinner fault gouge filling the fractures compared to (a). e) Higher magnification portion of the main shear fracture, showing the fault gouge and damage zone around the fracture. f) Microstructure away from the fracture in the semi-brittle regime (dry sample HBG-14, 80°C). g) Sample deformed up to 65% of its expected peak stress (HBG-35, T = 80°C, P_c = 10 MPa, dry) showing cracks (sub)parallel to the compression direction; no crack network or sample-scale shear fracture has yet been formed.

strength (20°C, 10 MPa confining pressure – Figure 4.10g) shows that crack growth has already initiated at this point, i.e. well before failure. Cracks are distributed throughout the sample, oriented sub-parallel to the compression direction, but do not yet form a crack network or sample scale fracture.

4.4.2 Semi-brittle regime: dry anhydrite

Samples deformed dry in this regime at 20 and 80°C show shear localisation, usually without loss of cohesion, together with a more distributed network of conjugate shear fractures. Thin sections of representative samples (HBG-49 and -14) show single fractures or braided shear bands, with an average orientation of 28-30° to the compression direction (as seen in sample HBG-14 - Figure 4.10d). Individual shear fractures and bands generally have an irregular outline. Single shear fractures resemble those observed in the brittle regime, while the braided shear fractures contain zones of fault gouge interfingered with slices of coherent but strongly damaged rock (Figures 4.10d and e). These often lens-shaped slices show intense dilatant fracturing, i.e. intragranular, transgranular, intergranular and en echelon microcracks. Overall, in the semi-brittle regime, the fault gouge is generally thinner than in the brittle regime (< 100-200 μm), while the damage zone is thicker (2-5 mm). Away from the damage zones, deformation features such as intergranular, transgranular and intragranular cracks are generally widespread but less abundant and shorter than in the brittle regime.

4.4.3 Semi-brittle regime: wet and wet/CO_2 experiments

Our wet and wet/CO_2 experiments displayed mechanical and microstructural characteristics similar to dry samples deformed in the semi-brittle regime. Generally, the samples show a distributed network of shear fractures together with shear localisation along a conjugate set of fractures at angles varying from 31-38° (wet/CO_2 experiments) to 37-45° (wet experiments) to the compression direction, which is far less steep than under dry conditions. The samples contain features such as irregular, braided fractures, thin fault gouge zones (< 200 μm) and thick damage zones (3-5 mm). In some samples, deformation was concentrated at one end of the sample. No visible evidence of reaction or of precipitation of secondary phases could be discerned in the fractures or at the ends of the samples.

4.5 Discussion

Our experiments on dry anhydrite have shown a brittle to semi-brittle transition.

Brittle failure was found to dominate at low confining pressures (up to 5-15 MPa, depending on temperature), while semi-brittle behaviour dominated at higher confining pressures. We did not observe pervasive cataclastic flow in the semi-brittle regime. For this reason, we choose the term "semi-brittle" to describe this regime rather than the term "ductile" [*Rutter*, 1986]. Our data have also demonstrated an increase in strength with increasing confining pressure, alongside a minor decrease in strength with increasing temperature. These strength data offer a basis for deriving failure envelopes for dry anhydrite, suitable for geomechanical applications, such as caprock integrity assessment.

We also found that $CaSO_4$ solution penetrated our deforming samples just prior to failure at room temperature, but only at or during failure at 80°C. By contrast, CO_2-saturated, $CaSO_4$ solution usually penetrated the samples prior to or from the start of deformation, at both room temperature and 80°C. Though the stage at which fluid penetrated the samples, and the detailed mechanical and volumetric behaviour, varied from sample to sample, samples penetrated by fluid prior to failure (HBG-16, -37, -42, and -46) showed stress-strain behaviour similar to dry samples deformed at the same effective confining pressure. Their volumetric behaviour, on the other hand, was similar to dry samples deformed at the same absolute confining pressure. Samples penetrated during failure, i.e. at the peak differential stress (HBG-20 and -21), were also barely affected, either mechanically or volumetrically, compared with dry samples tested at the same absolute confining pressure. Interestingly, the strength contribution associated with the work done achieving the measured volume changes (i.e. the $P_c \cdot de_v/de$ term identified by *Edmond and Paterson* [1972]) represents less than ± 5% of the measured stress values, indicating that volume change can be eliminated as significantly affecting sample strength.

On this basis, we infer that the short-term mechanical strength of anhydrite rock at fixed temperature is controlled by the effective stress principle and, crucially, by whether or not sufficient fluid can gain access to the (evolving) pore structure and/or microcrack network prior to failure. We did not observe any additional strength reduction due to chemical interactions in our short-term deformation experiments. Several questions remain to be answered, however. These include the effect of temperature on strength and dilatation of dry samples, the lack of a volumetric strain response to fluid penetration, the difference in penetration behaviour of $CaSO_4$ solution pressurised with and without CO_2, and the possible effect of any long-term chemical interactions.

In the following, we make use of our data for dry samples to develop failure and dilatation criteria for both room temperature and 80°C, and attempt to explain the effect of temperature on dry strength. We go on to compare our results with previous strength data on dry anhydrite, and then to discuss the effects and mechanisms of

penetration by $CaSO_4$ solution versus CO_2-saturated aqueous fluid. In addition, we consider the implications of our results for caprock integrity following reservoir depletion and CO_2 injection. Finally, we will discuss the likelihood of reaction and its possible long-term effects.

4.5.1 Failure and dilatancy criteria for dry anhydrite at 20 and 80°C

Our experiments have shown that, when Zechstein anhydrite is penetrated by pore fluid prior to failure, the short term failure behaviour of the material is controlled by the law of effective stress without any significant chemical weakening effects. This means that the failure criterion for dry anhydrite can be used to delineate the (effective) stress conditions under which intact anhydrite caprock will be stable vs. unstable, not only without pore fluid, but also with pore fluid penetration on timescales for which chemical interaction is negligible (short term strength).

To obtain suitable failure criteria, we employ the Mogi criterion [*Mogi*, 1971]. The Mogi failure criterion was chosen over the more conventional Mohr-Coulomb criterion, as it includes all three principal (effective) stresses, instead of just the maximum and minimum values. This allows better generalisation of our data for use in numerical modelling of the mechanical behaviour of caprock in response to changing 3-D stress conditions resulting from reservoir depletion or CO_2 injection. Though the Drucker-Prager criterion is generally adopted by finite element codes the Mogi criterion gives a better fit to a wide range of triaxial data.

The Mogi failure criterion is usually used to describe the results of true triaxial (polyaxial) compression experiments. However, it can also be used to accurately describe data from conventional triaxial tests [*Al-Ajmi and Zimmerman*, 2005]. The stress space of the Mogi failure criterion is defined in terms of the Mogi octahedral shear stress [MPa] and the effective Mogi mean stress [MPa], i.e. the mean value of the maximum and minimum principal stresses, given as

$$\tau_{oct} = \tfrac{1}{3}\sqrt{(\sigma_1 - \sigma_2)^2 + (\sigma_2 - \sigma_3)^2 + (\sigma_3 - \sigma_1)^2} \tag{4.1}$$

$$\sigma_{m,2} = (\sigma_1 - \sigma_3)/2 \tag{4.2}$$

For dry rock, σ_1, σ_2, and σ_3 are the principal stresses at failure [MPa], while for rock penetrated by pore fluid they represent the principal effective stresses at failure, defined as $\sigma_i^{eff} = \sigma_i - P_f$, where, P_f is the pore fluid pressure [MPa]. In the case where $\sigma_2 = \sigma_3$, such as in our experiments, the octahedral shear stress is reduced to $\tau_{oct} = \frac{\sqrt{2}}{3}(\sigma_1 - \sigma_3)$.

Mogi failure criteria describing the behaviour of our dry anhydrite samples were obtained by plotting the failure stress data for dry anhydrite deformed at 20°C and

80°C in the Mogi stress space, as shown in Figure 4.11. Though power laws generally give the best fit [*Haimson and Chang*, 2000; *Colmenares and Zoback*, 2002; *Al-Ajmi and Zimmerman*, 2005], our dry data are best described by the following parabolic failure envelopes:

$$\text{At } 20°\text{C: } \tau_{oct} = -2.44 \cdot 10^{-3}(\sigma_{m,2})^2 + 1.06\,\sigma_{m,2} - 0.32 \quad (R^2 = 0.99) \quad (4.3a)$$

$$\text{At } 80°\text{C: } \tau_{oct} = -1.23 \cdot 10^{-3}(\sigma_{m,2})^2 + 0.75\,\sigma_{m,2} + 15.29 \quad (R^2 = 0.99) \quad (4.3b)$$

As noted by *Al-Ajmi and Zimmerman* [2005], a linear trend through data described in the Mogi stress space can be used to derive the Coulomb failure parameters, i.e. the uniaxial compressive strength C_0 and the coefficient of friction μ, of the linearised form of the Mohr-Coulomb criterion $\sigma_1 = C_0 + q\sigma_3$. For our results at room temperature,

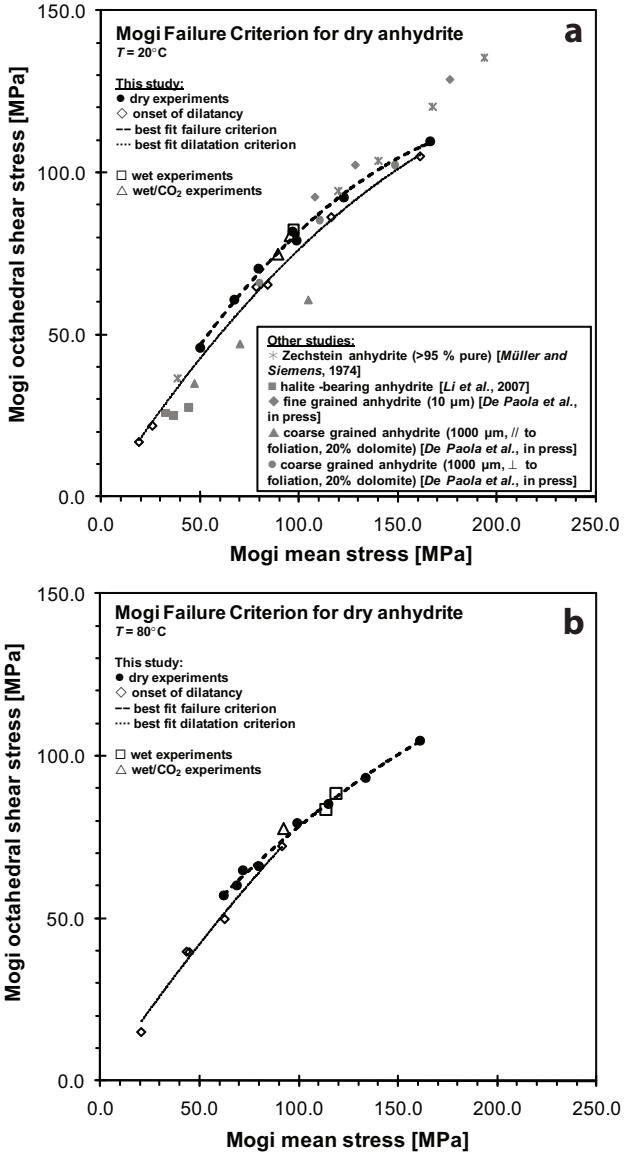

Fig. 4.11 Mogi failure and dilatancy envelopes drawn for anhydrite deformed dry at a) 20 and b) 80°C. The onset of dilatancy indicates the boundary between the permeable and impermeable regime. The dry data have been used to derive the best-fit failure and dilatation criteria shown. For comparative purposes, the data for our wet and wet/CO_2 experiments where fluid penetrated prior to failure are added to the plot, applying the effective stress principle to calculate the effective mean stress in case of fluid penetration. There is a close fit between the dry envelopes and the wet data, confirming that no major chemical weakening had occurred. For further comparison, anhydrite peak stress data obtained in other studies of dry anhydrite are added to (a) [after *Müller and Siemes*, 1974; *Liang et al.*, 2007; *De Paola et al.*, 2009]. Note that the onset of dilatancy is here defined as the point where the volumetric strain vs. axial strain curve deviates from linear compaction.

this approach yields C_0 = 123 MPa and μ = 0.4, while at 80°C we obtain C_0 = 124 MPa and μ = 0.5, respectively. This suggests that anhydrite is slightly stronger at 80°C then at 20°C. However, this is an effect of the linear fit, as at a given normal stress the material is on average weaker than at room temperature (compare Figure 4.11 a and b), especially at higher confining pressure.

In addition to the failure behaviour of our material, volumetric strain development, as a function of confining pressure and temperature, is also of interest. Since dilatation (i.e. opening of cracks) in an impermeable material leads almost immediately to permeability development as cracks connect [cf. *Zoback and Byerlee*, 1975b; *Stormont and Daemen*, 1992; *Peach and Spiers*, 1996], continuous volumetric strain measurements give an indication of the onset of dilatancy and hence of permeability development in deforming anhydrite. The onset of dilatancy, defined here in terms of the principal effective stresses at which the volumetric strain vs. axial strain curve deviates from linear compaction [following *Zoback and Byerlee*, 1975a; *Baud et al.*, 2000a], is also shown in Figures 4.11a and b for the dry samples used to derive our failure criteria. Note, that experiment HBG-4 was not taken into account as it showed dilatancy throughout the entire deformation cycle. Our data for the onset of dilatancy can accordingly be described by the following parabolic functions

$$\text{At } 20°\text{C: } \tau_{oct} = -1.71 \cdot 10^{-3}(\sigma_{m,2})^2 + 0.93\,\sigma_{m,2} \quad (R^2 = 0.99) \qquad (4.4a)$$

$$\text{At } 80°\text{C: } \tau_{oct} = -1.79 \cdot 10^{-3}(\sigma_{m,2})^2 + 0.94\,\sigma_{m,2} \quad (R^2 = 0.99) \qquad (4.4b)$$

These criteria clearly plot very close to the corresponding failure criteria. Any other definition of the onset of permeability, such as the dilatancy boundary, i.e. the transition from compaction to dilatation [*Alkan et al.*, 2007], would plot even closer.

4.5.2 Effect of temperature on strength and dilatation

We now address the effect of temperature on strength and dilatation. The failure criterion for 80°C shows ~10% lower shear strength than that at 20°C (cf. Figures 4.11a and b and equations 4.3a and b). This weakening may be related to deformation-independent processes, such as simply heating to 80°C as suggested by experiment HBG-43. Such an effect of temperature could potentially be caused by dehydration of gypsum, which occurs (slowly) at temperatures of 40-60°C at the conditions of our experiments [*Yamamoto and Kennedy*, 1969; *Mirwald*, 2008]. A sample of anhydrite of known mass heated to 80°C showed a mass loss of ~0.007 wt% in 24 hours, which means an absolute mass loss of ~0.015 g for one of our standard anhydrite samples (~200 g in weight). If mass loss was due to gypsum dehydration alone (i.e. water loss), this means a solid volume reduction of ~0.017 vol% (i.e. a ~10% increase of the initial, connected porosity of 0.1-0.3%). If the gypsum were mainly present in

grain boundaries, such a volume change implies the widening of grain boundaries in a manner similar to the opening of new (grain boundary) cracks, perhaps reducing the strength of the material. At the same time, released water (0.021 vol%) could have built up significant pore pressure. However, no gypsum (or other dehydration peaks) was detected by any of our analytical procedures, even TGA (resolution < 0.002 wt%). Moreover, pre-deformed and dilated samples with volume increases up to 1% did not show significant weakening compared with intact samples (HBG-22 vs. HBG-6). An alternative weakening mechanism may be one of thermally activated plasticity [*Müller and Siemes*, 1974; *Olgaard et al.*, 1995] or pre-testing annealing of dislocation structures. On the other hand, neither dehydration of gypsum nor enhanced plasticity explains the comparable or slightly higher strength observed at low confining pressure (< 5 MPa) at 80°C compared with room temperature. No systematic effect of temperature on strength of our wet ± CO_2 samples was observed, but these experiments are too few to attach significance to this.

Our dilatation data do give some further clues on the effect of temperature, however. From Figures 4.5b and c, it is evident that the amount of dilatation occurring at fixed strain is less at 80° than at room temperature. Similar observations were made for the volumetric behaviour seen in our wet ± CO_2 experiments (cf. Figures 4.8b and e and 4.9b and e). This effect of temperature on volumetric behaviour could again be related to deformation-independent processes, such as early gypsum dehydration or pre-test annealing of dislocation structures. However, dry, pre-heated sample HBG-43 showed volumetric behaviour similar to that of dry sample HBG-6 deformed directly at room temperature, suggesting that neither effect is important in controlling volumetric behaviour at 80°. The most likely alternative is that enhanced plastic flow explains the reduced dilatation observed at 80°C. Overall, then enhanced plasticity seems more the most consistent with the mechanical weakening and reduced dilatation observed with increasing temperature. However, the strengthening with temperature seen at low confining pressures (< 5 MPa) remains problematic. We conclude that we cannot explain the observed effect of temperature unambiguously at this stage.

4.5.3 Comparison with previous strength data

We now compare our strength data with results obtained in previous triaxial compression studies on anhydrite with both similar [*Müller and Siemes*, 1974] and different mineralogical [*Liang et al.*, 2007] as well as textural characteristics [*De Paola et al.*, 2009]. Materials of similar composition and structure, such as the Zechstein anhydrite studied by *Müller and Siemes* [1974] yield similar results for failure strength (see Figure 4.11a), though *Müller and Siemens* [1974] obtained higher strength at high mean stresses, perhaps due to the higher purity of their samples (> 95%). In contrast, the presence of rock salt (10-20 vol%) in the anhydrite tested by

Liang et al. [2007] reduced peak strength by more than 50% compared to our samples (~25% strength reduction in Mogi space at constant mean stress $\sigma_{m,2}$, Figure 4.11a). An increase in grain size by two orders of magnitude in the anhydrite investigated by *De Paola et al.* [2009] resulted in ~30% lowering in peak strength (10% in Mogi plot, Figure 4.11a). Furthermore, strength of foliated anhydrite depends on the compression direction, showing a ~50% reduction in peak strength going from compression normal to the foliation to compression parallel to the foliation [*De Paola et al.*, 2009].

Overall, this comparison suggests that mineralogical as well as textural characteristics significantly influence the strength of anhydrite rock. In particular, the observed trends suggest weakening by the addition of a "plastic" phase, such as halite. Relatively small quantities (< 40%) of a weaker, secondary phase may significantly affect brittle and/or semi-brittle strength [*Handy*, 1990]. In such cases, weakening occurs due to the effect of stress concentration on the rigid, load-bearing framework (i.e. anhydrite), while the weaker, minor phase supports less load as it is present in disconnected patches. A reduction in brittle failure strength is also to be expected in samples with coarse grain size, such as the anhydrite studied by *De Paola et al.* [2009]. This type of effect has been recently documented in experiments on marble [*Fredrich et al.*, 1990]. These experiments showed a clear inverse dependence of brittle and semi-brittle strength on grain size, attributed to the Hall-Petch effect [*Fredrich et al.*, 1990]. In this effect, with decreasing grain size more dislocations pile up at grain boundaries, so more stress is required to induce plastic deformation and grain boundary crack nucleation in finer grained materials. Finally, the low strength seen in foliated anhydrite compressed parallel to the foliation [*De Paola et al.*, 2009], as opposed to normal to it, is likely due to promotion of axial cracking.

In conclusion, we infer that our failure envelopes provide a good strength description for Zechstein anhydrite with typical dolomite content (10-30 wt%). Other anhydrites may have peak strength values 30 to 50% lower, failure envelopes plotting some 10-25% lower in the Mogi plot (Figure 4.11a), depending on the mineralogical composition and textural characteristics.

4.5.4 Effects and mechanisms of fluid penetration: water vs. CO_2

We have already inferred that the short-term failure strength of samples penetrated by fluid prior to failure is controlled by the principle of effective stress. This is supported by plotting our wet ± CO_2 data in the Mogi diagrams constructed for dry anhydrite (see □ and △ in Figure 4.11), using the effective Mogi mean stress, for samples showing fluid penetration prior to failure (omitting ambiguous sample HBG-40). The data nicely follow the trends set out by the dry samples, confirming that no major weakening effects of fluid-rock interaction processes, such as the reduction of crack surface energy, subcritical cracking [cf. Chapter 3 - *Hangx et al.*, 2009 (submitted)] or

reaction occurred on the time-scale of our wet experiments.

In contrast to the above strength effects, volumetric strain development in our wet and wet/CO_2 samples remained mainly unaffected by fluid penetration prior to failure (cf. Figures 4.8b, 4.9b and 4.9e). We propose that though microcracking occurs throughout the entire sample (see microstructures – Figures 4.10c and f), fluid penetration is mainly determined by cracks opening in the developing fault plane (see Figures 4.10a and d), which in turn control the strength of the material. So, while crack growth in the fault plane allows for fluid penetration, resulting in a decrease in strength, the (larger) remaining part of the sample may not be accessed by fluid due to insufficient dilatation and crack connectivity. This will lead to volumetric behaviour similar to dry samples deformed at the same absolute confining pressure, despite fluid penetration and strength reduction (Figures 4.8b, 4.9b and 4.9e).

This reasoning seems less consistent with the behaviour shown by samples penetrated by fluid ($CaSO_4$ solution) during failure, i.e. at the peak stress (samples HBG-20 and -21, Figures 4.8d, e). These samples showed both stress and volumetric strain development closely resembling that seen in dry samples at the same total pressure (Figures 4.8d, e). We suggest that this behaviour reflects a lack of time for fluid to penetrate the developing strength-controlling fault(s) before strength loss.

A final remaining issue related to mechanical behaviour and fluid penetration is the question of why samples deformed wet ± CO_2 showed semi-brittle behaviour with shear failure planes and fractures orientated at 31-38° (wet/CO_2 experiments) to 37-45° (wet experiments) compared with 26-30° seen in dry samples. This semi-brittle response may be partly due to the relatively high absolute confining pressure of 25 MPa used in these experiments, which may have established a semi-brittle damage pattern before fluid penetration, which influenced subsequent failure.

We now attempt to explain the observation that penetration by CO_2-saturated solution occurred prior to or from the start of the experiments, while $CaSO_4$ solution only penetrated prior to or at failure. This difference may reflect differences in wettability and/or viscosity between the aqueous and supercritical CO_2 phases in the pore fluid. The injection of high-pressure CO_2 (P_f = 15 MPa) significantly lowers the interfacial tension (IFT) of water to about half of the value at atmospheric pressure [*Pallas and Pethica*, 1983; *Wesch et al.*, 1997; *Chalbaud et al.*, 2006; *Chiquet et al.*, 2007]. In contrast, the viscosity of the CO_2-water mixture is hardly affected [*Bando et al.*, 2004]. Such a reduction in IFT could explain the penetration of our samples by CO_2-saturated solution but not by water, simply through a reduction in entry pressure. At the end of our wet/CO_2 experiments, the samples were wet indicating that penetration by CO_2-saturated solution had occurred. A reduction of IFT and entry pressure therefore seems the most likely explanation for easier penetration in the wet/CO_2 experiments.

4.5.5 Implications of mechanical data for seal integrity – a simple generic study of caprock flexure during depletion/injection

Our mechanical results can be used to predict the behaviour of anhydrite caprock during fluid depletion (e.g. oil and gas recovery) and injection (e.g. CO_2 storage). The Mogi failure envelope for Zechstein anhydrite under reservoir conditions is shown in Figure 4.11b, along with the boundary between the dilatant and non-dilatant stress regimes, i.e. the potentially permeable vs. "impermeable" fields (starting permeability $< 10^{-21}$ m^2). This failure/dilatancy diagram can be coupled with either analytical or finite element models to predict caprock response (e.g. failure, dilatation, permeability development) to changing stress states, as a result of reservoir depletion or injection.

In the following, we attempt to make a few simple generic calculations on the stress changes occurring in an anhydrite caprock during reservoir depletion and CO_2/fluid injection; we then assess the implications for caprock integrity. We start from the assumption that the poroelastic response of a reservoir rock to pore pressure changes [*Wang*, 2000] will typically result in an elastic deflection of the overlying caprock, generating bending stresses throughout the seal formation. The largest stresses will develop at the base and top of the formation at the point of greatest deflection, having the same magnitude but being opposite in sign (tensile vs. compressive). Computing the stress state evolution thus allows us to predict the likelihood of caprock failure (or dilatation and associated permeability development) due to caprock flexure in response to reservoir depletion or to CO_2 injection, making use of the failure envelopes and material properties obtained in our experiments.

Model for a hypothetical anhydrite seal formation

As a data source for our generic case study, we used the Dutch K12-B test site, which is located offshore in the Netherlands North Sea. The K12-B reservoir is a depleted gas reservoir overlain by Zechstein anhydrite caprock. Following geological data [*Van de Sande et al.*, 1996; *Van der Meer et al.*, 2006b], we take the sandstone reservoir and the anhydrite member at the base of the Zechstein to be 150 and 50 m thick respectively, with the reservoir-caprock interface located at a depth of ~3800 m (see Figure 4.12a). Though the K12-B reservoir is oval in plan view (5 km × 8.5 km), we consider a circular reservoir with a diameter of 10 km, and overlain by a disc-shaped plate of caprock. We assume that the caprock is homogeneous, isotropic, elastic, uniform in thickness and initially flat-lying. Our experiments indicated that the Young's Modulus of Zechstein anhydrite is ~50 GPa, which is approximately an order of magnitude larger than the caprock values used in most geo-mechanical modelling efforts (i.e. 1 to 10 GPa [*Skar and Beekman*, 2003; *Zweigel and Heill*, 2003; *Rutqvist et al.*, 2008]). As the *E* value obtained in our experiments was determined for relatively

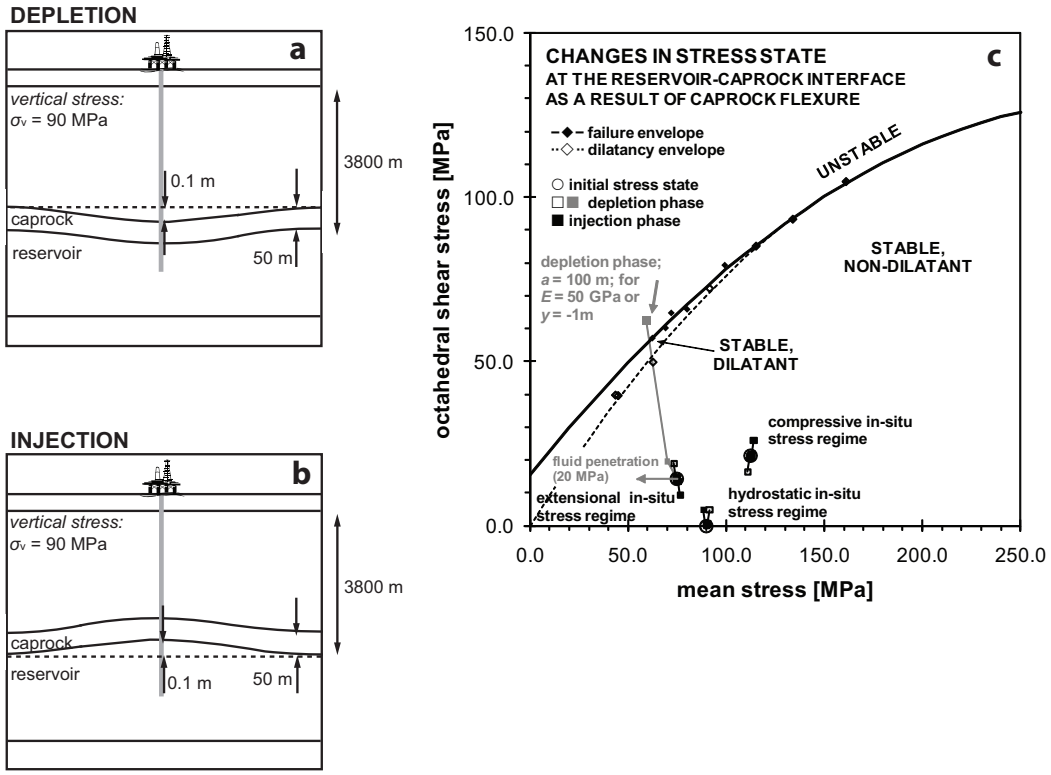

Fig. 4.12 a) Depletion and b) injection scenarios for a hypothetical, circular reservoir-caprock system, with the reservoir-caprock interface at 3800 m depth. c) Failure and dilatancy envelopes for dry anhydrite under reservoir conditions (T = 80°C) combined with calculated depletion (□, scenario a) and injection (■, scenario b) stress paths reflecting changes in stress at the base of the caprock, as a result of simple flexure of a caprock. Changes in stress state were calculated according to Case 3, described in Table 4.3, for E = 5 GPa, y = ± 10 cm, a = 100-5000 m and three different, initial, in-situ stress regimes (centre of ○), assuming no fluid penetration. If penetration does occur, e.g. through permeability development, the effective mean stress will be reduced (e.g. for P_f = 20 MPa, see arrow in the extensional stress regime). Note that under the given conditions, no permeability development or caprock failure is to be expected, either during depletion or injection, with the exception of cases of highly localised compaction/heave (see ■, for E = 50 GPa or y = -1 m, a = 100 m).

pristine samples, it may overestimate the elastic modulus for bulk material containing larger scale cracks and fractures (i.e. larger than the sample size). Therefore, we chose a lower value of 5 GPa for Young's Modulus, following the upscaling method of *Hoek and Brown* [1997]. Poisson's Ratio was taken to be 0.25, following results from *Liang et al.* [2007] and *Bell* [1981]. Furthermore, we assume the initial vertical stress (σ_v) to be equal to the overburden pressure, i.e. we took σ_v = 90 MPa at 3800 m depth for an assumed overburden density of 2500 kg/m^3. We initially assumed no fluid penetration of the caprock, and we took all stress changes in σ_1, σ_2 and σ_3 to be simply the result of caprock bending as a result of poroelastic contraction or expansion of the reservoir (see Figures 4.12a and b).

Bending stress relations and boundary conditions

There are numerous mathematical solutions for the elastic bending of beams and discs available in the literature [*Timoshenko*, 1940; *Young and Budynas*, 2002], for a range of boundary conditions. As 2-D beams and 3-D discs yield similar results, we chose to focus on the bending of 3-D discs. We calculated the changes in horizontal, in-plate stresses at the base of a caprock disc, as well as in vertical (overburden) stresses σ_v, for a variety of boundary conditions, including simple bending, simply supported uniform loading, and fixed-edge uniform loading (see Table 4.3 after *Timoshenko* [1940] and *Young and Budynas* [2002]). We investigated three different initial in-situ stress regimes, following *Rutqvist et al.* [2008]:

(1) hydrostatic, where $\sigma_v = \sigma_1 = \sigma_2 = \sigma_3$,

(2) compressive, where $\sigma_v = \sigma_3$ and $\sigma_1 = \sigma_2 = 1.5\ \sigma_3$, and

(3) extensional, where $\sigma_v = \sigma_1$ and $\sigma_3 = \sigma_2 = \sigma_1$,

taking compressive stresses as positive.

Furthermore, we performed our calculations for a series of different effective reservoir radii in the range 100 to 5000 m, taking into account that the equations shown in Table 4.3 require a minimum radius a of 2 times the caprock formation thickness t. This was done to simulate different extents of localised depletion and of CO_2 migration within the model reservoir. Caprock deflection was taken positive upwards and equal to -10 cm during fluid depletion (equivalent to ~ 0.07% strain in the reservoir centre – see Figure 4.12a), which is of the same order as for several depleted Dutch sandstone reservoirs [*Hettema et al.*, 2002]. Deflection was taken to be max. +10 cm for the case of fluid (CO_2) injection. We assumed that thermal effects of CO_2 injection are small. Furthermore, CO_2 injection pressure will be lower than the initial in-situ gas or oil pressure to prevent capillary breakthrough. This means that the caprock may move back to its original configuration prior to depletion, but will not go beyond that.

Gas and/or oil recovery – the depletion scenario

A summary of values obtained in our calculations for the depletion scenario, using the three different configurations given in Table 4.3 plus the stated reservoir and caprock properties, are shown in Table 4.4. This shows that the changes in horizontal, in-plate stress at the base of the caprock are small and similar for all loading scenarios at a given a value, roughly doubling in magnitude going from simple bending (Case 1) to the fixed-edge-configuration (Case 3). The changes in stress at the base of the caprock during depletion are tensile, while they are compressive at the top of the formation. Changes in vertical stress are smaller than the changes in horizontal stresses. We plotted the largest or worst case stress-change results, i.e. those obtained for Case

Table 4.3
Moment, deflection and bending stress formulas for flat, circular plates or discs subjected to varying boundary conditions [after *Timoshenko*, 1940; *Young and Budynas*, 2002]. Note that deflection is taken positive upward, moments are positive when creating compression in the top surface. Stresses are calculated for the top surface. Maximum bending stresses can be found using the maximum moment, through the equation $\sigma_{max} = 6M_{max}/t^2$ [Pa], while q denotes the change in vertical stress σ_v to generate deflection y. Note that the maximum stresses are generated at the top and bottom surfaces of the disc and are equal in magnitude, though opposite in sign.

Case 1. Simple bending along a spherical shape†		
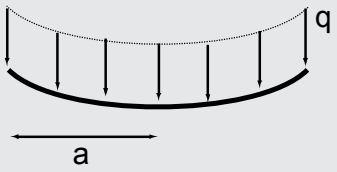	Maximum deflection	$y_{max} = \frac{-qa^4}{16D(1+\nu)}$
	Maximum moment	$M_{max} = \frac{qa^2}{8}$
Case 2. Simply supported; uniform load		
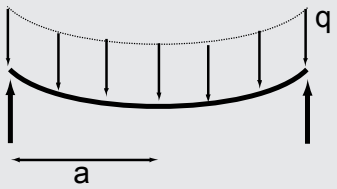	Maximum deflection	$y_{max} = \frac{-qa^4}{64D}\frac{(5+\nu)}{(1+\nu)}$
	Maximum moment	$M_{max} = \frac{qa^2}{16}(3+\nu)$
Case 3. Fixed edges; uniform load		
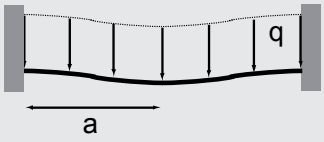	Maximum deflection	$y_{max} = \frac{-qa^4}{64D}$
	Maximum moment	$M_{max} = \frac{qa^2}{16}(1+\nu)$

Symbols: σ_{max} is the maximum bending stress [Pa], M_{max} is the maximum moment [Pa m], t is the thickness of the plate [m], D is the flexural rigidity, $Et^3/12(1-\nu^2)$ [Pa m^3], E is Young's Modulus of the material [Pa], ν is Poisson's Ratio [-], y_{max} is the maximum deflection as a result of the applied load [m], q is the uniform applied load or applied vertical stress σ_v [Pa], a is the radius of the plate [m].
† For simple bending, the stress components are constant over the surface of the plate.

3 loading, in our failure diagram for reservoir conditions (□-paths in Figure 4.12c, for E = 5 GPa, y = -10 cm, a = 100-5000m), superimposing the stress changes onto the three chosen, in-situ stress states (indicated by ○ in Figure 4.12c). Only the stresses at the base of the caprock are relevant, because this is where CO_2 penetration might occur later, possibly inducing failure. Our results show that no dilatation/permeability development or caprock failure will occur for any of the defined conditions.

Now, the computed changes in stress are linearly related to the amount of deflection and Young's Modulus. Hence, an order of magnitude increase in either will result in

Table 4.4
Changes in horizontal, in-layer stress ($\Delta\sigma_h$) and vertical stress ($\Delta\sigma_v$) components at the base of the caprock for the three configurations shown in Table 4.3. Deflection is taken to be -10 cm (i.e. simulating depletion), thickness *t* of the caprock is 50 m, Young's Modulus *E* is taken to be 5 GPa and Poisson's Ratio *v* is 0.25. Calculations are performed for various plate diameters 2*a* to examine the sensitivity to this parameter. Compression is taken to be positive so that the listed stress changes are tensile. Note that for injection, and an associated deflection of +10 cm, the same changes in stress will be generated, but opposite in sign (i.e. compressive).

plate diameter, *2a* [m]	**Case 1. simple bending [MPa]**		**Case 2. supported, uniform load [MPa]**		**Case 3. fixed, uniform load [MPa]**	
	$\Delta\sigma_h$	$\Delta\sigma_v$	$\Delta\sigma_h$	$\Delta\sigma_v$	$\Delta\sigma_h$	$\Delta\sigma_v$
200	-3.33	1.11	-4.13	0.85	-6.67	3.56
500	-0.53	0.028	-0.66	0.021	-1.07	0.09
1000	-0.13	0.0018	-0.17	0.0014	-0.27	0.0057
5000	-0.005	0.000003	-0.007	0.000002	-0.01	0.000009
10000	-0.001	0.0000002	-0.002	0.0000001	-0.003	0.000001

an order of magnitude increase in the change in stress components. This magnitude of variability would imply that the stress state in the caprock can approach failure, but only in the case where,

(a) Young's Modulus *E* is 50 GPa and *a* is approaching 100 m, or

(b) deflection *y* is -1 m and *a* is approaching 100 m,

and for the extensional in-situ stress regime (see the ■-path in Figure 4.12c). Even if in such cases failure does not quite occur, the base of the caprock may become sufficiently permeable to allow penetration of residual formation fluids. Concomitant lowering of the effective state of stress (i.e. reduction of the effective mean stress, as shown by the horizontal arrow in Figure 4.12c) may then promote shear failure, resulting in the creation of permeable pathways for leakage. However, such scenarios (i.e. a and b above) can be realised only by highly localised compaction of the reservoir, leading to localised bending of the caprock, and are unrealistically extreme. To our knowledge, such extreme reservoir-caprock deformations have never been recorded. For realistic values of *E*, deflection and effective reservoir radius, and recognising that we have our calculations on the worst case stress-change formula (Case 3, Table 4.4), it can therefore be safely inferred that the caprock will remain intact and impermeable ($< 10^{-21}$ m^2) during depletion. Even allowing for a reduction in strength of anhydrite caprock in the Mogi plot (Figure 4.12c) of 10-25%, due to compositional or microstructural factors discussed in Section 4.3, this remains the case.

CO_2 storage – the injection scenario

Fluid injection, and the concomitant uplift or reservoir heave, here taken to be max. + 10 cm (Figure 4.12b), results in predicted stress changes at the base of the caprock that are identical to those of the depletion case - but opposite in sign. In case of fluid injection into a pre-depleted reservoir, such as for a depleted gas or oil reservoir used for CO_2 storage, the resulting injection stress paths will move backwards along the depletion stress paths shown in Figure 4.12c (□), progressing towards the initial stress state. This assumes that depletion does not damage the caprock, as demonstrated above for realistic reservoir dimensions, so that E remains unchanged and no CO_2 penetrates. If CO_2 were to penetrate in any way (chemical or physical), the reduction in effective stress would still not lead to failure during injection (e.g. for P_f = 20 MPa, see the arrow indicated for the extensional in-situ stress regime, Figure 4.12c).

A slightly different scenario is expected for CO_2 injection into an anhydrite-topped aquifer, which can be considered to be comparable to a reservoir with no depletion phase. In this case, injection stress paths for the base of the caprock (see ■-paths in Figure 4.12c) remain distant from the failure and dilatancy envelopes, for our chosen values of y = +10 cm, E = 5 GPa and a = 100-5000 m, assuming a similar change in pore fluid pressure. However, though the stress state at the base of the aquifer caprock will not approach the failure envelope, the opposite may be true for the top, which will see a stress evolution following that indicated for the base of the caprock in the depletion phase (i.e. negative stress changes – see □-paths in Figure 4.12c). During CO_2 injection into an aquifer, in the extreme case of localised doming combined with large uplift (e.g. $a \rightarrow$ 100 m, uplift $\rightarrow$ 1 m), extensional failure of the top of the caprock may occur (see ■-path, Figure 4.12c), possibly leading to weakening of the caprock and aiding the creation of leakage pathways.

Despite this extreme case, our calculations show that for realistic conditions neither caprock failure nor dilatation/permeability development will occur during CO_2 injection into depleted reservoirs or aquifers as a result of changing stress state. Since predicted stress changes are small, this conclusion is unaffected by typical variations in anhydrite caprock composition and microstructure (cf. Figures 4.11b and 4.12c). Seepage of CO_2 through the base of the seal formation into interbedded, permeable carbonate beds, leading to lateral migration of CO_2, can therefore be ruled out for most practical purposes. However, to minimise risks, both injection and depletion rates should be chosen such that very localised reservoir heave or compaction (100 m-radius, > 10 cm amplitude) will not take place.

4.5.6 Possible long-term effects of reaction with supercritical CO_2 and water

While we have found no evidence for short-term weakening of anhydrite caprock through processes related to surface energy or subcritical (stress corrosion) cracking,

water-saturated CO_2 residing at the reservoir-caprock interface within a geological CO_2 storage system might react with the caprock minerals in the longer term. This could affect the porosity, permeability and mechanical properties of the seal formation. In particular, at sufficiently high CO_2 pressure, it is expected from natural analogue studies that reaction of anhydrite with CO_2 and water will occur as follows [*Pearce et al.*, 1996]

$$CaSO_4 + CO_2 + H_2O \rightarrow CaCO_3 + H_2SO_4 \qquad (4.5)$$

resulting in a 20% volume decrease in the solid phases. To establish if this reaction occurs at reservoir conditions, we performed a small number of preliminary reaction experiments under hydrostatic conditions using conventional, cold-seal reaction vessels. These showed that reaction (4.5) can occur at rates up to roughly ~10^{-8} mol/m^2 s under typical in-situ conditions (T = 80°C, P_{CO2} = 15 MPa). This may lead to caprock dissolution and porosity increase near injection wells with precipitation of secondary phases taking place either locally or in the further field of the reservoir. The likely effects are hard to predict, but could lead to either degradation or improvement of caprock properties, depending on the location of precipitation. The nature and suggested rate for reaction (4.5) imply that for simple CO_2 penetration by reaction with a static pore fluid (no long-range advective transport), the resulting penetration depth would be approximately 30 cm in 1000 years and ~3 m in 10000 years. For an anhydrite formation of 50 m thick, such as the Zechstein [*Van de Sande et al.*, 1996], this amounts to 0.6-6% penetration. In practice, this represents an upper bound, as the reaction will undoubtedly slow down as the reaction front advances into the anhydrite. Significant chemical degradation effects are therefore not expected, though further work on this, and on the penetration of anhydrite by water-saturated CO_2, is desirable.

4.6 Conclusions

In this study, we aimed to determine the effect of water and CO_2 on the mechanical strength and damage behaviour of anhydrite and to assess the implications for CO_2 storage in (depleted) reservoirs capped by anhydrite. To this end, we performed conventional triaxial compression experiments on anhydrite taken from the base of the Dutch Zechstein, under dry, water-wet and wet/CO_2 conditions at 20 and 80°C, and confining pressures of 1.5 to 50 MPa. Our main findings can be summarised as follows:

1. For dry anhydrite samples, in the confining pressure range of 1.5 to 50 MPa, we observed a transition from brittle to semi-brittle behaviour, an increase in

peak stress with increasing confining pressure and a slight weakening with increasing temperature.

2. The failure behaviour of dry Zechstein anhydrite can be accurately described by empirical Mogi criteria. At 20°C the criterion is given $\tau_{oct} = -2.44 \cdot 10^{-3}(\sigma_{m,2})^2 + 1.06\,\sigma_{m,2} - 0.32$, while at 80°C it is given as $\tau_{oct} = -1.23 \cdot 10^{-3}(\sigma_{m,2})^2 + 0.75\,\sigma_{m,2} + 15.29$. Similarly, the onset of dilatancy and permeability development in dry anhydrite can be described by the functions: $\tau_{oct} = -1.71 \cdot 10^{-3}(\sigma_{m,2})^2 + 0.93\,\sigma_{m,2}$ at room temperature and $\tau_{oct} = -1.79 \cdot 10^{-3}(\sigma_{m,2})^2 + 0.94\,\sigma_{m,2}$ at 80°C.
3. Fluid penetration prior to failure resulted in a reduction in failure strength of our wet ± CO_2 samples according to the effective stress principle, while the volumetric behaviour remained unchanged compared with dry samples. On the timescale of the experiments (~5h), no chemical effects of $CaSO_4$ solution or of CO_2-saturated fluid on the mechanical strength or dilatation of anhydrite were observed. Fluid penetration during failure appears to be too slow to influence mechanical response. Samples tested in the presence of pore fluid generally showed semi-brittle behaviour and shallow fracture orientation (~35-45°), probably established before fluid penetration.
4. CO_2-saturated solution appears to be able to penetrate Zechstein anhydrite with more ease than $CaSO_4$ solution. This can be explained by the lower interfacial tension of the former.
5. The mechanical data (failure and dilatancy envelopes) obtained for Zechstein anhydrite can be used together with geomechanical modelling to predict caprock response to changing stress states, as a result of fluid depletion or CO_2 injection. For a hypothetical circular reservoir-caprock system, simple analytical calculations have shown that changes in stress state, resulting from caprock deflection associated with reservoir compaction and heave (± 10 cm), are small and will not lead to dilatational damage, permeability development or failure at the base of such as caprock formation. The risk of caprock integrity being compromised by mechanical damage is therefore exceedingly low.
6. The long-term mechanical behaviour and transport properties of anhydrite rock can potentially be affected by reaction with CO_2, as dissolution of anhydrite and precipitation of carbonates results in a 20% solid volume decrease. This may affect caprock porosity depending on the sites of dissolution and precipitation (near injection wells or in the further field). For simple CO_2 penetration of the seal formation by reaction without long-range advective transport of the pore fluid, penetration depths of ~30 cm in 1000 years and ~3 m in 10000 years may be reached. This is insignificant for typical anhydrite caprock thicknesses (e.g. 30-50 m in the Netherlands), but further work is needed for better quantitative

underpinning.

Acknowledgements

This research was funded by Shell International Exploration and Production and performed within WorkPackage 4.1 (Subsurface mineralisation) of the Dutch national research project CATO, CO_2 capture, transport and storage. Conxita Taberner (Shell International Exploration Production) and Jan Penninga (Nederlandse Aardolie Maatschappij BV.) are thanked for supplying the sample material. We thank Eimert de Graaff, Gert Kastelein, and Peter van Krieken for technical assistance.

5

The effect of deformation on permeability development in anhydrite and implications for caprock integrity during geological storage of CO_2

S.J.T. Hangx, C.J. Spiers and C.J. Peach

Abstract

Geological storage of CO_2 in depleted oil and gas reservoirs is one of the most promising options for reducing emissions of CO_2 to the atmosphere. Of great importance to CO_2 mitigation strategies is maintaining caprock integrity. Worldwide many current injection sites and potential storage sites are overlain by anhydrite-bearing seal formations. However, little is known about the magnitude of the permeability change accompanying dilatation and failure of anhydrite under reservoir conditions. To this extent, we have performed triaxial compression experiments together with argon gas permeability measurements on Zechstein anhydrite, which caps many potential CO_2 storage sites in the Netherlands. Our experiments were performed at room temperature at effective confining pressures of 3.5 to 25 MPa. We observed a transition from brittle to semi-brittle behaviour over the experimental range, and peak strength could be described by a Mogi-type failure envelope. Dynamic permeability measurements showed a change from "impermeable" to permeable as a result of mechanical damage. The onset of measurable permeability was associated with an increase in the rate of dilatation at low pressures (3.5-5 MPa), and with the turning point from compaction to dilatation in the volumetric vs. axial strain curve at higher pressures (10-25 MPa). Sample permeability was largely controlled by the permeability of the shear faults developed. Static, post-failure permeability decreased with increasing effective mean stress. Our results demonstrated that caprock integrity will not be compromised by mechanical damage and permeability development.

5.1 Introduction

Depleted oil and gas reservoirs offer one of the most easily and cheaply implemented options for geological storage of CO_2 [*Baines and Worden*, 2004a; *Schrag*, 2007]. As CO_2 mineralisation reactions are slow and the mineralisation potential of most reservoirs is low [*Xu et al.*, 2004; *Zerai et al.*, 2006], stored CO_2 will mainly be present in the supercritical fluid phase and dissolved in the formation fluid [*Baines and Worden*, 2004b; *Gilfillan et al.*, 2009]. Long-term top-seal or caprock integrity is therefore pre-requisite for guaranteeing the performance of depleted reservoir storage systems.

Fluid-rock interaction, i.e. chemical attack, may affect caprock integrity in the long term. However, such effects alone are so slow that they are unlikely to be significant for typical shale, mudstone or anhydrite caprock compositions and thicknesses [*Baines and Worden*, 2004b; *Johnson et al.*, 2004; *Okamoto et al.*, 2004; *Hangx et al.*, 2009 (submitted) - see Chapter 4]. Probably more important is mechanical damage is the form of dilatation, fracturing, shear failure and associated permeability development [*Rutqvist and Tsang*, 2002; *Streit and Hillis*, 2004; *Hawkes et al.*, 2005; *Rutqvist et al.*, 2007; *Rutqvist et al.*, 2008; *Soltanzadeh and Hawkes*, 2008]. Damage phenomena of this type can potentially be caused by caprock deformation and the associated stress changes accompanying localised reservoir compaction during depletion, or localised heave during CO_2 injection [*Hangx et al.*, 2009 (submitted) - see Chapters 2 and 4].

One of the most widespread caprocks sealing hydrocarbon reservoirs and potential CO_2 storage sites around the world is anhydrite rock [*Li et al.*, 2005; *Chiaramonte et al.*, 2007; *Bennion and Bachu*, 2008]. In the Netherlands and North Sea, for example, many potential storage sites are overlain by the basal anhydrite of the Permian Zechstein evaporate sequence [*Van de Sande et al.*, 1996; *Van der Meer et al.*, 2006]. There is accordingly much interest in quantifying damage development in anhydrite. Recent work by *Hangx et al.* [2009 (submitted) - Chapter 4] has delineated the stress conditions under which anhydrite rock is mechanically stable, versus the conditions under which dilatant damage and failure occur, in terms of Mogi-type failure and dilatation criteria. However, the magnitude of the permeability change accompanying dilatation and failure of anhydrite under reservoir conditions remains unknown.

The present study aimed to determine the effect of stress and deformation on the permeability of Zechstein anhydrite under conditions ranging from mechanically stable (intact, non-dilatant), through dilatant conditions, (semi-brittle) failure and into the post-failure stage. To achieve this, conventional triaxial (i.e. axi-symmetric) compression experiments were performed at room temperature, confining pressures (P_c) of 3.5-25 MPa and strain rates of $\sim 10^{-6}$-10^{-7} s^{-1}, simultaneously measuring the permeability of the material to argon gas using transient pulse permeametry (P_p = 1-1.2 MPa). Our approach enabled us to complement our previous failure and dilatancy

envelopes for dry anhydrite [*Hangx et al.*, 2009 (submitted) - see Chapter 4] with permeability data, as well as providing data on the effect of stress state, notably mean stress, on gouge-filled fault permeability in anhydrite caprock.

5.2 Experimental methods

Two types of transient argon gas permeametry experiments, following the terminology of *Peach* [1991] and *Peach and Spiers* [1996], were carried out in combination with our triaxial tests on the Zechstein anhydrite:

(1) Dynamic experiments. These continuous, pressure-step-decay tests aimed to determine the relationship between dilatation and permeability development in deforming anhydrite loaded through failure.

(2) Static experiments. The second set consisted of conventional, transient pulse experiments carried out to investigate the effect of mean stress on post-failure (fault) permeability under conditions of zero further displacement.

Four deformation experiments were carried out in all (Table 5.1), with both dynamic and static permeability tests being conducted in each case. All experiments were performed at room temperature.

Table 5.1.
Conventional triaxial compression and permeability experiments performed on dry Zechstein anhydrite at 20°C, plus key parameters obtained in the present study.

experiment	P_c	P_p	P_c^{eff}	$(\sigma_1 - \sigma_3)_{max}$	e	E	κ_d	κ_h
	[MPa]	[MPa]	[MPa]	[MPa]	[%]	[GPa]	[m²]	[m²]
HBG-47b	3.5	1.2	2.3	127.6	0.66	15.4	$8.2 \cdot 10^{-17}$	$1.2 \cdot 10^{-16}$
HBG-50b	5.0	1.2	3.8	109.1	1.07	13.4	$2.8 \cdot 10^{-16}$	$2.7 \cdot 10^{-16}$
HBG-54a	10.0	1.0	9.0	121.1	1.82	21.0	$1.3 \cdot 10^{-17}$	$9.6 \cdot 10^{-18}$
HBG-54a*	25.0	1.0	24.0	-	-	-	-	$5.1 \cdot 10^{-18}$
HBG-54a*	50.0	1.0	49.0	-	-	-	-	$2.2 \cdot 10^{-18}$
HBG-50a	25.0	1.0	24.0	188.2	2.41	26.1	$1.0 \cdot 10^{-18}$	$4.3 \cdot 10^{-19}$

Symbols: P_c is the applied confining pressure [MPa]; P_p is the mean argon pore pressure applied to the sample [MPa]; P_c^{eff} is the effective confining pressure [MPa]; $(\sigma_1 - \sigma_3)_{max}$ is the peak differential stress [MPa]; E is the Young's Modulus obtained from a fit to the linear elastic part of the stress-strain curve [GPa]; e is the axial strain at failure [%]; κ_d is the static post-failure permeability [m²], measured before removal of the residual differential stress, while κ_h [m²] is the static value measured under hydrostatic pressure after complete unloading.
* Static permeability measurements performed on sample HBG-54a* after failure at the pressures shown.

5.2.1 Samples

As in our previous work [*Hangx et al.*, 2009 (submitted) - Chapter 4], the anhydrite rock used in the present experiments was obtained from core retrieved from the Hardenberg-5 well, Hardenberg, the Netherlands, courtesy of Shell International Exploration and Production (SIEP) and the Nederlandse Aardolie Maatschappij BV (NAM). The retrieval depth of the material used varied from 3209 to 3212 m depth, corresponding to the base of the Permian Zechstein formation (Zechstein 1 Anhydrite Member). Cylindrical plugs (~80 mm in length by 35 mm in diameter) were drilled from the core and then cut in half to obtain samples of ~40 mm in length. Finally, the ends were ground and polished, square and parallel, to a final length of ~37 mm. The relatively low aspect ratio of the samples was chosen to be sure that faults would traverse the whole sample lengths enabling meaningful permeametry.

As described by *Hangx et al.* [2009 (submitted) - Chapter 4], the prepared samples were greyish-white to grey in colour and appeared mostly quite homogeneous at the sample scale. Around 60 vol% of the material was made up of millimetre-sized, acicular anhydrite rosettes embedded in a fine, crystalline matrix. Some samples contained darker grey patches or bands of fine-grained material (bedding) at an angle of up to 60° to the sample axis. Thermogravimetric Analysis (TGA) plus Fourier Transform Infrared (FTIR) spectroscopy showed that besides anhydrite the samples contained between 10 and 33 wt% carbonate, mainly dolomite. Thin section analysis indicated that this was present as a fine-grained, matrix phase in the bands defining the bedding. The connected porosity of the intact samples varied from 0.1 to 0.3 %, while the permeability was unmeasurable, i.e. less than 10^{-21} m^2. Sample density varied between 2900 and 2960 kg/m^3.

5.2.2 Experimental apparatus

We performed the present experiments using the Heard triaxial machine described by *Hangx et al.* [2009 (submitted) - Chapter 4] linked to a transient pulse permeameter [see *Peach*, 1991; *Peach and Spiers*, 1996]. The triaxial machine consists of a furnace-clad pressure vessel, containing the sample plus silicone oil confining medium, connected to an auxiliary pressure vessel (Figure 5.1). Load is applied to the sample by advancing a yoke/piston assembly, driven by a motor/gearbox/ball-screw system. This displaces confining fluid from the main vessel to the auxiliary vessel, keeping system volume nominally constant. Viton O-rings are used in all dynamic and static seals. Axial load on the sample is measured using a semi-internal cell (400 kN range, resolution ± 0.035 kN) located at the top of the vessel [*Hangx et al.*, 2009 (submitted) - see Chapter 4]. Piston displacement is measured at the yoke using a linear variable differential transformer (LVDT, 100 mm range, resolution ± 0.8 μm). Sample volume changes are measured (resolution ± 20 μl) using a servo-controlled volumometric

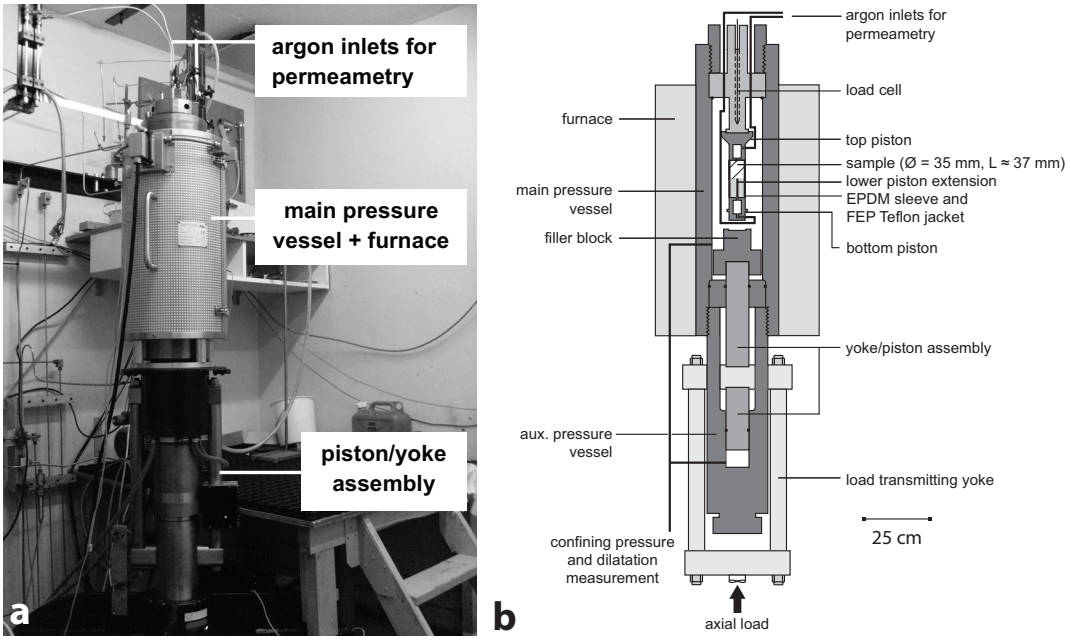

Fig. 5.1 Overview of the experimental set-up. a) The conventional triaxial apparatus used in our experiments, consisting of the main pressure vessel and a yoke/piston assembly. The permeametry set-up is connected via the fluid inlets at the top of the machine. b) Schematic diagram showing the internal details of the apparatus.

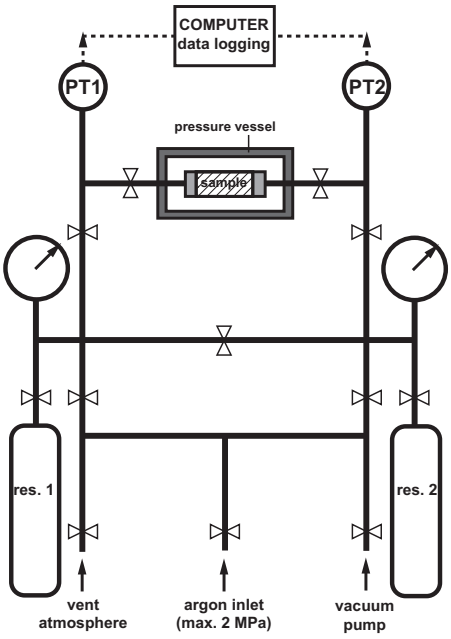

Fig. 5.2 Schematic diagram of the argon gas, transient-pulse, permeametry set-up used in combination with the triaxial compression apparatus shown in Figure 5.1.

pump set to maintain constant confining pressure. Confining pressure is measured using a Jensen pressure transducer (100 MPa range, accuracy ± 0.01 MPa, precision ± 0.005 MPa). Temperature can be controlled using a process controller (400°C range, accuracy ± 0.1 °C, precision ± 0.02 °C), plus K-type thermocouple located in the windings of the furnace. Sample temperature is measured midway along the sample using two K-type thermocouples, entering the main vessel through a port in the load cell. Pore fluid, i.e. argon in this study, is introduced into the sample through stainless steel tubes, connected to inlets at the top and bottom ends of the sample (see Figure 5.1).

Sample permeability was measured using a modified version of the argon gas permeametry set-up described by *Peach* [1991] and *Peach and Spiers* [1996] (see Figures 5.1 and 5.2). In essence, the permeameter consists of two symmetrical, low-volume tube/valve systems

that can be independently pressurised with argon at pressures up to 2 MPa, and connected together across the sample. The two halves can also be connected through a linking valve, allowing for pressure equilibration of the whole system before making a permeability determination. Measurements are then initiated by closing this linking valve and dropping the argon pressure in one half of the system by a pre-determined amount. For high permeability measurements (> 10^{-15} m^2), two additional large reservoirs, each with a volume of 2.8 l, can be used to supply the system with sufficient volumes of argon. The system can be evacuated using a vacuum pump attached to one of the vents in the system (Figure 5.2). A second vent (to the atmosphere) is used to purge the system, and to initiate experiments by reducing the gas pressure on one side of the sample. A third vent is attached to a regulated argon supply (99.9% pure) for charging the system. Though all fittings are tight, a background leak rate exists, equivalent to a system permeability of approximately ~$1 \cdot 10^{-21}$ m^{-2}. Argon pressure at the upstream and downstream ends of the sample is measured using two temperature-compensated pressure transducers (2 MPa range, resolution ± 0.02 MPa).

5.2.3 Sample assembly

We used the sample assembly described in our previous experiments on anhydrite samples of 75 mm length by 35 mm diameter [*Hangx et al.*, 2009 (submitted) - Chapter 4], compensating for the shorter length of the present samples (~37 mm) by inserting an extension to the lower sample piston (Figure 5.1b). The upper and (extended) lower pistons, contain a central bore, and are faced with radial and circumferential grooves to distribute pore fluid over the ends of the sample (Figure 5.3a). To reduce piston/sample friction and facilitate free flow of gas during the experiments, perforated Teflon sheets of 50 μm thickness were placed between each piston and the sample. The sample, plus the extended part of the lower piston, were jacketed using an EPDM (ethylene propylene diene monomer rubber) inner sleeve, 75 mm in length. This entire assembly was in turn jacketed by a larger, FEP (fluorinated ethylene propylene) outer sleeve, sealed against the upper and lower pistons using a wire tournique and underlying EPDM band countersunk in the piston surface. The EPDM sleeve was included to reduce the risk of outer jacket rupture during sample failure.

5.2.4 Experimental procedure

After sealing, the sample assembly was located in the Heard triaxial vessel, the appropriate confining pressure applied, and the system left to equilibrate at room temperature for ~3 hours. After this period, the permeametry system was evacuated, flushed and subsequently filled with argon at a set pressure of 1.5 MPa, making sure that the argon pressure was always less than the confining pressure. Appropriate

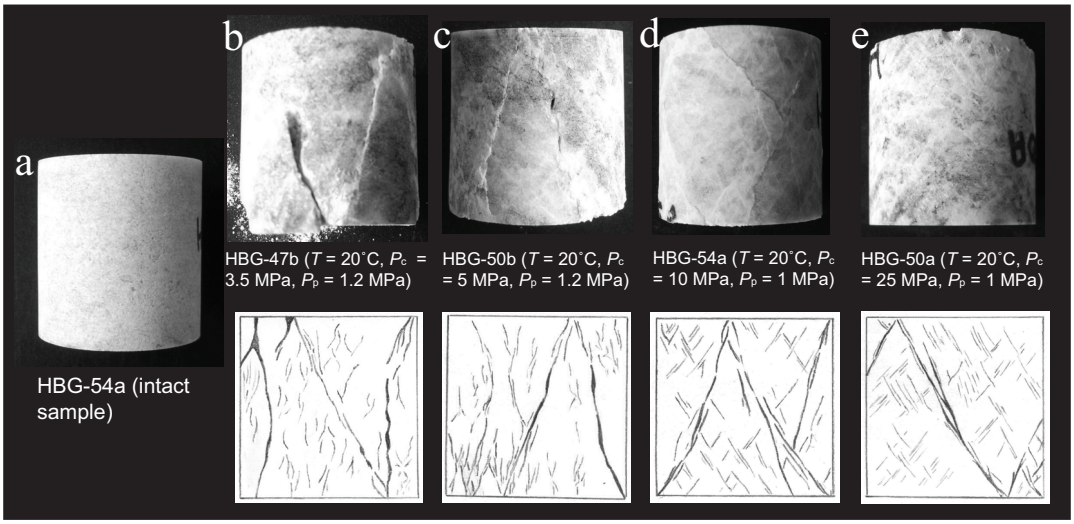

Fig. 5.3 Illustrations of undeformed and deformed anhydrite samples. a) Photograph of an undeformed anhydrite sample HBG-54a. b-e) Photographs and corresponding sketches of the macroscopic post-failure structures of samples deformed dry at 20°C and 3.5-25 MPa (P_p = 1-1.2 MPa). Sketches are presented as the main features (shear fractures, axial cracks) are not visible in images of the cut samples. Note that the length:diameter ratio of our samples is ~1:1, which may have influenced fracture orientation. T denotes temperature, P_c is confining pressure and P_p is pore pressure.

volumetric segments of the two halves of the permeametry system (V1 = 71.1 ml, V2 = 70.7 ml) were chosen to ensure large back-up volumes of argon, compared to the expected sample pore volume, while allowing easily measurable pressure changes to occur in a reasonable time (~10 h). The volumes used included the sample assembly, the sample connection tubes and the pressure transducers (refer Figure 5.2). The very low porosity and permeability of the intact samples (φ = 0.1-0.3%, $\kappa < 10^{-21}$ m^2) did not allow pressure equilibration with the sample to be measured reliably (permeability resolution ~10^{-21} m^2). It was therefore assumed that equilibrium was established when the upstream and downstream pressures remained constant beyond 1 h.

After equilibration of the entire experimental set-up, the sample assembly was isolated from the argon permeametry system, using the nearest set of valves, and the argon pressure was lowered by 0.5 to 1 MPa in one half of the system. Both deformation and (continuous) transient permeametry were then started by opening the argon valves to the sample and advancing the yoke/piston assembly at a constant rate. Subsequent deformation and argon pressure changes were then measured as a function of time, along with the evolving axial stress and sample volume change. Deformation was imposed in two stages at different strain rates. As dilatation and measurable permeability development generally did not occur until axial stresses ~80% of the peak differential stress were reached, initial loading was carried out at a strain rate of ~$1 \cdot 10^{-6}$ s^{-1}, up to approximately 50% of the expected peak stress - as estimated from our previous study on Zechstein anhydrite [*Hangx et al.*, 2009 (submitted) - Chapter 4]. This was followed by a second stage of deformation at a strain rate ~$1 \cdot 10^{-7}$

s^{-1}, which allowed sufficient time for meaningful monitoring the decay of the argon pressure gradient across the sample, as deformation progressed.

After failure of the samples (i.e. strength loss) at the strain rate of ~10^{-7} s^{-1}, deformation was stopped by halting the yoke/piston assembly and the stress supported by the sample monitored with time. While the sample remained under residual load, the initial argon pressure gradient was re-applied, and a static, transient pulse permeability measurement was made on the faulted sample. The sample was then fully unloaded by retracting the yoke/piston assembly, the initial argon pressure gradient was again applied, and a transient pulse permeability measurement was made under hydrostatic pressure conditions, i.e. at the confining pressure of the deformation test. In one case (experiment HBG-54a), post-failure permeability measurements were made at a series of confining pressures (Table 5.1). Finally, both the argon gas pressure and the confining pressure were vented, the samples were removed from the vessel, and the outer and inner sleeves were carefully cut off. The samples were then vacuum-impregnated with epoxy resin prior to sectioning.

5.2.5 Data acquisition and processing

Throughout the experiments, the internal axial load, piston displacement, confining pressure, sample temperature and system volume change signals were logged at time intervals of 10 s, using a PC equipped with a 12-bit National Instruments VI Logger system. The raw data were processed to yield differential stress ($\sigma_1 - \sigma_3$), axial strain (e), axial strain rate ($\dot{\varepsilon}$) and volumetric strain (e_{vol}) data as functions of time. Both the displacement and volume change data were corrected for apparatus distortion, using pre-determined polynomial stiffness calibrations. A separate 16-bit, Keller READ30 system logged the pressure and temperature recorded by both argon pressure transducers, on the same time base as the triaxial compression data.

Bulk sample permeability was calculated assuming that gas flow obeyed Darcy's law, given as

$$Q = \frac{-\kappa}{\mu} A \frac{dP}{dL} \tag{5.1}$$

where, Q is the volume flow rate per unit area [m^3/s], κ is the permeability [m^2] of the sample, μ is the dynamic viscosity of argon at test conditions [Pa s], A is the specimen cross sectional area [m^2], and dP/dL represents argon pressure gradient [Pa/m]. Assuming negligible sample porosity (~ 1 ml), compared with the up- and downstream apparatus (reservoir) volumes (~70 ml), and assuming constant sample permeability, Darcy's law implies that the decay of a transient pressure step imposed across a sample with time follows an exponential form expressed as

$$\Delta P_t = \Delta P_0 \, e^{-\alpha t} \tag{5.2a}$$

$$\text{with } \alpha = \frac{\kappa A}{\mu \beta L}\left[\frac{V_1 + V_2}{V_1 V_2}\right] \tag{5.2b}$$

as shown by *Sutherland and Cave* [1980]. Here, ΔP_0 is the initially imposed pressure difference at time $t = 0$, ΔP_t is the pressure difference at elapsed time t, V_1 is the volume of the upstream reservoir 1 [m^3], V_2 is the volume of the downstream reservoir [m^3] and β is the isothermal compressibility of the argon [Pa^{-1}]. The physical properties of argon, i.e. μ and β, were calculated using the M.I.T. Equation of State for argon [*Cook*, 1961]. Static permeability was calculated by performing linear regression fits to the pressure difference vs. time data expressed in the form, ln ΔP_t vs. t, with the slope of this fit yielding α (equation 5.2, Figure 5.4). Dynamic permeability was calculated by performing linear regression fits to the pressure difference vs. time data (Figure 5.4), using a moving pressure-difference interval. This was chosen such that the error in permeability was always less than ± 5%. Permeability changes were generally slow at a strain rate of 10^{-7} s^{-1}. Moreover, no pore filling effects were observed, thus validating the method for dynamic determinations.

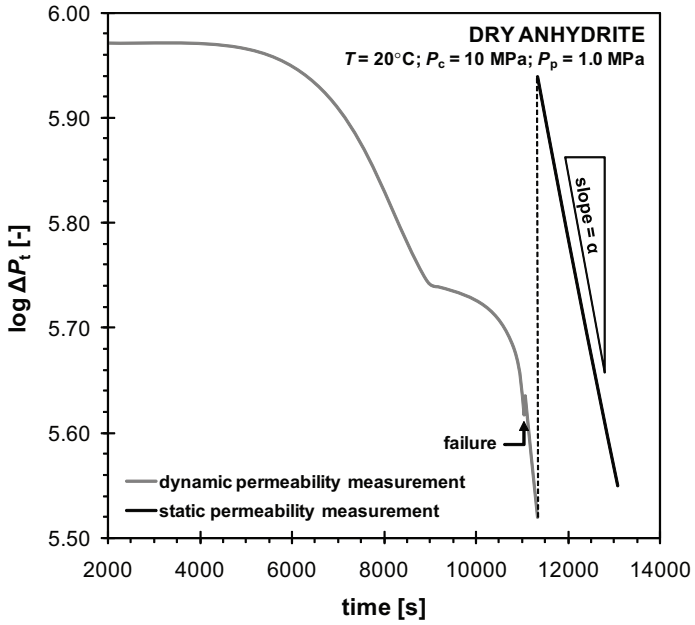

Fig. 5.4 Log pressure difference vs. time plot for a static (black curve) and a dynamic (grey curve) permeability measurement (HBG-54a, P_c = 10 MPa, P_p = 1 MPa). The slope of a linear regression fit to portions of these curves yields α in equation (5.2), which in turn depends on permeability. For the dynamic permeability calculations, we performed multiple linear regression fits using a moving pressure difference interval, chosen such that the error in calculated permeability was always less than 5%. *T* denotes temperature, P_c is confining pressure and P_p is pore pressure.

5.3 Results

In this paper, we adopt the convention that compressive stresses, compressive axial strains and dilatant volumetric strains (dilatation) are measured positive. The principal compressive stresses are denoted σ_i, with $\sigma_1 > \sigma_2 = \sigma_3 = P_c$, where P_c is the confining pressure. Principal effective stresses recorded in our test are accordingly denoted σ_i^{eff}, and are defined as $\sigma_i^{eff} = \sigma_i - P_p$, where P_p is the applied mean argon pressure [MPa]. In describing our results, we quote applied confining pressures rather than effective confining pressures ($P_c^{eff} = P_c - P_p$), as argon does not always penetrate the samples at the same stage of deformation. However, mean argon pressures, $P_p = ½(P_{upstream} - P_{downstream})$, were only 1.0-1.2 MPa, so that the uncertainty in effective pressure experienced by a given sample is a maximum only + 1.0 to + 1.2 MPa, i.e. the effective confining pressure never departs from the applied confining pressure by more than 1.0-1.2 MPa.

We further define peak strength as the maximum differential stress $(\sigma_1 - \sigma_3)_{max}$ supported by a given sample and failure as the loss of strength of the material beyond the peak, either through catastrophic brittle fracturing or more gradual strain softening. We define sample yield strength (σ_y) as the differential stress at which the differential stress-strain curve deviates from linearity, following *Fredrich et al.* [1989]. The apparent Young's Modulus (E) of individual samples was determined from the linear portion of the stress-strain curves [*Wong et al.*, 1997]. The onset of dilatancy was defined as the differential stress at which the volumetric vs. axial strain curve deviates from linearity [*Scholz and Kranz*, 1974; *Zoback and Byerlee*, 1975a; *Baud et al.*, 2000]. The experiments performed and key mechanical and permeability data obtained for our samples are shown in Table 5.1.

5.3.1 Mechanical data and sample failure modes

Typical differential stress and volumetric strain vs. time curves are plotted in Figure 5.5 for two experiments performed at 3.5 and 10 MPa confining pressure. Note that the knee in the curves at 1000-2000 s (× in Figure 5.5) is caused by the change in imposed strain rate from ~ 10^{-6} s^{-1} to ~ 10^{-7} s^{-1}. Differential stress and volumetric strain vs. axial strain data for all samples are shown in Figure 5.6, combining data obtained in both strain rate stages. The step down in strain rate does not appear to affect the stress-strain curve strongly (Figure 5.6a), though initial compaction is enhanced in the samples deformed at 10 and 25 MPa confining pressure (Figure 5.6b). In all samples, deformation is marked by a gradual non-linear increase in differential stress with axial strain, followed by a steeper linear increase, ultimately giving way to yielding and strain hardening towards a peak stress (Figure 5.6a). This is followed by abrupt failure or more gradual strain softening. Overall, two deformation regimes can be distinguished: a brittle regime up to 5 MPa confining pressure and a semi-brittle

regime above 5 MPa.

At low confining pressure (3.5-5 MPa – brittle regime), the stress-strain data show minor yielding prior to brittle failure at the peak differential stress (Figure 5.6a). Some residual strength is supported by the samples at ~3% axial strain. The volumetric strain vs. axial strain data (Figure 5.6b) show net dilatation (positive volume change) throughout more or less the entire deformation test. At higher confining pressure (P_c = 10-25 MPa) samples show more gradual yield, and more gradual strain softening after attaining the peak differential stress, indicative of semi-brittle behaviour (see Figure 5.6a). A residual strength is maintained after failure, at 3-4% axial strain. Volumetric behaviour is characterised by an initial stage of net compaction, followed by dilatation at higher axial strains (> 1% - see Figure 5.6b). In all experiments, volumetric strain increases almost linearly with axial strain during the yielding stage (see Figure 5.6b). Upon macroscopic examination, samples deformed at the lower effective pressures (3.5-5 MPa) showed cohesive, conjugate shear fractures developed at angles of ~10-30° to the compression direction and fine axial cracks. At higher confining pressure, samples displayed a more distributed network of cohesive, conjugate shear fractures and finer shear cracks/planes at 30-40° to compression – see Figures 5.3b to e.

The main trends observed in the mechanical data are summarised in Figure 5.7. Overall, there is an increase in peak differential stress supported, i.e. peak strength, with increasing confining pressure (Figure 5.7a). Net volumetric strain, measured at constant axial strain, shows a general trend from net dilatation at low confining pressure to net compaction at higher confining pressure, with the transition at 5-10 MPa confining pressure (see Figure 5.7b). We determined Young's Modulus (E) from the linear loading part of the differential stress vs. axial strain curves (see also

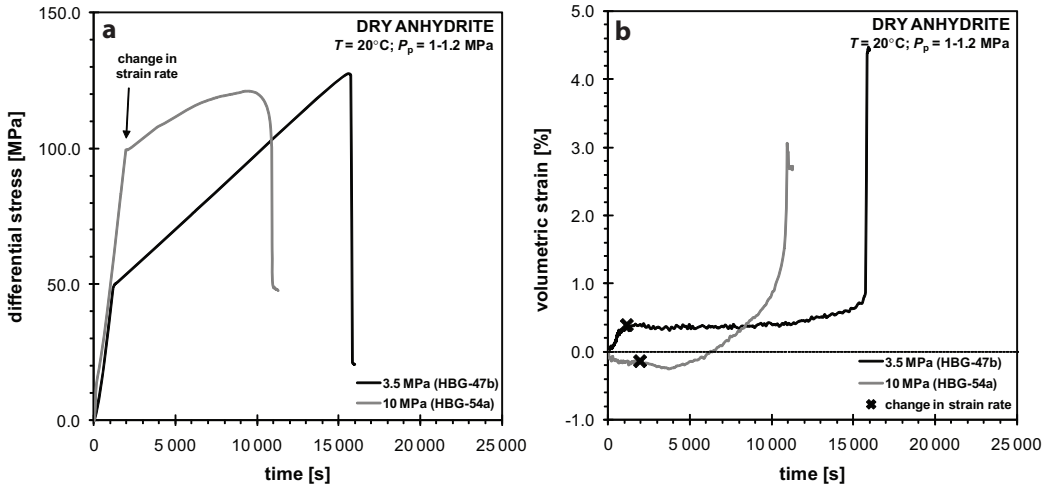

Fig. 5.5 a) Differential stress vs. time and b) volumetric strain vs. time plot for two experiments performed at room temperature (T = 20°C) and 3.5 and 10 MPa confining pressure (1-1.2 MPa argon pressure). Note the knee in the stress curves at 1000-2000 s, corresponding to the change in strain rate from the starting rate of ~10^{-6} s^{-1} to ~10^{-7} s^{-1}.

Chapter 4 and *Hangx et al.* [2009 (submitted)]). Values obtained fell between 13 and 26 GPa, apparently increasing with increasing confining pressure (see Table 5.1). For experiment HBG-50a, performed at the highest confining pressure (P_c = 25 MPa), we also determined the Bulk Modulus (K) and Poisson's Ratio (v) from the initial, linear, compactional part of the volumetric strain vs. axial strain curve. These yielded K = 14 GPa and v = 0.2, respectively.

5.3.2 Permeability data

5.3.2.1 Dynamic experiments

The permeability (κ) of all samples upon starting deformation was below the detection limit of the permeametry set-up, i.e. below ~10^{-21} m^2. Permeability could only be resolved once it exceeded this value. In all experiments, permeability became

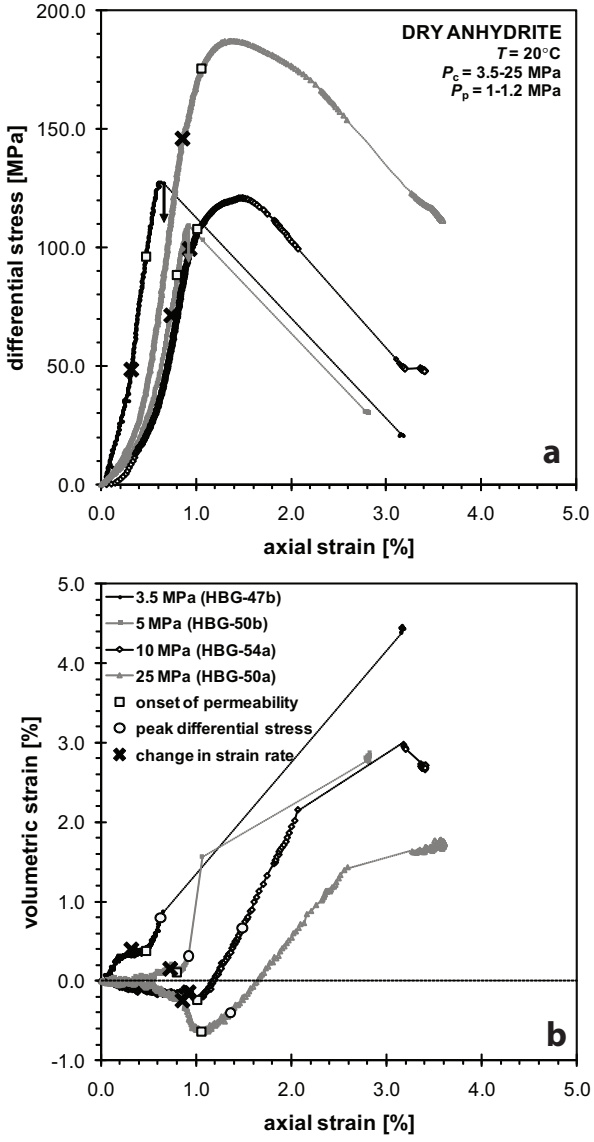

Fig. 5.6 a) Differential stress vs. axial strain and b) volumetric strain vs. axial strain plots for experiments performed on anhydrite at room temperature. Confining pressure (P_c) ranged from 3.5 to 25 MPa and pore pressure (mean argon pressure) from 1 to 1.2 MPa. At low confining pressure, failure occurred by abrupt brittle fracturing (indicated by arrows). At higher confining pressure (> 5 MPa) more gradual yielding plus strain softening was observed. Failure was characterised by an often rapid decrease in differential stress and a rapid increase in volumetric strain. Inferred differential stress and volumetric strain vs. axial strain behaviour during such rapid events is indicated by dotted lines. Marker symbols show the point at which the imposed strain rate was changed from 10^{-6} to 10^{-7} s^{-1}, the onset of measurable permeability, and the peak differential stress in (b). T denotes temperature, P_c is confining pressure and P_p is mean argon pressure.

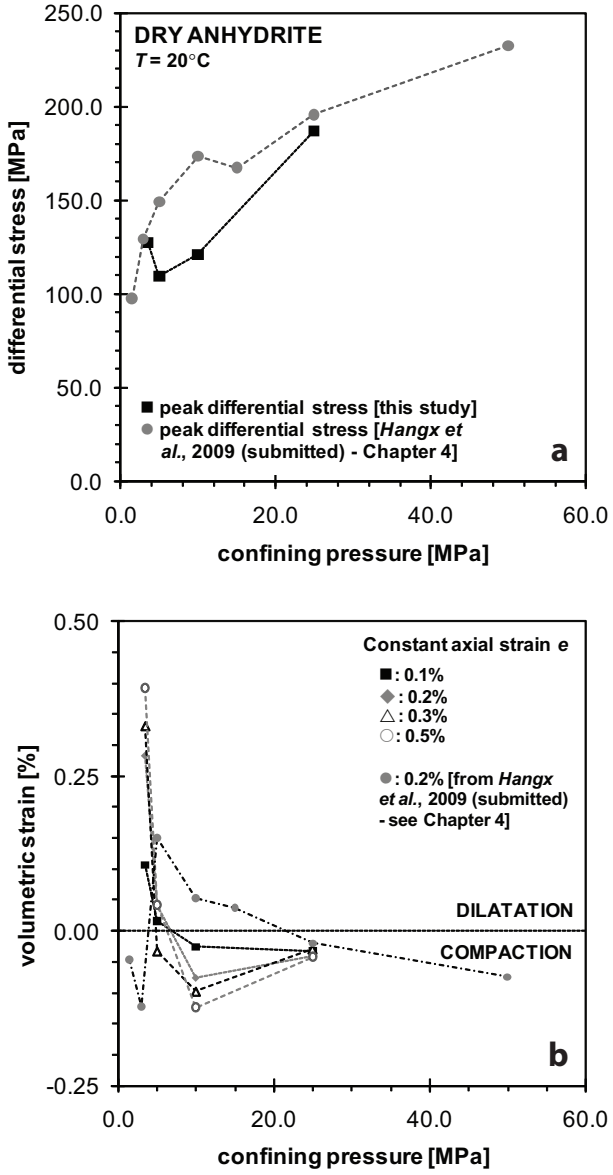

Fig. 5.7 Compilation of failure strength and volumetric strain data obtained in the present experiments on dry anhydrite at 20°C. a) Peak strength vs. effective confining pressure. b) Volumetric strain vs. effective confining pressure, at the constant axial strains *e* shown. For comparison peak stress and volumetric strain data from our previous experiments on the same Zechstein anhydrite are added [*Hangx et al.*, 2009 (submitted) - see Chapter 4]. Note that in both studies we observed a rough increase in peak stress and a decrease in volumetric strain with increasing confining pressure. The present volumetric data show a clear transition from net dilatancy to net compaction at 5-10 MPa confining pressure.

measurable close to yield in the stress-strain curve, i.e. the point where stress-strain behaviour deviates from linearity (Figure 5.6a). We will henceforth refer to the appearance of measurable permeability as the onset of measurable permeability, or simply as the onset of permeability.

Permeability is plotted as a function of volumetric strain in Figure 5.8 for all four experiments performed (T = 20°C, P_c = 3.5-25 MPa). For clarity, we added marker symbols, showing the point of peak differential stress, to the permeability curves shown in Figure 5.8. We also added markers, showing the onset of permeability to the stress-strain-volume curves given in Figure 5.6. With the exception of sample HBG-50a (P_c = 25 MPa), our experiments show an initially rapid increase in permeability with increasing volumetric strain (dilatation positive) at and beyond the onset of measurable permeability, i.e. at and beyond yield (compare Figures 5.8 and 5.6). The

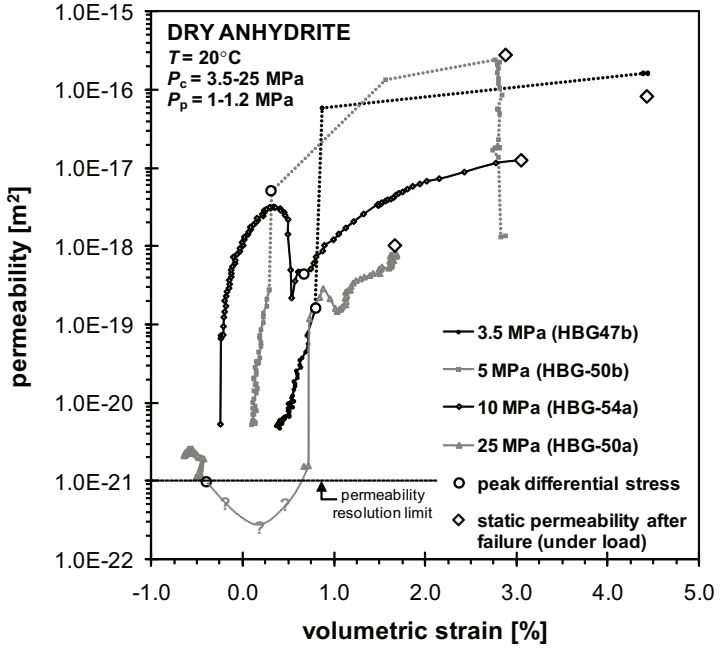

Fig. 5.8 Dynamic permeability vs. volumetric strain plots for permeability measurements made on deforming Zechstein anhydrite (T = 20°C, P_c = 3.5-25 MPa, P_p = 1-1.2 MPa). Note the rapid increase in permeability beyond the point at which it becomes measurable (close to the sample yield point), and the subsequent flattening off to attain a plateau value. In experiments HBG-50a and HBG-54a, we infer that argon flow conduit was temporarily constricted during deformation, resulting in the marked drop in permeability seen in these samples after initial permeability development. Errors in permeability are less than ± 5% and fall within the symbol size. Dotted lines denote interpolations between measured data points in segments of data corresponding to rapid failure of the samples.

rapid increase in permeability flattens off at higher volumetric strain (~ 1%), to reach a plateau value, most clearly seen at 3.5 to 10 MPa confining pressure. This plateau permeability value is crudely dependent on the effective confining pressure, tending to decrease with increasing confining pressure from 10^{-16} m^2 at 3.5-5 MPa to ~10^{-17} m^2 at 10 MPa. Sample HBG-50a (P_c = 25 MPa) shows similar behaviour, except that the first appearance of measurable permeability at yield is followed by a drop to again unmeasurable values during failure, and then a reappearance and flattening off after failure to a value around 10^{-18} m^2 (cf. Figures 5.8 and 5.6).

At low confining pressure (P_c = 3.5-5 MPa), the appearance of measurable permeability is associated with the onset of the more rapid, near-linear increase in dilatant volume change that accompanies yield (cf. Figures 5.8, 5.6b and 5.6a). At higher confining pressures (P_c = 10-25 MPa), the onset of permeability correlates with the transition from compaction to dilatation, which again accompanies yielding (Figures 5.6b). Beyond the onset of permeability, while volumetric strain increases in a more or less linear manner with axial strain (see Figure 5.6b), permeability increases strongly non-linearly with volumetric strain (Figure 5.8), except in the case of sample HBG-50a (P_c = 25 MPa), which shows a transient drop in permeability to

unmeasurably low values after yielding, as mentioned above. Somewhat similarly, the sample deformed at 5 MPa (HBG-50b) shows a drastic drop (2 orders of magnitude) in permeability immediately after failure. In both cases, the observed drop presumably reflects sudden but temporary constriction of the initially-established, gas conduction paths.

5.3.2.2 Static experiments

In addition to permeability measurements made during deformation, we also measured static, post-failure (fault) permeability, under the residual differential stress supported by the sample and under hydrostatic pressure after unloading. These measurements are plotted in Figure 5.9 as a function of effective mean stress σ_m^{eff}, defined as $\sigma_m^{eff} = \frac{1}{3}(\sigma_1 + 2\sigma_3) - P_p$, which equals P_c^{eff} when the sample is free of differential load. The data show a general trend of decreasing post-failure permeability with increasing effective mean stress, the sensitivity to mean stress being greater for the unloaded samples whereby permeability was measured at the deformation test pressure P_c. Permeability measurements made under load (i.e. under residual differential stress after failure) yielded higher values for κ than when the sample was unloaded (i.e. under hydrostatic pressure conditions). In the case of sample HBG-54a (deformed

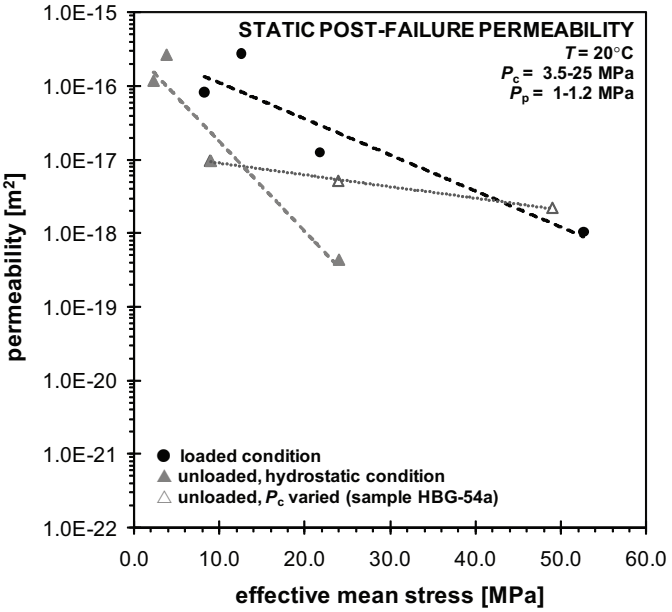

Fig. 5.9 Static post-failure permeability vs. effective mean stress, for samples subjected to permeametry under residually loaded (●) and hydrostatic (▲) conditions. For sample HBG-54a (△), we measured sample (fault) permeability under various hydrostatic pressures (P_c = 10-50 MPa, P_p = 1-1.2 MPa). Overall, we observed a decrease in static post-failure permeability with increasing effective mean stress. Errors in permeability are less than ± 5% and fall within the symbol size. Best fit lines show that under loaded conditions $\kappa = 3.43 \cdot 10^{-16} \exp(-0.11\sigma_m^{eff})$, while under unloaded, hydrostatic conditions $\kappa = 2.94 \cdot 10^{-16} \exp(-0.28\sigma_m^{eff})$. The permeability data for sample HBG-54a yielded $\kappa = 1.29 \cdot 10^{-17} \exp(-0.037\sigma_m^{eff})$.

at P_c = 10 MPa), for which we performed several permeability measurements after failure using various hydrostatic pressures (P_c = 10, 25 and 50 MPa; P_p = 1 MPa), the permeability decreases only slightly with increasing effective mean stress or effective pressure, i.e. by a factor of ~ 4 over the hydrostatic pressure range 10-50 MPa (Figure 5.9).

5.3.3 Microstructural observations

Analysis of thin sections of the undeformed starting material using optical microscopy shows a bimodal microstructure consisting of coarse (mm-sized) rosettes composed of acicular anhydrite (~60 vol-%) embedded in a banded matrix of fine, euhedral to subhedral anhydrite and dolomite grains (< 50 μm, ~35 vol-%) defining the bedding of the material. In addition, occasional, small aggregates (~5 vol-%) of subhedral anhydrite crystals (50-200 μm) are scattered throughout the material. The needles in the anhydrite rosettes display deformation and recrystallisation features such as undulose extinction, twinning, subgrain growth and grain boundary migration, as well as fluid inclusions (< 10 μm) near the rim of the needles. Both the acicular habit and the fluid inclusions in the needles indicate replacement of gypsum rosettes by anhydrite. Locally pre-existing, transgranular and intergranular cracks are present. Bedding is at ~60° to the sample axis.

Representative micrographs of the deformed samples are shown in Figure 5.10. From the mechanical data and sample-scale observations, we discerned two deformation regimes within the range of conditions investigated: (1) abrupt brittle failure involving cohesive cataclastic faulting at low confining pressure (3.5-5 MPa), and (2) semi-brittle deformation with more homogenously and finely distributed microcracking plus cohesive shear fracturing, at higher confining pressures (> 10 MPa).

At low confining pressure (brittle regime – 3.5-5 MPa P_c), we observed axial, transgranular and intergranular cracks and several (conjugate) sets of shear fractures developed at ~8-30° to the compression direction (see Figures 5.3b and c, and 5.10a and b). The shear fractures are filled with fault gouge (thickness < 100 μm) and are surrounded by a highly fractured damage zone (~3-5 mm in thickness), displaying mainly transgranular and intergranular dilatant (Mode I opening) cracks. The larger, transgranular, near-axial cracks visible on the sample-scale appear to connect, or almost connect, to the tips of the main shear fractures and are often gouge-filled (Figures 5.3b, 5.10a, b). In addition, many smaller transgranular cracks subparallel to the direction of compression were observed throughout the samples, branching from the main shear fractures into the damage zone and interconnecting with both gouge-filled and dilatant axial cracks (Figure 5.10b).

At higher confining pressure (semi-brittle regime – 10-25 MPa P_c), sample-scale

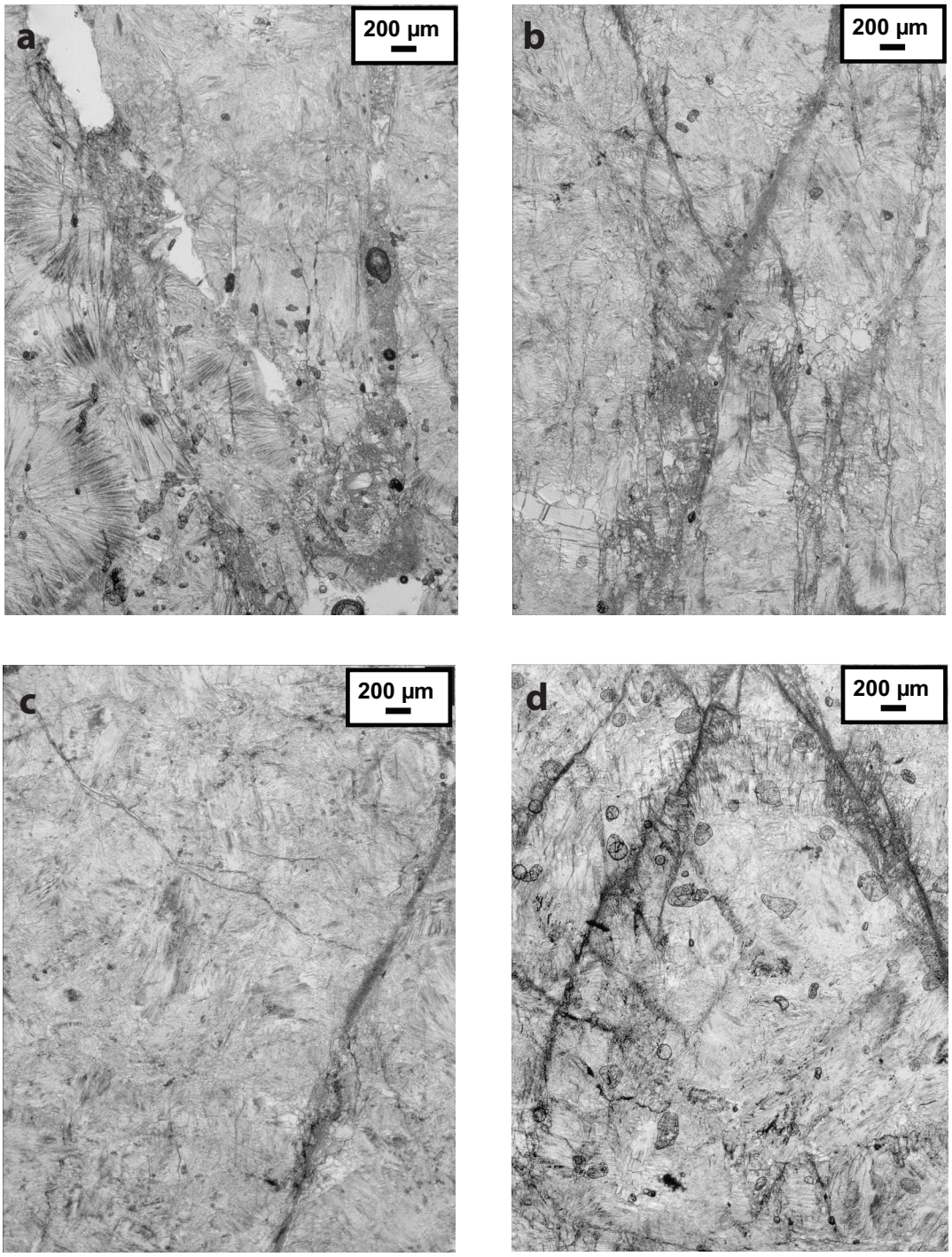

Fig. 5.10 Microstructures of representative, deformed samples (plane polarised light). Compression direction is vertical in all cases. a) Sample HBG-47b (P_c = 3.5 MPa) showing both dilatant and gouge-bearing axial and shear fractures surrounded by a highly fractured damage zone. b) Sample HBG-50b (P_c = 5 MPa) displaying a conjugate set of gouge-filled shear fractures interconnecting with both gouge-filled and dilatant axial cracks. c) Sample HBG-54a (P_c = 10 MPa) showing part of one of the main shear fractures. Note the high angle cracks (~45° to the compression direction). d) Sample HBG-50a (P_c = 25 MPa) showed failure along a conjugate set of shear fractures with associated en-echelon axial crack arrays.

deformation appears to be more homogenously distributed throughout the material, i.e. in a pervasive fracture network consisting of conjugate shear cracks at ~45° to the compression direction (see Figures 5.3d, e and 5.10d). In contrast to the samples deformed at lower confining pressure, well-defined shear fractures are difficult to discern on the sample-scale, though in thin section the microstructures show the presence of through-cutting, conjugate shear fractures at ~30° to the compression direction (Figures 5.3d, e). These fractures are filled with fault gouge (< 50 μm thick) and often associated with dense axial crack arrays, especially at 25 MPa confining pressure – see Figures 5.10c and d). As crack damage is generally more pervasive throughout the samples, no further damage zone could be distinguished around the main shear fractures. In the "bulk" material remote from the fracture, shear fractures are connected through (en echelon) cracks formed at a high angle (45°) to the compression direction.

5.4 Discussion

Our axi-symmetric compression experiments have shown a transition from brittle to semi-brittle behaviour in dry anhydrite at room temperature, in broad agreement with our previous experiments [see Chapter 4 - *Hangx et al.*, 2009 (submitted)]. We did not observe completely pervasive (grain-scale) cataclastic flow in the semi-brittle regime, so we have chosen the term "semi-brittle" rather than "ductile" [*Rutter*, 1986] to describe this regime. Also in line with our previous experiments, the present mechanical data demonstrated an increase in strength with confining pressure, with net dilatation at low confining pressures (3.5-5 MPa) and net compaction at higher confining pressure (10-25 MPa). In addition, our present permeability measurements have addressed the evolution of permeability during loading through failure. The results have shown that the onset of measurable permeability (> 10^{-21} m^2) roughly correlates with yield of the samples plus associated dilatation. Subsequent permeability evolution is non-linearly related to dilatant volume changes (i.e. porosity), and usually shows an initially very rapid (critical) increase with volumetric strain, eventually flattening off to reach a plateau value after failure (Figure 5.8). Syn- and post-failure permeability values lie in the range 10^{-15}-10^{-18} m^2 to 10^{-16}-$4{\cdot}10^{-19}$ m^2, respectively, both tending to decrease with increasing effective stress.

In the following, we will compare our failure and other mechanical data obtained in this study with those obtained by *Hangx et al.* [2009 (submitted) - Chapter 4], combining the two sets of data to obtain a slightly revised Mogi failure criterion for anhydrite at room temperature, and attempting to explain minor differences between the two data sets. We go on to combine the present dilatation and permeability data with the dilatation data reported by *Hangx et al.* [2009 (submitted) - Chapter 4] to

delineate, in Mogi stress space, the conditions under which deforming anhydrite becomes permeable and to what extent. We also attempt to explain the rapid, non-linear permeability changes seen in our experiments with strain beyond yield, as well as the observed relationship between fault permeability and effective (mean) stress state. Finally, we consider the implications of our results for caprock integrity during reservoir depletion and subsequent CO_2 injection.

5.4.1 Failure behaviour and permeability evolution

In Figure 5.11, we plot the peak differential stress data obtained in this study in Mogi stress space [cf. *Mogi*, 1971; *Hangx et al.*, 2009 (submitted) - see Chapter 4], together with that from our previous study on identical Zechstein anhydrite [*Hangx et al.*, 2009 (submitted)]. As emphasised by *Hangx et al.* [2009 (submitted) - Chapter 4] and other authors [*Mogi*, 1971; *Haimson*, 1978; *Haimson and Chang*, 2000; *Colmenares and Zoback*, 2002], the advantage of the Mogi Failure Criterion over the Mohr-Coulomb Failure Criterion is that it provides a relationship between all three principal stresses, instead of only the maximum and minimum principal stresses. This allows more general application of our data in modelling efforts directed at predicting the (hydro)mechanical behaviour of caprock in response to changes in stress related to reservoir depletion or CO_2 injection. In addition, the Mogi criterion generally gives a better fit to experimental data than the more commonly used Drucker-Prager criterion.

As seen in Figure 5.11, agreement is broadly good between the peak strength data points from this study and from our previous experiments [see Chapter 4 - *Hangx et al.*, 2009 (submitted)]. Though power law fits generally give a better description of strength data [*Haimson and Chang*, 2000; *Colmenares and Zoback*, 2002; *Al-Ajmi and Zimmerman*, 2005], our failure envelope for the combined data is best described by a parabolic function, given as follows:

$$\tau_{oct} = -2.32 \cdot 10^{-3}(\sigma_{m,2})^2 + 1.04\sigma_{m,2} - 0.47 \qquad (R^2 = 0.99) \qquad (5.3)$$

where τ_{oct} is the Mogi octahedral shear stress [MPa] and $\sigma_{m,2}$ is the Mogi mean stress [MPa].

While agreement is broadly good, the peak differential stresses obtained in the present experiments are mostly slightly lower than expected from our previous work (see Figures 5.7 and 5.11), especially for experiments HBG-50b and 54a, performed at 5 and 10 MPa effective confining pressure. The present experiments also showed higher axial strains at failure (0.7-2.4%), compared to our previous experiments (0.4-1.3%), as well as more pervasive damage in the form of axial cracks (lower confining pressure - Figures 5.3b,c) and shear cracks/planes (high confining pressure – Figures

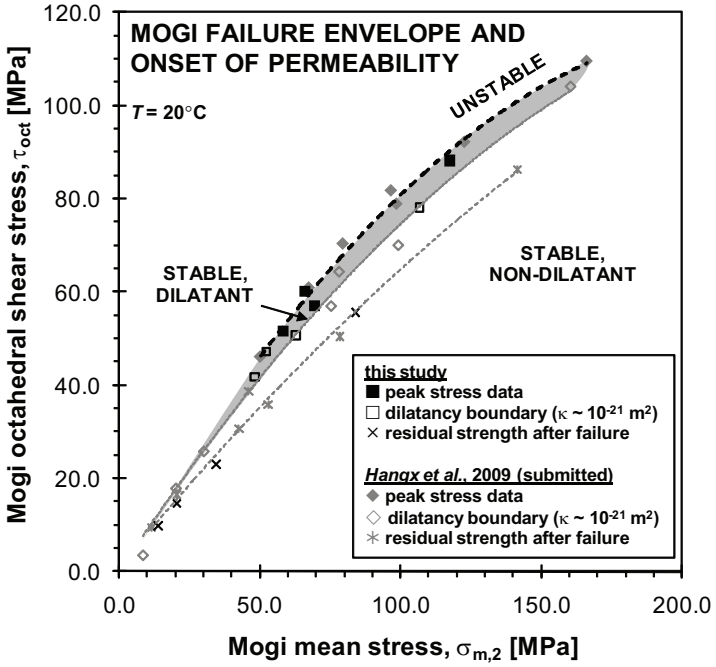

Fig. 5.11 Mogi plot showing failure envelope fitted to the present peak stress for dry anhydrite deformed at room temperature, combined with the previous data of *Hangx et al.* [2009 (submitted) - Chapter 4]. A permeability envelope corresponding to the onset of measurable permeability in the present tests is also displayed. In addition, we added results from our previous study on anhydrite [*Hangx et al.*, 2009 (submitted) - Chapter 4]. The envelope showing the onset of measurable permeability corresponds to a permeability of ~10^{-21} m^2 and in essence coincides with the boundary between the non-dilatant and dilatant stress fields. The stress space of the Mogi failure criterion is described $\tau_{oct} = 1/3\sqrt{[(\sigma_1-\sigma_2)^2 + (\sigma_2-\sigma_3)^2 + (\sigma_3-\sigma_1)^2]}$ and $\sigma_{m,2} = ½(\sigma_1 + \sigma_3)$. For dry rock, σ_1, σ_2 and σ_3 are the principal stresses at failure [MPa], while for rock penetrated by pore fluid they represent the principal effective stresses at failure, defined as $\sigma_i^{eff} = \sigma_i - P_p$, where, P_p is the pore fluid pressure (in this case, mean argon pressure [MPa]). In the case where $\sigma_2 = \sigma_3$, such as in our experiments, the octahedral shear stress is reduced to $\tau_{oct} = \sqrt{2}/3\ (\sigma_1-\sigma_3)$. The envelope delineating the residual strength after failure can be described by $\tau_{oct} = -9.41\cdot10^{-4}\ (\sigma_{m,2})^2 + 0.73\ \sigma_{m,2} - 0.92$ ($R^2 = 0.99$).

5.3d, e) [*Hangx et al.*, 2009 (submitted) - Chapter 4]. In addition, Young's Modulus determined in the current experiments was significantly lower than in our previous study, i.e. *E* values of 13.4-26.1 GPa versus 29.0-49.7 GPa, respectively. We interpret these differences to be due to effects of sample size on mechanical behaviour, comparable to those reported by *Uehara and Shimamoto* [2004], who performed failure experiments on cataclasite samples with similar length:diameter or L:D aspect ratios. In other words, we suggest that the observed difference in mechanical behaviour is related to the fact that L:D ≈ 1:1 in this study instead of the more common value of 2:1 or more [*Mogi*, 1966; *Paterson and Wong*, 2005], as used in our previous study. Conventional triaxial experiments on dolomite and granite [*Mogi*, 1966] have shown the effect of L:D is small at high confining pressure. However, *Mogi* [1966] also suggested that enhanced clamping and concomitant stress concentration at the end of the samples, could reduce the stress required for failure and the steepness of shear

failure planes, which may have happened in our experiments.

In addition to aspect ratio effects, the lower strain rates used in the current experiments may also have played a role in controlling mechanical behaviour. Though little effect of changing strain rate is seen in the present stress-strain curves (Figure 5.6), we observed a minor increase in compaction upon decreasing the strain rate, as well as more dilatation with increasing deformation, compared to our previous results [cf. *Hangx et al.*, 2009 (submitted) - Chapter 4]. This suggests that time-dependent creep processes, such as crystal plastic flow, resulting in slow pore compaction or time-dependent growth of (wing) cracks during the dilatant stage, are operating during deformation. The operation of such plastic flow mechanisms is strongly supported by the observed weakening effect of temperature on peak strength reported in our earlier work on anhydrite [*Hangx et al.*, 2009 (submitted) - Chapter 4].

Alongside our failure data, the present volumetric strain and permeability data (see Figures 5.6 and 5.8) can be used to contour the appearance or onset of measurable permeability ($\kappa > \sim 10^{-21}$ m^2) onto the Mogi plot shown in Figure 5.11. In addition, we can use the volumetric strain data from our previous study on anhydrite. For the present experiments with dilatant volume changes throughout the entire deformation test, i.e. at low confining pressure, the onset of permeability is typically characterised by an increase in the rate of positive volume change. At higher confining pressure, the onset of permeability correlates well with the transition from compaction to dilatation at the points of maximum compaction – i.e. the minimum turning point in the volumetric strain vs. axial strain curves (see Figures 5.6 and 5.8). This means that though the onset of dilatancy [see the dilatation criterion in Chapter 4 - *Hangx et al.*, 2009 (submitted)] delineates the stage of crack initiation, it is not until the turning point in the volumetric strain curve is reached that the material becomes measurably permeable at higher pressures. Using the above definitions for the onset of permeability, combining <u>all</u> data together (this and previous study over the entire pressure range), the resulting best fit relationship describing the onset of permeability as a function of effective Mogi mean stress $\sigma_{m,2}$ [MPa] is given as

$$\tau_{oct} = -1.93 \cdot 10^{-3} (\sigma_{m,2})^2 + 0.92\sigma_{m,2} \qquad (R^2 = 0.99) \qquad (5.4)$$

where τ_{oct} is the Mogi octahedral shear stress [MPa]. The agreement between the stress conditions delineating the onset of permeability in this study and the corresponding dilatation data from our previous study [*Hangx et al.*, 2009 (submitted) - Chapter 4] shows that the effect of strain rate is minor in the Mogi plot. As seen in Figure 5.11, the permeable, stable stress field is defined by only a thin band directly below the failure envelope. This demonstrates that no pervasive permeability changes will occur until the material is brought very close to failure. In the permeable, stable field material

permeability increases by ≥ 3-5 orders of magnitude from ≤ 10^{-21} (impermeable) to 10^{-15}-10^{-18} m^2, while in the permeable, unstable (post-failure) field, permeability varies from 10^{-16}-10^{-18} m^2.

5.4.2 Permeability development with strain - comparison with other studies of low porosity rocks

In general, there are several stages of deformation and permeability changes that can be discerned in low porosity, brittle and brittle-ductile rock materials, such as *Stormont and Daemen* [1992], *Zhang et al.* [1994], *Peach and Spiers* [1996], *Uehara and Shimamoto* [2004], *Mitchell and Faulkner* [2008], *Alkan* [2009], and *de Paola et al.* [2009]. During initial elastic deformation, low porosity rock typically compacts, resulting in closure of pre-existing cracks and a decrease in permeability. This decrease is usually of the order of a factor of 2-5 of the initial permeability [*Uehara and Shimamoto*, 2004; *Alkan et al.*, 2007; *Mitchell and Faulkner*, 2008; *De Paola et al.*, 2009]. Following this stage of largely elastic compaction, crack opening and growth lead to the onset of dilatancy, seen as a deviation from a linear decrease in volumetric strain with axial strain. However, it is generally not until the turning point between compaction and dilatation [*Alkan et al.*, 2007]) is reached that an increase in permeability is observed. At this point, permeability increases rapidly (critically) but eventually levels off again with increasing volume change [*Peach*, 1991; *Stormont and Daemen*, 1992; *Zhang et al.*, 1994; *Peach and Spiers*, 1996]. The overall change in permeability is typically 1 to 6 orders of magnitude, from 10^{-21} to 10^{-20}-10^{-14} m^2 [*Peach*, 1991; *Stormont and Daemen*, 1992; *Zhang et al.*, 1994; *Peach and Spiers*, 1996; *Alkan*, 2009] and is generally attributed to the establishment and growth of a connected or so-called "percolating" crack network.

Similar stages were observed in our experiments, though measurement of the earliest changes in sample permeability was not possible, as the initial permeability of our material was below the detection limit ($\kappa_{initial} \leq \sim 10^{-21}$ m^2). The onset of measurable permeability in our tests nonetheless correlates well with the compaction-dilatation turning point recorded in our experiments at high confining pressures (10-25 MPa, Figure 5.6b), while at lower confining pressures (3.5-5 MPa) no compaction was observed during deformation and the onset of permeability corresponded to an increase in dilatation rate with strain (Figure 5.6b). Permeability in our tests increased by ≥ 3-5 orders of magnitude during deformation (Figure 5.8b), eventually reaching a constant, post-failure value, which decreased with confining pressure from ~10^{-16} m^2 at 3.5-5 MPa to 10^{-19} m^2 at 25 MPa.

Since the very rapid permeability development with e and e_{vol} observed in our experiments is similar to that seen in other low porosity rocks, such as rock salt [*Peach*, 1991; *Stormont and Daemen*, 1992; *Peach and Spiers*, 1996; *Alkan*, 2009],

anhydrite [*De Paola et al.*, 2009], Carrara marble [*Zhang et al.*, 1994] and Westerly Granite [*Zoback and Byerlee*, 1975b; *Mitchell and Faulkner*, 2008], we infer that the rapid, dilatancy-induced permeability development observed in our experiments can be explained by the same mechanism envisaged for these materials, i.e. by crack connectivity development or "percolation theory" [*Gueguen and Dienes*, 1989; *Peach*, 1991; *Peach and Spiers*, 1996; *Zhu and Wong*, 1999; *Alkan*, 2009]. Permeability models based on percolation theory state that at the critical (percolation) threshold a connected or percolating microcrack network is first established, which then grows until a pervasive, connected network is developed and a constant permeability is approached [*Gueguen and Dienes*, 1989; *Peach*, 1991; *Peach and Spiers*, 1996; *Alkan*, 2009]. Connected porosity or crack models, such as the equivalent channel [*Walsh and Brace*, 1984] or penny-shaped crack model [*Gueguen and Dienes*, 1989], which predict a continuous (cubic) dependence of permeability on porosity, do not hold for the critical regime close to the percolation threshold as the connected network is still growing at this stage.

We now consider what the gas flow path was in our samples and why the permeability of some samples dropped transiently after initial establishment (see HBG-54a and -50a, Figure 5.8). *Uehara and Shimamoto* [2004] performed permeability experiments on deforming cataclasite from the Median Tectonic Line, Japan, and inferred that in their samples flow along through-going fractures was preferred over flow through fragmented, "matrix" material. Our microstructures show that our samples generally contained only 1-2 fractures that cut the entire length of the sample, embedded within a very finely fractured, dense matrix. In addition, the above-mentioned permeability data on samples HBG-54a and HBG-50a (10-25 MPa) show that on occasion permeability is suddenly dropped by more than an order of magnitude during ongoing deformation. If the permeability was controlled by flow in the main fractures, instead of being matrix flow-controlled [*Matthäi and Belayneh*, 2004], as in the case of *Uehara and Shimamoto* [2004], displacements along the main fractures, constricting flow at compressional jogs or dislodging material and clogging up the flow path, would most likely suffice to (temporarily) inhibit flow through the sample. From our microstructures and permeability data and by comparison with the work of *Uehara and Shimamoto* [2004], we hence infer that the permeability of our samples was most likely controlled by the main, through-going fractures. Sample permeability must therefore mainly reflect fault permeability.

5.4.3 Effect of mean stress on post-failure permeability

As seen in Figure 5.8b, for most samples the static, post-failure permeability (measured under load) did not deviate strongly from the final dynamic permeability. Note that the drastic drop in permeability at failure, observed in experiment HBG-

50b, was recovered during the static permeability measurement, supporting our interpretation that sample permeability was controlled by flow along the main faults of fractures.

Overall, we observed an inverse dependence of post-failure permeability on effective mean stress σ_m^{eff} under both loaded and unloaded (hydrostatic) conditions (see Figure 5.9). A similar dependence of rock and fault gouge permeability on effective mean stress σ_m^{eff} has also been described extensively in the literature [*Morrow et al.*, 1984; *David et al.*, 1994; *Zhang et al.*, 1999; *Faulkner and Rutter*, 2000; *Faulkner*, 2004; *De Paola et al.*, 2009]. For such materials, e.g. sandstones, anhydrite rock and natural and synthetic fault gouges, it is suggested that the following exponential relationship holds between permeability and effective mean stress [*Rice*, 1992]:

$$\kappa = \kappa_0 \, e^{-\gamma \sigma_m^{eff}} \tag{5.5}$$

where, κ is the permeability [m^2], κ_0 is a reference permeability at σ_m^{eff} = 0 MPa, γ is the stress sensitivity factor [MPa^{-1}] and σ_m^{eff} is the effective mean stress. For our experiments, similar best fit relationships can be derived for post-failure (fault) permeability, and are given as shown in Figure 5.9 as

$$\kappa = 3.43 \cdot 10^{-16} \, e^{-0.11 \sigma_m^{eff}} \qquad (R^2 = 0.86) \tag{5.6}$$

for samples measured under differential stress, and as

$$\kappa = 2.94 \cdot 10^{-16} \, e^{-0.28 \sigma_m^{eff}} \qquad (R^2 = 0.93) \tag{5.7}$$

for measurements under hydrostatic pressure.

The stress sensitivity factor appearing in these relations (i.e. γ = 0.11-0.28 MPa^{-1}) is similar to that predicted for large-scale fault zones [*Rice*, 1992].

Our data show that permeability under load is higher than under hydrostatic conditions (Figures 5.9 and 5.12). This can be explained by the partial, elastic backsliding and closure of dilatant voids in the main, flow-carrying fractures and damage zones when the axial stress is removed [cf. *Zoback and Byerlee*, 1975b].

Measuring permeability for the same sample (hence faults) at various hydrostatic pressures, as was done for experiment HBG-54a, showed only a factor 4 decrease in permeability with a factor 5 times increase in confining pressure. We observed the following best fit relationship between permeability and effective mean stress for this particular sample:

$$\kappa = 1.29 \cdot 10^{-17} \, e^{-0.037 \sigma_m^{eff}} \qquad (R^2 = 0.99) \tag{5.8}$$

The stress sensitivity factor obtained (γ = 0.037 MPa^{-1}) is similar to the average

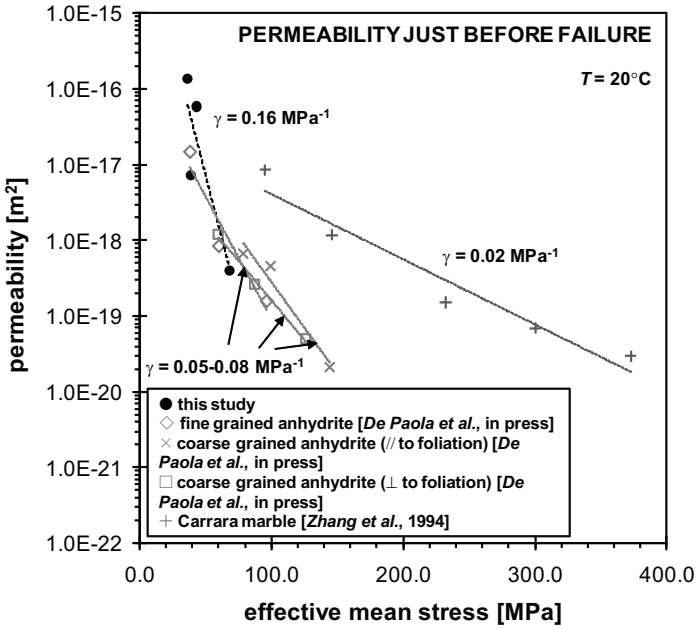

Fig. 5.12 Permeability just before failure as a function of effective mean stress, for samples deformed in this study as well as in studies on anhydrite by *De Paola et al.* [2009] and on Carrara marble by *Zhang et al.* [1994]. Note that permeability tends to become less sensitive to effective mean stress (i.e. shows lower *γ*-values), as mean stress increases.

stress sensitivity factor of ~ 0.01 MPa^{-1} obtained for hydrostatically compacted fault gouges by previous authors [*Morrow et al.*, 1984; *Zhang et al.*, 1999; *Faulkner and Rutter*, 2000]. The relatively low value of γ = 0.037 MPa^{-1} for sample HBG-54a indicates that closure of faults developed in anhydrite by increasing the confining pressure to values above that at failure is relatively difficult. Fracture roughness or fines on the fault plane may keep faults propped open, thus allowing fluid flow [*Zoback and Byerlee*, 1975b].

In addition, we have compared our results on permeability measurements obtained just before failure to those obtained in other studies [see Figure 5.12 - *Zhang et al.*, 1994; *De Paola et al.*, 2009]. The dependence of permeability on (mean) stress appears to become less strong with increasing stress. This is most clearly seen for Carrara marble [*Zhang et al.*, 1994]. This behaviour was recognised to be typical for low porosity rocks and coined "Type 1 behaviour" by *David et al.* [1994]. Our data, together with those of *De Paola et al.* [2009], suggest similar behaviour at higher effective mean stress values.

5.4.4 Implications for caprock integrity

The failure and permeability envelopes for Zechstein anhydrite obtained in this study and our previous study [*Hangx et al.*, 2009 (submitted) - Chapter 4] can be

used in numerical models to predict the damage or porosity-permeability response of anhydrite caprock to changes in stress state as a result of reservoir depletion and CO_2 injection. Our results indicate that such permeability changes, for example at the base of the caprock where it is exposed to injected CO_2, will occur only very close to failure (see Figure 5.11). In the stable, permeable field, permeability increases rapidly from less than 10^{-21} m^2 to 10^{-15}-10^{-18} m^2 prior to failure; after failure permeability varies from 10^{-16} to 10^{-19} m^2, decreasing with increasing mean stress (Figures 5.8, 5.9 and 5.12).

These permeability values represent maximum bulk values, as failure will generally be localised rather than pervasive. Our results may further be used to estimate the bulk permeability due to newly formed, localised fractures in an anhydrite caprock. In case of local failure under in-situ conditions, the deviatoric stress supported by the fault plane will probably lie between the residual and failure strength envelopes given in Figure 5.11, depending on the extent of displacement and elastic strain release following failure. The resulting bulk permeability of the caprock will be highly dependent on fracture width, volume and spacing within the formation. Our experimental faults, which seem to control sample permeability are of the order of 1 mm thickness with 1 cm spacing, so that the intrinsic fault permeability would be about 1 order higher than the sample value. Bulk permeability of a locally faulted anhydrite caprock may therefore easily be as much as 100-1000 times lower than the values suggested by our experiments. For a hypothetical reservoir at ~3 km depth, assuming an average rock density of ~2500 kg/m^3, the vertical overburden stress (σ_v) will be ~70 MPa. We can now use this value plus equation (5.3) to calculate σ_1 in case of a compressive in-situ stress regime, or σ_3 for an extensional regime, as at failure the Mogi Failure Criterion must be satisfied. This gives $\sigma_1 \approx 290$ MPa or $\sigma_3 \approx 12$ MPa, for the compressive and extensional stress regimes respectively. Assuming a typical CO_2 injection pressure of ~10-20 MPa [*Li et al.*, 2005], and taking the fault permeability in our samples to be 10 times the bulk values, equation (5.6) now predicts that the intrinsic permeability of newly created faults will be less than 10^{-22} or 10^{-17} m^2, respectively, at ~3 km depth. Taking into account the above-mentioned factor of 100-1000 to correct for the localised nature of failure would then imply bulk (failed) caprock permeability of 10^{-19}-10^{-25} m^2. Repeating this estimate for the residual strength envelope in Figure 5.11 yields similar bulk permeability values for failed caprock. These values are similar to permeabilities estimated for caprocks such as the shale caprock at the Sleipner pilot CO_2 injection site, which are considered to be safe and acceptable. However, as already indicated by our previous caprock flexure calculations [see Section 4.5.5, Chapter 4 - *Hangx et al.*, 2009 (submitted)], permeability development or failure of anhydrite caprock will only occur in the extreme cases of highly localised reservoir compaction or heave (100 m radius), combined with very large deflections (1 m). We conclude that in practice,

under realistic conditions and in the absence of reaction [see Section 4.5.6 of Chapter 4 - *Hangx et al.*, 2009 (submitted)], bulk permeability will be negligible and caprock integrity will not be compromised by mechanical damage.

A last point of importance is the observation in the literature that, though permeability is an intrinsic material property, a difference is often found between permeability measured using gases versus liquids [*Klinkenberg*, 1941; *Tanikawa and Shimamoto*, 2009]. This difference is due to the Klinkenberg effect, which results in "slip" of gas molecules on the fluid conduit walls, leading to slightly higher gas permeability compared to liquid permeability, especially at low permeability values where fluid conduits are narrow [*Peach*, 1991; *Peach and Spiers*, 1996]. According to *Tanikawa and Shimamoto* [2009], gas and liquid permeability can be related according to the following relationship

$$\kappa_G = \kappa_L\left[1 + \left(\frac{b}{P_p}\right)\right] = \kappa_L\left[1 + \left(\frac{0.15\kappa_L^{-0.37}}{P_p}\right)\right] \quad (5.9)$$

where, κ_G is the gas permeability [m^2], κ_L is the liquid permeability [m^2], b is the Klinkenberg slip factor [Pa] and P_p is the pore pressure, ½($P_{upstream}$ - $P_{downstream}$) [Pa]. *Tanikawa and Shimamoto* [2009] assume that the Klinkenberg slip factor b obtained in their experiments is applicable to all rocks. However, it should be noted that their measurements were performed on relatively permeable sandstones (10^{-14}-10^{-20} m^2), using argon and water. Assuming their equation is universal, we can estimate the fluid permeability of anhydrite using our gas permeability measurements. Our results yield that fluid permeability is a factor of only 1.2 to 2.2 lower than the measured gas permeability over the range of conditions investigated. Our permeability values for anhydrite can therefore be considered equally valid (or slight overestimates) for CO_2-charged pore water, liquid CO_2 and supercritical CO_2, as for gaseous CO_2 or argon, provided there are no reaction effects.

5.5 Conclusions

We have investigated the effect of deformation and dilatancy on permeability development in Zechstein anhydrite, by means of conventional triaxial compression experiments combined with argon gas permeametry. The experiments were conducted at room temperature and 3.5 to 25 MPa confining pressure, using mean argon pressures of 1-1.2 MPa. Our main findings can be summarised as follows:

1. At 5-10 MPa confining pressure, we observed a transition from brittle behaviour to more semi-brittle behaviour with pervasive deformation, plus an increase in peak strength from 109-188 MPa over the confining pressure range 3.5-25 MPa. Young's Modulus varied from 13 to 26 GPa, crudely increasing

with confining pressure. Overall, our results showed slightly lower values for peak strength (10-20%) and significantly lower Young's Modulus, compared to our previous study on identical material [*Hangx et al.*, 2009 (submitted) - see Chapter 4]. This difference is attributed to the lower aspect ratio (1:1 vs. 2:1) of the present samples, resulting in clamping and stress enhancement at the ends of the samples, as well as to the 10-100 times lower strain rate used in the present experiments, which promoted minor plastic deformation.

2. We obtained a Mogi-type failure envelope describing the strength of Zechstein anhydrite at room temperature. Our results agree well with the failure envelopes obtained in our previous experiments at room temperature (and 80°C), and can be expressed by the Mogi Criterion: $\tau_{oct} = -2.32 \cdot 10^{-3}(\sigma_{m,2})^2 + 1.04\sigma_{m,2} - 0.47$.
3. Argon gas permeametry performed during deformation showed a change from "impermeable" to permeable as a result of deformation and dilatation. The onset of measurable permeability ($\kappa > 10^{-21}$ m^2) is associated with an increase in rate of dilatation with axial strain at low confining pressure, and, at higher confining pressures, by the turning point from compaction to dilatation in the volumetric vs. axial stress-strain curve. The onset of permeability in stress space can be described in terms of a Mogi criterion: $\tau_{oct} = -1.93 \cdot 10^{-3}(\sigma_{m,2})^2 + 0.92\sigma_{m,2}$. For Zechstein anhydrite, permeability will not develop until close to failure. The changes in permeability that occur due to failure are from 10^{-21} m^2 to values in the range 10^{-19}-10^{-16} m^2, i.e. 3 to 5 orders of magnitude. The observed permeability development is related to the establishment of a connected crack/void network, which can be explained in terms of percolation theory for low permeability rocks undergoing microcrack damage and failure.
4. Sample permeability in our tests was largely controlled by the permeability of the shear faults developed. Static, post-failure permeability measurements made under differential stress show an exponential dependence of sample, and hence fault, permeability on effective mean stress: $\kappa = 3.43 \cdot 10^{-16} e^{-0.11\sigma_m^{eff}}$. Using this relation and taking into account the localised nature of caprock failure expected under in-situ conditions, the bulk permeability of failed caprock above a hypothetical reservoir at ~3 km depth was estimated to be of the order of 10^{-19}-10^{-25} m^2.
5. Our Mogi envelopes for failure and permeability development, coupled with our data on permeability development through failure, and on the mean stress dependence of post-failure permeability, demonstrate that the risk of damage-induced integrity loss is negligible, except in the extreme case of abnormally localised reservoir compaction or heave. This means that in practice, caprock integrity will not be compromised by mechanical damage and permeability development.

Acknowledgements

This research was funded by Shell International Exploration and Production and performed within WorkPackage 4.1 (Subsurface mineralisation) of the Dutch national research project CATO, CO_2 capture, transport and storage. Conxita Taberner (Shell International Exploration Production) and Jan Penninga (Nederlandse Aardolie Maatschappij BV.) are thanked for supplying the sample material. We thank Eimert de Graaff, Gert Kastelein, and Peter van Krieken for technical assistance.

6

Coastal spreading of olivine to control atmospheric CO_2 concentrations: a critical analysis of viability

S.J.T. Hangx and C.J. Spiers

International Journal of Greenhouse Gas Control (2009),
doi: 10.1016/j.ijggc.2009.07.001

Abstract

Qualitative proposals to control atmospheric CO_2 concentrations by spreading crushed olivine rock along the Earth's coastlines, thereby accelerating weathering reactions, are presently attracting considerable attention. This paper provides a critical evaluation of the concept, demonstrating quantitatively whether or not it can contribute significantly to CO_2 sequestration. The feasibility of the concept depends on the rate of olivine dissolution, the sequestration capacity of the dominant reaction, and its CO_2 footprint. Kinetics calculations show that offsetting 30% of worldwide 1990 CO_2 emissions by beach weathering means distributing of 5.0 Gt of olivine per year. For mean seawater temperatures of 15 to 25°C, olivine sand (300 μm grain size) takes 700-2100 years to reach the necessary steady state sequestration rate and is therefore of little practical value. To obtain useful, steady state CO_2 uptake rates within 15-20 years requires grain sizes <10 μm. However, the preparation and movement of the required material poses major economic, infrastructural and public health questions. We conclude that coastal spreading of olivine is not a viable method of CO_2 sequestration on the scale needed. The method certainly cannot replace CCS technologies as a means of controlling atmospheric CO_2 concentrations.

6.1 Introduction

Carbon dioxide capture and storage (CCS) is now widely seen as an essential strategy for reducing CO_2 emissions. One of the methods investigated to date involves CO_2 capture at source followed by industrial-scale reaction with naturally occurring Ca- or Mg-rich silicate minerals to form stable carbonates plus silica. Candidate minerals include olivine (particularly the more common Mg-rich end member, forsterite), pyroxenes (or pyroxenoids), and serpentine [see *Jia and Anthony*, 2002; *O'Connor et al.*, 2005; *Gerdemann et al.*, 2007]. The corresponding reactions generally anticipated can be represented as:

Olivine (forsterite): $Mg_2SiO_{4\,(s)} + 2CO_{2\,(g)} + 2H_2O_{(l)} \leftrightarrow 2MgCO_{3\,(s)} + H_4SiO_{4\,(aq)}$ (6.1a)

Pyroxenoid (wollastonite): $CaSiO_{3\,(s)} + CO_{2\,(g)} + 2H_2O_{(l)} \leftrightarrow CaCO_{3\,(s)} + H_4SiO_{4\,(aq)}$ (6.1b)

Serpentine: $Mg_3Si_2O_5(OH)_{4\,(s)} + 3CO_{2\,(g)} + 2H_2O_{(l)} \leftrightarrow 3MgCO_{3\,(s)} + 2H_4SiO_{4\,(aq)}$ (6.1c)

where $CO_{2\,(g)}$ represents CO_2 in either gas or supercritical fluid form, depending on pressure and temperature. However, these reactions are slow under atmospheric conditions. To accelerate them to rates appropriate for an industrial process, the rock or mineral feedstock must be crushed to a fine grain size (high surface area) [*Kojima et al.*, 1997; *O'Connor et al.*, 2000a; *Kakizawa et al.*, 2001; *Gerdemann et al.*, 2002; *Gerdemann et al.*, 2007] or pre-treated with large quantities of acid [*Goff and Lackner*, 1998; *Haywood et al.*, 2001; *Kakizawa et al.*, 2001]. In addition, temperature and CO_2 pressures of 100-185°C and 4-15 MPa are needed for optimum results [*Gerdemann et al.*, 2007]. The associated energy consumption, environmental impact and costs are therefore high and have placed industrial mineralisation low on the list of CCS options [*Huijgen et al.*, 2006].

A possible alternative may be to react the above minerals with CO_2 at ambient conditions, i.e. through natural weathering reactions at Earth surface conditions [*Wogelius and Walther*, 1991; 1992]. Following earlier articles in the scientific literature [*Schuiling*, 2006; *Schuiling and Krijgsman*, 2006], a superficially appealing idea, based on the concept of beach weathering of crushed natural olivine, was recently proposed by Schuiling, via the Dutch media [*Biersma*, 2007; *Eshuis*, 2007; *Tangerman*, 2009]. This "Green Beaches" proposal entails the spreading of crushed olivine rock along large parts of the Earth's coastlines, above the wave base, using coastal dumper-barges and/or beach bulldozing equipment. The notion put forward by Schuiling is that dissolution of sand-grade olivine (grain size 300 μm) will promote natural bicarbonate production, and hence oceanic uptake of CO_2 to rates that produce

a significant sequestration effect over several decades. The concept does not lead to CO_2 emissions reduction but is envisaged to offset emissions by removing carbon dioxide directly from the atmosphere and has been profiled in the media as offering a cheap, natural alternative to CCS technologies. Other alternatives put forward by *Schuiling* [*Schuiling and Krijgsman*, 2006] include terrestrial weathering of crushed olivine, notably in developing (sub)tropical countries. For all such ideas, it is argued that olivine supplies are more than adequate but must be mined and transported from the relatively localised major ultramafic occurrences, such as ophiolite complexes, found around the world, i.e. in regions such as Norway, Turkey and North America [see for example the ophiolite distribution map in *Coleman*, 1977].

The perceived low risk, low cost and green character of olivine beach weathering have led to much political and popular attention for the proposed method in the Netherlands and within international web-based fora (e.g. http://www.realclimate.org/index.php/archives/2008/03/air-capture/). However, the green beaches concept has not yet been quantitatively evaluated. Moreover, because weathering is a slow process [*Lackner et al.*, 1995; *O'Connor et al.*, 2000b; *Kakizawa et al.*, 2001; *Chen et al.*, 2006] much scepticism exists in the scientific community regarding CO_2 sequestration by weathering approaches.

This paper critically analyses the concept of beach weathering of crushed olivine, with the aim of demonstrating quantitatively whether or not it can contribute significantly to CO_2 sequestration targets. We do this by first reviewing the available data on the type and rate of the relevant olivine dissolution and CO_2 uptake reactions, and the effects upon these of environmental variables, such as temperature, pH and salinity. We go on to construct a simple model predicting the progress of beach olivine reaction and CO_2 uptake as a function of grain size and time. Finally, we consider the overall CO_2 footprint of the method itself, and the feasibility of using it to offset CO_2 emissions significantly by 2020 [*Commission of the European Union*, 2007], compared with the EU reduction target of 30%. Aspects of land-based weathering are also considered but much more work is needed on this before its feasibility can be reliably assessed.

6.2 Reaction of CO_2 with olivine and associated sequestration capacity

Key to coastal weathering of olivine is the sequestration capacity of the dominant sequestering reaction. At temperatures below 100°C and at slightly elevated CO_2 pressures (P_{CO2} = ~ 1 MPa), experimental studies have shown that reaction (6.1), seen in high-pressure mineralisation experiments, is replaced by the reaction

$$5Mg_2SiO_{4\,(s)} + 8CO_{2\,(g)} + 20H_2O_{(l)} \leftrightarrow 2[4MgCO_3 \cdot Mg(OH)_2 \cdot 4H_2O]_{(s)} + 5H_4SiO_{4\,(aq)} \quad (6.2)$$

hydromagnesite

whereby, hydromagnesite precipitates instead of magnesite ($MgCO_3$) [*O'Connor et al.*, 2002]. On the other hand, analysis of natural waters (ground waters in contact with carbonates or ultramafics and surface waters from alkaline soda lakes) shows that, under ambient conditions (15-25°C, $P_{CO2} = 10^{-5.0}$–$10^{-2.5}$ MPa), neither magnesite nor hydromagnesite generally precipitates, even at high supersaturation [*Hostetler*, 1964]. This is because carbonate minerals formed at ambient conditions are in a high free-energy state as a result of fine grain size, metastable ionic substitution, and crystal defect content [*Hostetler*, 1964]. Indeed, available evidence suggests that magnesite and hydromagnesite form in Earth surface environments via reactions (6.1a) and (6.2) only when strong evaporation occurs (e.g. in evaporitic or hot terrestrial soil environments).

Instead, natural mineral weathering processes generally remove CO_2 from the atmosphere via carbonic acid neutralisation to form soluble bicarbonates. In the case of olivine of typical natural composition (Mg:Fe ratio > 90%), reaction with water and atmospheric CO_2 leads to the formation of soluble bicarbonates through the reaction [*Lackner*, 2002; *Schuiling and Krijgsman*, 2006]

$$(Mg,Fe)_2SiO_{4\,(S)} + 4H_2O_{(l)} + 4CO_{2\,(g)} \leftrightarrow 2(Mg^{2+}, Fe^{2+})_{(aq)} + 4HCO_{3\,(aq)}^{-} + H_4SiO_{4\,(aq)} \quad (6.3)$$

Sequestering CO_2 in the form of bicarbonates via this reaction requires only 1 tonne of pure Mg-olivine to fix 1.25 t of CO_2 (CO_2:olivine uptake ratio $Q = 1.25$). If the products remain stable, this makes the reaction much more efficient than mineralisation via reactions (6.1a) or (6.2), which can sequester only 0.625 and 0.5 t of CO_2 per tonne of olivine, in magnesite and hydromagnesite respectively.

Extensive data on dissolution/precipitation kinetics in geomaterials in aqueous environments indicate that the rate limiting step of CO_2 mineralisation (reactions (6.1) and (6.2)), and of weathering reactions such as (6.3), is the dissolution rate of the reacting silicate minerals rather than the dissolution rate of CO_2 in solution or the precipitation of secondary phases [see these references and others therein - *Tödheide and Franck*, 1963; *Amrhein and Suarez*, 1992; *Lebrón and Suarez*, 1998; *Pokrovsky and Schott*, 2000; *Köhler et al.*, 2003]. Dissolution of olivine is controlled by the adsorption of H^+ on the olivine surface, exchanging Mg^{2+} ions for protons. The removal of protons from solution, increases pH and alkalinity and results in an increase in the dissolved inorganic carbon (DIC) content of the fluid phase, i.e. in

aqueous HCO_3^-, CO_3^{2-} and CO_2 concentrations [*Schulz et al.*, 2006]. This is the basic sequestration mechanism proposed by Schuiling.

Similar mechanisms of increasing seawater alkalinity to enhance marine CO_2 sequestration capacity have been suggested previously in the literature, notably via the addition of artificial alkali in the form of NaOH [*House et al.*, 2007], or by enhanced weathering of alkaline minerals, such as calcite [*Kheshgi*, 1995; *Archer et al.*, 1997; *Rau and Caldeira*, 1999; *Rau et al.*, 2007], sodium carbonate [*Kheshgi*, 1995; *Lackner*, 2002], and (ultra)mafic rocks [*Lackner*, 2002]. It is recognised by the authors, however, that such approaches may affect marine life and to date neither of these methods have been applied.

6.3 Dissolution of olivine under Earth surface conditions

In the following, we consider the available data on the kinetics of olivine dissolution and on the effects of solution composition and dissolution progress, as a basis for estimating CO_2 uptake rates through coastal weathering of crushed olivine.

6.3.1 Dissolution rate of olivine: Effect of pH and temperature

At pH values in the range $1 < pH < 8.5$, it is well-established that the steady state dissolution rate of forsteritic olivine (i.e. Fo_{89}-Fo_{100}, with Mg:Fe ratios of 89-100%) is proportional to the square root of the hydrogen ion concentration [*Blum and Lasaga*, 1988; *Wogelius and Walther*, 1991; 1992; *Pokrovsky and Schott*, 2000; *Oelkers*, 2001; *Golubev et al.*, 2005; *Hänchen et al.*, 2006]. The most recent data available on the dissolution rate parameter R_{diss} (mol/m^2 s) in solutions with controlled pH at 25°C are summarised in Figure 6.1. At Earth surface pH values [pH 4.0-8.2 - see for example *Millero et al.*, 1993; *Motavalli et al.*, 1995], the mean values of R_{diss} lies in the range $1.58 \cdot 10^{-10} \pm 1.40 \cdot 10^{-10}$ mol/m^2 s to $3.79 \cdot 10^{-9} \pm 2.85 \cdot 10^{-9}$ mol/m^2 s (Figure 6.1). The activation energy for the dissolution process has been determined to be 79.5 ± 10.5 kJ/mol in the temperature range 25 to 65°C, at a pH of 1.8 to 9.8 [*Wogelius and Walther*, 1992], and 52.9 ± 6.9 kJ/mol in the temperature range 90-150°C at pH 2 to 8.5 [*Hänchen et al.*, 2006]. Thus, taking the activation energy of 79.5 ± 10.5 kJ/mol for olivine dissolution determined by *Wogelius and Walther* [1992], increasing the temperature from 25°C to 30°C (tropical seawater) or 40°C (terrestrial tropics) will increase the mean dissolution rate by a factor of 1.6-3.8 (30°C) or of 1.8-5.7 (40°C). However, while 25°C may be a reasonable mean seawater temperature at low to intermediate latitudes (45°S-45°N), at higher latitudes, such as those of Western Europe, a typical mean seawater temperature of 15°C is more likely. Lowering the seawater temperature from 25 to 15 degrees decreases the dissolution rate of olivine

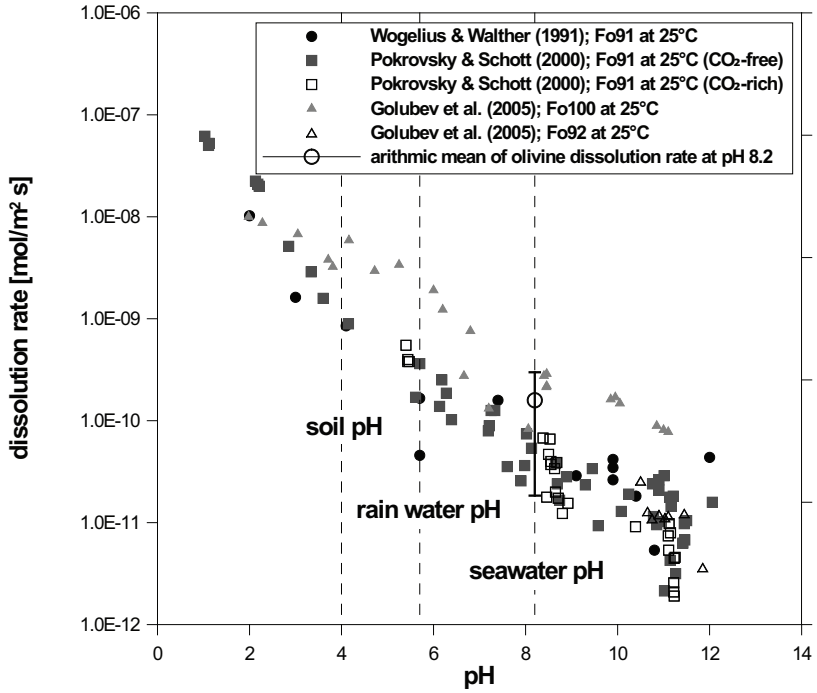

Fig. 6.1 Available data on the dissolution rate R_{diss} (mol/m^2 s) of olivine (Fo$_{91}$-Fo$_{100}$) in water as a function of pH at 25°C [after *Golubev et al.*, 2005; *Pokrovsky and Schott*, 2000; *Wogelius and Walther*, 1991]. The dissolution rate range representing seawater conditions, at a pH of ~ 8.2, is indicated and is given as $1.58 \cdot 10^{-10} \pm 1.40 \cdot 10^{-10}$ mol/m^2 s (see ○ and error bar). Thus one order of magnitude variability is present in the data at these conditions. Decreasing pH to 5.7 (rain water pH) and 4.0 (acid soil pH) increases the dissolution rate by approximately one and two orders of magnitude, respectively.

by a factor of 2.6 to 3.5. Compared to the dissolution rates of other minerals with a suitable composition for CO_2 trapping, such as Ca-rich feldspars, the dissolution rate of olivine is 1 to 2.5 orders of magnitude faster [*Amrhein and Suarez*, 1992; *Oxburgh et al.*, 1994] at 25°C and a typical seawater pH of ~ 8.2 [*Millero et al.*, 1993; *Krauskopf and Bird*, 1995]. It should be noted, however, that the dissolution rate of olivine is still very low.

6.3.2 Effect of fluid composition on dissolution rate

Aside from effects of pH through acid or alkali addition, relatively little research has been done on the effect of solution composition on the dissolution rate of olivine. In experiments performed at 25-65°C, atmospheric pressure and pH 1-12, it has been observed that the presence of aqueous magnesium or silica in solution at concentrations up to 4M, does not affect the dissolution rate R_{diss} [*Pokrovsky and Schott*, 2000; *Oelkers*, 2001; *Olsen*, 2007]. This is because olivine is highly unstable under such conditions and very far from equilibrium. Recent dissolution experiments performed on olivine in single electrolyte solutions containing $MgSO_4$, Na_2SO_4, $Mg(NO_3)_2$, or KNO_3, in the pH range 2 to 4 and of varying ionic strength ($I < 12$ M), show that these

components likewise have no significant effect on dissolution rate at ambient pressure and temperature [*Olsen*, 2007].

Accelerated olivine dissolution and reaction rates with CO_2 have been achieved at elevated pressure and temperature (8-15 MPa $P_{CO2,}$ 115-185°C) by the use of bicarbonate/salt solutions with a composition of 1 M NaCl and 0.5 to 0.64 M $NaHCO_3$ [*O'Connor et al.*, 2000a; *O'Connor et al.*, 2000b; *O'Connor et al.*, 2005; *Gerdemann et al.*, 2007]. *O'Connor et al.* [2000a] observed an increase in reaction rate by a factor of about four. This was attributed to the formation of intermediate magnesium chloride complexes, which reduce the activity of Mg^{2+} in solution, and hence increase the solubility of olivine [*O'Connor et al.*, 2000a]. On the other hand, *McKelvy et al.* [2005] claim little effect of NaCl but a substantial increase in reactivity (conditions: 185°C, 15 MPa P_{CO2}) due to the joint effect of HCO_3^- and $CO_{2\,(aq)}$. *Prigiobbe et al.* [2009] also observed no significant effect of NaCl (< 1 M) on the dissolution rate of olivine at elevated temperatures. It remains difficult to extrapolate results on the effects of NaCl obtained at elevated temperature and pressure to weathering conditions, so more uncertainty remains here. Nonetheless, a major effect of NaCl on olivine dissolution rate at ambient conditions seems unlikely.

The effect of carbonate ions in solution is unclear. *Pokrovsky and Schott* [2000] report that in alkaline solutions with pH > 8, olivine dissolution is strongly inhibited when the activity of carbonate ions ($a(CO_3^{2-})$) exceeds 10^{-4} M. However, in a more recent study by *Golubev et al.* [2005] it was shown that neither HCO_3^- nor CO_3^{2-} in solution has an effect on the olivine dissolution rates in the pH range 1-12 at 25°C. *Golubev et al.* [2005] noted that in the study of *Pokrovsky and Schott* [2000] both pH and CO_3^{2-} concentrations were subject to large uncertainties, which made it difficult to differentiate independently between the effects of pH and CO_2 on dissolution rates.

On the basis of all this, we assume that the dissolution rate parameter R_{diss} for olivine at 25°C and $4 \leq pH \leq 9$ (Figure 6.1), hence at Earth surface conditions, is probably not affected by the presence of bicarbonate or carbonate ions in solution, and is probably insensitive to common salts. In contrast, at temperatures in the range 25-150°C, organic acids, like citric acid, potassium hydrogen phthalate (KHP), and ascorbic acid (ASC), significantly enhance olivine dissolution rates, compared to rates measured in the same pH range in the absence of organics. The effect of organic acids is largest in the near-neutral pH range, $5 < pH < 7$, due to the formation of surface complexes [*Wogelius and Walther*, 1991; *Hänchen et al.*, 2006; *Prigiobbe et al.*, 2009], and can constitute an acceleration of a half to one order of magnitude. Such acids are particularly important in soils, so are of interest in relation to the possibility of terrestrial carbonation of olivine [*Jonckbloedt*, 1997]. We could find no data on the effects of organic acids in seawater, but in view of the relatively high pH of seawater (~ 8), it is reasonable to suppose that organic acids will be of minor importance in a

marine environment.

6.3.3 Effects at the dissolving olivine surface

Many silicates, like feldspars, micas and olivine, show the progressive formation of secondary coatings [*Murakami et al.*, 1998; *Hodson*, 2003; *McKelvy et al.*, 2005] or cation-depleted layers [*Inskeep et al.*, 1991; *Kalinowski and Schweda*, 1996; *Hellmann et al.*, 2003; *McKelvy et al.*, 2005] on dissolving surfaces. *Pokrovsky and Schott* [2000] suggested that preferential release of Si at pH > 9 could lead to the formation of an Si-depleted, $Mg(OH)_2$-like layer on the surface of olivine in solutions of pH > 9, which can inhibit olivine dissolution. At the lower pH's expected in Earth surface environments, an Mg-depleted surface layer develops with time [*Wogelius and Walther*, 1991; 1992]. Such Si-rich or $Mg(OH)_2$-like layers may progressively limit the dissolution rate, as diffusion of ions from the mineral surface through the depleted layer into solution will eventually become rate controlling. However, in a situation where olivine sand is distributed on beaches, it is likely that wave motion will abrade the grains, reducing any tendency to build up thick surface layers [*McKelvy et al.*, 2005]. Retarding effects of surface layer formation on dissolution rate are therefore expected to be minimal.

6.3.4 Practical estimates of R_{diss}

We have shown above that the dissolution kinetics of olivine in the pH range relevant for seawater [pH 7.9-8.4 - see *Millero et al.*, 1993] are insensitive to the presence of most salts and to the concentrations of Mg^{2+} and Si. Grain abrasion in coastal environments further implies that surface coating effects will be minimised. Additional processes, such as autogenous grinding of the grains in the surf zone, enhancing uptake rates, or the removal of material from the beach by wind and water influences, reducing uptake rates, are not taken into account, as these effects are site specific [*Martens*, 1931; *McBride et al.*, 1996]. We accordingly assume that the steady state dissolution rate parameter R_{diss} (Figure 6.1), with an activation energy of 79.5 kJ/mol [*Wogelius and Walther*, 1992], gives a reasonable upper bound for the dissolution rate of olivine in the pH range relevant to coastal spreading of olivine. For terrestrial spreading of olivine in the tropics, at 40°C and a soil pH of ~4, no organics considered, the same steady state data predict olivine dissolution rates some 200 to 600 times higher. Note, however, that the formation of surface coatings and the absence of grain abrading processes may strongly inhibit olivine dissolution in terrestrial environments.

6.4 Reaction progress with time and effect of grain size: a simple model

Applying the dissolution rate data presented in Figure 6.1, it is now possible to construct a model predicting how dissolution of a batch of olivine sand will proceed in a beach environment, in terms of dissolved mass or volume vs. time. This provides an upper bound basis for assessing CO_2 uptake rates via reaction (6.3) and whether or not the process is fast enough to be useful for CO_2 sequestration purposes in the coming decades. We assume that olivine sand is composed of spherical particles, which dissolve according to a shrinking core model with external mass removal of dissolved material. This is reasonable considering the washing effect of seawater on a beach. On this basis, the extent of dissolution of a single, instantaneously deposited batch of olivine, i.e. the fraction of reacted material as a function of time, can be expressed as

$$X_{olivine}(t) = \frac{d_0^3 - d(t)^3}{d_0^3} \times 100\% \quad (6.4a)$$

$$\text{with } d(t) = d_0 - 2R_{diss}\Omega t \quad (6.4b)$$

where $X_{olivine}$ is the amount of olivine to have dissolved [vol%], t is elapsed time since deposition [s], d_0 is the initial grain size [m], d is the grain size at time t [m], R_{diss} is the dissolution rate of olivine [mol/m^2 s] and Ω is the molar volume of olivine [43.02×10^{-6} m^3/mol]. As can be seen from Figure 6.1, at a solution pH of 8.2, as expected in natural seawater, the dissolution rate R_{diss} has an average value of $1.58 \cdot 10^{-10} \pm 1.40 \cdot 10^{-10}$ mol/m^2 s at 25°C. At 15°C, the dissolution rate of olivine will be 2.6-3.5 times slower, i.e. $5.93 \cdot 10^{-11} \pm 5.42 \cdot 10^{-11}$ mol/m^2 s.

The progress of the olivine reaction and of CO_2 uptake versus time after deposition, calculated from equation (6.4) and reaction (6.3) for a range of initial olivine grain sizes and for seawater temperatures of 25°C and 15°C, are shown in Figure 6.2. Recall here that one tonne of dissolved olivine traps 1.25 t of CO_2 (CO_2:olivine uptake ratio Q = 1.25). Reaction times (defined here as the time to dissolve 50-100%) of granular olivine are long even at grain sizes smaller than 300 μm. At 25°C for example (Figure 6.2a), olivine sand (grain size 300 μm), of the type proposed by Schuiling via the Dutch media, would take approximately 145 years to dissolve by half and 700 years to dissolve completely. Given the range of olivine dissolution rates at these conditions, the stated reaction times are only averages, since 50% dissolution of 300 μm grain size olivine may take between 75 and 1240 years, while complete dissolution may take between 370 and 6010 years. Decreasing the grain size strongly decreases reaction time, but will also require more energy for the grinding process. The corresponding times taken to trap 10, 25, 50 and 100% of the maximum amount of CO_2 that can be sequestered per tonne of olivine, through reaction (6.3) at 25°C, are also visible in Figure 6.2 and are listed in Table 6.1. Note that at 15°C (Figure 6.2b) reaction times

are about three times longer, as a result of the decrease in olivine dissolution rate. Thus on Western European coasts, 50% dissolution of sand-grade olivine (300 μm) will take on average about 450 years (225-3720 years). Clearly, grain size reduction to values < 10 μm is needed to accelerate the dissolution rate of olivine to levels that can contribute significantly to CO_2 sequestration in the next 15 years (Figure 6.2, Table 6.1).

To gain further insight into the progress of olivine dissolution and marine CO_2 uptake via reaction (6.3) under practical conditions, i.e. at a constant and continuous olivine supply rate, we have examined the situation where olivine of a given grain size d_0 is deposited at a steady, constant rate of S t/yr. For a constant, steady olivine supply scenario of this type, the rate of dissolution of a mass increment of olivine Sdt, at time

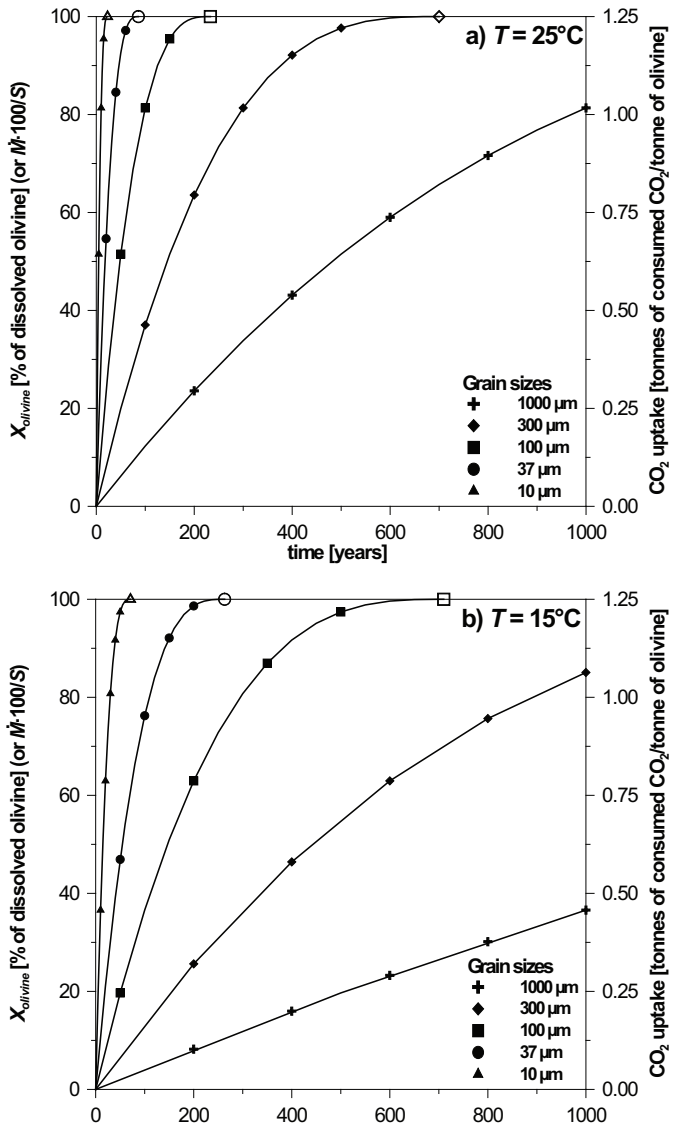

Fig. 6.2 The extent of granular olivine dissolution $X_{olivine}$ as a function of time. The left axis shows the extent of olivine dissolution reaction in terms of reacted mass-fraction (%) of deposited olivine, while the right axis shows the amount of CO_2 sequestered per tonne of dissolved olivine. The left axis also shows in %, the total normalised rate of olivine reaction where $\dot{M}$ is the total rate of reaction of olivine at time t in t/yr at a constant olivine supply rate of S t/yr. Open symbols indicate reaction times to reach steady state reaction, at constant olivine supply rate. It was assumed that dissolution of the olivine grains occurred by a shrinking core model. The amount of CO_2 sequestered per ton of olivine was calculated assuming reaction (6.3), which results in the formation of soluble magnesium bicarbonate salts and CO_2:olivine uptake ratio of 1.25 t CO_2 per ton olivine. a) Reaction progress at 25°C, assuming that the dissolution rate of olivine is $1.58 \cdot 10^{-10}$ mol/m^2 s (see Figure 6.1). b) Reaction progress at 15°C, with the olivine dissolution rate being $5.19 \cdot 10^{-11}$ mol/m^2 s (calculated using the dissolution rate at 25°C and an activation energy of 79.5 kJ/mol, following *Wogelius and Walther* [1992]).

t since deposition, is given by differentiation of (6.4) with respect to t to yield . The total rate of dissolution and hence reaction of olivine ($\dot{M}$) at any point τ in time, after initiation of olivine deposition, is then given by

$$\dot{M} = \frac{S}{100} \int_0^{\tau} \frac{\partial X_{olivine}(t)}{\partial t}\, dt = \frac{S}{100}\, X_{olivine}(\tau) \qquad (6.5)$$

where is measured in [t/yr] and t is time measured since deposition starts. This along with (6.4) demonstrates (a) that increases monotonically from zero with time, and (b) that when the rate of reaction attains a value equal to the supply rate of olivine S, a steady state situation is attained at which the olivine first deposited has been completely consumed ($X_{olivine}$ = 100%, $d(t) = 0$). From (6.4b), it is seen that this steady state is reached at a time t after deposition starts, given

$$t = \frac{d_0}{2\, R_{diss}\, \Omega} \qquad (6.6)$$

From equations (6.4) and (6.5), it thus emerges that when olivine is supplied at a fixed rate S, the total normalized rate of olivine reaction $\dot{M}(\frac{100}{S})$ evolves with time

Table 6.1
Summary of reaction times and CO_2 uptake for crushed olivine of various grain sizes (assuming beach reaction at 25°C)

Grain size [µm]	Time for 10% dissol. [years]	Time for 25% dissol. [years]	Time for 50% dissol. [years]	Time for 100% dissol. [years]
1000	80 (43-692)	213 (113-1832)	481 (255-4134)	2333 (1235-20039)
300	24 (13-207)	64 (34-550)	144 (76-1240)	700 (371-6012)
100	8 (4-69)	21 (11-183)	48 (25-413)	233 (124-2004)
37	3 (2-26)	8 (4-68)	18 (9-153)	86 (46-741)
10	1 (0.4-7)	2 (1-18)	5 (3-41)	23 (12-200)
CO_2 uptake [t CO_2/tonne olivine]	0.125	0.313	0.625	1.25

Dissolution of the olivine is assumed to follow a shrinking core model (equation 6.4). This will increase seawater alkalinity resulting in increased oceanic uptake of CO_2, and the sequestration of 1.25 t of CO_2 per tonne of olivine, according to reaction (6.3). Reaction time scales are calculated assuming the dissolution rate of olivine to be $1.58 \cdot 10^{-10} \pm 1.40 \cdot 10^{-10}$ mol/m^2 s at 25°C and pH = 8.2. Bracketed quantities represent the time scale range for the range of dissolution rates applying to beach reaction at 25°C ($1.58 \cdot 10^{-10} \pm 1.40 \cdot 10^{-10}$ mol/m^2 s).

exactly as depicted for $X_{olivine}$ in Figure 6.2 (equation (6.5)). Similarly, the steady state situation ($\dot{M} = S$), attained at $t = \frac{d_0}{2\, R_{diss}\, \Omega}$ is seen to correspond to the point in Figure 6.2 at which $X_{olivine}$, for individual grain sizes, attains the value of 100%. On this basis, we can see from equation (6.5) and Figure 6.2a, that to attain a steady state olivine consumption rate $\dot{M} = S$, and corresponding CO_2 uptake rate $\dot{C} = Q\dot{M} = 1.25\dot{M}$ for reaction (6.3), at 25°C, takes 700, 233, and 23 years for grain sizes of 300, 100, and 10 μm respectively. At 15°C, these times are increased by a factor of approximately 3.

It also emerges from (6.5) and from the relation $\dot{C} = 1.25\dot{M}$ that constant total

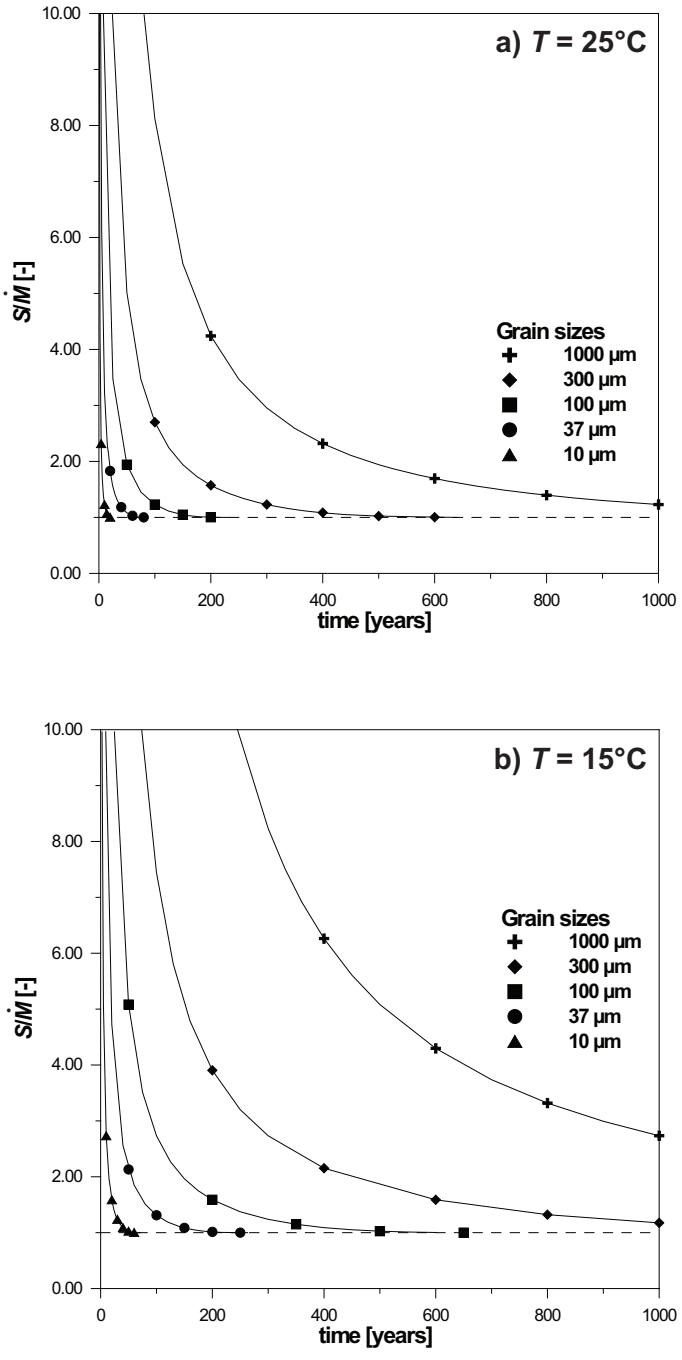

Fig. 6.3. Ratio of olivine supply rate S (t/yr) to total olivine dissolution or reaction rate $\dot{M}$ (t/yr) as a function of time. The graphs illustrate how supply rate S should vary with time to maintain a constant olivine consumption rate $\dot{M}$ and hence constant CO_2 uptake rate of $\dot{C} = 1.25\dot{M}$. Calculations were made with the same assumptions used in Figure 6.2, and using the relation $S/\dot{M} = 100/X_{olivine}(t)$. The plots show that very large quantities of olivine are required in the early stages of deposition, while smaller amounts will suffice as steady state is approached. a) Supply rate to dissolution rate ratio at 25°C. b) Supply rate to dissolution rate ratio at 15°C.

reaction and sequestration rates $\dot{M}$ and $\dot{C}$ can be achieved by varying the olivine supply rate S such that the product $SX_{olivine}(t)/100$ is constant, i.e. by varying S with time according to the relation $S = \frac{100\dot{M}}{X_{olivine}(t)}$ or $\frac{S}{\dot{M}} = \frac{100}{X_{olivine}(t)}$. However, this requires very large quantities of olivine to be deposited per year during the early stages of beach spreading (high S values), while smaller amounts of olivine (lower S values) will suffice as the steady state condition $\dot{M} = S$ is approached (see Figure 6.3). At 15°C for example (Figure 6.3b), the supply rate S of 300 μm grade olivine sand would have to be more than 10 times the target reaction rate $\dot{M}$ (hence more than 8 times the target CO_2 uptake rate $\dot{C} = 1.25\dot{M}$) for the first 80 years or so of olivine deposition. In addition, one should realise that once the method of coastal olivine weathering is applied on a large scale, the process itself cannot be stopped until all deposited olivine is consumed. It is safe to say that it is undesirable to create processes that keep absorbing CO_2 for decades or centuries to come.

6.5 CO_2 production due to mining and grinding

We have shown in Figure 6.2 and Table 6.1 that grain size reduction to values < 10-50 μm is needed to accelerate the dissolution rate of olivine to levels that can contribute significantly to CO_2 sequestration by beach reaction in the next 15 years. However, the overall efficiency of CO_2 sequestration depends on the amount of carbon dioxide produced during mining, grinding and transportation of the material. Though olivine-rich rocks are found in several major massifs around the world, they are very resistant to grinding, they are heavy (dense) and the source regions are often remote from the world's coastlines. The mining, crushing/grinding and transportation steps of beach weathering must therefore be considered carefully. For example, importing olivine to the Netherlands from the nearest source in Norway implies ~1000 km transportation. In this section, an attempt will be made to estimate the amount of CO_2 that is emitted during these various steps.

The estimates presented here are based on a study performed [*CIPEC*, 2005] by the Canadian Industry Program for Energy Conservation, on 7 open-pit gold and iron ore mines in Canada. Since the gold and iron ore in question is associated with (ultra) mafic rocks [*Nurmi*, 1991; *Stendal and Ünlü*, 1991] or materials of similar hardness, the data reported by CIPEC can be considered reasonably representative for the mining of olivine-rich rocks such as peridotite and dunite. Though the pure olivine content of peridotites and dunites generally varies between 60 and 90%, we assume these olivine sources to be 100% ore grade, following previous studies on olivine mining [*O'Connor et al.*, 2005; *Gerdemann et al.*, 2007]. Therefore, no beneficiation (i.e. ore quality improvement by separating ore from waste material) is considered. The use of

peridotites with only 60% olivine, instead of pure olivine, would clearly mean almost a doubling of the mass of material that has to be mined and processed, so a doubling of the associated CO_2 footprint.

In the following mining calculations, only energy consumption and hence CO_2 production during drilling, blasting, excavating, and transport (or hauling) to a crusher, are taken into account. Additional costs may be incurred in mine dewatering and in providing mine support equipment and services [*CIPEC*, 2005]. As can be seen in Table 6.2, the total energy consumption estimated for olivine mining is ~5 kWh/tonne. CO_2 emission rates for pulverised coal, coal gasification and natural gas power plants are reported to be 0.795 kg CO_2/kWh, 0.757 kg CO_2/kWh, and 0.358 kg CO_2/kWh, respectively [*Rubin et al.*, 2004]. Taking these emission rates, CO_2 production during olivine mining would fall in the range 1.5-3.3 kg CO_2/tonne CO_2 sequestered (Table 6.2).

After mining, a series of crushing and grinding procedures have to be performed to produce olivine of a suitable grain size distribution (Table 6.2). Firstly, primary in-pit crushing, performed by jaw or gyratory crushers [*Guimaraes et al.*, 2007], reduces the mined material to a grain size of approximately 1 to 300 mm [*TKRI*, 2004]. For gold or iron ore, this requires roughly 1.3 kWh/tonne of ore produced [*CIPEC*, 2005]. This value is similar to the 2.0 kWh/tonne determined for the crushing of olivine, serpentinite and wollastonite, based on data from the U.S. Bureau of Mining [*O'Connor et al.*, 2005]. In terms of CO_2 emissions, primary crushing would thus lead to the production of 0.37-0.82 kg CO_2/tonne CO_2 sequestered [*Rubin et al.*, 2004].

Primary crushing is followed by secondary grinding. The energy consumption W during this can be calculated using Bond's Equation [*Perry and Green*, 1987; *Morrel*, 2004]. This equation assumes grain size reduction from a feedstock with an 80% passing size of d_∞ to a product with an 80% passing size of d μm, and is written as

$$W = 10 W_i \left(\frac{1}{\sqrt{d}} - \frac{1}{\sqrt{d_\infty}} \right) \qquad (6.7)$$

where W is the energy [kWh/tonne] required to reduced the feedstock to the desired grain size and W_i is an empirical work index of the feedstock material [kWh/tonne]. The work index for olivine has been taken to be the average of those found for Fe_2O_3 (8.6 kWh/tonne) and silica sand (16.46 kWh/tonne) which have similar hardness, i.e. 12.38 kWh/tonne [*Perry and Green*, 1987]. For final grain sizes in the range 37-70 μm, *Perry and Green* [1987] added an empirical multiplying factor F to equation (6.7), given as $F = \frac{10.3 + d}{1.145d}$. Tertiary ultra-fine grinding, from 37 μm down to 10 μm, using a scalable stirred media detritor (SMD) mill has been shown, by direct measurement, to consume ~150 kWh/tonne for olivine, wollastonite and serpentinite [*O'Connor et al.*, 2005]. Assuming a typical average feedstock grain size of 200 mm, the grinding

Table 6.2
Energy consumption and CO_2 production during olivine mining, crushing, grinding and transportation

Mining procedures				
	Energy consumption during mining [kWh/t olivine][a]	**CO_2 emission[b] [kg CO_2/t CO_2 sequestered]**		
		(1)	**(2)**	**(3)**
Drilling	0.35	0.22	0.21	0.10
Blasting	0.44	0.28	0.26	0.13
Excavation	0.95	0.61	0.58	0.27
Transport/ hauling	3.49	2.22	2.11	1.00
Total	5.23	3.33	3.16	1.50

Crushing and grinding							
Grain size [µm]	**Energy consumption during crushing/ grinding procedures [kWh/t olivine][c]**				**Total CO_2 emission[b] [kg CO_2/t CO_2 sequestered]**		
	(A)	**(B)**	**(C)**	**Total (A+B+C)**	**(1)**	**(2)**	**(3)**
1000	1.3	3.64		4.94	3.14	2.99	1.42
300	1.3	6.87		8.17	5.20	4.94	2.34
100	1.3	12.10		13.40	8.52	8.11	3.84
37	1.3	22.41		23.71	15.08	14.36	6.79
10	1.3	22.41	150	173.71	110.48	105.20	49.75

Transport		
	CO_2 emission [g CO_2/t olivine]	**CO_2 emission [kg CO_2/100 km/ t CO_2 sequestered]**
Inland/coastal ships	30	2.4
Freight train	20	1.6
Trucks	138	11.0

[a] Note that 1 kWh = $3.6 \cdot 10^6$ J. Estimates based on gold/iron mining; see text.
[b] (1) powdered coal; (2) coal gasification; (3) natural gas power plant
[c] (A) primary in-pit crushing; (B) secondary grinding (to 37 µm); (C) tertiary grinding (ultra-fine grinding - 10 µm)

energy and CO_2 production values implied for various final grain sizes are shown in Table 6.2.

For synoptic purposes, the total CO_2 emissions produced by mining, crushing, and grinding one tonne of olivine, or per tonne CO_2 avoided, calculated as a function of grain size, are depicted in Figure 6.4. The pure olivine feedstock grain size has been set at 200 mm. It is clear from Figure 6.4 that carbon dioxide emissions (and of course costs) increase with decreasing final grain size. For final grain sizes larger than approximately 40 μm, carbon dioxide sequestration efficiency is reduced by less than 2% (< 20 kg/tonne CO_2 sequestered). However, at a final grain size of 10 μm, CO_2 emissions as a result of mining, crushing and grinding constitute between 5 and 11% of the total amount of sequestered CO_2.

The calculations presented so far do not include energy consumption associated with transport from the mine to the location of deposition. In general, the means of transportation may include ships, trains and trucks. A British study on CO_2 emissions from freight transport [*McKinnon*, 2006] has shown that CO_2 emissions per tonne of transported materialare 30 g/km for inland or coastal ships, 20 g/km for trains, and 138 g/km for trucks. This will result in an additional efficiency reduction of 1.6-11.0 kg CO_2/100 km/tonne CO_2 sequestered or of 0.1-1% (Table 6.2). Hence, for an 1000-4000 km boat haul to import crushed olivine from the nearest sources in Norway, Greenland or Turkey to Western Europe, an additional CO_2 output of at least 24-96 kg CO_2/tonne CO_2 sequestered would be generated.

This all means that the efficiency reduction of olivine beach sequestration would be around 10-20% for locations that are remote from the olivine sources (like Western Europe) and up to 10% for locations near source (e.g. coast of Turkey). Since most olivine-rich rocks are ~60% olivine, more realistic figures are probably 15-30% and

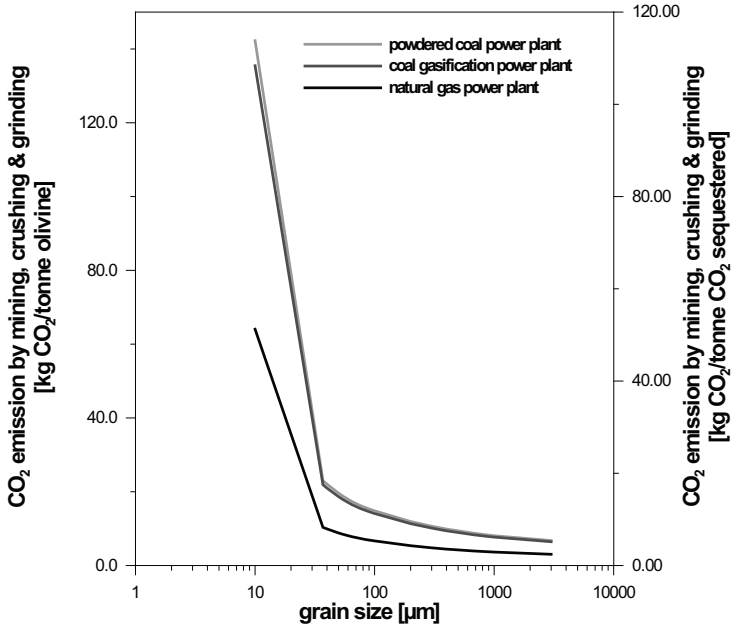

Fig. 6.4 Estimates of CO_2 emissions produced during mining, crushing and grinding of one tonne of pure olivine feedstock (grain size 200 mm) to a given grain size, assuming a four-stage process for the finest grain size (10 μm).

up to 15% respectively. In addition, CO_2 costs associated with building the extra production and transport facilities needed to mine and move large amounts of olivine will reduce sequestration efficiency further still, but this needs more research.

6.6 Feasibility of CO_2 sequestration via coastal spreading of olivine

In order to assess the feasibility of coastal spreading of olivine as s sequestration method, all of the factors discussed above have to be taken into account - the relevant reaction, the olivine dissolution rate, the reaction progress, the grinding, mining and transportation energies and the amount of olivine required. Our starting point is our reaction progress model for olivine "sand" embodied in equations (6.4) and (6.5). The assumption that reaction (6.3) will occur with a CO_2:olivine uptake rate Q of 1.25, the "upper bound" mean value of R_{diss} used and the assumption of pure olivine, mean that the model likely overestimates the effectiveness of beach reaction of olivine.

In the following, we apply our model to examine the feasibility of beach weathering of olivine to offset CO_2 emissions in two reference scenarios. To date no consensus has been reached on the required CO_2 emissions reductions. Within the EU it has been proposed that CO_2 emissions reductions of up to 30% of 1990 levels are required by 2020, and up to 80% by 2050 [*Commission of the European Union*, 2007]. Schuiling has suggested that coastal weathering of olivine can replace technological solutions, such as CCS, to achieve such targets [*Biersma*, 2007; *Eshuis*, 2007; *Tangerman*, 2009]. Our first reference scenario therefore involves offsetting 30% of global CO_2 emissions through coastal weathering of olivine by 2020, while the second scenario involves offsetting 30% of Dutch CO_2 emissions by 2020 (all percentages are of 1990 levels).

6.6.1 Global scenario

In 1990 the world's yearly CO_2 emission, resulting from the burning of fossil fuels, was approximately 21 Gt [*Bernstein et al.*, 2007]. Offsetting worldwide CO_2 emissions by 30% of 1990 levels through olivine weathering according to reaction (6.3) with Q = 1.25 would thus consume approximately 5.0 Gt of olivine per year. The mass needed for industrial mineralisation via reactions (6.1a) or (6.2) would be approximately twice this amount.

To illustrate the amount of olivine reacting $\dot{M}$, and the amount of CO_2 being consumed $\dot{C}$ per year, at a constant olivine supply rate of S = 5.0 Gt/yr, we constructed Figure 6.5a, using our reaction progress model (equations 6.4 and 6.5) applied for a mean global seawater temperature of 25°C and a dissolution rate in seawater of $1.58 \cdot 10^{-10}$ mol/m^2 s (Figure 6.1). From Figure 6.5a (see also Figure 6.2a), it can

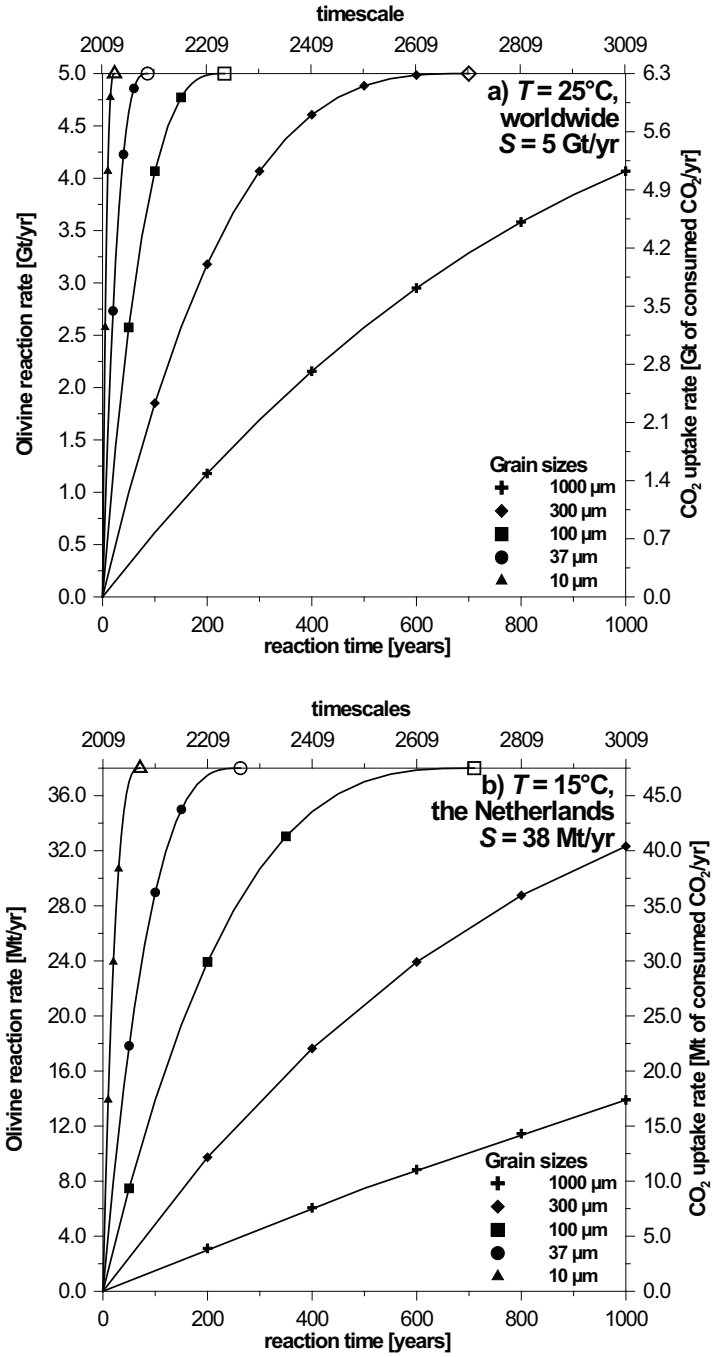

Fig. 6.5 The amount of granular olivine reacting per year ($\dot{M}$, left axis) and the equivalent amount of CO_2 consumed per year ($\dot{C}$, right axis) as a function of time, at constant olivine supply rates *S*. Open symbols indicate reaction times to reach steady state reaction (rate of olivine reaction balances rate of supply). It was assumed that dissolution of the olivine grains occurred by a shrinking core model. The amount of CO_2 sequestered per year was calculated assuming reaction (6.3), which results in the formation of soluble magnesium bicarbonate salts and a CO_2:olivine uptake ratio of 1.25 t CO_2 per tonne olivine. a) *S* = 5 Gt/yr, equivalent to a 30% reduction in worldwide CO_2 emissions. The dissolution rate of olivine was set at $1.58 \cdot 10^{-10}$ mol/m² s, assuming seawater temperature is 25°C (see Figure 6.1). b) *S* = 38 Mt/yr, equivalent to a 10% reduction in Dutch CO_2 emissions. Seawater temperature was assumed to be 15°C with the dissolution rate of olivine being $5.19 \cdot 10^{-11}$ mol/m² s (calculated using the dissolution rate at 25°C and an activation energy of 79.5 kJ/mol, following *Wogelius and Walther* [1992]).

be seen that at this supply rate it would take 700 years to reach the desired steady state olivine consumption and CO_2 uptake rates at a grain size of d_0 = 300 µm and a seawater temperature of 25°C. Similarly, at a grain size of d_0 of 100 µm or 10 µm it would take 230 and 23 years respectively (see also Section 6.4). To achieve a steady state emissions rate offset of 30% in 15 years (i.e. by 2024) at 25°C, equation (6.6) shows a grain size of approximately 6 µm would be required. Since the instantaneous rate of olivine consumption $\dot{M}$ scales linearly with supply rate (equation (6.5)), using olivine grain sizes greater than ~ 6 µm would require proportionally larger supplies of

olivine (> 5.0 Gt/yr), to achieve the same offset in atmospheric CO_2 concentrations in the same time. The (vast) magnitude of the increased olivine supply rates *S* needed are predicted by Figure 6.3, setting $\dot{M}$ at the steady state values $\dot{M} = S = 5.0$ Gt/y.

In colder regions, i.e. at 15°C, steady state sequestration rates take approximately three times longer to reach than at 25°C (Figure 6.2b), so the supply rate of olivine needed has to be tripled (15.0 Gt/yr), or else, following (6.6), three times smaller grain sizes are required (e.g. 2 μm), to achieve the same sequestration target within a given time scale (e.g. 15 years). Coastal spreading of olivine in warmer areas will decrease reaction times by a factor of 1.7 times if the temperature is raised to 30°C, and even by 4.6 times if temperature increases to 40°C. In this case of 40°C, equation (6.6) shows that grain sizes of 30 μm could be used to reach equivalent steady state reduction rates of 5.0 Gt/yr in 15 years.

The above shows that to offset global CO_2 emissions by 30% within a timescale of 15-20 years, by beach weathering alone, requires 5.0 Gt/yr, or more of fine (10 μm grade) olivine powder to be mined, handled, transported and spread. We have already shown that the CO_2 cost of such operations will be of the order of 15% of the CO_2 removed from the atmosphere. Assuming that the broader environmental impact is acceptable, the question remains as to whether the transportation of such vast solid masses is feasible. A truck can typically transport 50 t, while the most commonly used cargo ship, the so-called Handysize, can carry 25 kt on average. Sequestration levels equivalent to an approximate 30% reduction in 1990-level worldwide carbon dioxide emissions (i.e. 6.25 Gt/yr) would therefore mean moving 100 million truckloads, or 200,000 shiploads of olivine on a yearly basis, that is 1.9 million truckloads, or 3800 shiploads, on a weekly basis. Given that the entire worldwide fleet of Handysize cargo ships is around 2000 vessels, and assuming a roughly 1-week round trip for each vessel, this means that it would be necessary to roughly double the fleet within a few years, to reach the desired CO_2 uptake targets. While this neglects road transport aspects, it nonetheless illustrates the magnitude of the mass transport problem. Though it may be possible to expand the current fleet, the large ship building expenses will bring about a significant increase in the costs of the proposed method and will affect the "cheap" character it has been given in the media. Given the current world fleet, we infer that transporting 5.0 Gt of olivine per year is an impractical task and we suggest that the maximum achievable haulage would be between 5 and 10% of this figure. This implies that the maximum possible CO_2 uptake by beach reaction of olivine would be between 1.5% and 3% of 1990-level emission rates, neglecting the additional CO_2 costs of expanding the transport fleet to cope.

6.6.2 The Dutch scenario

We now consider what the above would all mean for an industrialised Northern

hemisphere country, like the Netherlands, in a situation where emissions trading is not possible. In 1990, the Dutch CO_2 emission rate was 158 Mt/yr [*Brandes et al.*, 2006]. A 30% reduction in this amounts to ~ 47 Mt/yr. Assuming a constant olivine supply rate of S = 38 Mt/yr (equivalent to a 30% reduction in CO_2 emissions by olivine weathering at steady state) and a mean seawater temperature of 15°C (R_{diss} = $5.19 \cdot 10^{-11}$ mol/m^2 s), our reaction progress model predicts the evolution of olivine reaction rate $\dot{M}$, and the CO_2 uptake rate $\dot{C}$ per year, depicted in Figure 6.5b. From this figure and the underlying equations (6.4, 6.5 and 6.6), it is clear that sand-grade olivine (100-300 μm) will simply react too slowly to have a significant impact in the coming decades, achieving CO_2 uptake rates of just 2-4 Mt/yr, which is equivalent to only 1-3% of 1990 Dutch emissions. In order to achieve an equivalent of a 30% steady state reduction in CO_2 emissions in approximately 15 years by olivine beach weathering, equation (6.6) shows that a grain size of 2 μm or less is required. This value approaches the theoretical limit of grain size reduction and would be highly energy/CO_2 inefficient in practice (Figure 6.4). In addition, the haulage of 38 Mt of olivine per year, that is 0.7 Mt per week, implies the movement of 14,600 50-t olivine trucks on the already choked Dutch road network, or the passing of 29 Handysize ships or dumper-vessels along the coast, on a weekly basis. On a yearly basis, the corresponding volume of olivine sand or powder deposited on Dutch beaches would be 16-32 Mm^3 (assuming 40% porosity, 50-100% olivine) equivalent to a strip of 10 m high, 100 m wide and 16-32 km long. As demonstrated by Figure 6.3b, to achieve a 30% equivalent emissions reduction ($\dot{C}$ = 43 Mt CO_2 per year, $\dot{M}$ = 38 Mt olivine per year) in the coming 15 years, using sand-grade (100-300 μm) olivine, would require an olivine deposition or supply rate S many tens or even hundreds of times greater, which is entirely impractical.

6.6.3 Synthesis

Our calculations for both the global (25°C) and Dutch (15°C) scenarios show that very fine-grained olivine (2-6 μm) is required to achieve significant steady state CO_2 uptake rates within a few decades. This makes beach spreading of olivine inefficient. In addition, impractically large amounts of olivine must be transported to achieve a significant impact in terms of CO_2 uptake. Moreover, it should not be forgotten that finely crushed olivine rock might very well pose a (wind-born) health risk, especially if the material contains fibrous serpentine minerals (asbestos), which it often does. Landward wind borne transport of such fine olivine powder could in itself pose problems. It is our conclusion that beach reaction is not a practical option for Northern hemisphere countries with mean coastal seawater temperatures of 15°C or less. On the other hand, given suitable emissions trading regulations, coastal weathering of olivine in hot, (sub)tropical areas, close to sites where olivine can be mined, could

perhaps contribute to offsetting global emissions at the 0.1-1% level. Such areas offer improved possibilities and costs, which may warrant further investigation from a niche market perspective. Clearly, coastal weathering of olivine cannot offer a stand-alone solution for CO_2 control and cannot replace CO_2 mitigation technologies, such as CO_2 capture and storage (CCS).

6.7 Coastal vs. land spreading

In addition to the 'Green Beaches' concept, the proposal by Schuiling to trap CO_2 from the atmosphere by terrestrial spreading olivine on acidified soils [*Schuiling and Krijgsman*, 2006; *Biersma*, 2007; *Eshuis*, 2007] also assumes reaction (6.3) and is expected to be controlled by olivine dissolution kinetics. We have shown above that coastal weathering is relatively slow and largely impractical. However, terrestrial spreading has several possible advantages over coastal spreading of olivine, as soils generally have a lower pH, typically around pH 4 and are rich in organic acids. These factors could potentially enhance olivine dissolution rates by a total of perhaps two orders of magnitude compared to dissolution in seawater (cf. Figure 6.1). In addition, terrestrial spreading of olivine in (sub)tropical areas would benefit from the higher temperatures, which will enhance dissolution rates further (up to 600 times at 40°C compared to 25°C). On the other hand, evaporation effects may lead to magnesite or hydromagnesite formation (reactions 6.1a and 6.2 instead of 6.3) reducing CO_2 uptake rates by up to a factor of 2. This all means that reaction rates for olivine spread on land in the tropics could be up to 200-600 times faster than for beaches. Though terrestrial spreading of olivine will encounter similar transport and infrastructural problems to coastal spreading, and while the possible impact upon agriculture, environment, ecology and human or animal health (fine olivine) remains to be clarified, it is inherently more promising and deserves further research.

6.8 Conclusions

This evaluation of the proposal to spread olivine sand (300 μm) along the coastlines of the world, in an attempt reduce atmospheric CO_2 concentrations through weathering reactions, has led to the following conclusions:

1. From the literature, we deduced that the dominant reaction is most likely $(Mg,Fe)_2SiO_{4\,(S)} + 4H_2O_{(l)} + 4CO_{2\,(g)} \leftrightarrow 2(Mg^{2+}, Fe^{2+})_{(aq)} + 4HCO_{3\,(aq)}^{-} + H_4SiO_{4\,(aq)}$, which has an uptake capacity of 1.25 t of CO_2 per tonne of olivine. Dissolution of olivine will be rate controlling, though verification of both the nature and rate of the dominant reaction is still required.

2. At temperatures of 15-25°C and pH's in the range 4.0 to 8.2, the dissolution rate of olivine is of the order of $1.6 \cdot 10^{-10} \pm 1.4 \cdot 10^{-10}$ mol/m^2 s to $3.8 \cdot 10^{-9} \pm 2.9 \cdot 10^{-9}$ mol/m^2 s. Increasing temperature, from 25°C to 30°C (tropical seawater) or 40°C (tropics, land), will increase olivine dissolution rates by up to about half an order of magnitude (factor 1.6 to 5.7).
3. For fixed rates of olivine supply, beach weathering of olivine with an initial grain size d_0 of 300 μm requires 700 years to reach a steady state CO_2 uptake rate at 25°C, and three times longer at 15°C (i.e. 2130 years). This is too slow to make a useful impact on atmospheric CO_2 levels in the coming decades. Grain size reduction to micrometer levels is needed on this timescale.
4. Mining, crushing and grinding of olivine to a grain size of less than 10 μm will reduce process efficiency by 5-11% for pure olivine and by 10-20% for typical olivine rock. An additional 0.1 to 1% efficiency reduction will be generated per 100 km of transport of one tonne of crushed olivine rock by ship, train, or truck. Typical transport distances in Europe would be ~1000 km.
5. Aiming for an equivalent of a global target of 30% steady state emissions reduction by 2020 would require coastal spreading of 5.0 Gt of 6 μm grain size (i.e. dust-grade) olivine per year, depending on seawater temperature (15-25°C). This is not feasible given the current global capacity of trucks and Handysize cargo ships. A 1.5-3% equivalent reduction might be feasible. It should be noted, however, that the necessary quantities of dust-grade mineral material (including asbestos-related serpentine minerals) may pose public health risks.
6. For an industrialised, Northern hemisphere country such as the Netherlands, with a mean seawater temperature of ~15°C, coastal olivine weathering would be very impractical. An equivalent target of 30% steady state emissions reduction by 2020 would require coastal spreading of 47 Mt of 2 μm, dust-grade olivine per year. This implies a vast increase in transport capacity, and again possible asbestos-related health risks. Spreading of 100-300 μm sized crushed olivine could result in a 1-3% offset in CO_2 emissions in the coming few decades.
7. We infer that coastal spreading of olivine is not a stand-alone solution for CO_2 sequestration and cannot replace technological options, such as CCS. However, beach weathering could contribute perhaps a 1% equivalent reduction as a niche activity, particularly in tropical regions where reaction rates are accelerated. More research on costs, logistics and seawater reaction rates is needed to clarify the possible contribution.
8. The biggest uncertainty in our calculations for beach weathering probably resides in the effect of seawater salt content, and other solute content, on the

dissolution rate of olivine. Available data suggest no effect of such solutes, but there is a possibility that Cl^- complexation may accelerate olivine dissolution to some minor extent. This needs further experimental investigation, but even if a doubling or tripling is observed, the rate of olivine dissolution in seawater will still be insufficient to render beach weathering a forefront CO_2 uptake method.

9. Terrestrial spreading of crushed olivine in tropical areas is more promising than beach reaction, especially on land with acidic soils. More research is needed on this, particularly on the reaction capacity and effect of the released Mg-ions on agriculture.

Acknowledgements

This research was financed by Shell International Exploration and Production (contract number 4600002284) and by the Dutch National Research Programme CATO (CO_2 capture, transport and storage) as part of WorkPackage 4 on Mineralisation. The motivation to conduct the work arose as a result of numerous questions raised in the Netherlands after media attention for the issue. Prof. Dr. R.D. Schuiling, Erik Lysen and an anonymous reviewer are thanked for their comments on earlier versions of this manuscript.

7

General conclusions and suggestions for future research

7.1 Conclusions

This thesis has presented the results of an experimental study, aimed at investigating the effect of CO_2 storage in geological formations on the chemical and mechanical behaviour of host or reservoir rocks and on overlying seal formations. The main aims included characterisation of key mineralisation reactions in feldspathic sandstones, determination of the effect of CO_2-water-rock interaction on creep phenomena in simulated sandstones, and determination of the effect of CO_2 injection and deformation on mechanical damage and permeability development in anhydrite caprock, i.e. on caprock integrity. These aims were tackled through in-situ batch reaction, compaction creep, triaxial compression and permeametry experiments. The work was carried out in the framework of the Dutch national carbon capture and storage research programme CATO, and focussed on issues relevant to the Dutch situation, notable to CO_2 storage in depleted natural gas reservoirs (sandstones) sealed by anhydrite caprock. Emphasis was placed on both chemical and mechanical phenomena and their interactions. Additional work was done on evaluating the concept of CO_2 removal from the atmosphere by beach weathering of olivine, in response to media attention for this as a possible alternative to CCS involving subsurface storage.

The principle conclusions of the study are summarised below, in relation to the main aims stated above.

7.1.1 CO_2 mineralisation reactions in feldspathic sandstones

From the batch reaction experiments on plagioclase feldspars (anorthite and albite) reported in Chapter 2, it is inferred that CO_2 mineralisation reactions are very slow, even under hydrothermal conditions (200-300°C, 0.4-15 MPa CO_2 partial pressure). Indeed, the reactions are too slow to be reliably quantified in laboratory experiments under in-situ conditions [*Hangx*, 2006]. In addition, the nature of the reactions strongly depends on conditions, fluid composition and fluid contamination, making comparison of experiments with geochemical modelling of subsurface mineralisation reactions difficult. It was expected that reaction of plagioclase feldspars with CO_2 and water or brine would give rise to carbonate precipitation (calcite and dawsonite). However, our experiments did not show precipitation of significant quantities of CO_2-bearing minerals. It was shown that carbonates would have been preserved if formed, and that a carbonate substrate was needed to promote precipitation. Instead of the expected carbonate-forming reactions, reactions precipitating boehmite, secondary clays (kaolinite and illite or smectite) and a hydrotalcite-like phase dominated. These minerals were also inferred to form under lower temperature CO_2 sequestration conditions (50-100°C), given systems with suitable fluid-rock composition. Our results imply that under CO_2 storage conditions in systems containing plagioclase, early clay precipitation may occur in advance of or alongside carbonate precipitation,

depending on the availability of suitable carbonate-substrate. Though an artefact in our experiments, hydrotalcite may play a positive role in the context of subsurface alkaline waste injection, by immobilising heavy metals, while carbonates will mineralise the CO_2.

7.1.2 Creep phenomena in sandstones and chemical-mechanical effects of CO_2 injection

Uniaxial compaction experiments have been performed on wet granular aggregates of quartz and feldspar (mean initial grain sizes between 25 and 425 μm) under a wide range of conditions (20-100°C, $4 \cdot 10^{-5}$-15 MPa CO_2 partial pressure, 20-100 MPa effective stress) and pore fluid compositions (organic acids, NaOH, $Ca(OH)_2$, NaCl, dry supercritical CO_2). Some experiments were complemented with acoustic emission measurements. Our results showed instantaneous compaction upon load application, followed by time-dependent deformation or creep. During the creep stage, which is the most relevant to assessing the long-term response of reservoir rock to CO_2 storage, increasing pH and salinity accelerated creep in both the quartz and feldspar samples. No evidence was found for pressure solution, dissolution processes or mineralisation reactions. For wet feldspar samples, a weak positive dependence of creep rate on grain size was observed, at fixed strains e ($\dot{\varepsilon} \propto d^{0.25}$). A power law crudely described the dependence of creep rate on applied effective stress ($\dot{\varepsilon} \propto \sigma^{1-2.5}$) at constant normalised porosity φ/φ_0 and we observed a weak Arrhenius dependence of creep rate on temperature with an apparent activation energy E_a of ~10 kJ/mol. The injection of high-pressure CO_2 into wet feldspar samples inhibited creep and enhanced the dependence of creep rate on grain size ($\dot{\varepsilon} \propto d^{0.5-2.5}$). In addition, injection of supercritical CO_2 into lab-dry, granular feldspar reduced creep rates even more than under lab-dry or wet/CO_2 conditions. From the mechanical, microstructural and acoustic emission data, it was inferred that the main compaction mechanism operating in wet quartz and feldspar samples, with and without added CO_2, was chemically enhanced microcracking leading to grain failure and particulate rearrangement. The rate of creep was controlled by subcritical crack growth, i.e. stress corrosion cracking. The effect of pH on this process suggests that the injection of CO_2 into quartz and plagioclase-bearing sandstones will inhibit grain-scale microcracking processes, under in-situ, reservoir conditions. Related geomechanical effects, such as reservoir compaction, surface subsidence, caprock bending and fracture, well-bore deformation and fault reactivation will therefore be negligible, both near injection wells and in the further field.

7.1.3 Mechanical behaviour of anhydrite caprock and the effect of CO_2

Triaxial compression experiments have been performed on anhydrite caprock samples taken from the base of the Dutch Zechstein Group, in order to assess the effect of fluids on the mechanical strength and volumetric behaviour of this material (Chapter 4). The experiments were done under dry, wet and wet/CO_2 conditions (T = 20-80°C, P_c = 1.5-50 MPa, P_f = 0.1-15 MPa). For our dry samples, we observed a transition from brittle to semi-brittle behaviour, an increase in peak strength with increasing confining pressure and a slight weakening with increasing temperature. Fluid penetration prior to failure led to a classical (Terzaghi-type) effective pressure effect on material strength, while volumetric strain evolution was unaffected. Fluid penetration during failure was too slow to affect mechanical or volumetric behaviour. No short-term chemical effects of aqueous fluids on the mechanical strength of anhydrite were observed, such as subcritical crack growth. However, the samples were penetrated with more ease by CO_2-saturated solution than by $CaSO_4$ solution, due to a lower interfacial tension of the former. We defined the failure and dilatation behaviour of dry Zechstein anhydrite at 20 and 80°C by determining corresponding envelopes in (Mogi) stress space. These envelopes are suitable for use with finite element modelling methods to predict caprock response to changing stress states, as a result of reservoir depletion or CO_2 injection. Simple analytical calculations showed that under, in-situ realistic conditions, changes in stress state resulting from caprock flexure are small and will not lead to mechanical damage or to any reduction in caprock integrity. Therefore, potential leakage of CO_2 into limestones interbedded with and overlying the anhydrite member at the base of the Dutch Zechstein is not expected. Though unlikely to compromise the integrity of caprock of typical thickness, long-term chemical interaction between anhydrite and CO_2 may affect material strength, transport properties and fault behaviour, as the reaction $CaSO_4 + H_2O + CO_2 \rightarrow CaCO_3 + H_2SO_4$ does occur under CO_2 storage conditions and results in a 20% decrease in solid volume. However, more work on this and on the penetration of anhydrite by water-saturated CO_2 is needed.

7.1.4 Permeability development in deforming anhydrite

As indicated under 3, mechanical damage development in anhydrite caprock under laboratory conditions results in dilatation and failure. Chapter 5 of this thesis investigated the effects of stress and deformation on the permeability of dry Zechstein anhydrite under conditions ranging from mechanically stable (intact, non-dilatant) through dilatant conditions and through failure. We performed triaxial experiments at room temperature and 3.5 to 25 MPa effective confining pressure, using argon gas transient pulse permeametry (P_p = 1-1.2 MPa). We again observed a transition from brittle behaviour to more semi-brittle behaviour with pervasive deformation, plus an

increase in peak strength with confining pressure. Overall, our results showed slightly lower values for peak strength and Young's Modulus, compared to the experiments on anhydrite summarised under point 3 above. This difference could be explained by the lower aspect ratio of the present samples, resulting in clamping and stress enhancement at the ends of the samples, as well as by the use of a 10-100 times lower strain rate. For anhydrite, the onset of (measurable) permeability ($\kappa > 10^{-21}$ m^2) is characterised by an increase in the rate of dilatation at low confining pressures, and by the turning point from compaction to dilatation in the volumetric vs. axial strain curves, at higher confining pressures. The observed permeability development is related to the establishment of a connected crack/void network, which can typically be explained by percolation theory for low permeability rocks undergoing microcrack damage. In addition, post-failure permeability measurements showed an inverse dependence of permeability on effective mean stress, which implied that new faults formed at depth (~ 3 km) will be of low permeability (< 10^{-19} m^2), and by virtue of their localized nature will impart negligible bulk permeability to a caprock formation. Coupled with the simple caprock flexure calculations described under point 3, confirm our results that caprock integrity loss due to mechanical damage will generally be negligible.

7.1.5 A critical analysis of coastal weathering of olivine

Chapter 6 provides a critical evaluation of the concept of CO_2 sequestration by coastal weathering of olivine sand (300 μm) concept, as proposed by Utrecht University emeritus Prof. R.D. Schuiling [*Biersma*, 2007; *Eshuis*, 2007; *Tangerman*, 2009]. This concept is postulated by Schuiling to have low risks, low costs and a green character, and is suggested to be a viable replacement for current CCS strategies. All this has led to much political and popular attention for the proposed method. Our study entailed a thorough review and analysis of the rate of olivine dissolution, the sequestration capacity of the dominant reaction, and the CO_2 footprint of the proposed process. Kinetics calculations showed that the dissolution rate of sand-grade olivine, at mean seawater temperatures of 15-25°C, is too slow for use as proposed by Schuiling, and would require grain sizes of < 10 μm (dust-grade) to be of practical value (i.e. steady state CO_2 uptake rates in 15-20 years). In addition, to offset 30% of worldwide 1990 CO_2 emissions by beach weathering within 15-20 years would require the distribution of vast quantities of olivine (≥ 5.0 Gt olivine/yr). The preparation and movement of the required material poses major economic, infrastructural and public health challenges. It was concluded that coastal spreading of olivine is not a viable method of CO_2 sequestration on the scale needed. The method certainly cannot replace CCS technologies as a means of controlling atmospheric CO_2 concentrations.

7.2 Suggestions for future research

The results described in this thesis have provided an experimental contribution to understanding chemical-mechanical processes operating within reservoir-caprock systems during CO_2 injection. However, many questions remain and new problems have arisen, which point the way forward for future research and improvements to what has been achieved here. Below, we summarise these new directions for research, together with suggestions on how they may be addressed in the future.

1. The feldspar-fluid batch reaction experiments described in Chapter 2 show that determining the nature and rates of reactions occurring under in-situ conditions strongly depends on fluid composition and experimental conditions. Contamination of nickel, derived from our K-Monel 500 reaction vessel, significantly affected the composition of the secondary phases formed, and thus the nature of the reactions that occurred. In future experiments, the contamination problem could be solved by using titanium for the construction of the reaction vessel. In addition, spectroscopic measurements performed under in-situ reservoir conditions offer a promising route for gaining insight into the nature of CO_2-water-rock and mineralisation reactions – see *Wolf et al.* [2004]. At the HPT-laboratory at Utrecht, a novel reaction cell has also been designed for use under in-situ pressure and temperature conditions in combination with Fourier Transform Infrared Spectroscopy. FTIR analysis of fine-grained material reacting with CO_2 and water or brine at elevated pressure and temperature may not only give insight into the nature of mineralisation reactions but possibly also into the rate of reaction.
2. The compaction experiments described in Chapter 3 show that the injection of CO_2 into wet quartz and feldspar sands inhibited creep. However, extrapolation of the increased dependency of creep rate on grain size seen in wet feldspar samples tested in the presence of high-pressure CO_2 indicates that for coarse grain size fractions (> 250 μm) creep may be enhanced in the presence of CO_2. Additional experiments on coarser grained aggregates will be necessary to elucidate if the observed CO_2 inhibition effect is maintained in such samples, and, if so, whether it has any implications for creep of reservoir sandstones. Also, improving the reproducibility of the wet/CO_2 experiments is important. Possible causes for the relatively poor reproducibility seen in the results of these experiments include the effects of O-ring friction; the injection of CO_2 sometimes led to swelling of the O-ring material (Viton). Lubrication, using silicon grease, may yield lower friction. Another possibility could be to use a different O-ring material, such as EPDM. However, our experiments have shown that, under the chosen experimental conditions, a significant flattening of this type of seals occurs, which led to CO_2 leakage. It was concluded in

the present study that the creep phenomena seen in our experiments on loose granular quartz and feldspar aggregates will be much slower in lower porosity sandstones, due to the lower stress concentrations at grain contacts. In addition, we saw no effects of reaction and suggested that these will be negligible in most reservoir sandstones (see point 4 below). Long-term effects of mineralisation reactions and fluid-rock interaction on creep behaviour need verification though.

3. As indicated by our experiments described in Chapter 4, anhydrite is more easily penetrated by CO_2-saturated solution, than by $CaSO_4$ solution. We inferred this to be an effect of the lower interfacial tension of the CO_2/water system. However, long-term geological storage of CO_2 is in part controlled by the capillary properties of the caprock [*Shah et al.*, 2008a], and a capillary barrier is only preserved if water-wettability is maintained and CO_2/water interfacial tension remains high. The capillary entry pressure of CO_2 is therefore important as it limits the allowable CO_2 injection pressure [*Hildenbrand et al.*, 2004; *Li et al.*, 2005; *Chiquet et al.*, 2007; *Shah et al.*, 2008b]. Gas breakthrough experiments are required for the Zechstein anhydrite to determine the capillary entry pressure to CO_2 for this caprock material.
4. Our study has mainly focussed on the short-term effects of chemical-mechanical processes in host and seal formations (Chapters 2-5). Our experiments yielded interesting results regarding the processes that will occur during and soon after injection. However, longer-term chemical and mechanical effects are also important, as they will determine the long-term stability of the reservoir-caprock system. Therefore, long-term mechanical experiments on sandstones in the presence of CO_2 are needed to improve insight into any long-term CO_2-induced creep processes not seen in the present tests. Expected long term effects include (carbonate) cement dissolution, and associated creep [for example, see *Le Guen et al.*, 2007], as well as slow strength reduction, which may lead to induced shear failure. In addition, long-term experiments on anhydrite caprock will give insight into the weakening effect of reaction, and the concomitant negative volume changes, on strength, dilatation/permeability and transport properties. Long-term pre-treatment of samples with CO_2 and water, before triaxial testing, is one, practical way to study such long-term effects. Use of higher temperatures to accelerate thermally activated processes, and use of synthetic ultra-fine grained rock materials to accelerate reaction and diffusion, also offers ways of addressing phenomena that may operate on long time scales.
5. As pointed out in the literature, reactivation of pre-existing faults in both the host and seal formations poses potential CO_2 leakage risks [*Hawkes et al.*, 2005;

Rutqvist et al., 2007]. Induced slip on large faults cutting through the reservoir and into the base of the caprock, or slip on faults within the caprock, may result in seal damage and possible leakage. A number of processes, leading to enhanced fault slip, can cause fault reactivation. First, there is the reduction of the normal stress on the fault plane, as a result of high-pressure fluid injection. This may induce slip through the reduction of the shear stress, which puts constraints on the injection pressure. This effect can be predicted numerically, using geomechanical models [*Streit and Hillis*, 2004; *Hawkes et al.*, 2005; *Rutqvist et al.*, 2007]. Second, the coefficient of friction could be lowered by the presence of high-pressure CO_2. Future, constant strain rate triaxial experiments on saw-cut samples, under dry, wet and wet/CO_2 conditions, will be able to show any effect of fluid on the frictional behaviour of existing faults. Thirdly, mineralisation reactions occurring in the fault plane may affect slip behaviour. Precipitation of secondary phyllosilicate minerals, such as expected to form in aluminosilicate-rich rocks, may enhance slip [cf. *Niemeijer and Spiers*, 2005]. Long-term shear experiments, performed on fault gouge in the presence of high-pressure CO_2, both in constant sliding rate and stick-slip modes, are needed to provide answers concerning the effect of (mineralisation) reactions on slip behaviour, as well as on fault healing and fault strength recovery. Again, long-term processes could be studied by increasing temperature and artificially refining the grain size of the rock and fault gouge materials used.

6. The results given in Chapter 2 indicated that alkaline industrial waste presents possibilities to enhance the mineralisation capacity of a reservoir or to seal (newly created) leakage pathways, such as leaky faults or well-bore systems [*Waring and Taylor*, 2001]. Waste products, such as fly ash, are highly alkaline and experiments have shown that this leads to high reactivity and high CO_2 mineralisation potential through carbonate precipitation [*Rendek et al.*, 2006; *Soong et al.*, 2006; *Montes-Hernandez et al.*, 2009]. Subsurface injection of ash suspensions or slurries will therefore result in rapid mineralisation and possibly a reduction in permeability, depending on suspension concentration and injection rate. Such procedures may offer favourable methods for fault or well sealing but may significantly decrease reservoir injectivity in attempts to mineralise reservoirs using fly ash suspensions, especially near the injection well. To evaluate the potential of fly ash injection, fault healing and sealing experiments can be performed by applying ash slurry to or injecting a suspension into the fault plane of a saw-cut sample, then introducing high-pressure CO_2 to let the fly ash react and presumably cement the fault together. Permeability measurements could then be performed on the healed fracture, together with triaxial compression experiments to determine fault strength,

prior to and after cementation. The effect of fly ash mineralisation on reservoir permeability can be assessed through experiments on injection of an ash suspension or slurry into a porous rock, followed by mineralisation using CO_2 and subsequent permeametry tests. Varying the sequence and rate of CO_2 vs. suspension injection might lead to a useful, subsurface fly ash mineralisation method, which provides a solution for fly ash disposal, immobilisation of its heavy metals content and fixation of CO_2. In addition, reaction rate experiments could be conducted to investigate the possibilities of decreasing the rate of carbonate precipitation occurring during fly ash mineralisation of reservoir rock, for example by the addition of phosphates to solution [*Zhang and Spiers*, 2005]. Such additives may retard reaction sufficiently to allow penetration of the ash and injected slurry further into the field, before precipitating carbonate in the longer term.

7. The short-term experiments performed in the context of this study yielded interesting results concerning reaction and deformation processes that occur more or less immediately after CO_2 injection, while many of our suggestions for future research focus on longer term experiments. However, it should be noted that though the latter will be long-term on a laboratory scale (weeks-months), they will always be relatively short-term when put in the context of CO_2 storage (decades-centuries). Therefore, it is essential to underpin laboratory studies with mechanism-based models describing the rates of the relevant kinetic processes controlling behaviour observed in experiments. Moreover, while the present experiments have addressed several coupled chemical-mechanical processes for the first time (e.g. the effect of CO_2 on creep of wet feldspar aggregates), addressing the complex interaction that will occur under subsurface conditions and over long time scales requires fully coupled hydrological, reactive transport and geomechanical modelling. This is an important challenge for the future, not only in relation to CO_2 storage, but also to many other processes going on in the Earth, such as diagenesis and movement along large-scale fault zones (earthquakes).
8. Beach or coastal weathering of sand-grade olivine was shown to be too slow to achieve useful CO_2 uptake rates within the next 15 years or so. However, the possible (positive) effect of salts, especially NaCl, on the dissolution rate of olivine needs to be investigated more closely. Furthermore, land weathering in the tropics is more promising in terms of dissolution rates, as a result of the presence of acid soils and higher temperatures, though transport issues, fine grain sizes (dust) and land use (negative effect of Mg-leaching on agriculture) remain problematic. In order to assess the feasibility of land weathering, more work is required on these factors.

Bibliography

Aagaard, P., E. H. Oelkers, and J. Schott (2004), Glauconite dissolution kinetics and applications to CO_2 storage in the subsurface, *Geochim. Cosmochim. Acta*, *68*, A-143.

Al-Ajmi, A. M., and R. W. Zimmerman (2005), Relation between the Mogi and the Coulomb failure criteria, *Int. J. Rock Mech. Min. Sci.*, *42*(3), 431-439.

Alkan, H., Y. Cinar, and G. Pusch (2007), Rock salt dilatancy boundary from combined acoustic emission and triaxial compression tests, *Int. J. Rock Mech. Min. Sci.*, *44*(1), 108-119.

Alkan, H. (2009), Percolation model for dilatancy-induced permeability of the excavation damaged zone in rock salt, *Int. J. Rock Mech. Min. Sci.*, *46*(4), 716-724.

Amma-Miyasaka, M., and M. Nakagawa (2002), Origin of anorthite and olivine megacrysts in island-arc tholeiites: petrological study of 1940 and 1962 ejecta from Miyake-jima volcano, Izu-Mariana arc, *J. Volcan. Geotherm. Res.*, *117*(3-4), 263-283.

Amrhein, C., and D. L. Suarez (1992), Some factors affecting the dissolution kinetics of anorthite at 25°C, *Geochim. Cosmochim. Acta*, *56*, 1815-1826.

Archer, D., H. Kheshgi, and E. Maier-Reimer (1997), Multiple timescales for neutralization of fossil fuel CO_2, *Geophys. Res. Lett.*, *24*(4), 405-408.

Atkinson, B. K. (1979), A fracture mechanics study of subcritical tensile cracking of quartz in wet environments, *Pure Appl. Geophys.*, *117*, 1011-1024.

Atkinson, B. K., and P. G. Meredith (1981), Stress corrosion cracking of quartz: a note on the influence of chemical environment, *Tectonophysics*, *77*, T1-T11.

Atkinson, B. K. (1984), Subcritical crack growth in geological materials, *J. Geophys. Res.*, *89*(B6), 4077-4114.

Bachu, S., W. D. Gunter, and E. H. Perkins (1994), Aquifer disposal of CO_2: hydrodynamic and mineral trapping, *Energy Convers. Manage.*, *35*(4), 269-279.

Bachu, S. (2000), Sequestration of CO_2 in geological media: criteria and approach for site selection in response to climate change, *Energy Convers. Manage.*, *41*, 953-970.

Bachu, S., and B. Bennion (2008), Effects of in-situ conditions on relative permeability characteristics of CO_2-brine systems, *Environ. Geol.*, *54*(8), 1707-1722.

Bachu, S., and D. B. Bennion (2009), Interfacial tension between CO_2, freshwater, and brine in the range of pressure from (2 to 27) MPa, temperature from (20 to 125)°C, and water salinity from (0 to 334 000) mg L^{-1}, *J. Chem. Eng. Data*, *54*(3), 765-775.

Back, M., M. Kühn, H. Stanjek, and S. Peiffer (2007), Carbon dioxide sequestration with brown coal fly ashes, *Geophys. Res. Abstr.*, *9*, 11400.

Baines, S. J., and R. H. Worden (2000), Geological CO_2 disposal: understanding the long term fate of CO_2 in naturally occurring accumulations, paper presented at Proceedings of 5th International Conference on Greenhouse Gas Control Technologies (GHGT-5).

Baines, S. J., and R. H. Worden (2004a), Geological storage of carbon dioxide, *Geological Society, London, Special Publications*, *233*(1), 1-6.

Baines, S. J., and R. H. Worden (2004b), The long-term fate of CO_2 in the subsurface: natural analogues for CO_2 storage, in *Geological storage of carbon dioxide*, edited by S. J. Baines and R. H. Worden, pp. 59-85, Geological Society of London, London.

Baker, J. C., G. P. Bai, P. J. Hamilton, S. D. Golding, and J. B. Keene (1995), Continental-scale magmatic carbon dioxide seepage recorded by dawsonite in the Bowen-Gunnedah-Sydney Basin system, eastern Australia, *J. Sediment. Res.*, *65*(3a), 522-530.

Bando, S., F. Takemura, M. Nishio, E. Hihara, and M. Akai (2004), Viscosity of aqueous NaCl solutions with dissolved CO_2 at (30 to 60)°C and (10 to 20) MPa, *J. Chem. Eng. Data*, *49*, 1328-1332.

Bandura, A. V., and S. N. Lvov (2006), The ionization constant of water over wide ranges of temperature and density, *J. Phys. Chem. Ref. Data*, *35*(1), 15-30.

Bateman, K., A. M. Turner, J. Pearce, D. J. Noy, D. Birchall, and C. Rochelle (2005), Large-scale column experiment: study of CO_2, porewater, rock reactions and model test case, *Oil Gas Sci. Tech.*, *60*(1), 161-175.

Baud, P., A. Schubnel, and T.-f. Wong (2000a), Dilatancy, compaction, and failure mode in Solnhofen limestone, *J. Geophys. Res.*, *105*(B8), 19289-19303.

Baud, P., W. Zhu, and T.-f. Wong (2000b), Failure mode and weakening effect of water on sandstone, *J. Geophys. Res.*, *105*(B6), 16371-16389.

Bell, F. G. (1981), Geotechnical properties of some evaporitic rocks, *Bull. Int. Assoc. Eng. Geol.*, *24*, 137-144.

Bénézeth, P., D. A. Palmer, L. M. Anovitz, and J. Horita (2007), Dawsonite synthesis and reevaluation of its thermodynamic properties from solubility measurements: Implications for mineral trapping of CO_2, *Geochim. Cosmochim. Acta*, *71*(18), 4438-4455.

Bennion, B., and S. Bachu (2008), Drainage and imbibition relative permeability relationships for supercritical CO_2/brine and H_2S/brine systems in intergranular sandstone, carbonate, shale, and anhydrite rocks, paper presented at SPE Europec 2006, Vienna, Austria.

Bernstein, L., P. Bosch, O. Canziani, Z. Chen, R. Christ, O. Davidson, W. Hare, S. Huq, D. Karoly, Z. Kundzewicz, J. Liu, U. Lohmann, M. Manning, T. Matsuno, B. Menne, B. Metz, M. Mirza, N. Nicholls, L. Nurse, R. Pachauri, J. Palutikof, M. Parry, D. Qin, N. Ravindranath, A. Reisinger, J. Ren, K. Riahi, C. Rosenzweig, M. Rusticucci, S. Schneider, Y. Sokona, S. Solomon, P. Stott, R. Stouffer, T. Sugiyama, R. Swart, D. Tirpak, C. Vogel, and G. Yohe (2007), Climate change 2007 - synthesis report: an assessment of the Intergovernmental Panel on Climate Change, 52 pp., IPCC.

Bertier, P., R. Swennen, B. Laenen, D. Lagrou, and R. Dreesen (2006), Experimental identification of CO_2-water-rock interactions caused by sequestration of CO_2 in Westphalian and Buntsantstein sandstones of the Campine Basin (NE-Belgium), *J. Geochem. Explor.*, *89*, 10-

14.

Bérubé, Y. G., and P. L. de Bruyn (1968), Adsorption at the rutile-solution interface: I. Thermodynamic and experimental study, *J. Colloid Interface Sci.*, *27*(2), 305-318.

Bethke, C. M. (1996), *Geochemical reaction modeling*, 397 pp., Oxford University Press, New York.

Biersma, R. (2007), Verkoelend olivijn (Cooling olivine), in *NRC Handelsblad (in Dutch)*, published 04/08/07.

Bjørkum, P. A., and O. Walderhaug (1990), Geometrical arrangement of calcite cementation within shallow marine sandstones, *Earth Sci. Rev.*, *29*, 145-161.

Blum, A., and A. Lasaga (1988), Role of surface speciation in the low-temperature dissolution of minerals, *Nature*, *331*, 431-433.

Brady, P. V., and J. V. Walther (1990), Kinetics of quartz dissolution at low temperatures, *Chem. Geol.*, *82*, 253-264.

Brady, P. V., and S. A. Carroll (1994), Direct effects of CO_2 and temperature on silicate weathering: possible implications for climate control, *Geochim. Cosmochim. Acta*, *58*(8), 1853-1856.

Brandes, L. J., G. E. M. Alkemade, P. G. Ruyssenaars, H. H. J. Vreuls, and P. W. H. G. Coenen (2006), Greenhouse gas emissions in the Netherlands 1990-2004: National Inventory Report, 228 pp., Netherlands Environmental Assessment Agency (MNP).

Brzesowsky, R. H. (1995), Micromechanics of sand grain failure and sand compaction, Ph.D. thesis, 180 pp., Utrecht University, Utrecht.

Canty, G. A., and J. W. Everett (2006), Alkaline injection technology: field demonstration, *Fuel*, *85*, 2545-2554.

Carroll, S. A., and J. V. Walther (1990), Kaolinite dissolution at 25°, 60°, and 80°C, *Am. J. Sci.*, *290*, 797-810.

Carroll, S. A., and K. G. Knauss (2005), Dependence of labradorite dissolution kinetics on $CO_{2(aq)}$, $Al_{(aq)}$, and temperature, *Chem. Geol.*, *217*, 213-225.

Casey, W. H., H. R. Westrich, G. W. Arnold, and J. F. Banfield (1989), The surface chemistry of dissolving labradorite feldspar, *Geochim. Cosmochim. Acta*, *53*, 821-832.

Casey, W. H., A. C. Lasaga, and G. V. Gibbs (1990), Mechanisms of silica dissolution as inferred from the kinetic isotope effect, *Geochim. Cosmochim. Acta*, *54*(12), 3369-3378.

Cavani, F., F. Trifirò, and A. Vaccari (1991), Hydrotalcite-type anionic clays: preparation, properties and applications, *Catal. Today*, *11*, 173-301.

Chalbaud, C., M. Robin, and P. Egermann (2006), Interfacial tension data and correlations of brine/CO_2 systems under reservoir conditions, paper presented at SPE Annual Technical Conference and Exhibition, San Antonio, Texas, USA.

Chang, L. L. Y., R. A. Howie, and J. Zussman (1996), *Non-silicates: sulphates, carbonates, phosphates, halides*, 383 pp., Longman Group Limited, Essex, England.

Charles, R. J. (1958), Static fatigue of glass. I, *J. Appl. Phys.*, *29*(11), 1549-1553.

Chen, Z.-Y., W. K. O'Connor, and S. J. Gerdemann (2006), Chemistry of aqueous mineral carbonation for carbon sequestration and explanation of experimental results, *Environ. Progr.*, *25*(2), 161-166.

Chester, F. M., J. S. Chester, A. K. Kronenberg, and A. Hajash (2007), Subcritical creep compaction of quartz sand at diagentic conditions: effects of water and grain size, *J. Geophys. Res.*, *112*, B06203.

Chester, J. S., S. C. Lenz, F. M. Chester, and R. A. Lang (2004), Mechanisms of compaction of quartz sand at diagenetic conditions, *Earth Planet. Sci. Lett.*, *220*, 435-451.

Chiaramonte, L., M. D. Zoback, J. Friedmann, and V. Stamp (2007), Seal integrity and feasibility of CO_2 sequestration in the Teapot Dome EOR pilot: geomechanical site characterization, *Environ. Geol.,* DOI 10.1007/s00254-007-0948-7.

Chiquet, P., D. Broseta, and S. Thibeau (2007a), Wettability alteration of caprock minerals by carbon dioxide, *Geofluids*, *7*, 112-122.

Chiquet, P., J.-L. Daridon, D. Broseta, and S. Thibeau (2007b), CO_2/water interfacial tensions under pressure and temperature conditions of CO_2 geological storage, *Energy Convers. Manage.*, *48*, 736-744.

Chuhan, F. A., A. Kjeldstad, K. Bjørlykke, and K. Høeg (2003), Experimental compression of loose sands: relevance to porosity reduction during burial in sedimentary basins, *Can. Geotech. J.*, *40*(5), 995-1011.

Canadian Industry Program for Energy Conservation (CIPEC) (2005), Benchmarking the energy consumption of Canadian open-pit mines, in *Mining Association of Canada and Natural Resources Canada*, 56 pp.

Coleman, R. G. (1977), *Ophiolites: ancient oceanic lithosphere*, 229 pp., Springer-Verlag, New York, USA.

Colmenares, L. B., and M. D. Zoback (2002), A statistical evaluation of intact rock failure criteria constrained by polyaxial test data for five different rocks, *Int. J. Rock Mech. Min. Sci.*, *39*(6), 695-729.

Cook, G. A. (1961), *Argon, helium and the rare gases: the elements of the helium group, Vol. 1. History, occurrence and properties*, 427 pp., Interscience Publisher.

Commission of the European Communities (2007), Communication from the Commission to the Council, the European Parliament, the European Economic and Social Committee and the Committee of the Regions - Limiting global climatic change to 2 degrees Celcius: the way ahead for 2020 and beyond, edited, 13 pp.

David, C., T.-f. Wong, W. Zhu, and J. Zhang (1994), Laboratory measurement of compaction-induced permeability change in porous rocks: Implications for the generation and maintenance of pore pressure excess in the crust, *Pure Appl. Geophys.*, *143*(1), 425-456.

de Boer, R. B. (1977), Influence of seed crystals on the precipitation of calcite and aragonite, *Am. J. Sci.*, *277*, 38-60.

De Paola, N., D. R. Faulkner, and C. Collettini (2009), Brittle versus ductile deformation as a the main control on the transport properties of low porosity anhydrite rocks, *J. Geophys. Res.*, *114,* B06211, DOI 10.1029/2008JB005967.

Dewers, T. A., and A. Hajash (1995), Rate laws for water-assisted compaction and stress-induced water-rock interaction in sandstones, *J. Geophys. Res.*, *100*(B7), 13093-13112.

Dickson, J. L., G. Gupta, T. S. Horozov, B. P. Binks, and K. P. Johnston (2006), Wetting phenomena at the CO_2/water/glass interface, *Langmuir*, *22*(5), 2161-2170.

Dove, P., and M. F. Hochella Jr. (1993), Calcite precipitation mechanisms and inhibition by orthophosphate: in situ observations by scanning force microscopy, *Geochim. Cosmochim. Acta*, *57*, 705-714.

Dove, P. (1995), Geochemical controls on the kinetics of quartz fracture at subcritical tensile stresses, *J. Geophys. Res.*, *100*(B11), 22349-22359.

Dove, P. M., and S. F. Elston (1992), Dissolution kinetics of quartz in sodium chloride solutions: analysis of existing data and a rate model for 25°C, *Geochim. Cosmochim. Acta*, *56*, 4147-4156.

Duan, Z., and R. Sun (2003), An improved model calculating CO_2 solubility in pure water and aqueous NaCl solutions from 273 to 533 K and from 0 to 2000 bar, *Chem. Geol.*, *193*, 257-271.

Duan, Z., R. Sun, C. Zhu, and I.-M. Chou (2006), An improved model for the calculation of CO_2 solubility in aqueous solutions containing Na^+, K^+, Ca^{2+}, Mg^{2+}, Cl^-, and SO_4^{2-}, *Mar. Chem*, *98*, 131-139.

Dubrawski, J. V., A.-L. Channon, and S. S. J. Warne (1989), Examination of the siderite-magnesite series by Fourier transform infrared spectroscopy, *Am. Miner.*, *74*, 187-190.

Dunning, J., B. Douglas, M. Miller, and S. McDonald (1994), The role of the chemical environment in frictional deformation: stress corrosion cracking and communition, *Pure Appl. Geophys.*, *143*, 151-178.

Dusseault, M. B., M. S. Bruno, and J. Barrera (1998), Casing shear: causes, cases, cures, paper presented at 6th International Oil & Gas Conference and Exhibition, Beijing, China.

Dyni, J. R. (1996), Sodium carbonate resources at the Green River Formation, 39 pp., U.S. Geological Survey.

Edmond, J. M., and M. S. Paterson (1972), Volume changes during the deformation of rocks at high pressures, *Int. J. Rock Mech. Min. Sci. Geomech. Abstr.*, *9*(2), 161-182.

Ennis-King, J., and L. Paterson (2002), Rate of dissolution due to convective mixing in the underground storage of carbon dioxide, paper presented at Greenhouse Gas Control Technologies 6, Kyoto, Japan.

Eshuis, K. (2007), CO_2 opslaan onder de grond (Storing CO_2 underground), in *Financieel Dagblad (in Dutch)*, published 12/06/07.

Faulkner, D. R., and E. H. Rutter (2000), Comparisons of water and argon permeability in natural clay-bearing fault gouge under high pressure at 20°C, *J. Geophys. Res.*, *105*, 16415-11642.

Faulkner, D. R. (2004), A model for the variation in permeability of clay-bearing fault gouge with depth in the brittle crust, *Geophys. Res. Lett.*, *31,* L19611, DOI 10.1029/2004GL020736.

Fernandez-Bastero, S., T. García, A. Santos, and L. Gago-Duport (2005), Geochemical potentiality of glauconitic shelf sediments for sequestering atmospheric CO_2 of anthropogenic origin, *Ciencas Marinas*, *31*(4), 593-615.

Fisk, G. A., and T. A. Michalske (1985), Laser-based and thermal studies of stress corrosion in vitreous silica, *J. Appl. Chem.*, *58*(7), 2736-2741.

Fredrich, J. T., B. Evans, and T.-f. Wong (1989), Micromechanics of the brittle to plastic transition in Carrara marble, *J. Geophys. Res.*, *94*(B4), 4129-4145.

Fredrich, J. T., B. Evans, and T.-f. Wong (1990), Effect of grain size on brittle and semibrittle strength: implications for micromechanical modelling of failure in compression, *J. Geophys. Res.*, *95*(B7), 10907-10920.

Gadsen, J. A. (1975), *Infrared spectra of minerals and related inorganic compounds*, 277 pp., Butterworth and Co. Ltd.

Gaus, I., C. Le Guern, J. Pearce, J. Pauwels, T. Shepard, G. Hatziyannis, and A. Metaxis (2004), Comparison of long-term geochemical interactions at two natural CO_2-analogues: Montmiral (Southeast Basin, France) and Messokampos (Florina Basin, Greece) case studies, in paper presented at Proceedings of 7th International Conference on Greenhouse Gas Control Technologies (GHGT-7), Vancouver, Canada.

Gaus, I., M. Azaroual, and I. Czernichowski-Lariol (2005), Reactive transport modelling of the impact of CO_2 injection on the clayey cap rock at Sleipner (North Sea), *Chem. Geol.*, *217*, 319-337.

Gerdemann, S. J., D. C. Dahlin, and W. K. O'Connor (2002), Carbon dioxide sequestration by aqueous mineral carbonation of magnesium silicate minerals, paper presented at Proceedings of 6th International Conference on Greenhouse Gas Control Technologies (GHGT-6), Kyoto, Japan.

Gerdemann, S. J., W. K. O'Connor, D. C. Dahlin, L. R. Penner, and H. Rush (2007), Ex situ aqueous mineral carbonation, *Environ. Sci. Technol.*, *41*, 2587-2593.

Giammar, D. E., R. G. Bruant, and C. A. Peters (2005), Forsterite dissolution and magnesite precipitation at conditions relevant for deep saline aquifer storage and sequestration of carbon dioxide, *Chem. Geol.*, *217*, 257-276.

Gilfillan, S. M. V., B. S. Lollar, G. Holland, D. Blagburn, S. Stevens, M. Schoell, M. Cassidy, Z. Ding, Z. Zhou, G. Lacrampe-Couloume, and C. J. Ballentine (2009), Solubility trapping in formation water as dominant CO_2 sink in natural gas fields, *Nature*, *458*(7238), 614-618.

Giorgis, T., M. Carpita, and A. Battistelli (2007), 2D modeling of salt precipitation during the injection of dry CO_2 in a depleted gas reservoir, *Energy Convers.*

Manage., *48*(6), 1816-1826.

Goff, F., and K. S. Lackner (1998), Carbon dioxide sequestering using ultramafic rocks, *Environ. Geosci.*, *5*(3), 89-101.

Golubev, S. V., O. S. Pokrovsky, and J. Schott (2005), Experimental determination of the effect of dissolved CO_2 on the dissolution kinetics of Mg and Ca silicates at 25°C, *Chem. Geol.*, *217*, 227-238.

Gratz, A. J., P. E. Hillner, and P. K. Hansma (1993), Step dynamics and spiral growth on calcite, *Geochim. Cosmochim. Acta*, *57*, 491-495.

Gueguen, Y., and J. Dienes (1989), Transport properties of rocks from statistics and percolation, *Math. Geol.*, *21*(1), 1-13.

Guimaraes, M. S., J. R. Valdes, A. M. Palomino, and J. C. Santamarina (2007), Aggregate production: fines generation during rock crushing, *Int. J. Miner. Process.*, *81*, 237-247.

Gunter, W. D., E. H. Perkins, and T. J. McCann (1993), Aquifer disposal of CO_2-rich gases: Reaction design for added capacity, *Energy Convers. Manage.*, *34*(9-11), 941-948.

Gunter, W. D., E. H. Perkins, and I. Hutcheon (2000a), Aquifer disposal of acid gases: modelling of water-rock reactions for trapping of acid wastes, *Appl. Geochem.*, *15*(8), 1085-1095.

Gunter, W. D., E. H. Perkins, and I. Hutcheon (2000b), Aquifer disposal of acid gases: modelling of water-rock reactions for trapping of acid wastes, *Appl. Geochem.*, *15*, 1085-1095.

Haimson, B., and C. Chang (2000), A new true triaxial cell for testing mechanical properties of rock, and its use to determine rock strength and deformability of Westerly granite, *Int. J. Rock Mech. Min. Sci.*, *37*(1-2), 285-296.

Haimson, B. C. (1978), The hydrofracturing stress measuring method and recent field results, *Int. J. Rock Mech. Min. Sci. Geomech. Abstr.*, *15*(4), 167-178.

Hajash, A., T. D. Carpenter, and T. A. Dewers (1998), Dissolution and time-dependent compaction of albite sand: experiments at 100°C and 160°C in pH-buffered organic acids and distilled water, *Tectonophysics*, *295*, 93-115.

Hänchen, M., V. Prigiobbe, G. Storti, T. M. Seward, and M. Mazzotti (2006), Dissolution kinetics of forsterite olivine at 90-150°C including effects of the presence of CO_2, *Geochim. Cosmochim. Acta*, *70*, 4403-4416.

Handy, M. R. (1990), The solid-state flow of polymineralic rocks, *J. Geophys. Res.*, *95*(B6), 8647-8661.

Hangx, S. J. T. (2006), Reactions, reaction rates and porosity-permeability models for CO_2-injected sandstone rocks, 66 pp.

Hangx, S. J. T., and C. J. Spiers (2009), Reaction of plagioclase feldspars with CO_2 under hydrothermal conditions, *Chem. Geol.*, *265*(1-2), 88-98.

Hangx, S. J. T., C. J. Spiers, and C. J. Peach (2009a (submitted)), Creep of simulated reservoir sands and coupled chemical-mechanical effects of CO_2 injection.

Hangx, S. J. T., C. J. Spiers, and C. J. Peach (2009b (submitted)), Mechanical behaviour of anhydrite capcrock and implications for CO_2 sealing integrity.

Hawkes, C., P. J. McLellan, and S. Bachu (2005), Geomechanical factors affecting geological storage of CO_2 in depleted oil and gas reservoirs, *J. Can. Petrol. Technol.*, *44*(10), 52-61.

Haywood, H. M., J. M. Eyre, and H. Scholes (2001), Carbon dioxide sequestration as stable carbonate minerals - environmental barriers, *Environ. Geol.*, *41*, 11-16.

Hellmann, R., C. M. Eggleston, M. F. Hochella, and D. A. Crerar (1990), The formation of leached layers on albite surfaces during dissolution under hydrothermal conditions, *Geochim. Cosmochim. Acta*, *54*(5), 1267-1281.

Hellmann, R. (1994), The albite-water system: part I. The kinetics of dissolution as a function of pH at 100, 200, and 300°C, *Geochim. Cosmochim. Acta*, *58*(2), 595-611.

Hellmann, R. (1995), The albite-water system: Part II. The time-evolution of the stoichiometry of dissolution as a function of pH at 100, 200, and 300°C, *Geochim. Cosmochim. Acta*, *59*(9), 1669-1697.

Hellmann, R., J.-M. Penisson, R. L. Hervig, J.-H. Thomassin, and M.-F. Abrioux (2003), An EFTEM/HRTEM high-resolution study of the near surface of labradorite feldspar altered at acid pH: evidence for interfacial dissolution-reprecipitation, *Phys. Chem. Miner.*, *30*, 192-197.

Hertz, H. (1881), Ueber die Berührung fester elastischer Körper, *Journal für die reine und angewandte Mathematik*, *92*, 156-171.

Hettema, M., E. Papamichos, and P. M. T. M. Schutjens (2002), Subsidence delay: field observations and analysis, *Oil Gas Sci. Tech.*, *57*(5), 443-458.

Hiemstra, T., and W. H. van Riemsdijk (1990), Multiple activated complex dissolution of metal (hydr) oxides: A thermodynamic approach applied to quartz, *J. Colloid Interface Sci.*, *136*(1), 132-150.

Hildenbrand, A., S. Schlömer, B. M. Krooss, and R. Littke (2004), Gas breakthrough experiments on pelitics rocks: comparitive study with N_2, CO_2 and CH_4, *Geofluids*, *4*, 61-80.

Hitchon, B. (1996), *Aquifer disposal of carbon dioxide: hydrodynamic and mineral trapping - proof of concept*, 165 pp., Geoscience Publishing Ltd., Sherwood Park, Alberta, Canada.

Hodson, M. E. (2003), The influence of Fe-rich coatings on the dissolution of anorthite at pH 2.6, *Geochim. Cosmochim. Acta*, *67*(18), 3355-3363.

Hoek, E., and E. T. Brown (1997), Practical estimates of rock mass strength, *Int. J. Rock Mech. Min. Sci.*, *34*(8), 1165-1186.

Holloway, S. (1996), *The underground disposal of carbon dioxide, Final Report of JOULE II Project No. CT92-0031*, 355 pp., British Geological Survey.

Hostetler, P. B. (1964), The degree of supersaturation of magnesium and calcium carbonate minerals in natural waters, *Int. Assoc. Sci. Hydr. Pub.*, *64*, 34-49.

House, K. Z., C. H. House, D. P. Schrag, and M. J. Aziz (2007), Electrochemical acceleration of chemical weathering as an energetically feasible approach to mitigating anthropogenic climate change, *Environ. Sci. Technol.*, DOI 10.1021/es0701816.

Huertas, F. J., S. Fiore, F. Huertas, and J. Linares (1999), Experimental study of the hydrothermal formation of kaolinite, *Chem. Geol.*, *156*, 171-190.

Huijgen, W. J. J., G. J. Witkamp, and R. N. J. Comans (2006), Mechanisms of aqueous wollastonite carbonation as a possible CO_2 sequestration process, *Chem. Eng. Sci.*, *61*(13), 4242-4251.

Inskeep, W. P., E. A. Nater, P. R. Bloom, D. S. Vandervoort, and M. S. Erich (1991), Characterization of laboratory weathered labradorite surfaces using X-ray photoelecton spectroscopy and transmission electron microscopy, *Geochim. Cosmochim. Acta*, *55*, 787-800.

Jia, L., and E. J. Anthony (2002), Mineral carbonation and ZECA, paper presented at Proceedings of 6th International Conference on Greenhouse Gas Control Technologies (GHGT-6), Kyoto, Japan.

Johnson, J. W., J. J. Nitao, C. I. Steefel, and K. G. Knauss (2001), Reactive transport modeling of CO_2 sequestration in saline aquifers: the influence of intra-aquifer shales and the relative effectiveness of structural, solubility, and mineral trapping during prograde and retrograde sequestration, paper presented at First National Conference on Carbon Sequestration, Washington, D.C.

Johnson, J. W., J. J. Nitao, and J. P. Morris (2004), Reactive transport modeling of cap rock integrity during natural and engineered CO_2 storage, 52 pp., Lawrence Livermore National Laboratory.

Jonckbloedt, R. C. L. (1997), The dissolution of olivine in acid - a cost effective process for the elimination of waste acids, 114 pp., Utrecht University, Utrecht, The Netherlands.

Kakizawa, M., A. Yamasaki, and Y. Yanagisawa (2001), A new CO2 disposal process via artificial weathering of calcium silicate accelerated by acetic acid, *Energy*, *26*(4), 341-354.

Kalinowski, B. E., and P. Schweda (1996), Kinetics of muscovite, phlogopite, and biotite dissolution and alteration at pH 1-4, room temperature, *Geochim. Cosmochim. Acta*, *60*(3), 367-385.

Kanezaki, E. (1998), Direct observation of a metastable solid phase of Mg/Al/CO_3-layered double hydroxide by means of high temperature in situ powder XRD and DTA/TG, *Inorg. Chem.*, *37*, 2588-2590.

Karner, S. L., F. M. Chester, A. K. Kronenberg, and J. S. Chester (2003), Subcritical compaction and yielding of granular quartz sand, *Tectonophysics*, *377*, 357-381.

Kaszuba, J. P., D. R. Janecky, and M. G. Snow (2003), Carbon dioxide reaction processes in a model brine aquifer at 200°C and 200 bars: implications for geologic sequestration of carbon, *Appl. Geochem.*, *18*, 1065-1080.

Kaszuba, J. P., D. R. Janecky, and M. G. Snow (2005), Experimental evaluation of mixed fluid reactions between supercritical carbon dioxide and NaCl brine:

relevance to the integrity of a geologic carbon repository, *Chem. Geol.*, *217*, 277-293.

Kharaka, Y. K., D. R. Cole, S. D. Hovorka, W. D. Gunter, K. G. Knauss, and B. M. Freifeld (2006), Gas-water-rock interactions in Frio Formation following CO_2 injection: implications for the storage of greenhouse gases in sedimentary basins, *Geology*, *34*(7), 577-580.

Kheshgi, H. S. (1995), Sequestering atmospheric carbon dioxide by increasing ocean alkalinity, *Energy*, *20*(9), 915-922.

Klinkenberg, L. J. (1941), The permeability of porous media to liquids and gases, *Drilling and Production Practice, American Petroleum Institute*, 200-213.

Kloprogge, J. T., H. D. Ruan, and R. L. Frost (2002), Thermal decomposition of bauxite minerals: infrared emission spectroscopy of gibbsite, boehmite and diaspore, *J. Mater. Sci.*, *37*(6), 1121-1129.

Köhler, S. J., F. Dufaud, and E. H. Oelkers (2003), An experimental study of illite dissolution kinetics as a function of pH from 1.4 to 12.4 and temperature from 5° to 50°C, *Geochim. Cosmochim. Acta*, *67*(19), 3583-3594.

Kojima, T., A. Nagamine, N. Uene, and S. Uemiya (1997), Absorption and fixation of carbon dioxide by rock weathering, *Energy Convers. Manage.*, *38*, S461-S466.

Kontrec, J., D. Kralj, and L. Brecevic (2002), Transformation of anhydrous calcium sulphate into calcium sulphate dihydrate in aqueous solutions, *J. Cryst. Growth*, *240*, 203-211.

Kovanda, F., D. Koloušek, Z. Cílová, and V. Hulínský (2005), Crystallization of synthetic hydrotalcite under hydrothermal conditions, *Appl. Clay. Sci.*, *28*, 101-109.

Krauskopf, K. B., and D. K. Bird (1995), *Introduction to geochemistry*, third ed., 647 pp., McGraw-Hill, Inc., New York.

Kutchko, B. G., B. R. Strazisar, D. A. Dzombak, G. V. Lowry, and N. Thaulow (2007), Degradation of well cement by CO_2 under geologic sequestration conditions, *Environ. Sci. Technol.*, *41*(13), 4787-4792.

Lackner, K. S., C. H. Wendt, D. P. Butt, E. L. Joyce, and D. H. Sharp (1995), Carbon dioxide disposal in carbonate minerals, *Energy*, *20*(11), 1153-1170.

Lackner, K. S. (2002), Carbonate chemistry for sequestering fossil carbon, *Annu. Rev. Energy Env.*, *27*, 193-232.

Lagneau, V., A. Pipart, and H. Catalette (2005), Reactive transport modelling of CO_2 sequestration in deep saline aquifers, *Oil Gas Sci. Tech.*, *60*(2), 231-247.

Le Guen, Y., F. Renard, R. Hellmann, E. Brosse, M. Collombet, D. Tisserand, and J.-P. Gratier (2007), Enhanced deformation of limestone and sandstone in the presence of high PCO_2 fluids, *J. Geophys. Res.*, *112*, B05421, DOI 10.1029/2006JB004637.

Lebrón, I., and D. L. Suarez (1996), Calcite nucleation and precipitation kinetics as affected by dissolved organic matter at 25°C and pH > 7.5, *Geochim. Cosmochim. Acta*, *60*(15), 2765-2776.

Lebrón, I., and D. L. Suarez (1998), Ki-

netics and mechanisms of precipitation of calcite as affected by P_{CO2} and organic ligands at 25°C, *Geochim. Cosmochim. Acta*, *62*(3), 405-416.

Lehner, F. K. (1995), A model for intergranular pressure solution in open systems, *Tectonophysics*, *245*, 153-170.

Li, H. C., and P. L. De Bruyn (1966), Electrokinetic and adsorption studies on quartz, *Surf. Sci.*, *5*(2), 203-220.

Li, S., M. Dong, Z. Li, S. Huang, H. Qing, and E. Nickel (2005), Gas breakthrough pressure for hydrocarbon reservoir seal rocks: implications for the security of long-term CO_2 storage in the Weyburn field, *Geofluids*, *5*(4), 326-334.

Liang, W., C. Yang, Y. Zhao, M. B. Dusseault, and J. Liu (2007), Experimental investigation of mechanical properties of bedded salt rock, *Int. J. Rock Mech. Min. Sci.*, *44*, 400-411.

Lin, Y.-P., and P. C. Singer (2005), Effects of seed material and solution composition on calcite precipitation, *Geochim. Cosmochim. Acta*, *69*(18), 4495-4504.

Liteanu, E., and C. J. Spiers (2009), Influence of pore fluid salt content on compaction creep of calcite aggregates in the presence of supercritical CO_2, *Chem. Geol.*, *265*(1-2), 134-147.

Liu, L., Y. Suto, G. Bignall, A. Yamasaki, and T. Hashida (2003), CO_2 injection to granite and sandstone in experimental rock/hot water systems, *Energy Convers. Manage.*, *44*, 1399-1410.

Martens, J. H. C. (1931), Persistence of feldspar in beach sand, *Am. Miner.*, *16*, 526-531.

Matter, J. M., T. Takahashi, and D. Goldberg (2007), Experimental evaluation of in situ CO_2-water-rock reactions during CO_2 injection in basaltic rocks: Implications for geological CO_2 sequestration, *Geochem. Geophys. Geosyst.*, *8*(2).

Matthäi, S. K., and M. Belayneh (2004), Fluid flow partitioning between fractures and a permeable rock matrix, *Geophys. Res. Lett.*, *31*, L07602, DOI 10.1029/2003GL019027.

McBride, E. F., A. Abel-Wahab, and T. A. McGilvery (1996), Loss of sand-size feldspar and rock fragments along the South Texas Barrier Island, USA, *Sedim. Geol.*, *107*, 37-44.

McKelvy, M. J., A. V. G. Chizmeshya, K. Squires, R. W. Carpenter, and H. Béarat (2005), A novel approach to mineral carbonation: enhancing carbonation while avoiding mineral pretreatment process cost, 46 pp.

McKinnon, A. (2006), CO_2 emissions from freight transport in the UK, 57 pp., Logistics Research Centre, Heriot-Watt University, Edinburgh.

Michalske, T. A., and B. C. Bunker (1987), Steric effects in stress corrosion fracture of glass, *J. Am. Chem. Soc.*, *70*(10), 780-784.

Millero, F. J., J.-Z. Zhang, S. Fiol, S. Sotolongo, R. N. Roy, K. Lee, and S. Mane (1993), The use of buffers to measure the pH of seawater, *Mar. Chem*, *44*(2-4), 143-152.

Mirwald, P. W. (2008), Experimental study of the dehydration reactions gypsum-bassanite and bassanite-anhydrite at high pressure: Indication of anomalous

behavior of H_2O at high pressure in the temperature range of 50-300°C, *J. Chem. Phys.*, *128*(7), 074502-074507.

Mitchell, T. M., and D. R. Faulkner (2008), Experimental measurements of permeability evolution during triaxial compression of initially intact crystalline rocks and implications for fluid flow in fault zones, *J. Geophys. Res.*, *113,* B11412, DOI 10.1029/2008JB005588.

Mito, S., Z. Xue, and T. Ohsumi (2008), Case study of geochemical reactions at the Nagaoka CO2 injection site, Japan, *Int. J. Greenhouse Gas Control*, *2*(3), 309-318.

Mogi, K. (1966), Some precise measurements of fracture strength of rocks under uniform compressive strength, *Felsmech. Ingenieurgeol. (Rock Mech. Eng. Geol.)*, *4*, 41-55.

Mogi, K. (1971), Fracture and flow of rocks under high triaxial compression, *J. Geophys. Res.*, *76*(5), 1255-1269.

Montes-Hernandez, G., R. Pérez-López, F. Renard, J. M. Nieto, and L. Charlet (2009), Mineral sequestration of CO_2 by aqueous carbonation of coal combustion fly-ash, *J. Hazard. Mater., 161*(2-3), 1347-1354.

Moore, J., M. Adams, R. Allis, S. Lutz, and S. Rauzi (2005), Mineralogical and geochemical consequences of the long-term presence of CO_2 in natural reservoirs: an example from the Springerville-St. Johns Field, Arizona, and New Mexico, U.S.A., *Chem. Geol.*, *217*, 365-385.

Morrel, S. (2004), An alternative energy-size relationship to that proposed by Bond for the design and optimisation of grinding circuits, *Int. J. Miner. Process.*, *74*, 133-141.

Morrow, C. A., L. Q. Shi, and J. D. Byerlee (1984), Permeability of fault gouge under confining pressure and shear stress, *J. Geophys. Res.*, *89*(B5), 3193-3200.

Motavalli, P. P., C. A. Palm, W. J. Parton, E. T. Elliott, and S. D. Frey (1995), Soil pH and organic C dynamics in tropical forest soils: Evidence from laboratory and simulation studies, *Soil Bio. Biochem.*, *27*(12), 1589-1599.

Müller, N., R. Qi, E. Mackie, K. Pruess, and M. J. Blunt (2009), CO_2 injection impairment due to halite precipitation, *Energy Proc.*, *1*(1), 3507-3514.

Müller, P., and H. Siemes (1974), Festigkeit, verformbarkeit und gefügeregelung von anhydrit -- experimentelle stauchverformung unter manteldrucken bis 5 kbar bei temperaturen bis 300°C, *Tectonophysics*, *23*(1-2), 105-127.

Murakami, T., T. Kogure, H. Kadohara, and T. Ohnuki (1998), Formation of secondary minerals and its effect on anorthite dissolution, *Am. Miner.*, *83*, 1209-1219.

Nakashima, S. (1995), Diffusivity of ions in pore water as a quantitative basis for rock deformation rate estimates, *Tectonophysics*, *245*(3-4), 185-203.

Niemeijer, A. R., C. J. Spiers, and B. Bos (2002), Compaction creep of quartz sand at 400-600°C: experimental evidence for dissolution-controlled pressure solution, *Earth Planet. Sci. Lett.*, *195*(3-4), 261-275.

Niemeijer, A. R., and C. J. Spiers (2005), Influence of phyllosilicates on fault

strength in the brittle-ductile transition, in *High strain zones: structure and physical properties*, edited by D. Bruhn and L. Burlini, pp. 303-327, Geological Society of London, London, UK.

Nurmi, P. A. (1991), Geological setting, history of discovery and exploration economics of Precambrian gold occurrences in Finland, *J. Geochem. Explor.*, *39*, 273-287.

O'Connor, W. K., D. C. Dahlin, D. N. Nilsen, G. E. Rush, R. P. Walters, and P. C. Turner (2000a), CO_2 storage in solid form: a study of direct mineral carbonation, paper presented at Proceeding of 5th International Conference on Greenhouse Gas Technologies (GHGT-5), Cairns, Australia.

O'Connor, W. K., D. C. Dahlin, D. N. Nilsen, R. P. Walters, and P. C. Turner (2000b), Carbon dioxide sequestration by direct mineral carbonation with carbonic acid, paper presented at Proceedings of 25th International Technical Conference on Coal Utilization and Fuel Systems, Clearwater, Florida.

O'Connor, W. K., D. C. Dahlin, D. N. Nilsen, S. J. Gerdemann, G. E. Rush, L. R. Penner, R. P. Walters, and P. C. Turner (2002), Continuing studies on direct aqueous mineral carbonation for CO_2 sequestration, paper presented at Proceedings of 27th International Technical Conference on Coal Utilization and Fuel Systems, Clearwater, Florida.

O'Connor, W. K., D. C. Dahlin, G. E. Rush, S. J. Gerdemann, L. R. Penner, and D. N. Nilsen (2005), Aqueous mineral carbonation: mineral availability, pretreatment, reaction parametrics, and process studies, 20 pp.

Oelkers, E. H., and J. Schott (1995), Experimental study of anorthite dissolution and the relative mechanism of feldspar hydrolysis, *Geochim. Cosmochim. Acta*, *59*(24), 5039-5053.

Oelkers, E. H. (2001), An experimental study of forsterite dissolution rates as a function of temperature and aqueous Mg and Si concentrations, *Chem. Geol.*, *175*, 485-494.

Oelkers, E. H., and J. Schott (2001), An experimental study of enstatite dissolution rates as a function of pH, temperature, and aqueous Mg and Si concentration, and the mechanism of pyroxene/pyroxenoid dissolution, *Geochim. Cosmochim. Acta*, *65*(8), 1219-1231.

Ogawa, M., and H. Kaiho (2002), Homogeneous precipitation of uniform hydrotalcite particles, *Langmuir*, *18*, 4240-4242.

Okamoto, I., X. Li, and T. Ohsumi (2004), Effect of supercritical CO_2 as the organic solvent on cap rock sealing performance for underground storage, *Energy*, *30*(11-12), 2344-2351.

Okamoto, I., T. Yajima, Y. Mizuochi, T. Kato, A. Ninomiya, and T. Ohsumi (2006), In-situ test on CO_2 fixation by serpentinite rock mass in Japan, paper presented at Greenhouse Gas Control Technologies 8, Trondheim, Norway.

Olgaard, D. L., S.-c. Ko, and T.-f. Wong (1995), Deformation and pore pressure in dehydrating gypsum under transiently drained conditions, *Tectonophysics*, *245*, 237-248.

Olsen, A. A. (2007), Forsterite dissolution kinetics: applications and implica-

tions for chemical weathering, 98 pp, Virginia Polytechnic Institute and State University, Blacksburg, Virginia.

Orr Jr., F. M. (2004), Storage of carbon dioxide in geologic formations, *J. Petrol. Technol.*, *56*(9), 90-97.

Oxburgh, R., J. I. Drever, and Y.-T. Sun (1994), Mechanism of plagioclase dissolution in acid solution at 25°C, *Geochim. Cosmochim. Acta*, *58*(2), 661-669.

Palandri, J. L., and Y. K. Kharaka (2005), Ferric iron-bearing sediments as a mineral trap for CO_2 sequestration: iron reduction using sulfur-bearing waste gas, *Chem. Geol.*, *217*, 351-364.

Palandri, J. L., R. J. Rosenbauer, and Y. K. Kharaka (2005), Ferric iron in sediments as a novel CO_2 mineral trap: CO_2-SO_2 reaction with hematite, *Appl. Geochem.*, *20*, 2038-2048.

Pallas, N. R., and B. A. Pethica (1983), The surface tension of water, *Colloids Surf.*, *6*(3), 221-227.

Parks, G. A. (1967), Aqueous surface chemistry of oxides and complex oxide minerals: isoelectric point and zero point of charge, in *Equilibrium concepts in natural water systems*, pp. 121-160.

Paterson, M. S., and T.-f. Wong (2005), *Experimental rock deformation: the brittle field*, 2nd ed., 347 pp., Springer, Berlin.

Pauwels, H., I. Gaus, Y. M. Le Nindre, J. Pearce, and I. Czernichowski-Lauriol (2007), Chemistry of fluids from a natural analogue for a geological CO_2 storage site (Montmiral, France): lessons for CO_2-water-rock interaction assessment and monitoring, *Appl. Geochem.*, *22*, 2817-2833.

Peach, C. J. (1991), Influence of deformation on the fluid transport properties of salt rocks, Ph.D. thesis, 238 pp, Utrecht University, Utrecht.

Peach, C. J., and C. J. Spiers (1996), Influence of crystal plastic deformation on dilatancy and permeability development in synthetic salt rock, *Tectonophysics*, *256*, 101-128.

Pearce, J. M., S. Holloway, H. Wacker, M. K. Nelis, C. Rochelle, and K. Bateman (1996), Natural occurrences as analogues for the geological disposal of carbon dioxide, *Energy Convers. Manage.*, *37*(6-8), 1123-1128.

Pearce, J. M., I. Czernichowski-Lauriol, C. A. Rochelle, N. Springer, E. Brosse, B. Sanjuan, K. Bateman, and S. Lanini (2000), How will reservoir and caprock react with injected CO_2 at Sleipner?: preliminary evidence from experimental investigations, paper presented at Greenhouse Gas Control Technologies 5, Cairns, Australia.

Perry, R. H., and D. W. Green (1987), *Perry's Chemical Engineers' Handbook*, 2240 pp., McGraw-Hill, New York.

Piantone, P., F. Bodénan, and L. Chatelet-Snidaro (2004), Mineralogical study of secondary mineral phases from weathered MSWI bottom ash: implications for modelling and trapping of heavy metals, *Appl. Geochem.*, *19*, 1891-1904.

Plechov, P. Y., T. A. Shishkina, V. A. Ermakov, and M. V. Portnyagin (2008), Formation conditions of allivalites, olivine-anorthite crystal enclaves, in the

volcanics of the Kuril-Kamchatka arc, *Petrology*, *16*(3), 232-260.

Plummer, L. N., and E. Busenberg (1982), The solubilities of calcite, aragonite and vaterite in CO_2-H_2O solutions between 0 and 90°C, and an evaluation of the aqueous model for the system $CaCO_3$-CO_2-H_2O, *Geochim. Cosmochim. Acta*, *46*, 1011-1040.

Pokrovsky, O. S., and J. Schott (2000), Kinetics and mechanism of forsterite dissolution at 25°C and pH from 1 to 12, *Geochim. Cosmochim. Acta*, *64*(19), 3313-3325.

Pokrovsky, O. S., S. V. Golubev, and J. Schott (2005), Dissolution kinetics of calcite, dolomite, and magnesite at 25°C and 0 to 50 atm *p*CO_2, *Chem. Geol.*, *217*(3-4), 239-255.

Pokrovsky, O. S., S. V. Golubev, J. Schott, and A. Castillo (2009), Calcite, dolomite and magnesite dissolution kinetics in aqueous solutions at acid to circumneutral pH, 25 to 150 °C and 1 to 55 atm pCO_2: New constraints on CO_2 sequestration in sedimentary basins, *Chem. Geol.*, *260*(3-4), 317-329.

Prigiobbe, V., G. Costa, R. Baciocchi, M. Hänchen, and M. Mazzotti (2009), The effect of CO_2 and salinity on olivine dissolution kinetics at 120°C, *Chem. Eng. Sci.*, *64*(15), 3510-3515.

Rau, G. H., and K. Caldeira (1999), Enhanced carbonate dissolution: a means of sequestering waste CO_2 as ocean bicarbonate, *Energy Convers. Manage.*, *40*(17), 1803-1813.

Rau, G. H., K. G. Knauss, W. H. Langer, and K. Caldeira (2007), Reducing energy-related CO_2 emissions using accelerated weathering of limestone, *Energy*, *32*, 1471-1477.

Rendek, E., G. Ducom, and P. Germain (2006), Carbon dioxide sequestration in municipal solid waste incinerator (MSWI) bottom ash, *J. Hazard. Mater.*, *128*(1), 73-79.

Rice, J. R. (1992), Fault stress states, pore pressure distributions, and the weakness of the San Andreas fault, in *Earthquake mechanics and transport properties of rocks*, edited by B. Evans and T.-F. Wong, pp. 475-503, Academic Press, London.

Roelofs, J. C. A. A., J. A. van Bokhoven, A. J. van Dillen, J. W. Geus, and K. P. de Jong (2002), The thermal decomposition of Mg-Al hydrotalcites: effect of interlayer anions and characteristics of the final structure, *Chem. Eur. J.*, *8*(24), 5571-5579.

Rosenbauer, R. J., T. Koksalan, and J. L. Palandri (2005), Experimental investigation of CO_2-brine-rock interactions at elevated temperature and pressure: Implications for CO_2 sequestration in deep-saline aquifers, *Fuel Process. Technol.*, *86*(14-15), 1581-1597.

Rubin, E. S., A. B. Rao, and C. Chen (2004), Comparitive assessments of fossil fuel power plants with CO_2 capture and storage, paper presented at Proceedings of 7th International Conference on Greenhouse Gas Control Technologies (GHGT-7), Vancouver, Canada.

Rutqvist, J., and C.-F. Tsang (2002), A study of caprock hydromechanical changes associated with CO_2-injection into a brine formation, *Environ. Geol.*, *42*, 296-305.

Rutqvist, J., J. Birkholzer, F. Cappa, and C. F. Tsang (2007), Estimating maximum sustainable injection pressure during geological sequestration of CO_2 using coupled fluid flow and geomechanical fault-slip analysis, *Energy Convers. Manage.*, *48*(6), 1798-1807.

Rutqvist, J., J. T. Birkholzer, and C.-F. Tsang (2008), Coupled reservoir-geomechanical analysis of the potential for tensile and shear failure associated with CO_2 injection in multilayered reservoir-caprock systems, *Int. J. Rock Mech. Min. Sci.*, *45*, 132-143.

Rutter, E. H. (1986), On the nomenclature of mode of failure transitions in rocks, *Tectonophysics*, *122*, 381-387.

Sass, B. M., N. Gupta, J. A. Ickes, M. H. Engelhard, D. R. Baer, P. Bergman, and C. Byrer (2002), Interaction of rock minerals with carbon dioxide and brine: a hydrothermal investigation, *J. Energy Environ. Res.*, *2*(1), 23-31.

Scholz, C. H., and R. Kranz (1974), Notes on dilatancy recovery, *J. Geophys. Res.*, *79*(14), 2132-2135.

Schrag, D. P. (2007), Preparing to Capture Carbon, *Science*, *315*(5813), 812-813.

Schuiling, R. D. (2006), Mineral sequestration of CO_2 and recovery of the heat of reaction, in *Macro-engineering: a challenge for the future*, edited by V. Badescu, R. B. Cathcart and R. D. Schuiling, 318 pp.

Schuiling, R. D., and P. Krijgsman (2006), Enhanced weathering: an effective and cheap tool to sequester CO_2, *Clim. Change*, *74*, 349-354.

Schulz, K. G., U. Riebesell, B. Rost, S. Thoms, and R. E. Zeebe (2006), Determination of the rate constants for the carbon dioxide to bicarbonate inter-conversion in pH-buffered seawater systems, *Mar. Chem.*, *100*, 53-65.

Schutjens, P. M. T. M. (1991), Experimental compaction of quartz sand at low effective stress and temperature conditions, *J. Geol. Soc. London*, *148*, 527-539.

Schweizer, C. (1999), Calciumsilikathydrat-Mineralien: Lösumgskinetik und ihr Einfluss auf das Auswwaschverhalten von Substanzen aus ein Ablagerung mit Rückständen aus Müllverbrennungsanlagen, 113 pp, Swiss Federal Institute of Science and Technology Zürich.

Shah, K. R., and T.-f. Wong (1997), Fracturing at contact surfaces subjected to normal and tangential loads, *Int. J. Rock Mech. Min. Sci.*, *34*(35), 727-739.

Shah, V., D. Broseta, and G. Mouronval (2008a), Capillary alteration of caprocks by acid gases, paper presented at SPE/DOE Improved Oil Recovery Symposium, Tulsa, Oklahoma, USA.

Shah, V., D. Broseta, G. Mouronval, and F. Montel (2008b), Water/acid gas interfacial tensions and their impact on acid gas geological storage, *Int. J. Greenhouse Gas Control*, *2*(4), 594-604.

Shiraki, R., and T. L. Dunn (2000), Experimental study on water-rock interactions during CO_2 flooding in the Tensleep Formation, Wyoming, USA, *Appl. Geochem.*, *15*, 265-279.

Skar, T., and F. Beekman (2003), Modelling the influence of tectonic compression

on the in situ stress field with implications for seal integrity: the Haltenbanken area, offshore mid-Norway, *Geological Society, London, Special Publications*, *212*(1), 295-311.

Soltanzadeh, H., and C. Hawkes (2008), Semi-analytical models for stress change and fault reactivation induced by reservoir production and injection, *J. Petrol. Sci. Eng.*, *60*, 71-85.

Soong, Y., D. L. Fauth, B. H. Howard, J. R. Jones, D. K. Harrison, A. L. Goodman, M. L. Gray, and E. A. Frommell (2006), CO_2 sequestration with brine solution and fly ashes, *Energy Convers. Manage.*, *47*(13-14), 1676-1685.

Sorai, M., T. Ohsumi, M. Ishikawa, and K. Tsukamoto (2007), Feldspar dissolution rates measured using phase-shift interferometry: Implications to CO_2 underground sequestration, *Appl. Geochem.*, *22*(12), 2795-2809.

Span, R., and W. Wagner (1996), A new equation of state for carbon dioxide covering the fluid region from the triple-point temperature to 1100K at pressures up to 800 MPa, *J. Phys. Chem. Ref. Data*, *25*(6), 1509-1596.

Spiers, C. J., S. De Meer, A. R. Niemeijer, and X. Zhang (2004), Kinetics of rock deformation by pressure solution and the role of thin aqueous films, in *Physico-chemistry of water in geological and biological systems*, edited by S. Nakashima, C. J. Spiers, L. Mercury, P. A. Fenter and J. M. F. Hochella, pp. 129-158, Univerisal Academy Press, Inc., Tokyo, Japan.

Stendal, H., and T. Ünlü (1991), Rock geochemistry of an iron ore field in the Divrigi region, Central Anatolia, Turkey - a new exploration model for iron ores in Turkey, *J. Geochem. Explor.*, *40*, 281-289.

Stormont, J. C., and J. J. K. Daemen (1992), Laboratory study of gas permeability changes in rock salt during deformation, *Int. J. Rock Mech. Min. Sci. Geomech. Abstr.*, *29*(4), 325-342.

Streit, J. E., and R. R. Hillis (2004), Estimating fault stability and sustainable fluid pressures for underground storage of CO_2 in porous rock, *Energy*, *29*, 1445-1456.

Suekane, T., T. Nobuso, S. Hirai, and M. Kiyota (2008), Geological storage of carbon dioxide by residual gas and solubility trapping, *Int. J. Greenhouse Gas Control*, *2*(1), 58-64.

Sutherland, H. J., and S. P. Cave (1980), Argon gas permeability of New Mexico rock salt under hydrostatic compression, *Int. J. Rock Mech. Min. Sci. Geomech. Abstr.*, *17*(5), 281-288.

Suto, Y., L. Liu, N. Yamasaki, and T. Hashida (2007), Initial behavior of granite in response to injection of CO_2-saturated fluid, *Appl. Geochem.*, *22*, 202-218.

Sverjensky, D. A., and N. Sahai (1998), Theoretical prediction of single-site enthalpies of surface protonation for oxides and silicates in water, *Geochim. Cosmochim. Acta*, *62*(23-24), 3703-3716.

Tanikawa, W., and T. Shimamoto (2009), Comparison of Klinkenberg-corrected gas permeability and water permeability in sedimentary rocks, *Int. J. Rock Mech. Min. Sci.*, *46*(2), 229-238.

Tangerman, H. (2009), Olivijn: de

knalgroene klimaatredder? (Olivine: the green saviour of the climate?), in *Kijk (in Dutch)*, published August 2009.

Timoshenko, S. (1940), *Theory of plates and shells*, 492 pp., McGraw-Hill Book Company, Inc., New York, USA.

TKRI (2004), Mineral Processing Catalog, 18 pp.

Tödheide, K., and E. U. Franck (1963), Das Zweiphasengebiet und die kritische Kurve im System Kohlendioxide-Wasser bis zu Drucken von 3500 bar, *Z. Phys. Chemie Neue Folge*, *37*, 387-401.

Ueda, A., K. Kato, T. Ohsumi, T. Yajima, H. Kaieda, H. Ito, D. Savage, R. Metcalfe, and H. Takase (2005), Experimental and theoretical studies on CO_2 sequestration into geothermal fields, paper presented at World Geothermal Congress, Antalya, Turkey.

Uehara, S.-i., and T. Shimamoto (2004), Gas permeability evolution of cataclasite and fault gouge in triaxial compression and implications for changes in fault-zone permeability structure through the earthquake cycle, *Tectonophysics*, *378*(3-4), 183-195.

Van Bergen, F., T. Tambach, C. Hofstee, and P. David (2008), Geochemical consequences of CO_2 injection in the Barendrecht and Barendrecht-Ziedewij gas fields, 77 pp., TNO.

Van de Sande, J. M. M., T. J. A. Reijers, and N. Casson (1996), Multidisciplinary exploration strategy in the northeast Netherlands Zechstein 2 Carbonate play, guided by 3D seismic, in *Geology of gas and oil under the Netherlands*, edited by H. E. Rondeel, D. A. J. Batjes and W. H. Nieuwenhuijs, pp. 125-142, Kluwer Academic Publishers, Dordrecht, the Netherlands.

van der Lee, J., L. De Windt, V. Lagneau, and P. Goblet (2002), Presentation and application of the reactive transport code Hytec, in *Computational methods in water resources*, edited by S. M. Hassanizadeh, R. J. Schotting, W. G. Gray and G. F. Pinder, pp. 599-606, Elsevier.

van der Lee, J., L. De Windt, V. Lagneau, and P. Goblet (2003), Module-oriented modeling of reactive transport with HYTEC, *Comput. Geosci.*, *29*(3), 265-275.

Van der Meer, L. G. H., E. Kreft, C. R. Geel, D. D'Hoore, and J. Hartman (2006a), CO_2 storage and testing enhanced gas recovery in the K12-B reservoir, paper presented at 23rd World Gas Conference Amsterdam, the Netherlands.

Van der Meer, L. G. H., E. Kreft, C. R. Geel, D. D'Hoore, and J. Hartman (2006b), Enhanced gas recovery testing in the K12-B reservoir by CO_2 injection, a reservoir engineering study, 6 pp.

van Noort, R., C. J. Spiers, and G. M. Pennock (2008), Compaction of granular quartz under hydrothermal conditions: Controlling mechanisms and grain boundary processes, *J. Geophys. Res.*, *113,* B12206, DOI 10.1029/2008JB005815.

Voormeij, D. A., and G. J. Simandl (2002), Geological and mineral CO_2 sequestration options: a technical review, *Geological Fieldwork*, *Paper 2003-1*, 265-275.

Walderhaug, O., and P. A. Bjørkum

(1992), Effect of meteoric water flow on calcite cementation in the Middle Jurassic Oseberg Formation, well 30/3-2, Veslefrikk Field, Norwegian North Sea, *Mar. Petrol. Geol.*, *9*, 308-318.

Walsh, J. B., and W. F. Brace (1984), The effect of pressure on porosity and the transport properties of rock, *J. Geophys. Res.*, *89*(B11), 9425-9431.

Wang, H. F. (2000), *Theory of linear poroelasticity with applications to geomechanics and hydrogeology*, 287 pp., Princeton University Press.

Waring, C. L., and J. R. Taylor (2001), Applications of neutral barrier technology for greenhouse gas containment, paper presented at Proceedings of 5th International Conference on Greenhouse Gas Control Technologies (GHGT-5).

Wawersik, W. R., J. W. Rudnicki, P. Dove, J. Harris, J. M. Logan, L. Pyrak-Nolte, F. M. Orr Jr., P. J. Ortoleva, F. Richter, N. R. Warpinski, J. L. Wilson, and T.-f. Wong (2001), Terrestrial sequestration of CO_2: an assessment of research needs, *Adv. Geophys.*, *43*, 97-177.

Wesch, A., N. Dahmen, and K. E. J. Schön (1997), Grenzflächenspannungen, Tropfengrößen und Kontaktwinkel im Zweiphasensystem H_2O/CO_2 bei Temperaturen von 298 bis 333 K und Drücken bis 30 MPa, *Chemie Ingenieur Technik - CIT*, *69*(7), 942-946.

Wiederhorn, S. M., and H. Johnson (1973), Effect of electrolyte pH on crack propagation in glass, *J. Am. Chem. Soc.*, *56*(4), 192-197.

Wilkinson, M., and M. D. Dampier (1990), The rate of growth of sandstone-hosted calcite concretions, *Geochim. Cosmochim. Acta*, *54*, 3391-3399.

Wogelius, R. A., and J. V. Walther (1991), Olivine dissolution at 25°C: effects of pH, CO_2, and organic acids, *Geochim. Cosmochim. Acta*, *55*, 943-954.

Wogelius, R. A., and J. V. Walther (1992), Olivine dissolution kinetics at near-surface conditions, *Chem. Geol.*, *97*, 101-112.

Wolf, G. H., A. V. G. Chizmeshya, J. Diefenbacher, and M. J. McKelvy (2004), In situ observation of CO_2 sequestration reactions using a novel microreaction system, *Environ. Sci. Technol.*, *38*, 932-936.

Wong, T.-f., C. David, and W. Zhu (1997), The transition from brittle faulting to cataclastic flow on porous sandstones: mechanical deformation, *J. Geophys. Res.*, *102*(B2), 3009-3025.

Wu, S. Z., K. T. Chau, and T. X. Yu (2004), Crushing and fragmentation of brittle spheres under double impact test, *Powder Technology*, *143-144*, 41-55.

Xiao, Y., and A. C. Lasaga (1994), Ab initio mechanical studies of the kinetics and mechanisms of silicate dissolution: H^+ (H_3O^+) catalysis, *Geochim. Cosmochim. Acta*, *58*(24), 5379-5400.

Xu, T., J. A. Apps, and K. Pruess (2004), Numerical simulation of CO_2 disposal by mineral trapping in deep aquifers, *Appl. Geochem.*, *19*, 917-936.

Xu, T., J. A. Apps, and K. Pruess (2005), Mineral sequestration of carbon dioxide in a sandstone-shale system, *Chem. Geol.*, *217*, 295-318.

Xu, T., E. Sonnenthal, N. Spycher, and K. Pruess (2006), TOUGHREACT--A simulation program for non-isothermal multiphase reactive geochemical transport in variably saturated geologic media: Applications to geothermal injectivity and CO_2 geological sequestration, *Comput. Geosci.*, *32*(2), 145-165.

Yamamoto, H., and G. C. Kennedy (1969), Stability relations in the system $CaSO_4$-H_2O at high temperatures and pressures, *Am. J. Sci.*, *267A*, 550-557.

Yang, D., Y. Gu, and P. Tontiwachwuthikul (2008), Wettability determination of the reservoir brine-reservoir rock system with dissolution of CO_2 at high pressures and elevated temperatures, *Energy Fuels*, *22*(1), 504-509.

Young, W. C., and R. G. Budynas (2002), *Roark's formulas for stress and strain*, 736 pp., McGraw-Hill, New York, USA.

Zerai, B., B. Z. Saylor, and G. Matisoff (2006), Computer simulation of CO_2 trapped through mineral precipitation in the Rose Run Sandstone, Ohio, *Appl. Geochem.*, *21*, 223-240.

Zhang, J., T.-f. Wong, and D. M. Davis (1990), Micromechanics of pressure-induced grain crushing in porous rocks, *J. Geophys. Res.*, *95*(B1), 341-352.

Zhang, S., S. F. Cox, and M. S. Paterson (1994), The influence of room temperature deformation on porosity and permeability in calcite aggregates, *J. Geophys. Res.*, *99*(B8), 15761-15775.

Zhang, S., T. E. Tullis, and V. J. Scruggs (1999), Permeability anisotropy and pressure dependency of permeability in experimentally sheared gouge materials, *J. Struct. Geol.*, *21*(7), 795-806.

Zhang, X., and C. J. Spiers (2005), Compaction of granular calcite by pressure solution at room temperature and effects of pore fluid chemistry, *Int. J. Rock Mech. Min. Sci.*, *42*, 950-960.

Zhu, W., and T.-f. Wong (1999), Network modeling of the evolution of permeability and dilatancy in compact rock, *J. Geophys. Res.*, *104*(B2), 2963-2971.

Zoback, M. D., and J. D. Byerlee (1975a), The effect of microcrack dilatancy on the permeability of Westerly granite, *J. Geophys. Res.*, *80*(5), 752-755.

Zoback, M. D., and J. D. Byerlee (1975b), The effect of cyclic differential stress on dilatancy in Westerly granite under uniaxial and triaxial conditions, *J. Geophys. Res.*, *80*(11), 1526-1530.

Zweigel, P., and L. K. Heill (2003), Studies on the likelihood for caprock fracturing in the Sleipner CO_2 injection case - a contribution to the Saline Aquifer CO_2 Storage (SACS) project, 27 pp., SINTEF Petroleum Research.

Samenvatting voor de leek

Bij de verbranding van fossiele brandstoffen (steenkool, aardolie en aardgas) komen grote hoeveelheden CO_2 vrij. De uitstoot van deze, door menselijk handelen geproduceerde, CO_2 heeft als gevolg dat het CO_2-gehalte in de atmosfeer stijgt waardoor de (gemiddelde) temperatuur op aarde toeneemt (broeikaseffect). De sociale en economische gevolgen van klimaatverandering hebben er toe geleid dat er de laatste jaren veel aandacht is voor strategieën die de uitstoot van CO_2 in de atmosfeer kunnen verminderen. De Europese Commissie heeft voorgesteld om een reductie te willen bereiken van 30% ten opzichte van de CO_2-uitstoot in 1990 in 2020, en zelfs tot wel 80% in 2050.

Eén van de meest veelbelovende manieren om ons van CO_2 te ontdoen is via Carbon Capture and Storage (CSS, letterlijk Koolstof Afvang en Opslag). Dit houdt in dat CO_2 wordt afgevangen bij de bron (voornamelijk energiecentrales), om vervolgens voor lange tijd op grote diepte (enkele km's) opgeslagen te worden. Mogelijke opslaglocaties zijn onder andere lege olie- en gasvelden, waterhoudende gesteentelagen en diepe steenkoollagen. De eerste optie is vooral interessant voor landen met een uitgebreide olie- en gasproductie en -transport infrastructuur, zoals Nederland.

Maar wat houdt het nou precies in om CO_2 in een leeg olie- of gasveld op te slaan? Een olie- of gasveld bestaat uit een reservoir (een poreuze gesteentelaag, waar zich de olie of het gas bevindt) met daarop een laag ondoorlatend gesteente dat het reservoir als het ware afdekt en voorkomt dat olie of gas kan ontsnappen. Zodra alle winbare olie en gas uit een reservoir gehaald is, kan er (vloeibaar) CO_2 in de beschikbare ruimte gepompt worden. Van nature bevatten olie- en gasreservoirs ook CO_2, in Nederland ongeveer 10%. Daarnaast zijn er wereldwijd natuurlijke CO_2-velden bekend, met soms wel 90% puur CO_2 dat zich al duizenden jaren diep in de ondergrond bevindt. De aanwezigheid van CO_2 in reservoirs diep onder het oppervlak is dus geen nieuw concept. Ondergrondse opslag van CO_2 door de mens wel.

Voordat er met ondergrondse opslag van CO_2 begonnen kan worden, dient er wel rekening mee gehouden te worden dat op de langere termijn een aantal chemische

en mechanische processen in gang kunnen worden gezet in het reservoir en/of de deklaag. Sommige van deze processen, zoals mineralisatie reacties, kunnen ertoe leiden dat (een deel van) de CO_2 opgeslagen kan worden in vaste vorm (als een mineraal). Andere echter zouden kunnen leiden tot lekkage van de deklaag en het langzaam ontsnappen van CO_2 terug naar de atmosfeer. Het is belangrijk dat deze processen eerst onderzocht worden.

Mijn werk heeft zich vooral toegespitst op het verkrijgen van een fundamenteel begrip van het effect van CO_2 opslag op mineralisatie reacties en mogelijke langere termijn effecten die plaats kunnen vinden in het reservoir en de deklaag als het gevolg hiervan. De effecten van druk veranderingen, ten gevolge van ondergrondse CO_2 injectie, op het reservoirgesteente en de overliggende, afdichtende gesteentelagen zijn eveneens onderzocht.. Aangezien het werk deel uit maakt van het nationale project CATO (CO_2 Afvang, Transport en Opslag) ligt de nadruk op twee voor Nederland belangrijke gesteentetypen: 1) zandsteen, als potentieel reservoirgesteente, en 2) anhydriet (een zout), als mogelijk dekgesteente voor toekomstige opslaglocaties.

Het eerste deel van dit proefschrift (hoofdstukken 2 en 3) legt de nadruk op de chemische en mechanische effecten van CO_2 opslag in zandsteenreservoirs. De resultaten van de experimenten laten zien dat mineralisatie reacties sterk afhankelijk zijn van de mineraalinhoud van het gesteente, aangezien alleen reactie met specifieke mineralen zal zorgen voor de vorming van CO_2-rijke mineralen (zoals $CaCO_3$, kalksteen). Daarnaast zijn de reacties langzaam en kan het honderden jaren duren voordat vastlegging van CO_2 door mineralen een rol gaat spelen. Verder laten de resultaten zien dat mechanische effecten, zoals inklinking en bodemverzakking, niet versterkt zullen worden door de injectie van CO_2.

Het tweede deel van mijn werk (hoofdstukken 4 en 5) concentreert zich op de effecten van drukveranderingen in het reservoir op de afdichtende kwaliteit van de deklaag. Experimenten, gecombineerd met mechanische berekeningen, laten zien dat het onwaarschijnlijk is dat, binnen de te verwachten drukveranderingen, de deklaag zal breken of doorlatend zal worden als het gevolg van CO_2 opslag. Het effect van lange termijn reacties (reacties van CO_2 met de afdeklaag) op de sterkte van afdeklagen zal in de toekomst nog verder onderzocht moeten worden.

Het laatste gedeelte van mijn onderzoek (hoofdstuk 6) is een reactie op een idee van Emeritus Prof. R.D. Schuiling dat veel media aandacht heeft gekregen in de afgelopen jaren (zie Financieel Dagblad, juni 2007; NRC Handelsblad, augustus 2007; Kijk, augustus 2009). Het concept bestaat uit het delven en verpulveren van grote hoeveelheden olivijn (een mineraal), om het vervolgens op stranden te verspreiden waar oplossing van olivijn in het zeewater ervoor zal zorgen dat meer CO_2 uit de atmosfeer wordt opgenomen door de zee. Er wordt gesuggereerd dat het verspreiden

van olivijn met een korrelgrootte van 0.1-0.3 mm (zand) op het strand binnen enkele tientallen jaren ervoor kan zorgen dat alle menselijke uitstoot van CO_2 gecompenseerd zal worden met deze methode. Op deze manier zou CCS overbodig zijn.

Gezien het gebrek aan enige (openbare) kwantitatieve onderbouwing en de grote interesse vanuit de media is mij gevraagd enkele berekeningen uit te voeren aan het voorstel. Belangrijke punten waar naar gekeken is, zijn:

1. Wat is de oplossnelheid van olivijn?
2. Als we binnen 15-20 jaar resultaat willen boeken, is olivijn van 0.1-0.3 mm korrelgrootte dan haalbaar?
3. Hoeveel CO_2 wordt er uit gestoten bij het delven, verpulveren en transporteren van de olivijn, de zogenaamde CO_2 voetafdruk?
4. Hoeveel olivijn zou er wereldwijd nodig zijn om alle CO_2 uitstoot te compenseren?

Gebruikmakend van de voorhanden zijnde literatuur, samen met enkele berekeningen, is gebleken dat olivijn zand niet snel genoeg zal oplossen (200-700 jaar) om een significante bijdrage te leveren. Om op korte termijn resultaat te boeken is zeer fijn olivijn nodig (10 tot 30 keer fijner, stof). Dit kan mogelijk gezondheidsproblemen opleveren in verband met asbest dat van nature aanwezig is in olivijn-houdend gesteente. Daarentegen is de CO_2 voetafdruk tijdens het delven, verpulveren en transporteren (van locaties als Groenland, Noorwegen en Turkije) acceptabel en zal deze ongeveer 10-20% bedragen van de hoeveelheid CO_2 die met deze methode wordt opgenomen. Echter, er zal per jaar ongeveer 5.000.000.000 ton olivijn gedolven, vermalen en getransporteerd moeten worden om de gewenste reductie in CO_2 uitstoot (-30% voor 2020) te bewerkstelligen. Dit staat gelijk aan 3800 scheepsladingen (van 25.000 ton per stuk) per week, terwijl de huidige wereldvloot bestaat uit slechts 2000 schepen van dit formaat. De conclusie is dan ook dat het verspreiden van olivijn geen vervanging kan zijn voor CCS en hooguit op zeer kleine schaal toepasbaar is.

Acknowledgements

“Thanks...

Wow, you made it to the last pages of my thesis (or did you just skip everything else to get to the good part - now be honest!). Though the acknowledgements are usually not the largest part of a book, they are definitely not unimportant as it gives the author the chance to reminisce on all the people that have come on his/her way in the process. As with many things in life, you never get where you are on your own. In my case, I would therefore very much like to thank the people at the HPT-lab, my sponsors at Shell, friends and family.

First of all, a big thanks goes out to my supervisor Chris Spiers. By now we go “way back”, ever since you lured me away from my interest for geochemistry and introduced me to rock mechanics in your *Continuum Mechanics* class. It is probably the best thing that happened to me during my study, because I love it - there is nothing better than breaking rocks! Ofcourse, the learning curve continued (and steepened) during my PhD - I believe that is even true for the both of us. I wouldn’t have gotten where I am now without the endless discussions, motivational speeches and kick-in-the-butts. Thank you for helping me get to where I am now.

When working in the lab, I had a lot of help from Colin Peach, especially when working on the Heard apparatus. You know all the ins and outs - literally - of all the machinery in the lab and were never too busy to share that knowledge. I truly enjoyed learning how to work with the Heard apparatus and the permeametry set-up.

I guess I had the least contact with Hans de Bresser, though our contact increased when we started the weekly PhD-meetings. You were always interested in my progress, even though you were not so much involved in my project. And ofcourse, as already mentioned many times before, your experience with microstructural analysis has been a big help when I would get stuck again in the maze of cracks and fracs.

None of the experiments performed for this thesis would ever have been done without the help of our technicians. When I started my PhD, the lab was relatively new to working with CO_2 and most of the equipement needed to be adapted or built. Ofcourse, as with all new things, this resulted in interesting surprises as CO_2 has the tendency to make working set-ups go south...- oh, it leaks...again...it’s not supposed

to...sh*t. Our technicians Eimert de Graaff, Gert Kastelein, Peter van Krieken and Thony van der Gon have always done an excellent job to create, modify, fix or assist with all the equipement in the lab. They can be proud of the different set-ups they created over the past years, as not many labs in the world can say they can do these types of experiments.

Also thank you to Magda Marthens, our secretary, who always helped with any administratieve issues that are intertwinned with doing a PhD - I did hand in all my hour-sheets, didn't I? Saskia ten Grotenhuis spend quite some time with me behind the SEM to analyse my samples. She and Quintijn Clevis were also so kind to help me prepare for my interviews, which was a big help! Pieter Kleingeld helped me to get samples to Tokyo to get analysed, and Otto Stiekema prepared the many thin sections produced during my research. I also had "my" students who participated in my project: Leslie, Willemijn, Christiaan and Alwin. I hope I taught you as much as you taught me.

I would also like to thank the people from my sponsor *Shell International Exploration and Production* in Rijswijk, who have taken a serious interest in my project (and me) over the past few years: Claus Otto, Nadja Müller, Rick Wentinck, Niels van Wageningen, Conxita Taberner, Suzanne Hurter (now at Schlumberger) and Michiel Groeneveld (now at the University of Twente).

The people I met through the *CATO programme* have introduced me to the world behind CCS, which has left me intrigued as there is so much more to it than "just pumping some gas into the ground". Getting in contact with (expert) people on other aspects involved with CCS has shown me the many, many subtleties involved with this potential solution for global warming. Therefore, thanks to Erik Lysen, Sander van Egmond, Henk Pagnier, Frank van Bergen and Joris Koornneef, amongst many others.

I am grateful to my reviewing committee for their very positive feedback on my manuscript: Prof. Andy Hajash, Prof. Phil Meredith, Prof. Teng-fong Wong, Prof. Wim Turkenburg and Dr. John Kaszuba.

At work, I spent most of my less-serious-work-time with my fellow PhD's: Emilia, Reinier, Sander, Esther, Sabine and Sabrina. We would go for coffee at Gutenberg's (so much better than that bogwater from the machine), enjoy the sandwiches at Tricolore or have some fiery discussions over lunch - work-related or other.

On D-Day, I will be backed-up by my colleague and friend Reinier, who will be one of my paranymphs. We have spend over 8000 hours in the same office during my/our PhD(s) - I did the math! Remember how we sometimes called it an office-marriage, I guess it's time for a divorce, honey... ☺ We have had many good times, and also some lesser ones when we both were too stressed out about our work. I was your paranimph a little over a year ago, and I trust you will do great as mine! I wish

you all the best on your current and future research - remember what Jorge said: Post-doc is a valid job substitute! (and he is right).

My other paranimph will be Emilia, with whom I spend a lot of hours outside of the office as well and who has become one of my best friends. OMG, Emi... how did that come about?? - just kiddin'- We are so different, but it is great to have you as my friend. Sweetie, we kicked ass together these past 4 years (The CO_2 Twins - Emazing Emi and SuperSu), it was great to have someone at more or less the same stage in her PhD. Somebody to complain, cry and laugh with, to do crazy dancing with on weird Romanian tunes at Tivoli, making cakes with (eating cakes with), or just getting drunk at België (where else?). Coffee Company at 15.30h this weekend?? Bizzz

A ginormous thanks goes out to the rest of my friends, who managed to put up with me during all this time. I know I haven't always been easy to be around, especially when the heat was on and I started to forget about that other life, outside of research! Lucy, our weekly dinners have really been a great help in keeping me in touch with reality, you will always be my psychologist ☺. Wanneer kom je mijn afwas weer eens doen, ik kook!!. Maartje, lief vriendinnetje, whenever we are together (either in the flesh or virtually - long live Skype!) it's fun and I miss having you around for our usual cup-a-tea afternoons. No matter where you are (or where I will be), I will come and visit you! Annejan, we met just before I started this PhD at the lousiest job on the planet. Since then we have had many discussions on life, love and the troubles of the soul and I hope we have many more in the future (now I finally have time for it again). Kristen (Lill'Bit, I wouldn't dare to call you Kris), we met so shortly before you had to leave again, but we had a great time together. I miss our fake-boyfriend-arrangement, going to our yoga classes and me coming over to your place to feed you dinner after Brad had to go back to the US (you would have starved otherwise, I'm sure of it).

Of course there have been many more friends that stuck around all these years. We have had a lot of fun times, going out for drinks, movies, lunches or dinners: Sake, Hein, Dineke, Rolf (wanneer is de volgende conferentie??), Ineke, Veya, Brad, Savvas, Côme (Mr. Frenchie), Laurie, Ahmet, Wiebke, Baresh and Peter.

Last, but definitely not least, I would like to thank my family. Mam, pap, ontzettend bedankt voor jullie steun al deze jaren, geloof me, ik had het nodig! Het was fijn om te weten dat ik altijd thuis even stoom kon komen afblazen. Kaatje, jij bent mijn favoriete zusje. Ik ben ontzettend trots op wat je zelf allemaal bereikt hebt en ik wens je veel geluk samen met Jeroen. Het is niet altijd even makkelijk geweest voor ons als familie de afgelopen jaren, maar ik denk dat het ons uiteindelijk dichter tot elkaar heeft gebracht. Ik hou van jullie…

Suzanne

And now the work begins
And now the joy begins
Now the years of preparation
Of tedious study and
Exciting learning are explained.

The jumble of words and
Tangle of great and small ideas
Begin to take order and
This morning you can see
A small portion of the large
Plan of your future.

Make a difference
Use this degree which you
Have earned to increase
Virtue in your world

You will be surprised that in time
The days of single-minded research
And the nights of crippling, cramming
Will be forgotten.

You will be surprised that these years of
Sleepless nights and months of uneasy
Days will be rolled into
An altering event called the
"Good old days". And you will not
Be able to visit them even with an invitation
Since that is so you must face your presence.

You are prepared
Go out and transform your world

Congratulations

- taken from *Commencement Address* in *Letters to my daughter*
by Maya Angelou -

“Curriculum Vitae

Suzanne Johanna Theodora Hangx was born on the 12th of July 1981 in Weert, the Netherlands. In this city in southern Holland she went to primary school and high school. In 1999, she acquired her high school diploma at the Philips van Horne Scholengemeenschap in Weert. In the same year, she moved to Utrecht and began her studies in Geology at Utrecht University, the Netherlands. Though initially interested in Geochemistry, she eventually obtained her MSc. degree (with distinction) with a specialisation in Rock Mechanics and Earth Materials in 2004. Her MSc. project left her intrigued by CO_2 storage and fluid-rock interaction, and by the end of 2004 she started her PhD project on geological storage of CO_2 at the HPT-laboratory at Utrecht University. This got her submerged in a world filled with rock mechanics, fluid-rock interaction, CO_2 injection, climate change and politics. She got the opportunity to present her work at international conferences, universities and companies, where it was received very positively. After 4.5 years, this thesis is the fruitful result of her work performed at the HPT-laboratory.